



**FRIEDRICH-SCHILLER-  
UNIVERSITÄT  
JENA**

---

# **Searching for runaway stars in twelve Galactic supernova remnants**

---

**DISSERTATION**

zur Erlangung des akademischen Grades  
doctor rerum naturalium (Dr. rer. nat.)

vorgelegt dem Rat der  
PHYSIKALISCH-ASTRONOMISCHEN FAKULTÄT  
der  
FRIEDRICH-SCHILLER-UNIVERSITÄT JENA

von

**M. Sc. Oliver Lux**

geboren am 17.03.1988 in Witten

Jena, 07.01.2021

GUTACHTER:

1. Prof. Dr. Ralph Neuhäuser

*Astrophysikalisches Institut und Universitäts-Sternwarte  
Friedrich-Schiller-Universität Jena*

2. Prof. Dr. Ulrich Heber

*Dr. Karl Remeis-Sternwarte  
Friedrich-Alexander-Universität Erlangen-Nürnberg*

3. Assoc. Prof. Mgr. Ernst Paunzen, Dr.

*Department of Theoretical Physics and Astrophysics  
Masaryk University Brno*

TAG DER DISPUTATION: 22.06.2021

# Abstract

Runaway stars are moving faster than typical field stars and can be ejected either from dynamical interactions in dense stellar systems or clusters, or from supernova explosions disrupting binary or multiple systems. In this dissertation, we try to identify young runaway stars within supernova remnants from core-collapse supernovae. A clear identification of a runaway star will yield the exact time and place of the supernova as well as pre-supernova binary parameters. We then also get insights into the kinematic effects of supernovae and supernova remnant expansion. Previous studies mainly focused on O- and B-type runaway stars because they are always young in absolute terms, namely not much older than the lifetime of the supernova progenitor (up to about 32 million years), and easier to find. Also, it is assumed that supernova progenitors (i.e. massive stars) usually have massive companion stars. We also search for late-type, i.e. low-mass runaway stars, attempting to constrain their fraction among all runaway stars. We used *Gaia* data to identify runaway candidates in twelve nearby supernova remnants. With the VLT and the Subaru telescope, we took spectra of 39 runaway star candidates, e.g. to search for the lithium 6708 Å absorption line, which is a youth indicator for stars with the spectral types F, G, K and M. We found lithium in the spectra of eleven stars, but a clear identification of a runaway star ejected from a core-collapse supernova was not possible. We present the spectral analysis, including measurements of radial velocities, atmospheric parameters and lithium abundances. Then we estimate the ages of our targets from the Hertzsprung-Russell diagram and with the lithium test, present a selection of promising runaway candidates from *Gaia* data, discuss our findings in the individual supernova remnants and draw constraints on the number of ejected runaway stars compared to model expectations. The work is accompanied by H $\alpha$  images of supernova remnants, taken at the University Observatory Jena, which are presented in the appendix. We determined the light centres in these images, yielding estimates of the explosion sites, which should be compared to light centres in different wavelengths in the future. The averaged centre positions could then be used for future searches for runaway stars.



# Zusammenfassung

Schnellläufersterne bewegen sich schneller als typische Feldsterne. Sie können entweder durch dynamische Wechselwirkungen in dichten stellaren Systemen beziehungsweise Sternhaufen oder durch Supernovae in Doppel- oder Mehrfach-Sternsystemen freigesetzt werden. In der vorliegenden Dissertation sollen junge Schnellläufersterne identifiziert werden, die sich innerhalb der Überreste von Kernkollaps-Supernovae befinden. Eine Verknüpfung zu einem Schnellläuferstern ergibt den genauen Zeitpunkt und Ort der Supernova sowie die Parameter des vorherigen Doppelsternsystems. Wir erhalten dann auch Erkenntnisse zu den kinematischen Effekten einer Supernova und der Ausdehnung eines Supernova-Überrests. Vorherige Arbeiten haben sich hauptsächlich mit Schnellläufersternen der Spektraltypen O und B beschäftigt, da diese immer jung, nämlich nicht viel älter als die Lebensdauer des Vorläufersterns (bis zu etwa 32 Millionen Jahren), und einfacher zu finden sind. Zudem wird vermutet, dass Supernova-Vorläufer (d.h. massereiche Sterne) in der Regel auch massereiche Partnersterne haben. Wir suchen hingegen auch nach Spät-Typ Schnellläufersternen (massearm), um ihren Anteil an allen Schnellläufersternen einzugrenzen. Mit *Gaia*-Daten wurden Schnellläufer-Kandidaten in zwölf nahen Supernova-Überresten identifiziert. Mit dem VLT und dem Subaru-Teleskop wurden Spektren von 39 Schnellläufer-Kandidaten aufgenommen, um beispielsweise nach der Lithium 6708 Å Absorptionslinie zu suchen, die für Sterne der Spektralklassen F, G, K und M als Indikator für ein geringes Alter genutzt werden kann. In den Spektren von elf Sternen wurde Lithium gefunden, jedoch konnte letztlich kein Kandidat zweifelsfrei als Schnellläuferstern von einer Kernkollaps-Supernova bestätigt werden. Wir zeigen die Spektralanalyse, inklusive Messungen der Radialgeschwindigkeit, atmosphärischer Parameter und des Lithium-Gehalts. Mithilfe des Hertzsprung-Russell-Diagramms und des Lithium-Tests schätzen wir das Alter der beobachteten Sterne ab. Anschließend präsentieren wir eine Auswahl vielversprechender Schnellläufer-Kandidaten aus *Gaia*-Daten, diskutieren unsere Ergebnisse für die einzelnen Supernova-Überreste und grenzen die Zahl freigesetzter Schnellläufersterne im Vergleich zu Modellrechnungen ein. Im Anhang enthält die Arbeit zudem  $H\alpha$ -Bilder von Supernova-Überresten, die an der Universitäts-Sternwarte Jena aufgenommen wurden. Wir ermittelten die Lichtschwerpunkte in diesen Bildern, was Abschätzungen der Explosionsorte ermöglicht, die

---

in Zukunft mit Lichtschwerpunkten aus verschiedenen Wellenlängen verglichen werden sollten. Die gemittelten Zentren können dann für zukünftige Suchen nach Schnellläufersternen genutzt werden.

# List of Figures

2.1	Onion shell structure . . . . .	8
2.2	Overview of stellar evolution . . . . .	10
2.3	Hertzsprung-Russell diagram with evolutionary tracks . . . . .	11
2.4	Supernova classification scheme . . . . .	13
2.5	Comparison of different supernova light curves . . . . .	18
2.6	Composite image of Cassiopeia A . . . . .	20
2.7	SNRs of different morphological types . . . . .	21
2.8	High-mass binary evolution . . . . .	28
2.9	Velocity distribution of young <i>Hipparcos</i> stars . . . . .	30
3.1	Positions of the SNRs in the Galaxy . . . . .	39
3.2	Centre of the Vela SNR from different wavelengths . . . . .	42
3.3	2D kinematics of a runaway star candidate . . . . .	43
3.4	Hertzsprung-Russell diagram (HRD) of the runaway star candidates to exclude giants . . . . .	45
3.5	Surface gravity versus effective temperature of the runaway star candidates to exclude giants . . . . .	46
4.1	Schematic layout of UVES . . . . .	51
5.1	Spectra of the six Li stars between $\sim 6700 \text{ \AA}$ and $6730 \text{ \AA}$ . . . . .	58
5.2	Disentangling the spectrum of the double-lined spectroscopic binary TYC159-251-1 . . . . .	59
5.3	Absorption lines of TYC8152-550-1 for fitting the atmospheric parameters . . . . .	63
5.4	Quadratic fits to extrapolate curves of growth for Li $6708 \text{ \AA}$ . . . . .	66
5.5	Li equivalent widths in open clusters . . . . .	70
5.6	HRD of the observed stars in comparison to isochrones . . . . .	72
5.7	Zoom-in of Fig. 5.6 and HRD with low-metallicity isochrones and TYC159-343-1 . . . . .	74

## LIST OF FIGURES

---

5.8	$T_{\text{eff}}$ versus $EW_{\text{Li}}$ for the Li stars in comparison to stellar clusters . . . . .	77
5.9	Li abundances of the six Li stars, compared to Pleiades and Hyades stars . . . . .	79
6.1	The runaway star candidates in the Vela SNR . . . . .	90
6.2	The runaway star velocity distribution from a population synthesis . . . . .	91
6.3	The runaway star candidates in the investigated SNRs – Part 1 . . . . .	96
6.4	The runaway star candidates in the investigated SNRs – Part 2 . . . . .	97
B.1	Spectral format for our setup at HDS/Subaru . . . . .	B2
B.2	Overscan regions of the HDS/Subaru CCDs . . . . .	B3
B.3	Bias images for HDS/Subaru . . . . .	B3
B.4	Master bias images for HDS/Subaru . . . . .	B4
B.5	Master flatfields for HDS/Subaru . . . . .	B5
B.6	Normalised master flatfields for HDS/Subaru . . . . .	B6
B.7	2D HDS spectrum of TYC3344-124-1 before flatfielding . . . . .	B6
B.8	ThAr frame for HDS/Subaru wavelength calibration . . . . .	B8
B.9	89th echelle order from the ThAr line atlas for HDS/Subaru . . . . .	B8
B.10	Wavelength calibration – fitting . . . . .	B9
B.11	Normalisation and wavelength calibration for TYC3344-124-1 . . . . .	B10
B.12	<i>Kepler</i> workflow for the reduction of UVES data . . . . .	B12
B.13	Spectrum location for HD 261393 . . . . .	B14
B.14	Wavelength calibration for HD 261393 . . . . .	B15
B.15	Spectrum extraction for HD 261393 . . . . .	B16
C.1	Comparison of the Li stars to standard star spectra . . . . .	C2
C.2	Comparison of the early-type candidates to standard star spectra . . . . .	C3
D.1	Determination of radial velocities with <i>IRAF</i> . . . . .	D4
E.1	<i>iSpec</i> : Continuum normalisation parameters . . . . .	E2
E.2	<i>iSpec</i> : Continuum normalisation – fitted continuum . . . . .	E2
E.3	<i>iSpec</i> : Barycentric correction . . . . .	E3
E.4	<i>iSpec</i> : Determination of radial velocities . . . . .	E3
E.5	<i>iSpec</i> : Atmospheric parameter fits . . . . .	E4
E.6	<i>iSpec</i> : Atmospheric parameter fits for the Li-rich stars around $H\alpha$ . . . . .	E5
E.7	<i>iSpec</i> : Atmospheric parameter fits for TYC159-251-1 A and B around $H\alpha$ . . . . .	E6
H.1	$H\alpha$ observing frames for SNR G119.5+10.2 . . . . .	H2
H.2	$H\alpha$ image processing for IC 443 . . . . .	H7



---

H.3	H $\alpha$ image of IC 443 with geometry, geometric centre and light centre . . . . .	H9
H.4	H $\alpha$ images – Part 1 . . . . .	H14
H.5	H $\alpha$ images – Part 2 . . . . .	H15
H.6	H $\alpha$ images – Part 3 . . . . .	H16
H.7	H $\alpha$ images – Part 4 . . . . .	H17
H.8	GSH images of the Crab nebula . . . . .	H18

## LIST OF FIGURES

---

# List of Tables

2.1	Properties of nuclear burning stages in a $15 M_{\odot}$ star . . . . .	8
2.2	Historical supernovae . . . . .	12
2.3	Phases of SNR evolution . . . . .	24
3.1	Positions, sizes and radio fluxes of the SNRs studied in this work . . . . .	40
3.2	Distances, ages and spectral type limits of the SNRs studied in this work . . . . .	41
3.3	Post-MS stars rejected from the analysis . . . . .	47
4.1	List of stars observed with UVES/VLT . . . . .	54
4.2	List of stars observed with HDS/Subaru . . . . .	56
5.1	Velocities of the lithium stars and the early-type runaway candidates . . . . .	61
5.2	Atmospheric parameters of the Li stars . . . . .	64
5.3	Parameters of the quadratic fits to extrapolate curves of growth for Li 6708 Å . . . . .	65
5.4	Li equivalent widths and abundances of the Li stars . . . . .	66
5.5	Effective temperatures, spectral types and magnitudes of the Li stars and remaining early-type candidates . . . . .	73
5.6	Ages of the Li stars and the remaining early-type candidates, estimated from the Hertzsprung-Russell diagram . . . . .	75
5.7	Ages of the Li stars, estimated from the Li depletion test . . . . .	78
6.1	Numbers of runaway candidates with $G < 17$ mag in the SNRs covered in this work . . . . .	82
6.2	List of detected runaway star candidates . . . . .	83
B.1	Gain of HDS/Subaru CCDs . . . . .	B2
C.1	Spectral types of UVES targets in comparison to standard stars . . . . .	C2
D.1	RV determination for the remaining early-type runaway candidates . . . . .	D2
D.2	RV determination for TYC159-251-1 . . . . .	D3

## LIST OF TABLES

---

F.1	<i>Gaia</i> DR2 data of the observed stars – Positions and kinematics . . . . .	F2
F.2	<i>Gaia</i> DR2 data of the observed stars – Magnitudes and stellar parameters . . . .	F3
F.3	<i>StarHorse</i> parameters of the observed stars . . . . .	F4
F.4	Calculated parameters of the observed stars . . . . .	F5
F.5	<i>Gaia</i> DR2 data of the runaway candidates – Positions and kinematics . . . . .	F6
F.6	<i>Gaia</i> DR2 data of the runaway candidates – Magnitudes and stellar parameters . . . .	F8
F.7	<i>StarHorse</i> parameters of the runaway candidates . . . . .	F10
F.8	Calculated parameters of the runaway candidates . . . . .	F12
G.1	Effective temperatures of the Li-rich stars and the remaining early-type candidates . . . . .	G2
H.1	Overview of SNRs observed in $H\alpha$ . . . . .	H3
H.2	Overview of the SNR observers . . . . .	H4
H.3	Results of the analysis of SNR $H\alpha$ images . . . . .	H10
I.1	Overview of observed SNR frames . . . . .	I2

# Notation and Abbreviations

The following abbreviations are used across the thesis and most of them will also be introduced when they appear the first time:

## General abbreviations

AD	Anno Domini	JD	Julian date
AGB	Asymptotic giant branch	LMXB	Low-mass X-ray binary
BC	Barycentric correction	LSR	Local standard of rest
BES	Binary supernova ejection scenario	MS	Main-sequence
BH	Black hole	NS	Neutron star
BJD	Barycentric Julian date	PSR	Pulsar
CEP	Common-envelope phase	PWN	Pulsar wind nebula
CMD	Colour-magnitude diagram	RA	Right ascension
DEC	Declination	RGB	Red giant branch
DES	Dynamical ejection scenario	RLO	Roche-lobe overflow
EW	Equivalent width	RMS	Root mean square
FOV	Field of view	RV	Radial velocity
FWHM	Full width at half maximum	SB2	Double-lined spectroscopic binary
GC	Geometric centre	S/N	Signal-to-noise ratio
HMXB	High-mass X-ray binary	SN	Supernova
HRD	Hertzsprung-Russell diagram	SNR	Supernova remnant
HVS	Hypervelocity star	UT	Universal time
IMF	Initial mass function	WD	White dwarf
IMXB	Intermediate-mass X-ray binary	WR	Wolf-Rayet (star)
ISM	Interstellar medium	ZAMS	Zero-age main-sequence

**Instrumentation, Organisations and catalogues**

ADC	Atmospheric dispersion corrector
ADU	Analog digital units
ASTRO	( <i>Gaia</i> ) Astrometric Instrument
CCD	Charge-coupled device
CD	Cross-disperser
DR	( <i>Gaia</i> ) Data Release
DSS	(ESO) Digitized Sky-Survey
ESA	European Space Agency
ESO	European Southern Observatory
ETC	Exposure time calculator
FLECHAS	Fibre Linked ECHelle Astronomical Spectrograph (at GSH)
GSH	Großschwabhausen
HDS	High-Dispersion Spectrograph (at NAOJ Subaru Telescope)
HST	<i>Hubble</i> Space Telescope
ILLSS	Identification list of lines in stellar spectra (catalogue)
IRAF	Image Reduction and Analysis Facility
NAOJ	National Astronomical Observatory of Japan
NASA	National Aeronautics and Space Administration
RVS	( <i>Gaia</i> ) Radial Velocity Spectrometer
STK	Schmidt Teleskop Kamera (at GSH)
TGAS	<i>Tycho-Gaia</i> Astrometric Solution
ThAr	Thorium-Argon (lamp for spectral wavelength calibration)
UofM	University of Manitoba (catalogue)
UVES	Ultraviolet and Visual Echelle Spectrograph (at ESO VLT)
VLT	Very Large Telescope (ESO)

**Chemical elements**

Ar	Argon	He	Helium	Ni	Nickel
C	Carbon	Li	Lithium	O	Oxygen
Ca	Calcium	Mg	Magnesium	Si	Silicon
Co	Cobalt	N	Nitrogen	S	Sulfur
Fe	Iron	Ne	Neon	Th	Thorium
H	Hydrogen				

## Units

Besides the SI-units (International System of Units) and the metric prefixes, we use the following SI-derived units, cgs-units (centimetre-gram-second system) and further special units that are common in astronomy. Angular distances are usually given in  $^{\circ}$ ,  $'$  and  $''$ . For clarity, arcminutes are often given as arcmin, e.g. in table headers, milli-arcseconds are always given as mas.

1 Å	= $10^{-10}$ m = 0.1 nm	Ångstrom
1 AU	= $1.4960 \times 10^{11}$ m	Astronomical unit
1 d	= 86400 s	Day
1 dex	= $10^1$	Order of magnitude (for dimensionless quantities)
1 erg	= $10^{-7}$ J	(cgs-unit of energy)
1 eV	= $1.6022 \times 10^{-19}$ J	Electron-volt
1 G	= $10^{-4}$ T = $10^{-4}$ kg A $^{-1}$ s $^{-2}$	Gauss (magnetic flux density)
1 h	= 3600 s	Hour
1 Hz	= $1$ s $^{-1}$	Hertz
1 Jy	= $10^{-26}$ W Hz $^{-1}$ m $^{-2}$	Jansky (spectral flux density)
1 $L_{\odot}$	= $3.828 \times 10^{26}$ W	Solar luminosity
1 $M_{\odot}$	= $1.989 \times 10^{30}$ kg	Solar mass
mag	$m_1 - m_2 = -2.5 \log(\frac{L_1}{L_2})$	Logarithmic brightness scale
1 mas	= $10^{-3}$ arcsec	Milli-arcsecond
1 min	= 60 s	Minute
1 pc	= $3.0857 \times 10^{16}$ m	Parsec
1 yr	= 365.2242 d = $3.1557 \times 10^7$ s	(Tropical) year

Further abbreviations refer to star names, e.g. HD 37424 is an object from the *Henry Draper* catalogue (Cannon and Pickering, 1993) and TYC8150-2802-1 is from the *Tycho-2* catalogue (Høg et al., 2000). Terms like *Ori* (Orion), *Aur* (Auriga), *Col* (Columba) and *Sgr* (Sagittarius) refer to the constellation where an object is located. Greek letters give the brightness rank of the star within the constellation. Then there are the stellar spectral types O, B, A, F, G, K, M, in order of decreasing effective temperature. The term *OB association* refers to a stellar group that contains stars with spectral types O and B. When giving individual stellar spectral types, these main designations are usually followed by an Arabic numeral for the subtype and/or a Roman numeral for the luminosity class, e.g. G2 V in the case of the sun. Abbreviations in the names of supernova remnants have various origins and are not explained for each one in detail. In the case of spectral lines, we often give the corresponding ionisation state and/or wavelength in addition to the chemical element, e.g. Li I 6707.8 Å (not ionised) or Fe II (single ionised).





*to my dad*



*„Die Tatsache, dass man etwas über den Himmel  
weiß, ändert an seinem Zauber nichts.“*

— Harald Lesch —

Originalzitat

*”The fact that you know something about the  
sky does not change its magic.“*

— Harald Lesch —

Free English translation



# Contents

<b>1</b>	<b>Introduction</b>	<b>3</b>
<b>2</b>	<b>Basics</b>	<b>7</b>
2.1	Evolution of massive stars . . . . .	7
2.2	Supernovae . . . . .	12
2.3	Supernova remnants . . . . .	18
2.4	Compact stellar remnants . . . . .	24
2.5	Binary systems . . . . .	26
2.6	Runaway stars . . . . .	29
<b>3</b>	<b>Candidate selection</b>	<b>35</b>
3.1	Catalogues . . . . .	35
3.2	Selection of supernova remnants . . . . .	38
3.3	Selection of runaway star candidates . . . . .	40
<b>4</b>	<b>Observations and data reduction</b>	<b>49</b>
4.1	VLT UVES . . . . .	49
4.2	Subaru HDS . . . . .	53
<b>5</b>	<b>Spectral analysis</b>	<b>57</b>
5.1	TYC159-251-1 – A new spectroscopic binary . . . . .	57
5.2	Radial and space velocities . . . . .	59
5.3	Atmospheric parameters . . . . .	61
5.4	Lithium equivalent widths and abundances . . . . .	64
5.5	Stellar ages . . . . .	67
5.6	Age estimation . . . . .	72
<b>6</b>	<b>Discussion</b>	<b>81</b>
6.1	Overview of the candidates . . . . .	81

## CONTENTS

---

6.2	Individual supernova remnants . . . . .	84
6.3	Constraints on runaway star production . . . . .	94
<b>7</b>	<b>Conclusions</b>	<b>99</b>
7.1	Summary . . . . .	99
7.2	Future prospects . . . . .	101
	<b>Appendix</b>	<b>A1</b>
<b>A</b>	<b><i>Python</i> code for the calculation of trajectories</b>	<b>A1</b>
<b>B</b>	<b>Data reduction</b>	<b>B1</b>
<b>C</b>	<b>Comparison to standard stars</b>	<b>C1</b>
<b>D</b>	<b>Determination of radial velocities with <i>IRAF</i></b>	<b>D1</b>
<b>E</b>	<b>Spectral analysis with <i>iSpec</i></b>	<b>E1</b>
<b>F</b>	<b>Additional data</b>	<b>F1</b>
<b>G</b>	<b>Effective temperatures</b>	<b>G1</b>
<b>H</b>	<b>H<math>\alpha</math> observations of supernova remnants</b>	<b>H1</b>
<b>I</b>	<b>Overview of the H<math>\alpha</math> observations</b>	<b>I1</b>
<b>J</b>	<b><i>Python</i> code for calculating SNR light centres</b>	<b>J1</b>
	<b>Bibliography</b>	<b>K1</b>
	<b>Additional Documents</b>	<b>L1</b>

# Chapter 1

## Introduction

Among the more than 100 billion stars in the Milky Way, the vast majority shows a continuous orbital motion around Sagittarius A\* (Sgr A\*), the supermassive black hole in the Galactic centre. This means that at a given place in the Galaxy most stars have quite similar velocities and directions. However, there are exceptions which seem to counteract the laws of Galactic rotation. They have different directions and often also higher velocities, some even exceeding the Galactic escape velocity. We are talking about runaway- and hypervelocity stars. Stellar astrophysicists become more and more interested in this exciting field which made a big leap forward with the first discovery of an associated pair of a runaway star and a neutron star (NS) in a supernova remnant (SNR) by Dinçel et al. (2015). SNRs are the birth sites of NSs and therefore also a convenient place to search for runaway stars (Guseinov et al., 2005), which can be ejected by the supernova (SN) explosion of a massive star in a binary system. By tracing the runaway star HD 37424 and the NS J0538+2817 back to a common origin close to the geometric centre (GC) of the SNR S147, Dinçel et al. (2015) were able to define the time and place of a pre-historical SN with unprecedented precision. Eight Galactic SNe were observed by mankind (by naked eye) within the last 2000 years, so their age is accurately known. However, for a precise localisation of the explosion site, a NS or a runaway star are required, which could be traced back over the corresponding time span to locate their origin. Besides HD 37424, Boubert et al. (2017) suggested three further likely runaway stars, namely TYC 2688-1556-1, BD+50 3188 and HD 261393 in the nearby SNRs Cygnus Loop, HB 21 and Monoceros Loop.

The scenario described above was first introduced by Blaauw (1961) and is called *binary supernova ejection scenario* (BES). A binary becomes unbound if more than half of the total system mass gets ejected during the SN. Another possibility to eject a runaway star are gravitational interactions in dense stellar environments or clusters. This scenario was described by Poveda et al. (1967) and is called *dynamical ejection scenario* (DES). Finally, the *Hills mecha-*

*nism* (Hills, 1988) is responsible for the highest stellar velocities. Dynamical interactions with Sgr A\* can accelerate stars to over  $1000 \text{ km s}^{-1}$ . These often exceed the local Galactic escape velocity and are then called hypervelocity stars (HVSs, Brown 2015). The three ejection scenarios are described in more detail in Section 2.6.

Previous searches for runaway stars mainly focused on O- and B-type stars. Their brightness makes them easier to find and observe and due to their high consumption of nuclear fuel they are always young in absolute terms. Youth is a requirement for runaway stars in core-collapse SNRs because its former companion star, the SN-progenitor, burns its fuel rapidly and SNRs are only visible for up to  $\sim 100 \text{ kyr}$ . The main-sequence (MS) lifetime of a star is given by the nuclear timescale for the fusion of hydrogen:

$$t_{\text{MS}} = t_{\odot} \left( \frac{M}{M_{\odot}} \right)^{-2.5}, \quad (1.1)$$

where we made use of the mass-luminosity relation  $L \propto M^{3.5}$  (as in Kippenhahn and Weigert 1990). The solar MS lifetime is  $t_{\odot} = 10^{10} \text{ yr}$ . So the MS lifetime of a SN progenitor which has  $M \gtrsim 8 M_{\odot}$  is  $t_{\text{MS}} \lesssim 55 \text{ Myr}$ . The subsequent burning cycles are much shorter (up to  $\sim 20 \%$ , see Table 2.1). Runaway stars outside of SNRs can be much older, finding their origin by tracing back their trajectory through the Galactic gravitational potential becomes more and more difficult for higher ages. Note that the MS lifetime inferred from Eqn. 1.1 is only a rough estimate. Stellar evolution models can yield more precise values. For our final decision if a runaway candidate is young enough (see Section 5.6), we use an upper limit of  $32 \text{ Myr}$ , obtained from Ekström et al. (2012, Table 3, corresponding to the lower mass limit  $M = 8 M_{\odot}$ ).

Searches for runaway stars outside of SNRs were e.g. done by Tetzlaff et al. (2010; 2011a; 2013; 2014a), who presented birth associations for 18 young NSs and assembled a catalogue of 2547 young runaway stars from the *Hipparcos* catalogue (Perryman et al., 1997). Hoogerwerf et al. (2000; 2001) traced back the trajectories of 56 runaway stars from *Hipparcos* data and suggested a common origin of the O-type star  $\zeta \text{ Oph}$  and the pulsar (PSR) B1929+10. Although this association was falsified by later works (Chatterjee et al., 2004; Tetzlaff et al., 2010; Zehe et al., 2018), the suggested BES origin set the ground for further studies of its origin which recently resulted in a major discovery: Neuhäuser et al. (2019) connected  $\zeta \text{ Oph}$  to PSR B1716–16 and traced both objects back to a common origin in Upper Centaurus Lupus. The SN that disrupted the system would have happened  $1.78 \pm 0.21 \text{ Myr}$  ago at a distance of  $d = 107 \pm 4 \text{ pc}$ . This is close enough that the SN could have contributed to radioactive  $^{60}\text{Fe}$  that was found in the Earth crust and ocean sediments, dated to have arrived at the Earth  $\sim 1.5\text{--}3.2 \text{ Myr}$  ago (Breitschwerdt et al., 2016; Knie et al., 1999; Wallner et al., 2016). The half-life of  $2.6 \text{ Myr}$  ensures that it must have an extraterrestrial origin. This discovery shows



how SNe can affect the Earth and that runaway stars can be used to identify such events.

The currently known SNRs are further away and will probably not deposit significant amounts of  $^{60}\text{Fe}$  onto the Earth crust, but identifying the explosion times and sites will allow detailed studies of their expansion and therefore of the enrichment of the interstellar medium (ISM) with heavy elements and new material for future generations of stars. SNe and their remnants will be introduced in Sections 2.2 and 2.3, respectively.

The goal of this doctoral thesis is to find more examples of runaway stars in SNRs to yield information about the evolution of massive binary systems (for the basics see Sections 2.1 and 2.5). When a runaway star is ejected by a supernova, it flies away with about its former orbital velocity. So we can determine the pre-SN orbital parameters using Kepler's third law. If the time since the SN is known, from observations of the SNR we can constrain SNR expansion models (see Section 2.3.2) and the distance of the runaway star will also be the most precise distance of the SNR (e.g. Dinçel et al. 2015). If a NS can be associated with the system, we can determine the kinematic age and infer further properties like the SN birth kick and the spin-velocity alignment (e.g. Noutsos et al. 2013). The explosion site and time can then also be determined much more precisely. Once a sufficiently high number of runaway stars is identified, one can compare the numbers of runaway stars ejected from binary SNe and from dynamical interactions. By also looking for late-type runaways, we try to derive constraints on the numbers of low-mass companions in massive binaries.

We perform spectroscopic observations to check the runaway nature of our candidates by determining the spectral type, the radial velocity (RV) and the atmospheric parameters. For late-type stars (mid-F to M), a low age is indicated by the existence of the resonance absorption line from the atmospheric, neutral lithium-7 ( $^7\text{Li}$ ) at  $6707.8 \text{ \AA}$  (see Section 5.5).

After presenting the candidate selection (Chapter 3), we describe the observations (Chapter 4) and the spectral analysis (Chapter 5). In Chapter 6, we will present our most promising runaway candidates and discuss the individual SNRs as well as the contributions of this work to the research field. Finally, we conclude the work in Chapter 7. In Appendix H, we also present a new approach for the determination of SNR GCs, for which we use  $\text{H}\alpha$  images obtained from the University Observatory Jena. This might help to better constrain SN explosion sites also in SNRs where no runaway stars or NSs are yet known.

Large parts of the Chapters 3–7 are based on our paper *A search for runaway stars in twelve Galactic supernova remnants* (Lux et al., 2021).

---

# Chapter 2

## Basics

Many different aspects of stellar astrophysics are important for the analysis of runaway stars ejected from core-collapse SNe. The evolution of the SN-progenitors, massive stars with  $M \gtrsim 8 M_{\odot}$ , is described in Section 2.1, for which we mainly use Carroll and Ostlie (2007) and Woosley et al. (2002) as references. The final point of their evolution is the SN<sup>1</sup>, discussed in Section 2.2. These events usually leave colourful nebulae of gas and dust, expanding into the surrounding ISM, presented in Section 2.3. The core of the extinguished star becomes a compact stellar remnant, a NS or a black hole (BH)<sup>2</sup>. These are described in Section 2.4. For the ejection of a runaway star during a core-collapse SN, a binary or multiple system is needed. Information about the fraction of multiple systems and the evolution of massive binary systems can be found in Section 2.5. Then we describe the production channels for runaway stars and the numbers expected from the BES in Section 2.6.

### 2.1 Evolution of massive stars

The most important parameter which rules the evolution of a star is its mass. The mass largely determines the lifetime of a star as given by Eqn. 1.1 and also its effective temperature (i.e. the spectral type), luminosity, nuclear burning yields and its death. A rough division can be made at  $M \approx 8 M_{\odot}$ . Stars with a lower mass, e.g. the Sun, have a relatively long MS lifetime (e.g. solar-mass stars have  $t_{\text{MS}} \approx 10$  Gyr) and after their MS they will expand to red giants, eventually igniting helium (He) if they are initially more massive than  $\sim 0.3 M_{\odot}$  (Kippenhahn and Weigert, 1990). At their final nuclear burning stages, they become more and more unstable, losing their local thermodynamic equilibrium. So they begin to lose their envelope in a

---

<sup>1</sup>Note that very massive stars could directly collapse to a black hole without undergoing a SN (see Woosley et al. (2002) for details).

<sup>2</sup>Note that very massive stars of  $\sim 130\text{--}260 M_{\odot}$  explode in a pair-instability SN which does not leave a compact remnant (Woosley et al., 2002).

## 2.1. Evolution of massive stars

TABLE 2.1: Properties of nuclear burning stages in a  $15 M_{\odot}$  star (Woosley et al. 2002; Pols 2009).

burning stage	$T$ [ $10^9$ K]	$\rho$ [ $\text{g/cm}^3$ ]	fuel	main products	$\tau$ [yr]
hydrogen	0.035	5.8	H	He	$1.1 \times 10^7$
helium	0.18	$1.4 \times 10^3$	He	C, O	$2.0 \times 10^6$
carbon	0.83	$2.4 \times 10^5$	C	O, Ne	$2.0 \times 10^3$
neon	1.6	$7.2 \times 10^6$	Ne	O, Mg	0.7
oxygen	1.9	$6.7 \times 10^6$	O, Mg	Si, S	2.6
silicon	3.3	$4.3 \times 10^7$	Si, S	Fe, Ni	$4.9 \times 10^{-2}$

pulsating manner over a relatively long time span, forming a planetary nebula, while their core with the nuclear burning yields (He or CO) remains as a *white dwarf* (WD), cooling over a long time span.

The final fate of stars with  $M \gtrsim 8 M_{\odot}$  looks very different. Their MS lasts only a few up to several tens of Myrs and they reach much higher core temperatures and densities, so that after He burning, carbon (C), neon (Ne), oxygen (O) and silicon (Si) will also be ignited, consecutively. At the same time, shell burning continues between the different layers. This leads to an *onion shell structure* (see Fig 2.1) with heavier and heavier elements towards the centre of the star. The star has expanded to a red supergiant. For stars with tens of solar masses, stellar wind mass loss plays a more and more important role, potentially stripping off the entire remaining H envelope. The star then becomes a *Wolf-Rayet* (WR) star (Woosley et al. 2002; Carroll and Ostlie 2007).

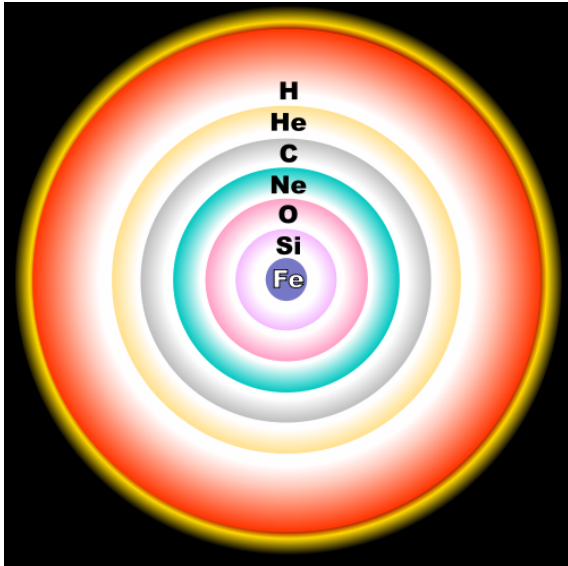


FIGURE 2.1: Onion shell structure of a massive star at the end of its life, just before the core-collapse. Figure taken from [hildaandtrojanasteroids.net](http://hildaandtrojanasteroids.net)<sup>3</sup>

<sup>3</sup>[http://hildaandtrojanasteroids.net/Evolved\\_star\\_fusion\\_shells.png](http://hildaandtrojanasteroids.net/Evolved_star_fusion_shells.png)

Table 2.1 summarises the temperatures  $T$ , densities  $\rho$ , timescales  $\tau$  and the involved elements of the nuclear burning stages of a  $15 M_{\odot}$  star (Woosley et al. 2002; Pols 2009). With increasing core temperature and density, heavier and heavier elements are burned on shorter and shorter timescales, accompanied by increasing neutrino losses, which contribute to shorten the timescales. Note that the timescale for O burning is higher than for Ne burning, which is mainly due to the higher mass fraction of O.

The last nuclear burning phase is Si burning, lasting only 18 days in the case of a  $15 M_{\odot}$  star (Woosley et al. 2002; Pols 2009) and producing a core consisting of  $^{56}\text{Fe}$  and

other isotopes of the iron group, though not via direct fusion of two  $^{28}\text{Si}$  atoms, but via a series of  $\alpha$  captures, gradually increasing the mean atomic weight of the nuclei in the core. Once a significant amount of iron group elements is produced, this means that the fusion processes come to a halt, because Fe and Ni are the most stable elements with the highest binding energy per nucleon, i.e. no energy can be gained from nuclear fusion. Due to the high core temperatures, photodisintegrations and electron captures strongly reduce the stabilising gas pressure, so that eventually the core collapses under its own gravity - the start of a core-collapse SN (see next section). The collapse of the Fe core leads either to the formation of a NS or, in the case of stars with  $M \gtrsim 25 M_{\odot}$ , of a BH (see Section 2.4).

Fig. 2.2 summarises the outcome of stellar evolution for Population I stars<sup>4</sup>. Depending on the initial mass, the final masses of the evolved star before (blue) and after (orange) the stellar death are shown. The final fate (i.e. the SN type) and the corresponding compact remnant are given, as well as the amount of mass loss and whether the star becomes a WR star. The typical divisions at  $\sim 8 M_{\odot}$  and  $\sim 25 M_{\odot}$  are indicated, between stars producing WDs, NSs and BHs. Note that stars with  $\sim 8-11 M_{\odot}$  mark a transition region. They can ignite C burning, but their core temperatures never reach high enough to ignite stable Ne and O burning. Therefore, they cannot form an Fe core and will not explode as a core-collapse SN. Instead, depending on their exact mass, composition and mass loss, they will either end as an ONeMg WD or experience unstable burning cycles (not in hydrostatic equilibrium), where eventually the Ne core will ignite by electron capture at the *Chandrasekhar* mass<sup>5</sup>, leading to an electron capture SN and leaving a NS (Woosley et al., 2002).

For  $M \gtrsim 30 M_{\odot}$ , the mass loss is so strong that the star may become a WR star. For very strong WR mass loss, indicated by the thin-dashed lines, there could even be a region from  $\sim 50-80 M_{\odot}$  where the remnant is a NS, encompassed by higher- and lower-mass stars that form BHs.

**Hertzsprung-Russell diagram.** The evolution of stars can be traced in the Hertzsprung-Russell diagram (HRD), where the brightness is plotted over the effective temperature (see Fig 2.3). Here one can display computed evolutionary tracks for stars of different masses, where the different burning cycles can be seen. After the pre-MS evolution (not shown here), which follows the *Hayashi* line ( $M \approx 0.08-3 M_{\odot}$ ) and/or the *Henyey* line ( $M \gtrsim 3 M_{\odot}$ ), the zero-age MS (ZAMS) is reached, indicated by the diagonal line on the left. The ZAMS is the starting

<sup>4</sup>The present generation of stars that formed in galactic discs, roughly having solar metallicity. In contrast, Population II stars are much older, can be found in galactic halos (mainly in globular clusters) and have significantly lower metallicities. Population III stars were the first generation of stars in the universe. They had zero metallicity, could have hundreds of solar masses and have long been extinct.

<sup>5</sup> $M_{\text{Ch}} = 1.4575 \times (2Y_e)^2 M_{\odot}$ , where  $Y_e$  is the mean number of electrons per nucleon (e.g. Woosley et al. 2002)

## 2.1. Evolution of massive stars

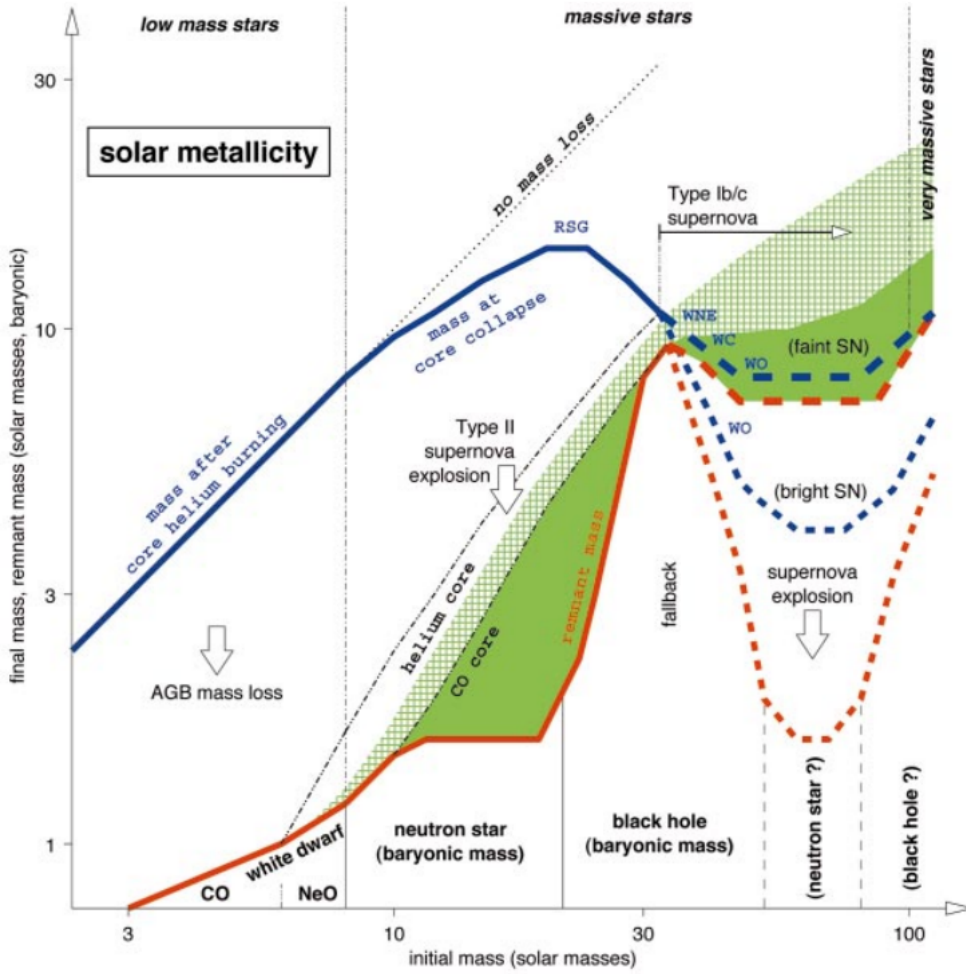


FIGURE 2.2: Final masses of a star after He burning (blue) and of its stellar remnant (orange) versus its initial mass. Also shown are the masses of the He- and CO-core, where the filled green colour shows regions of heavy-element synthesis and cross-hatched green shows regions of partial He burning to C and O. Figure taken from Woosley et al. (2002).

point of the MS, indicated by the left hatched area, where H is fused to He either via the proton-proton chain ( $M \lesssim 1.2 M_{\odot}$ ) or the CNO cycle ( $M \gtrsim 1.2 M_{\odot}$ , Carroll and Ostlie 2007). After core H exhaustion, the core contracts due to the gravitational pressure until further H has heated up sufficiently in order to start fusing in a shell around the core. The phase of H shell burning expands and cools the stellar envelope on the *sub-giant branch* and, after the first dredge-up, on the *red giant branch* (RGB). The onset of He core burning marks the next milestone in stellar evolution. Once a stable He core burning via the triple- $\alpha$  chain is established, the star is on a second MS, indicated by the right hatched area in Fig. 2.3. After He is exhausted in the core, the star enters the *asymptotic giant branch* (AGB). Also the potential subsequent burning cycles follow the same pattern of fuel exhaustion in the core, core contraction, ignition of shell burning and ignition of the next core burning, on shorter and shorter timescales. Shell burning

continues at all boundaries between fuels and ashes. Finally, the post-AGB corresponds to the end of the stellar life, where strong wind mass loss due to pulsations strips off the envelope until either a WD or a WR star is left, or a core-collapse SN terminates the process.

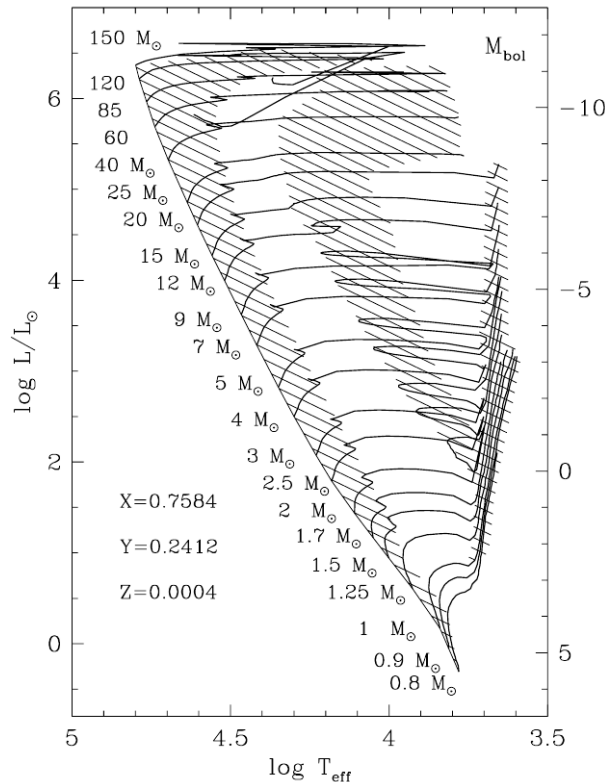


FIGURE 2.3: Hertzsprung-Russell diagram with evolutionary tracks, showing luminosity versus effective temperature for stars with different masses between  $0.8 M_{\odot}$  and  $150 M_{\odot}$ . The hatched areas show slow phases of nuclear core burning, i.e. the left hatched area corresponds to H core burning. The tracks are calculated for an initial He fraction of  $Y = 0.2412$  and metal fraction  $Z = 0.0004$  (the solar metal fraction is  $Z = 0.0152$ ; Bressan et al. 2012). Figure taken from Lejeune and Schaerer (2001).

The evolutionary tracks of massive stars in the HRD, however, do not look as complex as we would expect from the various burning cycles. The advanced burning cycles happen on such short timescales that they barely change the outer composition and appearance. Also, the *Humphreys-Davidson* luminosity limit (Carroll and Ostlie, 2007, p. 523) inhibits the evolution of the most massive stars to red supergiants. Additionally, different properties like metallicity and rotation have to be taken into account. A star with higher metallicity has a lower effective temperature compared to a star with the same mass and lower metallicity. Stellar rotation affects the mixing of elements inside the star and can enhance mass loss.

Besides evolutionary tracks, isochrones are an important tool in the HRD. These connect stars of different masses, having the same age. They are usually constructed from observations of stellar clusters, in which all stars have roughly the same age, in comparison to stellar evolution models. In Section 5.5 we will show how isochrones can be used to estimate stellar ages.

An alternative to the HRD is the colour-magnitude diagram (CMD), where photometric colour and absolute magnitude are plotted instead of temperature and luminosity. This is useful to plot observational data more quickly and without the necessity to apply a bolometric correction and determine the temperature. Mixed forms are possible, too, e.g. plotting temperature and absolute magnitude, as we will do in this thesis (see Section 5.6).

## 2.2. Supernovae

TABLE 2.2: Historical supernovae. The data were taken from Green and Stephenson (2003) and an unpublished table assembled by Ralph Neuhäuser. Further references are given as footnotes. The years are given in AD.

Year	Constellation	Mainly observed in	Max. $V$ mag.	SNR	d [kpc]	SN Type
1604	Oph	Europe (Kepler), Korea	$-3.0^1$	G004.5+06.8	$3.4^1$	Ia(?)
1572	Cas	Europe (Brahe), China	$-4.5^1$	G120.1+01.4	$2.35^1$	Ia
1181	Cas	China, Japan	$\sim 0.7^2$	G130.7+03.1	$2.9^{3,4}$	II
1054	Tau	China, Japan	$-4.8^5$	G184.6-05.8	$1.85^6$	II
1006	Lup	China, Japan, Arabia	$-7.5^7$	G327.6+14.6	$2.18^7$	Ia
393	Sco	China	$\sim -1 \pm 1^8$	G347.3-00.5(?)	$1.3^9$	(?)
386	Sgr	China	$\lesssim 2^{10}$	(?)	$4.4^{11}$	II
369	(?)	China	$\lesssim 2^{10}$	(?)	(?)	(?)
185	Cen	China	$-7.5 \pm 2^1$	(?)	$5.2^{12}$	Ia(?)

<sup>1</sup> Schaefer (1996a); <sup>2</sup> Schaefer (1996b); <sup>3</sup> Green and Gull (1982); <sup>4</sup> Bietenholz (2006); <sup>5</sup> Pskovskii (1978); <sup>6</sup> Davidson and Fesen (1985); <sup>7</sup> Winkler et al. (2003); <sup>8</sup> Wang et al. (1997); <sup>9</sup> Cassam-Chenaï et al. (2004), if SNR association is correct; <sup>10</sup> Stephenson and Green (2002), general limit for naked-eye detection of *guest stars*; <sup>11</sup> Kilpatrick et al. (2016); <sup>12</sup> Gaensler et al. (1999)

## 2.2 Supernovae

In the 16th century, it was believed that the sphere of fixed stars, i.e. every celestial body beyond the sun, the moon, the planets and transient phenomena like comets, that were assumed to be atmospheric, is unchanging. However, in 1572 AD a new star appeared in the sky, a *guest star*, which was observed by the Danish astronomer Tycho Brahe. Its position was clearly *fixed* within the sphere of other fixed stars, therefore challenging the *Aristotelian doctrine* that all visual changes on the celestial sphere must be related to sub-lunar phenomena (e.g. Green and Stephenson 2003). This discovery significantly contributed to the understanding that the universe is much larger than the Earth or the solar system.

The new development was pushed further by another guest star observation only 32 years later, carefully documented by Johannes Kepler who provided precise positional data. The guest stars described by Brahe and Kepler were the first SNe that were extensively observed in Europe. However, seven other historical SNe were observed much earlier already, mainly from China, Japan and Arabia (see Table 2.2).

Today we know that SNe do not only mark the end of a stellar life, but their pressure waves can also trigger star formation in nearby molecular clouds, where the ejected stellar material might serve as constituent of a new generation of stars.

### 2.2.1 Supernova types

Historically, SNe were divided in two subgroups according to their spectra at maximum brightness: SNe of Type I do not show H in their spectra, whereas SNe of Type II do. With an increasing number of SN light curves and spectra, more and more subclasses were established,



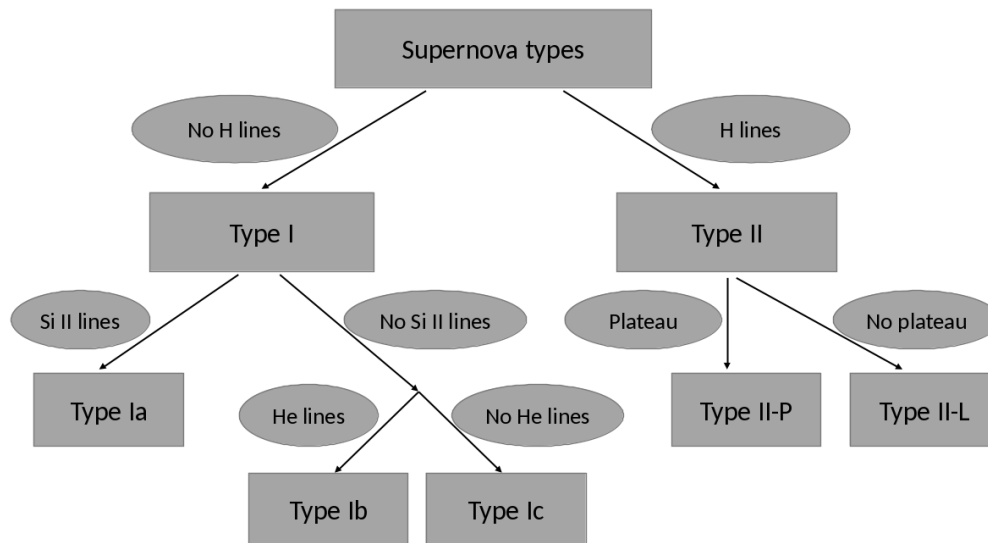


FIGURE 2.4: Supernova classification scheme based on Carroll and Ostlie (2007, Fig. 15.9).

e.g. Type Ib showing He lines or Type Ic not showing He lines. Today we can classify SNe by means of stellar evolution, considering the physical processes that lead to the explosion. Namely, we can divide between core-collapse and thermonuclear SNe. However, the naming of subtypes is still based on the historical scheme. Fig. 2.4 shows this classification scheme, based on Carroll and Ostlie (2007, Fig. 15.9). E.g., thermonuclear SNe (Type Ia) are characterised by a lack of H while showing strong Si II lines.

### Core-collapse supernovae

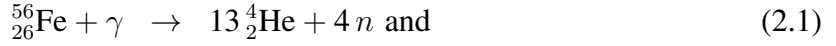
A core-collapse SN marks the final fate of a massive star. Phenomenologically, core-collapse SNe can be divided into Type II, Type Ib and Type Ic, depending on whether the progenitor star lost its H envelope before the explosion (Type Ib) or even its He envelope (Type Ic). Core-collapse SNe are only observed in spiral galaxies, in regions of recent star formation, because their progenitor stars die young and therefore do not travel far away from their birth sites.

As described in Section 2.1, in the late nuclear burning stages of massive stars, heavier and heavier elements are produced, eventually resulting in a core composition with nuclei of the iron group, in particular  ${}^{56}_{26}\text{Fe}$ , but also e.g.  ${}^{54}_{26}\text{Fe}$  or  ${}^{56}_{28}\text{Ni}$ . These elements represent a peak of binding energy per nucleon, so fusing even heavier elements would not contribute to the luminosity of the star. At the very high temperatures in the core during the phase of Si burning,

## 2.2. Supernovae

---

photons are energetic enough to destroy nuclei by *photodisintegration* reactions, e.g.



This endothermic process counteracts the nuclear burning processes and can lead to a nuclear statistical equilibrium which moves towards the iron group elements for increasing temperature. Just before the collapse, electrons begin to be captured by heavy nuclei and protons, producing neutrons and neutrinos:



This reaction is called *neutronisation* and starts at densities of  $10^{10} \text{ g cm}^{-3}$  (Woosley and Janka, 2005). Anti-neutrinos are also produced (by positron-capture of neutrons), as well as neutrinos of different flavours. Eventually, the degeneracy pressure of electrons is so strongly reduced that the core can no longer resist the gravitational pressure and begins to collapse rapidly. The collapse of the inner core is homologous, whereas the outer core exceeds the local sound speed, reaching up to  $70,000 \text{ km s}^{-1}$ , which leads to an inhomologous collapse, decoupling the layers. The collapse ends when the inner core density reaches  $\sim 8 \times 10^{17} \text{ kg m}^{-3}$ , where the neutron degeneracy pressure is able to stabilise the core against further collapse. At this stage, a proto-NS is formed (except for stars with  $\gtrsim 25 M_{\odot}$ , which continue collapsing to a BH). The core then rebounds and produces pressure waves which travel outwards, eventually forming a shock wave when exceeding the sound speed. However, this shock then loses most of its kinetic energy when it passes and heats the infalling heavy nuclei of the outer core, which leads to further photodisintegrations. The shock nearly comes to a halt only a few milliseconds after the bounce (Woosley and Janka, 2005), just consumes further infalling matter and is therefore called *accretion shock*. The picture changes again when further neutronisations behind the shock (in the inner region) lead to heating of the shocked material by neutrinos, which cannot easily penetrate the extremely dense material. So the shock can start to propagate outwards again, if the material is heated up quickly enough. Otherwise, the mass of the infalling matter will quickly cause the proto-NS to collapse to a BH and no explosion will happen.

Simulations often failed to reproduce the final explosion, as the efficiency of neutrino absorption and re-emission depends on the temperature- and density distribution around the proto-NS, as well as on rotation and magnetic fields. The latter might be required to provide the energy for sufficient heating, while neutrino heating alone might not be sufficient to explode the star (Woosley and Janka, 2005).

A typical core-collapse SN is described by three characteristic energies: (i) The total energy

is about  $10^{53}$  erg, of which 99 % are emitted as neutrinos. (ii) The kinetic energy drives the expansion of the ejected material and contributes  $\sim 1$  %, i.e.  $10^{51}$  erg = 1 bethe. (iii) As soon as the material becomes optically thin at about 100 AU (Carroll and Ostlie, 2007), the photon energy is released. Although with  $10^{49}$  erg this only contributes 0.01 % to the total energy, the luminosity of up to  $\sim 10^9 L_{\odot}$  is comparable to an entire galaxy.

It is suggested that very energetic SNe of stars with very high masses (often referred to as *hypernovae*) could be connected to the formation of a *long-soft gamma-ray burst*. In this scenario, ejected material forms a debris disk around a newly formed BH and accretion, together with strong magnetic fields, leads to the formation of a highly relativistic jet which produces the gamma-rays burst.

SN can be highly asymmetric. This depends on the exact composition, rotation and magnetic fields of the progenitor, but asymmetries can even occur for non-rotating stars, as convective streams during the first second after collapse may impart significant momentum on the newly formed NS (Woosley and Janka, 2005). This *birth kick* explains why NSs are much faster on average than regular stars. Also, the birth kick can support the disruption of a binary system.

### Thermonuclear supernovae

Thermonuclear SNe, including the phenomenological Type Ia, are, in contrast to core-collapse SNe, not related to the final fate of a massive star, but to a WD reaching a critical mass limit for explosive C burning, which is by chance very close to the *Chandrasekhar* limit. The mass growth can either be explained by accretion of matter from a MS- or red giant companion in a close binary system (single-degenerate scenario), or by merging with another WD (double-degenerate scenario).

In the single-degenerate scenario, a CO WD is in an orbit with a non-degenerate companion, which transfers mass onto the WD by *Roche lobe* overflow. As soon as the critical mass is reached, either the degenerate He ignites in a He flash, which consecutively triggers the ignition of C and O in the interior (*double-detonation scenario*, e.g. Livne 1990), or C and O ignite directly because the Fermi pressure of electrons can no longer support the mass of the WD. The Double-degenerate scenario assumes a close WD binary. The orbits of the components shrink because gravitational radiation carries away angular momentum. Eventually, the secondary (larger) WD will fill its Roche lobe and transfer mass to the primary via an accretion arm (García-Berro and Lorén-Aguilar, 2017), until it gets disrupted. The infalling material increases the accretor's mass beyond the *Chandrasekhar mass*, resulting in a detonation.

The advantage of the double-degenerate scenario is that it naturally describes the lack of H in the observed SN Type Ia spectra. On the other hand, simulations suggest that the WD-WD

merger should rather result in a collapse to a NS, not in a complete disruption, and the Type Ia light curves as well as observed abundances of heavy elements in the spectra can be better explained by the single-degenerate scenario (Carroll and Ostlie, 2007).

Since the explosion is triggered by reaching a well defined mass limit, all SNe Type Ia reach a very similar peak brightness of  $M_V \approx -19.3$  mag (Carroll and Ostlie, 2007). This allows to use them as *standard candles*, i.e. to determine the distance of their host galaxy with the distance modulus:

$$m - M = 5 \log(d/\text{pc}) - 5. \quad (2.4)$$

Here,  $m$  is the measured apparent brightness,  $M$  the constant absolute brightness and  $d$  the distance. This relation (converted to cosmological scales, i.e. taking redshift into account) was used to observe Type Ia SNe at high redshifts, proving that the expansion of the universe is accelerating (Perlmutter et al. 1998; Riess et al. 2007. Nobel Prize for Saul Perlmutter, Brian P. Schmidt, Adam G. Riess 2011).

In contrast to core-collapse SNe, thermonuclear SNe do not leave a compact remnant but entirely disrupt the star<sup>6</sup>. Another difference is that thermonuclear SNe can also be observed in regions without star formation, e.g. in elliptical galaxies or globular clusters.

Both the historical SNe observed by Tycho Brahe (1572) and Johannes Kepler (1604) as well as the exceptionally bright sighting of 1006 AD were of Type Ia (Reynolds et al. 2007; Koyama et al. 2008; Krause et al. 2008).

### 2.2.2 Supernova light curves

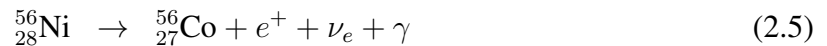
The brightness evolution of a SN is mainly determined by the following parameters: (i) Total kinetic energy, (ii) density profile and chemical composition of the progenitor, (iii) circumstellar material, e.g. from stellar wind mass loss, (iv) radioactive decay of isotopes that were produced and ejected by the explosion (Pols, 2009).

Fig. 2.5 shows that most SNe are characterised by a steep increase of the luminosity which is connected to the quick expansion of the radiating sphere, starting with the time where the sphere becomes optically thin. A pulse of soft X-rays is radiated at that point, lasting about 30 min. Type Ia SNe are brighter than core-collapse SNe and show an inverse correlation between peak brightness and the rate of decline (Phillips, 1993). Therefore, even if an observer misses the light-curve peak, the peak brightness and -time can be reconstructed from the rate of decline.

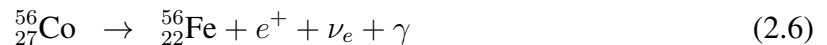
---

<sup>6</sup>Note that there are also subluminous SNe Type Ia, which are thought to leave a partially burnt WD remnant (Vennes et al., 2017)

The light curves of core-collapse SNe show a much higher diversity. The majority belongs to Type II-P, showing a plateau-shape. Their progenitors had moderate masses and kept most of their H-envelopes prior to the explosion. The plateau is mainly shaped by energy which the shock deposited in the H-rich envelope. After being ionised by the shock, the H atoms recombine continuously over a span of  $\sim 100$  d at a temperature of  $\sim 5000$  K. Subsequently, the light curve is governed by radioactive decay of particles that were mainly produced by the shock front interaction with the stellar material. Particularly relevant are the  $\beta^+$ -decays of  $^{56}_{28}\text{Ni}$ ,



with  $\tau_{1/2} = 6.1$  d, and of the decay product,  $^{56}_{27}\text{Co}$ ,



with  $\tau_{1/2} = 77.7$  d. When the decay of  $^{56}_{27}\text{Co}$  becomes dominant, the light curve flattens because the decay is slower. Other radioactive isotopes are produced as well, e.g. the results of the s- (slow-) and r- (rapid) neutron capture reactions<sup>7</sup> (e.g. Woosley et al. 2002). Depending on their abundance and half-life, they can also contribute to the light curve. Type II-L light curves correspond to progenitors which lost significant parts of their H-envelopes before, so that the signatures of the radioactive decay become visible almost immediately. Type Ia light curves are more strongly governed by radioactive decay because they generally produce a larger mass of iron-group elements ( $\sim 0.6 M_{\odot}$ , Vink 2012).

Further subtypes of Type II can be divided from their spectra, namely Type IIn which show narrow emission lines on top of the regular, broad emission lines, probably resulting from strong mass loss before the explosion, and Type IIb which change their spectral signatures from Type II to Type Ib (Pols, 2009).

The famous core-collapse SN observed in the *Large Magellanic Cloud*, SN 1987A, was the first SN from which neutrinos could be detected. Over a time span of 12.5 s, 20 neutrinos with energies between 8 MeV and 40 MeV yielded a glimpse of the neutronisation process during the collapse to a NS. Neutrinos are used as a precursor for SNe because due to their weak interactions with matter they can escape the exploding star hours before the photons. The photon light curve revealed that SN 1987A belonged to a further subtype of core-collapse SNe, namely it was sub-luminous. The progenitor was a  $20 M_{\odot}$  *blue* supergiant, i.e. much smaller and therefore denser than a *red* supergiant. Probably, at the time of explosion, it was on a blue

---

<sup>7</sup>The s-process forms elements heavier than Fe in environments with a low neutron density, e.g. during nuclear burning of a star. The formed isotope undergoes  $\beta$ -decay before it captures another neutron. The r-process rapidly forms very neutron-rich isotopes in neutron-rich environments like proto-neutron stars, where the neutron captures happen faster than  $\beta$ -decays.

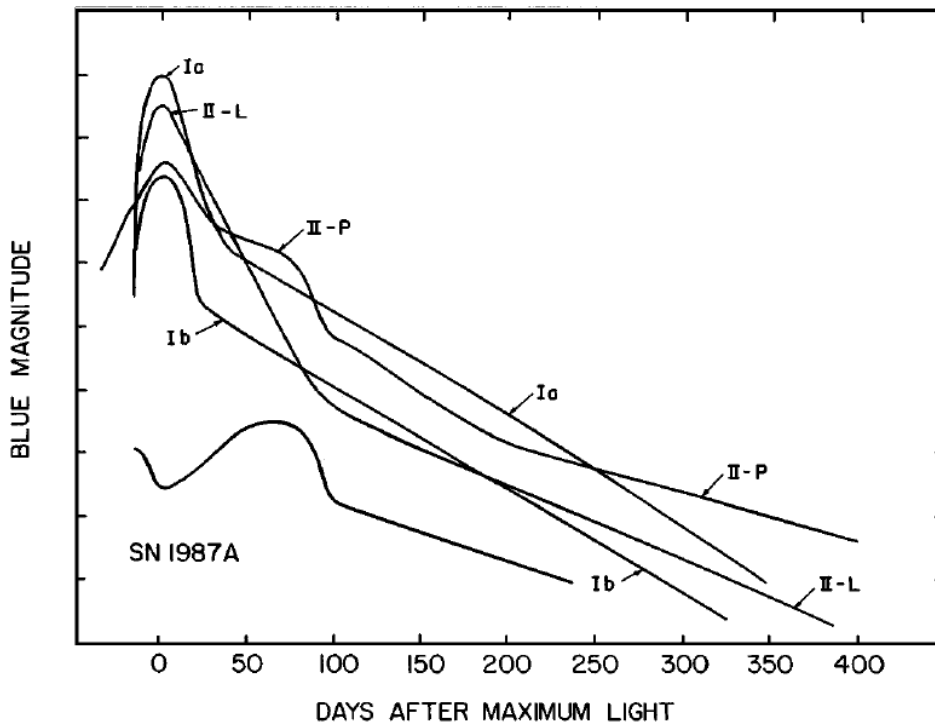


FIGURE 2.5: Comparison of different schematic supernova light curves. The curves were constructed from observational data, where the curve for SN Ib represents an average of Ib and Ic. The two SNe used for the SN II-L curve might have been over-luminous. Figure taken from Filippenko (1997).

loop, as shown in Fig. 2.3 for stars with  $\geq 40 M_{\odot}$ . Therefore, much more energy was required to lift the denser envelope and less energy was left to leave the scene as photons. The peak magnitude,  $M_{\text{bol}} = -15.5$  mag, was about 2.5 mag fainter than for typical Type II SNe and with  $\sim 80$  d the peak was only reached after a much longer time. On the other hand, extremely massive stars can explode in a *hypernova*, which can be even  $\sim 2$  mag brighter than a SN Type Ia.

A typical SN in the Milky Way remains visible for  $\sim 1-2$  yrs, until most of the radioactive isotopes are decayed. According to Green and Stephenson (2003), the historical SNe were visible between three months (SN 386) and three years (SN 1006).

## 2.3 Supernova remnants

After the fading of the SN light, the remaining witnesses of the stellar fatality are the supernova remnant (SNR), a cloud of ejected stellar material sweeping up the interstellar medium, and, in the case of a core-collapse SN, a compact stellar remnant, i.e. a NS or a BH. This section (and the term *supernova remnant* in general) refers to the expanding clouds of gas and dust, while

NSs and BHs will be covered in Section 2.4. The information given here were mainly collected from the review by Vink (2012).

### 2.3.1 Classification of supernova remnants

Today, 294 confirmed SNRs are known in the Milky Way (Green, 2019), among which about 83 % should result from core-collapse SNe in a Sbc-type galaxy like the Milky Way (Mannucci et al., 2005). A classification of SNRs based on their SN type would be preferable but is hard to establish, especially for old SNRs that swept up a large mass of ISM material. It requires a careful analysis of the SNR composition. Therefore, SNRs are usually classified based on their morphology, using the four categories *shell type*, *filled centre*, *composite* and *mixed morphology* (Vink, 2012).

**Shell type.** This is the most popular and most abundant category, characterised by a bright spherical edge. This shell is produced by the propagation of the shock wave through the ISM, leaving an expanding region of shock heated plasma which then radiates in different wavelengths. The exact production mechanisms of the different types of radiation, related to the chemical composition, the ISM density, magnetic fields, shock wave physics etc., are beyond the scope of this thesis. Roughly speaking, SNRs produce (i) thermal X-rays, e.g. via bremsstrahlung due to heating of the ISM at the shock front, (ii) non-thermal X-rays from synchrotron radiation, (iii) cosmic rays, e.g. electrons and ions accelerated by the shock, (iv) gamma-rays from pion decay and inverse Compton scattering, (v) radio waves, mainly from synchrotron radiation, (vi)  $H\alpha$  emission, caused by excitation and subsequent recombination of neutral ISM hydrogen at the shock front and (vii) recombination lines and radioactive decay of heavy elements. Furthermore, different parts of a SNR can be seen in different wavelengths. This is illustrated by composite images like in Fig. 2.6, where the young shell type SNR Cassiopeia A is shown in the light of four different wavebands from infrared (*Spitzer*) over optical (*Hubble*) to X-rays (*Chandra*). Although Cassiopeia A has irregularities and some X-ray emission is also produced close to the centre (in projection), the brightest emission is seen close to the edge. Further examples of shell type SNRs are CTB1, the Cygnus Loop, or the SNRs left by the *Tycho* and *Kepler* SNe.

**Filled centre.** Filled centre SNRs, also known as *Plerions*, are identified by a bright central region, whereas the brightness of the shell is negligible. Their emission is not powered by the shock front, but by a central compact object, a rapidly rotating NS. A pulsar loses energy by magnetic dipole radiation, producing a *pulsar wind nebula* (PWN), a wind of relativistic electrons and positrons, which terminates in a shock. The PWN emits synchrotron radiation

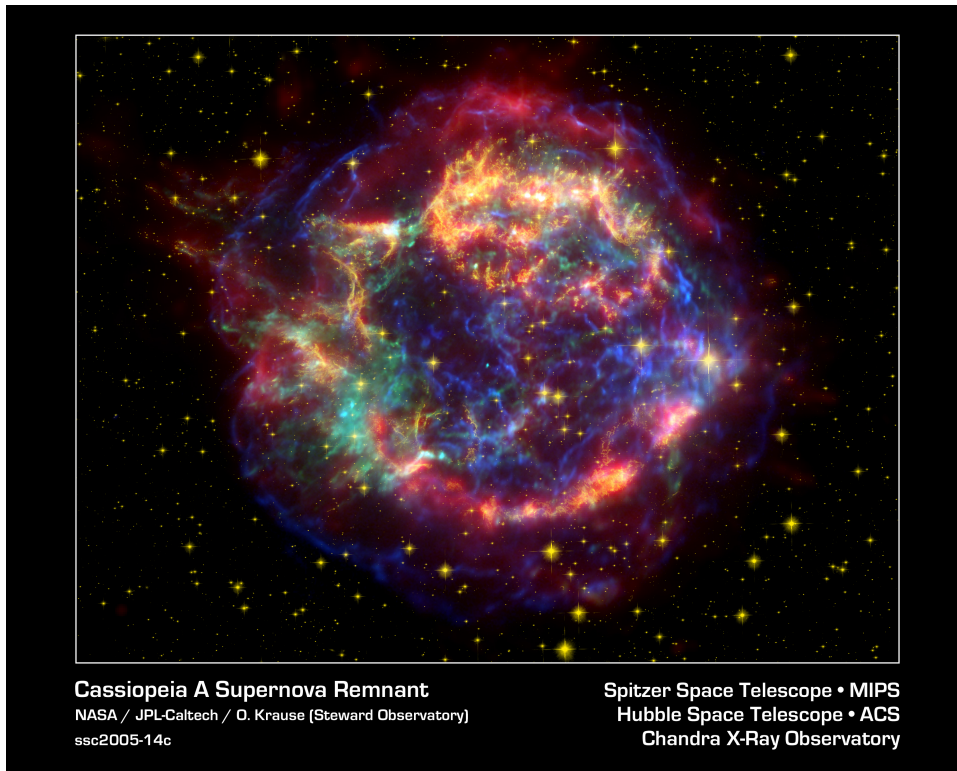


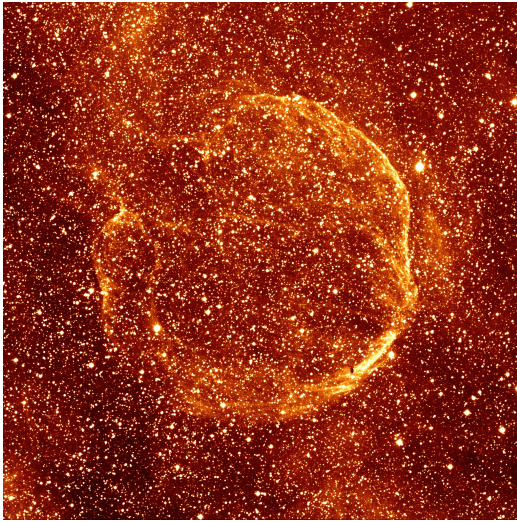
FIGURE 2.6: Composite image of Cassiopeia A. Infrared emission recorded by *Spitzer* is shown in red, visible light from the *Hubble Space Telescope* in yellow and X-ray data from *Chandra* in green and blue.

from radio to soft gamma-rays and inverse Compton radiation from gamma-rays to the TeV regime. Since the emission is powered by the pulsar and not by the SN ejecta, PWNs are generally not SNRs. They are also found around older NSs without any SNR association. However, the most famous PWN, the *Crab nebula*, is connected to the historical SN of 1054 AD and also shows optical emission from SN ejecta. Therefore it can be safely called SNR. It is unclear why plerionic SNRs like the Crab nebula or 3C58 do not show a SNR shell.

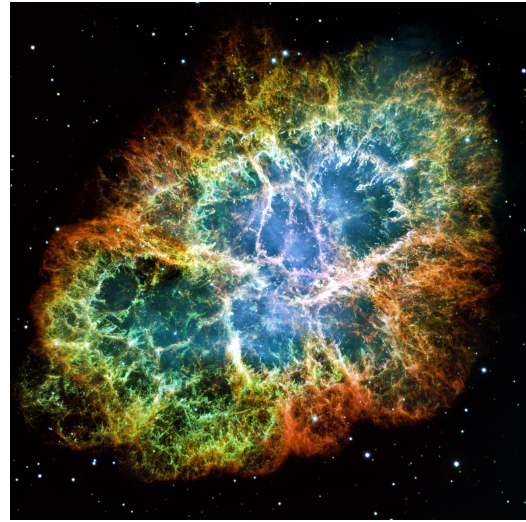
**Composite.** Composite SNRs are combined shell-type and plerionic SNRs, i.e. they have a PWN in the centre as well as shell emission from the shock front. Examples are Vela and RCW 89.

**Mixed morphology.** This class, also referred to as *thermal composite*, was only discovered after the beginning of X-ray observations in the 1980s. These SNRs (not listed as a separate class in Green 2019) are characterised by different morphologies in different wavebands. In particular, they appear shell-type in the radio, whereas their X-ray emission rather comes from the centre. They are usually associated with old SNRs and a dense ISM (Vink, 2012). A comparison of the four morphological types with four example SNRs is given in Fig. 2.7.





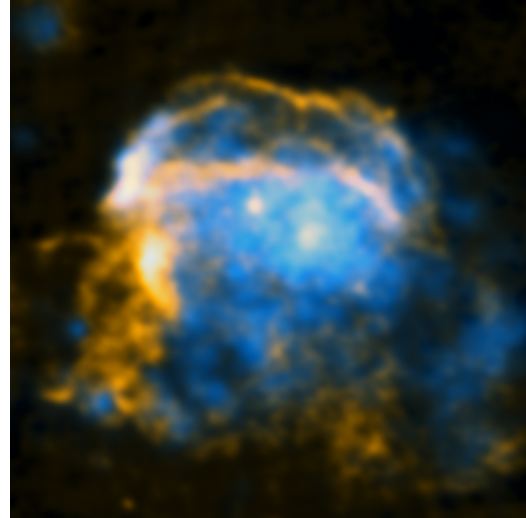
(a) The shell-type SNR CTB1. Image taken in  $H\alpha$  with the *Schmidt Teleskop Kamera* (STK) at the University Observatory Jena, GSH.



(b) The Crab nebula, a filled-centre SNR. Optical image taken with the HST. Image credit: NASA, ESA, J. Hester and A. Loll (Arizona State University).



(c) The composite SNR Vela. Image taken in  $H\alpha$ , O III and optical. Image credit: Marco Lorenzi, 2010.



(d) The mixed-morphology SNR W28 observed in X-rays with ROSAT (blue) and in radio with the VLA (Dubner et al., 2000). Image credit: Chandra press office.

FIGURE 2.7: SNRs of different morphological types

### 2.3.2 Phases of supernova remnant expansion

The evolution of a SNR is generally described by the following four phases: (i) Free expansion, (ii) Sedov-Taylor, (iii) Radiative and (iv) Merging to the ISM, as firstly done by Woltjer (1972). For a given explosion energy  $E$ , the evolution of the shock radius  $R_s$ , the shock velocity  $v_s$  and the temperature  $T$  can be traced until the SNR merges into the ISM after  $\sim 100$ – $200$  kyr, when

### 2.3. Supernova remnants

---

$v_s$  and  $T$  become similar to the values of the turbulent motion in the ISM. For the following equations, it is assumed that the SNR evolves into a homogenous ISM with density  $\rho_0$  (Vink 2012; Tetzlaff 2013). Note that this is a very simplified model, due to the often inhomogenous ISM and asymmetric SNe. Therefore, different parts of a real SNR can be in different phases.

**Free expansion.** Shortly after the SN, the density of the ejected material is much higher than of the surrounding ISM. Therefore, it can expand almost freely into space and the radius can be described by

$$R_s = v_s t \quad (2.7)$$

with an almost constant velocity  $v_s$  and  $t$  the time since the SN. This phase lasts until  $M_{\text{ej}} \approx M_{\text{sw}}$ , i.e. the mass of ejected material becomes similar to the mass of swept-up ISM material, usually after a few hundred years.

**Sedov-Taylor.** This phase is also called *adiabatic*, because radiative energy losses do not yet play a significant role. Actually, the free expansion phase is also adiabatic, although radiative losses can be important shortly after the SN (e.g. Sorokina et al. 2004) and also escaping cosmic rays should be considered. The adiabatic phase starts when  $M_{\text{ej}} \approx M_{\text{sw}}$ . At this point, a reverse shock is formed which travels inwards in mass coordinate and heats the interior. This thermal pressure then drives the further SNR expansion. The adiabatic phase is named after Leonid Iwanowitsch Sedov and Sir Geoffrey Ingram Taylor, who described the formation and evolution of an explosion-triggered blast wave (Taylor 1950; Sedov 1959). Their equations can be used as long as no energy losses occur:

$$R_s = \left( \xi \frac{Et^2}{\rho_0} \right)^{1/5}, \quad (2.8)$$

$$v_s = \dot{R}_s = \frac{2}{5} \left( \xi \frac{Et^2}{\rho_0} \right)^{1/5} t^{-3/5} = \frac{2R_s}{5t}, \quad (2.9)$$

where the dimensionless constant  $\xi = 2.026$  holds for a non-relativistic, monatomic gas (adiabatic constant  $\gamma = 5/3$ ). Modifications to above equations can be made to consider non-uniform density profiles, e.g. to take into account stellar wind mass loss prior to the explosion. More detailed models that also take into account the density distribution of the ejecta are given by Chevalier (1982) and Truelove and McKee (1999).

**Radiative.** After  $\sim 30$ – $40$  kyr, the interior has cooled down and the pressure becomes negligible, so that radiative losses become dominant, at a post-shock temperature of  $\sim 5 \times 10^5$  K.

The radiative phase is also called *snowplough phase* or *momentum conservation phase*, named after the law that governs the radial expansion. So we have

$$p = Mv_s = \frac{4}{3}\pi R_s^3 \rho_0 \dot{R}_s = \text{const.} \quad (2.10)$$

Radiative losses become important at the time  $t_{\text{rad}}$  when the SNR has the radius  $R_{\text{rad}}$  and the velocity  $v_{\text{rad}}$ . These parameters can be calculated with the Sedov-Taylor solution. Integration over time yields an expression for the age:

$$t = t_{\text{rad}} + \frac{R_{\text{rad}}}{4v_{\text{rad}}} \left[ \left( \frac{R_s}{R_{\text{rad}}} \right)^4 - 1 \right]. \quad (2.11)$$

This can be solved for the radius  $R_s$  and with Eqn. 2.10 we can then calculate the velocity  $v_s$ .

**Transition to the ISM.** The maximum age of a SNR is not clearly defined. Generally, when temperature and velocity adopt to the values of the surrounding ISM, also the emission will fade away after a few  $10^5$  yrs. However, exceptions are possible for very closeby objects. The most remarkable example is the Antlia SNR with an angular diameter of  $24^\circ$ , by far the largest among all SNRs. It was discovered in  $H\alpha$  and X-rays by McCullough et al. (2002). Tetzlaff et al. (2013) found PSR J0630–2834 to be the possible compact remnant of the SN which would constrain the SNR age to  $1.20_{-0.18}^{+0.26}$  Myr, almost one order of magnitude older than any other known SNR. The distance would then be  $138 \pm 17$  pc, about half the distance to the next nearby SNRs (Vela and Lupus). Although McCullough et al. (2002) and Tetzlaff et al. (2013) provide good indication that a SN happened in the Antlia Pneumatica constellation, the remnant already reached the merging phase and its shape is rather irregular. So it is questionable if it can still be defined as a SNR and it is not listed in the *Green* catalogue (Green, 2019).

According to the SNR catalogue provided by the University of Manitoba<sup>8</sup> (Ferrand and Safi-Harb, 2012), the next oldest SNR is G141.2+5.0 with  $\sim 350$  kyr. It was discovered by Kothes et al. (2014) as a PWN, but they also found a slowly ( $\sim 6 \text{ km s}^{-1}$ ) expanding HI shell which already shares the systemic velocity of the local standard of rest (LSR) in its environment. Despite the large distance of  $\sim 4$  kpc it is still visible, indicating that it could be in its late radiative phase.

A simplified overview of the evolutionary stages is given in Table 2.3, which gives the age  $t$ , the radius  $R_s$ , the velocity  $v_s$  and the total mass  $M$  of the SNR at the transition points between the four phases. The calculation is based on the initial values  $E = 10^{50}$  erg,  $V_0 = 10,000 \text{ km s}^{-1}$ ,  $M_0 = 0.1 M_\odot$  and  $\rho_0 = 1 \text{ cm}^{-3}$ .

<sup>8</sup><http://snrcat.physics.umanitoba.ca/SNRtable.php>

## 2.4. Compact stellar remnants

TABLE 2.3: Quantities characterising the phases of SNR evolution, taken from Woltjer (1972). The Roman numerals refer to (I) Free expansion, (II) Sedov-Taylor, (III) Radiative and (IV) ISM-transition phase.

Phase transition	$t$ [yr]	$R_s$ [pc]	$v_s$ [km s <sup>-1</sup> ]	$M$ [ $M_\odot$ ]
I–II	90	0.9	10000	0.2
II–III	22000	11	200	180
III–IV	750000	30	10	3600

## 2.4 Compact stellar remnants

During the core-collapse, the stellar core either contracts to a NS (if the *Fermi* pressure of neutrons is able to support the star against gravitational pressure) or to a BH. The transition is expected to occur at about  $\sim 25 M_\odot$ , although some more massive WR stars might experience such strong mass loss that they could also end as a NS (see Fig. 2.2). In the following subsections, we will briefly explain these exotic objects. WDs, the compact stellar remnants of low-mass stars, are not covered here.

### 2.4.1 Neutron stars

The existence of NSs, including its formation during a SN, was firstly suggested by Baade and Zwicky (1934), shortly after the discovery of the neutron (Chadwick, 1932). NSs have masses between  $\sim 1.1 M_\odot$  and  $\sim 2.1 M_\odot$ . A typical NS mass of  $\sim 1.4 M_\odot$ , compressed on a radius of only  $\sim 10$  km, corresponds to an average density of  $\sim 6.7 \times 10^{14}$  g cm<sup>-3</sup>, larger than the density of nuclear matter,  $\sim 2.7 \times 10^{14}$  g cm<sup>-3</sup> (Lorimer and Kramer, 2005). Their very high densities and magnetic fields,  $B \approx 10^8 - 10^{15}$  G, make them an unprecedented laboratory to study matter under extreme conditions. While the surface layer still consists mainly of degenerate electrons, neutrons become dominant a few hundred meters below the surface, where the density reaches the *neutron drip* at  $\sim 4 \times 10^{11}$  g cm<sup>-3</sup>. The composition of the inner core is still a matter of debate and might involve exotic matter like pions or quarks. The exact density profile and, hence, the equation of state is a matter of current research, requiring measurements of mass and radius. These can be most accurately done for binary pulsars but were also obtained for isolated X-ray pulsars by using the gravitational redshift (Hambaryan et al., 2014, 2017).

**Pulsars.** Most NSs are rapidly rotating with spin periods between about 1 ms and 10 s, losing rotational energy by magnetic dipole radiation:

$$\dot{E}_{\text{dip}} = -\frac{2B^2 R^6 \Omega^4 \sin^2 \alpha}{3c^3} = I\Omega\dot{\Omega} = \dot{E}_{\text{rot}} \quad (2.12)$$

with the magnetic field  $B$ , the radius  $R$ , the angle between the magnetic field axis and the spin axis  $\alpha$ , the speed of light  $c$ , the angular rotational frequency  $\Omega = 2\pi/P$  and its temporal derivative (Lorimer and Kramer, 2005; Lux, 2013). A generalised version of the spin-down law can be given as

$$\dot{P} = K P^{2-n}, \quad (2.13)$$

where the rotation is expressed in terms of the period  $P$ , the slowing is characterised by the braking index  $n$  and the other terms are summarised to the constant  $K$ . Integration of Eqn. 2.13 yields an expression for the age  $T$ :

$$T = \frac{P}{(n-1)\dot{P}} \left[ 1 - \left( \frac{P_0}{P} \right)^{n-1} \right]. \quad (2.14)$$

For pure magnetic dipole braking, we have  $n = 3$ . Furthermore, it is often assumed that the initial period is much smaller than the current period,  $P_0 \ll P$ . Plugging these assumptions into Eqn. 2.14 yields a simple expression for the age, yielding the *characteristic age*  $\tau_c$ :

$$\tau_c = \frac{P}{2\dot{P}}. \quad (2.15)$$

The period and its derivative can be precisely measured for most pulsars by radio and X-ray timing observations and therefore the age can be estimated. However, the assumption  $P_0 \ll P$  means that  $\tau_c$  should be seen as an upper limit.

**Velocity distribution.** NSs generally have much higher space velocities than normal stars. This is related to the kick velocities that they can obtain during their birth in an asymmetric SN (Burrows and Hayes, 1996; Janka et al., 2005; Tauris, 2015). Arzoumanian et al. (2002) describe the velocities by adding two Maxwellian distributions, representing a low-velocity group dominated by the pre-SN orbital velocity, and a high-velocity group governed by the SN birth kick. However, Hobbs et al. (2005) investigated a larger sample of 233 NSs and found that a single Maxwellian yields the better fit. They found the maximum of the 3D velocity distribution to be at  $400 \pm 40 \text{ km s}^{-1}$ , with a root mean square (RMS) of  $\sigma = 265 \text{ km s}^{-1}$ , while the fastest individual objects are B2011+38 and B2224+64 with  $v \approx 1600 \text{ km s}^{-1}$  in 2D.

### 2.4.2 Black Holes

BHs are the compact remnants of stars with  $M \gtrsim 25 M_{\odot}$ . According to the *initial mass function* (IMF) (e.g. Salpeter 1955; Kroupa and Weidner 2005), the number of stars with these masses is relatively low. The *Salpeter* IMF, which is a good approximation in the case of high-mass stars, yields a fraction of stars with  $M \geq 25 M_{\odot}$  of  $\sim 0.9\%$ .

In the case of NSs, the degeneracy pressure of neutrons supports the star against further gravitational collapse. However, if the core mass exceeds the *Tolman-Oppenheimer-Volkoff limit* (Oppenheimer and Volkoff 1939; Bombaci 1996), the gravitational pressure is too high, so that the core collapses further until it becomes a BH, i.e. an object of infinite density, which can be completely described by mass, angular momentum and electric charge and which causes a singularity in the four-dimensional space-time. The spatial boundary of a BH is often defined as the *event horizon*, where the escape velocity becomes equal to the speed of light. Therefore, not even light can escape a BH and the object will always appear *black* when we observe it.

BHs occur on different mass scales. While a stellar core would collapse to a *stellar-mass BH*, accreted material can increase its mass. In the centres of galaxies the density of matter can be very high, so that accreted material and mergers with other BHs can increase the mass of a central BH to millions or even billions of solar masses. The object is then called a *supermassive BH*. The most famous example is Sgr A\* with  $(4.151 \pm 0.017) \times 10^6 M_{\odot}$  in the centre of the Milky Way (Gravity Collaboration et al., 2019). Furthermore, it is suggested that also *intermediate-mass BHs* with up to a few thousand solar masses exist, which could form e.g. in the centres of globular clusters.

The distribution of BH birth kicks is not known. However, it is suggested that the higher amount of fallback material would dampen the kick and lead to lower kick velocities than for NSs (see Renzo et al. 2019 and references therein).

## 2.5 Binary systems

A significant fraction of stars are located in multiple systems, where the multiplicity fraction strongly increases from low-mass to high-mass stars. While  $26 \pm 3\%$  of stars with  $0.1 M_{\odot} \leq M \leq 0.5 M_{\odot}$  are in multiple systems, the multiplicity fraction among stars with  $M \geq 16 M_{\odot}$  (O-type stars) is more than  $80\%$  (Duchêne and Kraus, 2013).

Multiplicity can have strong impacts on stellar evolution, especially for close systems. When the primary enters its post-MS and expands to a red giant, it can fill its Roche lobe and transfer mass to the secondary. This process rejuvenates the secondary, providing additional fuel, although its subsequent evolution can then be accelerated due to the increased mass. In

the case of high-mass binaries<sup>9</sup> with a mass ratio of  $q = M_2/M_1 \approx 1$ , this can even lead to the secondary exploding first. The mass ratio distribution is still a matter of debate. While e.g. Pinsonneault and Stanek (2006) and Chini et al. (2013) find evidence that massive stars tend to form binaries with similar masses, other works (Sana and Evans 2011; Sana et al. 2012; Moe and Di Stefano 2017) find a flat mass ratio distribution down to  $q \approx 0.2$ . Unfortunately, the regime of the most extreme mass ratios,  $q < 0.1$ , is usually not covered by multiplicity studies, because the extreme flux ratios as well as lower precision of RV measurements in the case of early-type stars make low-mass companions hardly to detect. However, there is no reason to assume that the mass ratio distribution should change for  $q < 0.1$ .

In the case of wide orbits, the effects on stellar evolution are small and the mass ratio distribution becomes almost consistent with random pairings from the IMF (Moe and Di Stefano, 2017).

Depending on the initial orbital separation and mass ratio, high-mass binaries can experience a variety of complex evolutionary stages like common-envelope evolution, low-mass X-ray binaries and high-mass X-ray binaries (Tauris and van den Heuvel, 2006). The endpoints of the evolution can be either disrupted systems or binaries consisting of various combinations of compact remnants. The latter will eventually lose more and more orbital energy by gravitational wave radiation. The final spiral-in and merger of these systems can be detected with gravitational wave detectors (LIGO Scientific Collaboration et al., 2016).

In Fig. 2.8, taken from Renzo et al. (2019), we sketch the possible evolution of an initially close high-mass binary until after the first SN. In this example, the primary initially has  $M = 20 M_\odot$  and the secondary  $M = 15 M_\odot$ . Phase (A.) represents the MS evolution, which proceeds faster for the primary (blue). The Roche lobe radii are indicated by the dotted line, which is exceeded by the primary in state (B.), because it evolved to a post-MS giant. Now begins a phase of stable, almost conservative case B Roche-lobe overflow (RLO, Kippenhahn and Weigert 1967), during which the orbit widens and  $\sim 70\%$  of the primary mass are transferred to the secondary, i.e. almost the whole H envelope. The primary remains as a WR star. However, for very close systems with  $q \ll 1$ , the expansion of the primary is faster than the secondary can accrete its mass. The envelope of the primary then expands beyond the secondary orbit, so that a *common-envelope phase* (CEP) starts, during which the orbit shrinks due to drag forces and the deposition of orbital energy possibly ejects the envelope (Tauris and van den Heuvel, 2006). The in-spiral during the CEP may also lead to a merger of both stars. According to Renzo et al. (2019), this happens for  $22_{-9}^{+26}\%$  of all massive binaries.

---

<sup>9</sup>We define a *high-mass binary* or *massive binary* such that the primary component has  $M \geq 8 M_\odot$ , i.e. is a SN progenitor

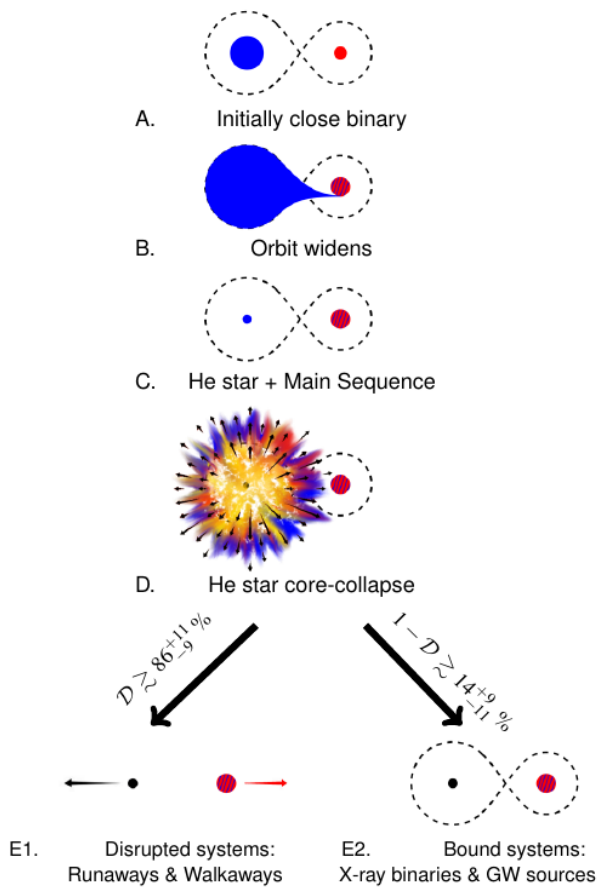


FIGURE 2.8: High-mass binary evolution of an initially close binary until after the first SN. The percentages give the probability of the system to get disrupted (E1.) or to remain bound (E2.). Numbers and figure taken from Renzo et al. (2019).

time of these systems and due to the long-lasting mass accretion the NS can spin up to periods of  $P \lesssim 30$  ms. It is then called *millisecond pulsar* or *recycled pulsar*. Compared to regular pulsars, these objects are older, spinning faster, have a lower magnetic field and are almost always found in binaries.

**Intermediate-mass X-ray binaries** (IMXBs) have donor stars with  $1 M_{\odot} \leq M \leq 10 M_{\odot}$ . Despite their name, these systems are hard to be detected in X-rays, because they are very short-lived (a few thousand years). If the accretor is a NS, the donor often has a much higher mass and therefore, RLO phases will be unstable and characterised by a high mass transfer rate. Possibly emitted X-rays are then mostly absorbed by the dense material surrounding the NS. However, if the accretor is a BH, it might be massive enough so that stable RLO is possible.

In the example of Fig. 2.8, after the mass-transfer phase the primary undergoes the subsequent nuclear fusion processes for  $\sim 1.2$  Myr (C.), until it explodes in a Type Ib core-collapse SN (D.). The result is then usually the disruption of the binary system (E1.), where the secondary gets ejected as a *runaway star*. The ejection mechanisms will be discussed in Section 2.6. In  $14^{+9}_{-11}$  % of the cases the binary system remains bound (E2.) and forms a compact binary. Possible outcomes are briefly described in the following (see Tauris and van den Heuvel 2006).

**Low-mass X-ray binaries** (LMXBs) consist of a compact object (NS or BH) and a non-degenerate companion star with  $M \leq 1 M_{\odot}$ , transferring mass onto the compact object by RLO. The accretion-induced X-ray radiation is soft ( $kT < 10$  keV) but often shows X-ray bursts from thermonuclear fusion of accreted matter at the NS surface (Tauris and van den Heuvel, 2006). The low mass of the companion allows for a long life-



**High-mass X-ray binaries** (HMXBs) have donor stars with  $M \geq 10 M_{\odot}$ . Their accretion is not powered by RLO, but by the strong wind mass loss of their donors. HMXBs emit hard X-rays ( $kT > 15$  keV) and do not show bursts, but periodic X-ray pulsations. The largest observed subgroup are systems where the donor is a B-type emission line star (Be star). These have relatively wide orbits ( $P_{\text{orb}} = 20\text{--}250$  d) and a wide range of eccentricities, up to  $e \approx 0.5$ . Their periodic X-ray emission is generated when the NS approaches the periastron of its orbit, passing through the wind emitted by the Be star.

**Gravitational wave sources.** For LMXBs and IMXBs, the donor will end as a WD. Among binary pulsars, He WDs are the most common companions, followed by CO and ONeMg WDs. In the case of HMXBs, the system experiences a second SN when the donor ends its life. If it remains bound after that, it forms a system of two compact objects (i.e. NS-NS, NS-BH or BH-BH). These systems are a unique tool to test the predictions of general relativity and to constrain the NS equation of state (e.g. Taylor 1992; Kramer and Wex 2009). The orbital parameters of NS-NS binaries, that are modified by energy loss through gravitational wave radiation, can be precisely measured with radio timing observations. PSR B1913+16 was the first detected double NS (Hulse and Taylor, 1975), while today the double pulsar J0737–3039 is known to be the most relativistic double NS (Kramer and Wex, 2009). It will continuously increase its gravitational wave emission and eventually merge in about 85 Myr (Burgay et al., 2003).

## 2.6 Runaway stars

When a binary system gets disrupted during the SN, the companion flies away with its former orbital velocity and is then called a *runaway star*. This *binary supernova ejection scenario* (BES) was described by Blaauw (1961), who also used this process to explain the observed high-velocity tail in the velocity distribution of O- and B-type stars. Stone (1979) determined space velocities of 47 O-type stars and found a bimodal distribution which he modelled with two Maxwellian distributions, one for the low-velocity group and one for the high-velocity group. Tetzlaff et al. (2011b; 2013) continued this approach by calculating the peculiar velocities of 7663 young *Hipparcos* stars. The resulting distribution is shown in Fig. 2.9. Despite the much larger sample, including also late spectral types, the general trend is still comparable to Stone (1979). The low- and high-velocity group intersect at  $v_{\text{pec}} \approx 25 \text{ km s}^{-1}$ . This limit is commonly used to define a runaway star. In practice, since the two distributions overlap, one has to consider the contamination with stars from the other group. According to Tetzlaff (2013), 30 % of runaway stars actually have  $v_{\text{pec}} < 25 \text{ km s}^{-1}$ , while 10 % of the stars in the

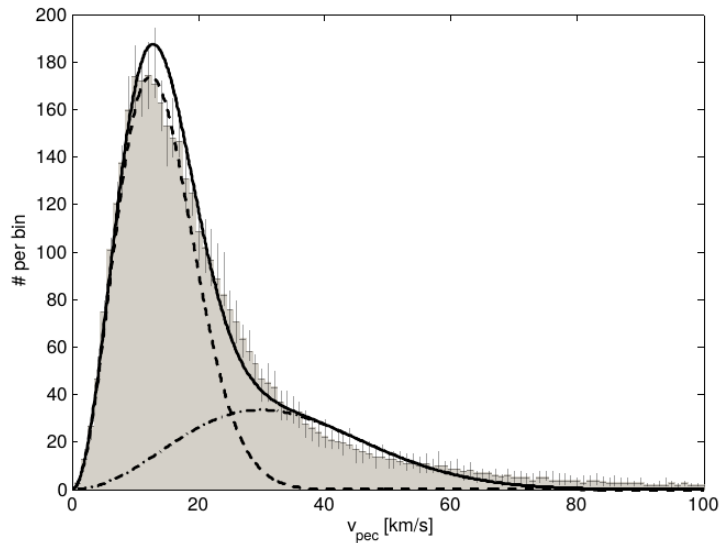


FIGURE 2.9: The velocity distribution of young *Hipparcos* stars, taken from Tetzlaff (2013). The dashed line marks the Maxwellian fit of the low-velocity group, the dash-dotted line the one for the high-velocity group and the solid line the sum of both.

low-velocity group have  $v_{\text{pec}} > 25 \text{ km s}^{-1}$ .

However, Renzo et al. (2019) performed an extensive population synthesis of massive binaries and emphasise that up to 95% of SN-ejected MS companions are expected to have  $v_{\text{pec}} \leq 30 \text{ km s}^{-1}$  and should be called *walkaway stars*. In this work, we will not divide between *runaway* and *walkaway* stars. All stars with a possible BES origin will be classified as runaway star candidates, regardless of their velocity.

The high fraction of BES-produced stars with  $v_{\text{pec}} \leq 30 \text{ km s}^{-1}$  might indicate that most stars with higher space velocities might be better explained by the *dynamical ejection scenario* (DES, Poveda et al. 1967). Here, the ejection of the star is caused by a close encounter of multiple stellar systems, usually in dense stellar environments like clusters. In the following, the BES, the DES and the *Hills mechanism*, which is responsible for the production of HVSs, are described in more detail.

### 2.6.1 Binary supernova ejection scenario

If a companion gets unbound from a binary system during the SN of the primary can be calculated from the *virial theorem*, as done by Blaauw (1961), who found that more than half of the total system mass needs to get ejected. In a first step, we give the total specific orbital energy

of the system as

$$E = T + \Omega \quad (2.16)$$

$$= \frac{1}{2}v_{\text{orb}}^2 - \frac{G(M_1 + M_2)}{R} \quad (2.17)$$

$$= -\frac{G(M_1 + M_2)}{2a}. \quad (2.18)$$

$T$  and  $\Omega$  are the specific kinetic and potential energy ( $[E] = [T] = [\Omega] = \text{J/kg}$ ),  $v_{\text{orb}}$  is the orbital velocity of the secondary,  $G \approx 6.674 \times 10^{-11} \text{ m}^3 \text{ kg}^{-1} \text{ s}^{-2}$  the gravitational constant,  $M_1$  and  $M_2$  the masses of primary and secondary, respectively,  $R$  the separation of the components and  $a$  the semi-major axis of the system. The sign of the orbital energy defines the shape of the orbit. The two bodies have an elliptical orbit, if  $E < 0$ , a parabolic orbit if  $E = 0$  and a hyperbolic orbit if  $E > 0$ . So  $E = 0$  defines the boundary between bound and unbound orbits. In the following, we assume a circular initial orbit ( $a = R$ ) and set  $G \equiv 1$ . We use index 0 for the parameters before the SN and index  $f$  for the parameters after the SN. Before the SN, we can write Eqn. 2.18 as:

$$E_0 = -\frac{M_{1,0} + M_2}{2R_0} \quad (2.19)$$

$$= T_0 - \frac{M_{1,0} + M_2}{R_0} \quad (2.20)$$

$$= T_0 + \Omega_0. \quad (2.21)$$

We can assume that  $M_2$  remains constant during the SN and introduce the mass reduction factor  $q_r$  as the fraction between final and initial mass of the primary:

$$q_r = \frac{M_{1,f}}{M_{1,0}} \Leftrightarrow M_{1,f} = q_r M_{1,0}. \quad (2.22)$$

Due to the mass loss during the SN, the potential energy changes rapidly to  $\Omega_f$ , whereas the kinetic energy is first conserved (and only changes over a longer time span). Therefore, shortly after the SN we have

$$E_f = \Omega_f + T_0 \quad (2.23)$$

$$= \Omega_f + E_0 - \Omega_0 \quad (2.24)$$

$$= E_0 + \frac{(1 - q_r)M_{1,0}}{R_0} \quad (2.25)$$

$$= \frac{(1 - 2q_r)M_{1,0} - M_2}{2R_0}. \quad (2.26)$$

Hyperbolic orbits are obtained if the numerator is positive, i.e.

$$(1 - 2q_r)M_{1,0} - M_2 > 0 \quad (2.27)$$

$$\Leftrightarrow q_r < \frac{1}{2} \left( \frac{M_{1,0} - M_2}{M_{1,0}} \right) \quad (2.28)$$

$$\Leftrightarrow M_{1,0} - M_{1,f} > \frac{1}{2}(M_{1,0} + M_2). \quad (2.29)$$

This criterion, also known as *Blaauw kick*, gives a good estimate if a binary system gets disrupted. However, additional complication is added in real life, e.g. by the SN kick. Even if the two companions have very similar masses, so that Eqn. 2.29 will not be fulfilled, the birth kick  $v_k$  imparted onto the NS due to an asymmetric SN can disrupt the system. Depending on amplitude and kick direction, also the opposite can happen, i.e. a moderate kick into the same direction of the momentary orbital velocity of the secondary can avoid the disruption of the system. Generally speaking, (i) for  $v_k \gg v_{\text{orb}}$  the system will always get disrupted, (ii) for  $v_k \simeq v_{\text{orb}}$  a disruption depends on the kick direction and (iii) for  $v_k \ll v_{\text{orb}}$  the system will not get disrupted (except from a possible Blaauw kick), only the orbit will change, e.g. it will get a higher eccentricity (Renzo et al., 2019).

BES runaway stars can have a wide range of velocities. Hoogerwerf et al. (2001) state that they have velocities of  $v_{\text{pec}} \approx 30\text{--}150 \text{ km s}^{-1}$ , corresponding to their former orbital velocity. However, the SN kick can largely increase the maximum velocity, up to  $v_{\text{pec}} \approx 1050 \text{ km s}^{-1}$  for G/K dwarfs with  $M \approx 0.9 M_{\odot}$  and  $v_{\text{pec}} \approx 540 \text{ km s}^{-1}$  for B-type companions with  $M \approx 3.5 M_{\odot}$  (Tauris, 2015). These velocities are reached for NS birth kick velocities between  $\sim 1000 \text{ km s}^{-1}$  and  $1200 \text{ km s}^{-1}$ . Late-type stars can reach higher velocities because they can have closer pre-SN orbits and therefore higher orbital velocities. Also, momentum transfer, e.g. from the SN ejecta, has a larger effect on their velocity due to their lower mass.

Although such extreme velocities are possible, they are very unlikely, as they would require finetuning of the pre-SN orbital parameters, the explosion symmetry and the exact time of the SN with respect to the orbital motion. From their population synthesis of massive binaries, Renzo et al. (2019) found a peak in the velocity distribution of BES-ejected stars at only  $v_{\text{pec}} = 6 \text{ km s}^{-1}$ , while 95 % of the stars would have  $v_{\text{pec}} < 30 \text{ km s}^{-1}$  and 98.9 % would have  $v_{\text{pec}} < 60 \text{ km s}^{-1}$ . Therefore, our search for runaway stars will not only focus on targets with  $v_{\text{pec}} > 25 \text{ km s}^{-1}$ , but also on slower objects which are called *walkaway stars* by Renzo et al. (2019).

Besides their kinematic peculiarities, BES-ejected stars should also show characteristic spectral features. If they accreted mass from the primary prior to the SN, they should be polluted with He- and/or N-rich material (Blaauw, 1993; Renzo et al., 2019), can have enhanced magnetic fields (Schneider et al., 2016) and their rotational velocity should be increased. Addi-

tionally, the SN ejecta should deposit heavy- and  $\alpha$ -elements onto the stellar surface that could be detected through high-resolution spectroscopy (e.g. Przybilla et al. 2008).

## 2.6.2 Dynamical ejection scenario

An alternative production channel for runaway stars was suggested by Poveda et al. (1967): The DES, where gravitational encounters between multiple stellar systems in dense, compact clusters<sup>10</sup> can eject one or more runaway stars or, rarely, even runaway multiple systems (Hoogerwerf et al., 2001). DES-ejected stars are generally faster than BES-ejected stars. Their maximum velocity can reach up to  $v_{\text{pec}} \approx 1400 \text{ km s}^{-1}$  (Leonard, 1991), corresponding to the velocity that a low-mass star would need to escape from the surface of the star with the highest mass involved in the encounter. However, according to Perets and Šubr (2012), only  $\sim 1\%$  of DES runaway stars would have  $v_{\text{pec}} > 200 \text{ km s}^{-1}$ .

A famous example for the DES are AE Aur,  $\mu$  Col and  $\iota$  Ori. AE Aur and  $\mu$  Col have space velocities of  $\sim 100 \text{ km s}^{-1}$  and fly away from the Trapezium cluster in the Orion star-forming region in almost opposite directions. They were suggested by Blaauw and Morgan (1954) to share a common origin in Orion, where they were ejected  $\sim 2.6$  Myr ago. Their place of origin would then be close to the position of the highly eccentric double-lined spectroscopic binary  $\iota$  Ori, which was suggested by Gies and Bolton (1986) to be the surviving binary after a binary-binary encounter that ejected AE Aur and  $\mu$  Col as runaway stars. Further evidence for this hypothesis was given by Hoogerwerf et al. (2001), who modelled the past trajectories of these objects with 10,000 Monte Carlo simulations.

### Ejection of hypervelocity stars by the Hills mechanism

A peculiar form of dynamical ejection is the *Hills mechanism* which describes a binary encounter with Sgr A\*, the supermassive BH in the Galactic centre (Hills, 1988). This process is responsible for the highest observed Galactic stellar velocities. It can produce HVSs which have velocities exceeding the local Galactic escape velocity<sup>11</sup>. The theoretical maximum velocities even exceed  $4000 \text{ km s}^{-1}$  (Hills, 1988). Observational evidence for this scenario was given by Brown et al. (2005), who discovered the first HVS in the Galactic halo, a B-type star moving with a Galactic rest frame velocity of  $v_{\text{grf}} \gtrsim 709 \text{ km s}^{-1}$ , whereas the escape velocity at its Galactocentric distance of 50 kpc is  $\sim 367 \text{ km s}^{-1}$  (Brown, 2015). Since then, many more examples have been found (see Brown 2015 for a review).

<sup>10</sup>Although the process could theoretically also happen in the field, the probability is much higher in stellar clusters due to the high stellar density.

<sup>11</sup>The local Galactic escape velocity  $v_{\text{esc}}(\vec{x})$  depends on the Galactic gravitational potential  $\Phi(\vec{x})$  as  $v_{\text{esc}}(\vec{x}) = \sqrt{-2\Phi(\vec{x})}$ , where  $\vec{x}$  is the location in Galactocentric coordinates (Irrgang, 2014).

### Alternative ejection scenarios

A very interesting case that challenges the separate formation scenarios of runaway- and hypervelocity stars is HD 271791 (Heber et al., 2008; Przybilla et al., 2008). This B-type star moves at  $v_{\text{grf}} = 530\text{--}920 \text{ km s}^{-1}$  (Heber et al., 2008), exceeding the local escape velocity of  $430 \text{ km s}^{-1}$ . So it can be called a HVS, but it cannot have originated at the Galactic centre. Its lifetime of  $\sim 25 \text{ Myr}$  is much shorter than the required travel time of  $\sim 75 \text{ Myr}$  and its proper motion rather indicates a birth at the edge of the Galactic disk. The star was found to have a very high rotational velocity of  $v \sin(i) = 124 \pm 2 \text{ km s}^{-1}$  and Przybilla et al. (2008) discovered an enhancement of  $\alpha$ -elements. Therefore, they suggested that HD 271791 was ejected from a SN in a binary which would make it the first *hyperrunaway star*. Since the escape velocity and the BH birth kick would be higher than expected for the BES, Gvaramadze (2009) suggest an alternative scenario where the original massive binary system first remained bound after the SN, before it experienced a dynamical encounter with another binary system in its parent cluster, which ejected HD 271791.

The hypervelocity hot subdwarf<sup>12</sup> US 708 has long been suspected to originate in a thermonuclear SN (Justham et al. 2009; Geier et al. 2013; Geier et al. 2015). Recently, Neunteufel (2020) found that this ejection scenario may account for hypervelocity hot subdwarfs with ejection velocities of up to  $1150 \text{ km s}^{-1}$  (for B-type hot subdwarfs in the mass range  $0.19\text{--}0.25 M_{\odot}$  and assuming a *Chandrasekhar*-mass accretor). Furthermore, a HVS could also be ejected during an encounter with an intermediate-mass BH, as described by Gualandris and Portegies Zwart (2007).

We conclude that many different ejection mechanisms are at work, producing fast stars with a wide range of velocities. In most velocity ranges, different explanations are possible, so detailed individual studies of runaway stars are required. By finding their birth places and analysing their spectral features, their evolutionary history can be examined.

While it is widely accepted that all the above mentioned production channels of high-velocity stars are active, it is a matter of debate whether one of them is dominant. By finding runaway stars in SNRs we can draw constraints on the fraction of runaway stars from the BES and compare these to model expectations. According to Renzo et al. (2019), we expect that  $67_{-26}^{+17} \%$  of high-mass binaries or  $55_{-21}^{+13} \%$  of core-collapse SNe eject a runaway star, assuming that  $\sim 1.22$  core-collapse SNe happen in each high-mass binary system (Boubert et al., 2017).

<sup>12</sup>Hot subdwarfs are core He-burning stars that lost almost its entire H envelope due to mass transfer in a binary. Therefore, they have low masses of  $\sim 0.5 M_{\odot}$  and appear as spectral types O or B (Geier et al., 2015)

# Chapter 3

## Candidate selection

For the selection of runaway star candidates, the *Gaia* catalogue was used, containing astrometric data of more than 1.7 billion stars in data release (DR) 2. This, as well as the catalogues used to obtain the SNR data, is described in Section 3.1. In the subsequent Sections 3.2 and 3.3 we define the criteria that were used to select the relevant SNRs and to compile the list of runaway candidates.

### 3.1 Catalogues

#### 3.1.1 *Gaia*

The *Gaia* spacecraft (Gaia Collaboration et al., 2016b) was designed by the *European Space Agency* as a successor of the *Hipparcos* mission (Perryman, 1989; Perryman et al., 1997). It was launched in 2013 and reached an orbit around the *Lagrange* point L2,  $1.5 \times 10^6$  km from earth. It observed  $\sim 1.7$  billion stars and provides the most precise and most complete astrometric and photometric database of celestial objects, yielding insights not only about individual stars but also about the dynamical and chemical structure of the Milky Way and its surroundings. The spacecraft contains three instruments sharing the same focal plane, namely (i) the Astrometric Instrument (ASTRO), (ii) the Photometric Instrument and (iii) the Radial Velocity Spectrometer (RVS)<sup>1</sup>. ASTRO measures positions, proper motions and parallaxes by collecting the light between 330 nm and 1050 nm, providing the photometric band *G*. While very bright stars with  $G \lesssim 3$  mag require a special treatment, the instrument is sensitive down to a limiting magnitude of  $G \approx 20.7$  mag (Gaia Collaboration et al., 2016b). The Photometric Instrument measures the spectral energy distribution between 330 nm and 1050 nm with a prism spectrograph and divides it into a blue part (330–680 nm, *BP*) and a red part (640–1050 nm, *RP*), whereas

---

<sup>1</sup><https://sci.esa.int/web/gaia/home>

### 3.1. Catalogues

---

the RVS collects narrow-band spectra (845–872 nm) to provide RV measurements of more than seven million stars. The *Gaia* data were made available in two major releases which are described in the following.

***Gaia* DR1** (Gaia Collaboration et al., 2016a) was published on 2016 Sep 14 and provides measurements taken with ASTRO, namely positions and  $G$  band magnitudes of about 1.1 billion objects as well as proper motions and parallaxes of about two million objects. For the latter, the *Gaia* measurements were combined with data from the *Tycho-2* catalogue (Høg et al. 2000, recorded with the *Hipparcos* satellite), yielding the five-parameter *Tycho-Gaia Astrometric Solution* (TGAS). Furthermore, *Gaia* DR1 provided light curves of 3000 variable stars as well as positions and magnitudes of 2000 quasars that were used to calibrate the celestial reference frame.

***Gaia* DR2** (Gaia Collaboration et al., 2018) was published on 2018 Apr 25 and enhanced the provisioning of data from ASTRO, containing positions and  $G$  magnitudes of  $\sim 1.7$  billion objects. Furthermore, parallaxes, proper motions and data from the Photometric Instrument ( $BP$ ,  $RP$ ) were given for  $\sim 1.3$  billion targets. From these, further stellar parameters were inferred as described in Andrae et al. (2018), namely effective temperatures  $T_{\text{eff}}$  (161 million stars,  $G < 17$  mag), extinction and reddening (88 million stars) as well as radius and luminosity (77 million stars). These data are accompanied by extended datasets for variable stars, quasars and solar system objects.

The data were accessed via the *VizieR* database<sup>2</sup>. Care has to be taken when using  $T_{\text{eff}}$  from *Gaia* DR2. The machine learning algorithm used to obtain the temperature estimates was only trained up to 10,000 K and therefore the  $T_{\text{eff}}$  tend to be underestimated when approaching this limit. Furthermore, the distances deviate from the inverse values of the parallaxes due to the non-linearity of the transformation. The effect increases for larger distances. Bailer-Jones et al. (2018) accounted this problem and used a Bayesian approach to provide more accurate distances from *Gaia* parallaxes<sup>3</sup>.

An updated set of astrometric data has been made available recently as the *early data release* (EDR) 3 (Gaia Collaboration et al., 2020), which provides positions,  $G$  magnitudes, parallaxes and proper motions for about 100 million more sources than DR2 and which has an increased precision due to a longer time series of measurements. Further stellar parameters as well as information e.g. about variable sources will be published in 2022 with the full DR3.

---

<sup>2</sup><https://vizier.u-strasbg.fr/viz-bin/VizieR>

<sup>3</sup>Note that the distances from Bailer-Jones et al. (2018) should be treated with care in the case of actual runaway stars. The choice of the prior is unclear in these cases due to the different velocity vectors.



### 3.1.2 D.A. Green: A catalogue of Galactic supernova remnants

David A. Green has established a database of Galactic SNRs (Green, 1984) and has continuously updated the catalogue (Green, 1988; 1991; 1996; 2004; 2009; 2014; 2019) which is also available online<sup>4</sup>. It provides positions, sizes, morphological types, flux densities at 1 GHz and spectral indices. The catalogue is based on radio data, where the SNR morphology usually is best visible. Errors of right ascension (RA) and declination (DEC) for small SNRs are given as “to the nearest few seconds of time and the nearest minute of arc, respectively”, while rounded to coarser values for larger SNRs.

### 3.1.3 University of Manitoba: High-energy observations of Galactic supernova remnants

The second important SNR catalogue is maintained by the Department of Physics and Astronomy at the University of Manitoba (UofM), Canada, and presented in Ferrand and Safi-Harb (2012). From the online database<sup>5</sup>, one can obtain multiple parameters and properties of the Galactic SNRs. The table gives an overview of the high-energy observations made of each SNR, while also observations in other wavelength regimes were used to compile the given parameters. The ranges of distances and ages usually correspond to the lowest and highest values given in the literature. The number of Galactic SNRs given in the UofM catalogue (383) is higher than in the Green catalogue because also pulsar wind nebulae as well as questionable and pre-validated sources are listed, some of which might turn out to be H II regions.

### 3.1.4 *StarHorse* catalogue

The *StarHorse* catalogue (Anders et al., 2019) provides Bayesian distances, extinctions and stellar atmospheric parameters by using parallaxes and photometric data from *Gaia* DR2, Pan-STARRS1, 2MASS and AllWISE. These are compared to stellar evolutionary models by using the *StarHorse* code (Queiroz et al., 2018), which calculates the posterior probability distribution of the selected parameters based on the observational input data and a set of priors. In this chapter, we only use the *StarHorse* surface gravities as an indicator if a star is a red giant. Later, we use *StarHorse* extinctions to calculate absolute magnitudes (Section 5.6). Several *StarHorse* parameters are used in the discussion (Section 6.2) and an overview of the relevant parameters is given in Tables F.3 and F.7.

<sup>4</sup><http://www.mrao.cam.ac.uk/surveys/snrs/>

<sup>5</sup><http://snrcat.physics.umanitoba.ca/SNRtable.php>

## 3.2 Selection of supernova remnants

To find suitable SNRs, the two above described references were used. (i) The Green catalogue (Green, 2014; 2019) for positions and sizes and (ii) the UofM catalogue (Ferrand and Safi-Harb, 2012) for ages and distances.

One of the goals of this thesis is to find runaway stars with the latest possible spectral types. Therefore, we set a distance and, hence, magnitude limit so that we are able to observe runaway candidates with as late spectral types as possible. The limiting magnitude of the main instrument we use, the *UV-Visual Echelle Spectrograph* (UVES), is  $m_{V,\text{lim}} = 19.5$  mag, corresponding to a signal-to-noise ratio of  $S/N \approx 10$  in 90 min exposure time. This value is given in the UVES user manual (Sbordone and Ledoux, 2017) for the Red Arm and favourable conditions. However, for our setup (described in Section 4) and our requirements, i.e. a maximum exposure time of one hour and a minimum  $S/N$  of  $\sim 30$ , a limiting magnitude of  $m_G \equiv G = 17$  mag was used, corresponding to  $m_V \equiv V = 17.13$  mag for a G0 V star, which is a typical example for our selection<sup>6</sup>.

Henry and McCarthy (1993) presented relations between stellar mass and brightness for different mass ranges:

$$\log(M/M_\odot) = -0.1681 M_V + 1.4217 \quad (3.1)$$

for  $0.5 M_\odot > M > 0.18 M_\odot$  and

$$\log(M/M_\odot) = 0.002456 M_V^2 - 0.09711 M_V + 0.4365 \quad (3.2)$$

for  $2 M_\odot > M > 0.5 M_\odot$ ,

where  $M_V$  is the absolute visual brightness. The project was started in 2016, before *Gaia* DR2 became available. Therefore, *Gaia* DR1 TGAS was initially used for the target selection. Eqn. 3.2 was used to define a distance limit of  $d = 1.6$  kpc for the stars selected from *Gaia* DR1, containing much fewer stars than DR2. The conversion between absolute and apparent brightness was done with the distance modulus (Eqn. 2.4).

The distance limit was introduced as a compromise between studying as many SNRs as possible and being able to observe the latest possible spectral types. At  $d = 1.6$  kpc, we could find 25 SNRs and stars with masses down to  $M = 0.86 M_\odot$ , corresponding to spectral type K0.5 (Pecaut and Mamajek, 2013, Table 5). For stars from *Gaia* DR2, we strengthened the distance limit in order to be still able to create feasible observing projects with a moderate number of targets. At a distance limit of  $d = 0.5$  kpc, with the given magnitude limit, we could principally reach down to  $M = 0.60 M_\odot$  (Eqn. 3.2), corresponding to spectral type K8. Only 4 SNRs are

<sup>6</sup>the conversion between  $G$  and  $V$  was done by using the polynomial relations by Evans et al. (2018) with  $BP - RP = 0.782$  given in Pecaut and Mamajek (2013, Table 5) for a G0 V star.

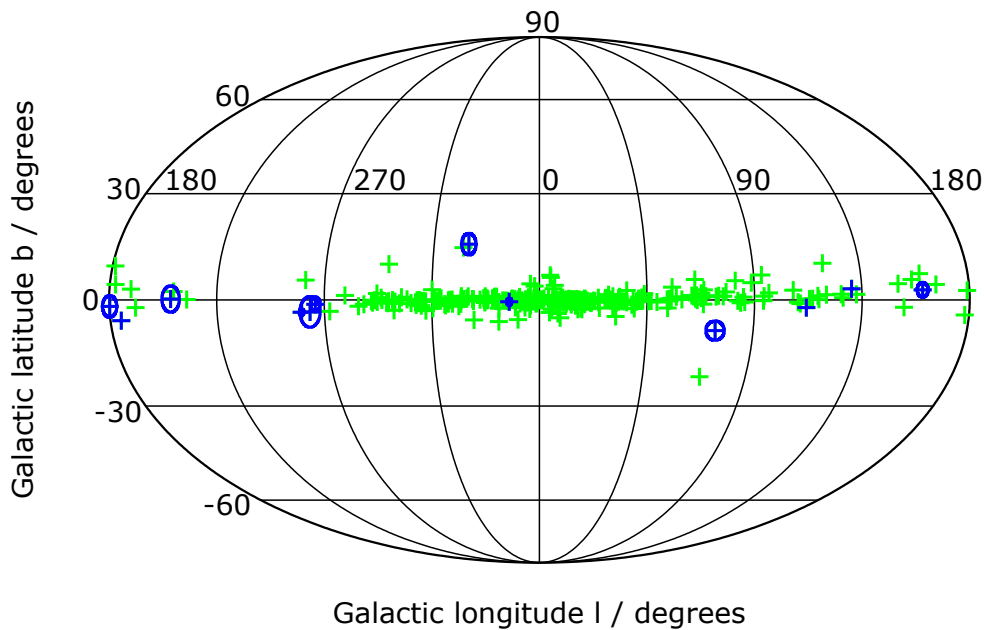


FIGURE 3.1: The distribution of the SNRs in the sky, shown with Galactic coordinates in a Mollweide projection, which was done with a code by Roberto Lineros. The green crosses show all SNRs listed in the Green catalogue (Green, 2019), the blue crosses, where also the sizes are shown, represent the SNRs investigated in this thesis. The conversion to Galactic coordinates was done with a NASA online calculator<sup>7</sup>.

located within this distance. However, we also continued to analyse four SNRs with  $0.5 \leq d \leq 1.6$  kpc as well as four historical SNRs with distances of up to 3.5 kpc (Cassiopeia A). In the case of individual targets which distances are closer than the limits described above, of course we could also get down to later spectral types. On the other hand, extinction could reduce the range of observable spectral types.

The parameters of the twelve investigated SNRs, including the limiting spectral type of each SNR at the corresponding distance, are given in Tables 3.1 and 3.2. Their positions are displayed in Fig. 3.1 in Galactic coordinates, whereon their G-names are based. Our sample is displayed with blue crosses, where ellipses also show their sizes. The central positions of the remaining Galactic SNRs from Green (2019) are shown in green. One can see that their positions are all close to the Galactic plane, where their progenitors were born. Due to their short lifetime, core-collapse SN progenitors cannot travel far from the Galactic plane. SNRs from SNe of Type Ia can, in principal, be located further from the Galactic plane. The Lupus Loop, which has the second largest angular distance to the Galactic plane among the SNRs from Green (2019) and which SN type is not known, is one of the closest SNRs, making the angular distance appear larger.

<sup>7</sup><https://heasarc.gsfc.nasa.gov/cgi-bin/Tools/convcoord/convcoord.pl>

### 3.3. Selection of runaway star candidates

TABLE 3.1: Properties of the SNRs studied in this work, namely their equatorial coordinates RA/DEC, angular diameters  $\Theta$ , morphological types (S: Shell, F: Filled-centre, C: Composite) and radio fluxes  $S_{1\text{GHz}}$ , taken from Green (2014).

SNR Name	Alternative Name	RA [h:m:s]	DEC [d:m]	$\Theta$ [arcmin]	Type	$S_{1\text{GHz}}$ [Jy]
G074.0−08.5	Cygnus Loop	20:51:00	+30:40	230 × 160	S	210
G160.9+02.6	HB9	05:01:00	+46:40	140 × 120	S	110
G180.0−01.7	S147	05:39:00	+27:50	180 × 180	S	65
G205.5+00.5	Monoceros Loop	06:39:00	+06:30	220 × 220	S	140
G260.4−03.4	Puppis A	08:22:10	−43:00	60 × 50	S	130
G263.9−03.3	Vela	08:34:00	−45:50	255 × 255	C	1750
G266.2−01.2	Vela Jr.	08:52:00	−46:20	120 × 120	S	50
G330.0+15.0	Lupus Loop	15:10:00	−40:00	180 × 180	S	350
G111.7−02.1*	Cassiopeia A	23:23:26	+58:48	5 × 5	S	2720
G130.7+03.1*	3C58 (SN 1181)	02:05:41	+64:49	9 × 5	F	33
G184.6−05.8*	Crab Nebula	05:34:31	+22:01	7 × 5	F	1040
G347.3−00.5*	SN 393	17:13:50	−39:45	65 × 55	S?	30

\* Historical SNR

Generally, since we want to shed light on the binary evolution of massive stars and compare our findings to corresponding models, we focus on SNRs from core-collapse SNe. SNRs that are known to originate from a SN Type Ia are not considered here.

### 3.3 Selection of runaway star candidates

In the twelve selected SNRs, we searched for runaway candidates in *Gaia* DR1 TGAS and, as soon as it became available, in *Gaia* DR2. To define a search area, we need to know the SN explosion site, which is approximated with the geometric centre (GC). In most cases, we chose the coordinates from Green (2014), which are mainly based on radio observations. Alternatively, we can search the literature for images of different wavelengths, determine the GC for each image and use the mean coordinates for the search. This was done for the Vela SNR (see Fig. 3.2), where we used a radio image (843 MHz) from Bock et al. (1998), a X-ray image from Sushch et al. (2011) and the position from Green (2014). The average position, adopted as the actual GC, is shown by a red cross with corresponding  $1\sigma$  error ellipse in Fig. 3.2 (c). Note that the runaway candidates identified in *Gaia* DR2 were not traced back to this average GC but to the position of the Vela pulsar at the time of the SN.

Besides the explosion site, also the maximum possible velocity of a runaway star is needed to define a search area. From simulations of massive binary evolution, including Blaauw kick and SN kick, Tauris (2015) gives a maximum possible ejection velocity of  $v_{\text{max}} = 1050 \text{ km s}^{-1}$  for stars with  $0.9 M_{\odot}$ . After adding the Galactic rotational velocity,  $\sim 230 \text{ km s}^{-1}$ , this corresponds to a maximum galactocentric rest frame velocity of  $v_{\text{max}}^{\text{grf}} \approx 1280 \text{ km s}^{-1}$ . However, such extreme cases are very rare (Renzo et al., 2019). For this thesis, we adopt  $v_{\text{max}} = 1000 \text{ km s}^{-1}$ .

TABLE 3.2: Properties of the SNRs studied in this work. Distances  $d$  and ages  $t$  are taken from Ferland and Safi-Harb (2012) and references therein, where the errors come from the range between the lowest and highest values in the given literature. For 3C58, Crab Nebula and G347.3–00.5, the ages are accurately known from the associations to the historical SNe. Column 5 gives the angular search radius as the maximum range where a runaway star could be found (see Eqn. 3.3) and column 6 gives the limiting stellar spectral type  $\text{SpT}_{\text{lim}}$  observable at the corresponding nominal distance and a limiting magnitude of  $m_G = 17.0$  mag.

SNR Name	Alternative Name	$d$ [kpc]	$t$ [kyr]	$r_{\text{search}}$ [deg]	$\text{SpT}_{\text{lim}}$
G074.0–08.5	Cygnus Loop	$0.79 \pm 0.21$	$15 \pm 5$	$1.5970 \pm 0.5896$	K5
G160.9+02.6	HB9	$0.80 \pm 0.40$	$5.5 \pm 1.5$	$0.4758 \pm 0.2605$	K5
G180.0–01.7	S147	$1.30 \pm 0.20$	$30 \pm 4$	$1.3513 \pm 0.2735$	K1.5
G205.5+00.5	Monoceros Loop	$1.44 \pm 0.54$	$90 \pm 60$	$4.7910 \pm 3.8437$	K1.5
G260.4–03.4	Puppis A	$1.3 \pm 0.3$	$4.08 \pm 0.38$	$0.1364 \pm 0.0370$	K1.5
G263.9–03.3	Vela	$0.275 \pm 0.025$	$18 \pm 9$	$3.8328 \pm 1.9367$	M0.5
G266.2–01.2	Vela Jr.	$0.75 \pm 0.25$	$3.8 \pm 1.4$	$0.2928 \pm 0.1428$	K5
G330.0+15.0	Lupus Loop	$0.33 \pm 0.18$	$23 \pm 8$	$4.8975 \pm 2.7871$	M0.5
G111.7–02.1*	Cassiopeia A	$3.50 \pm 0.20$	$0.334 \pm 0.018$	$0.0056 \pm 0.0004$	F9
G130.7+03.1*	3C58 (SN 1181)	$2.60 \pm 0.60$	0.839	$0.0189 \pm 0.0043$	G2
G184.6–05.8*	Crab Nebula	$1.85 \pm 0.35$	0.966	$0.0305 \pm 0.0057$	G9
G347.3–00.5*	SN 393	$1.3 \pm 0.4$	1.627	$0.0952 \pm 0.0224$	K1.5

\* Historical SNR

With age  $t$  and distance  $d$  of the SNR as given by the UofM catalogue, the search radius can be calculated as

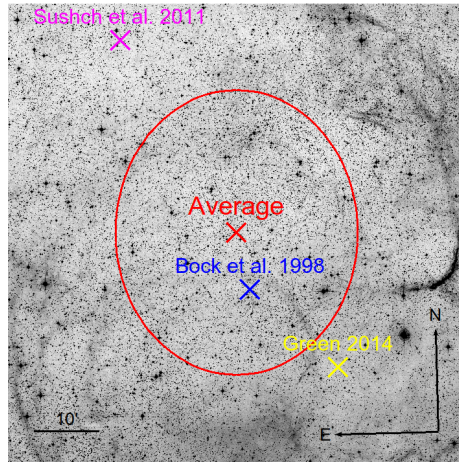
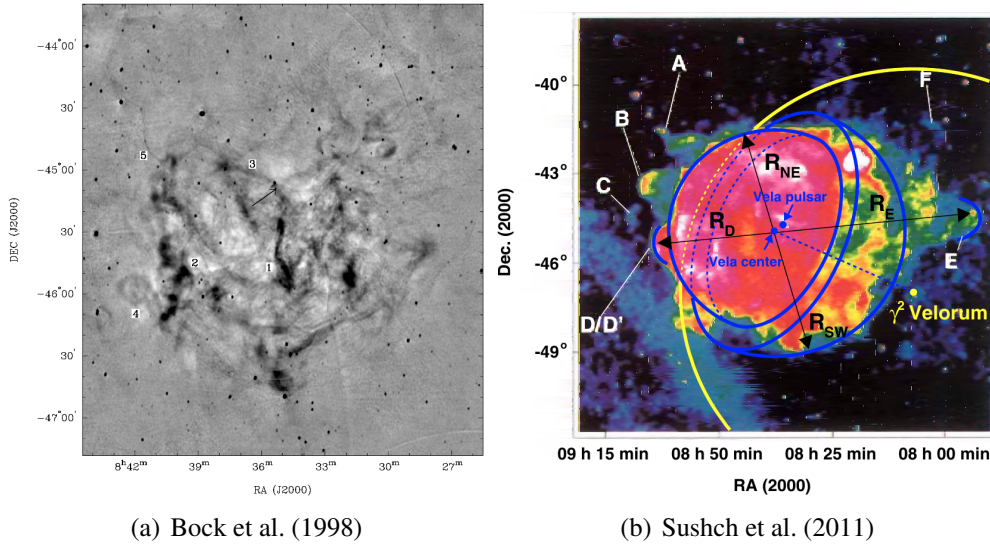
$$r_{\text{search}} = 3.4934 \times \frac{t/\text{yr}}{d/\text{pc}} \text{ arcmin}. \quad (3.3)$$

For the cone search in *Gaia*, we converted the values to degrees and used the upper limit  $r_{\text{search,max}} = r_{\text{search}} + \Delta r_{\text{search}}$ , taking into account the uncertainties of distance and age. The values  $r_{\text{search}}$  are given in Table 3.2.

SNR expansion velocities are larger than typical runaway star velocities during the *Sedov-Taylor* phase, which is the current state of most of our SNRs. So we expect potential runaway stars to still be located inside the SNR.

This assumption was also used by Dinçel et al. (2015), who did not consider  $v_{\text{max}}$ , but investigated only OB-type runaway candidates within one sixth of the radius of the 48 selected SNRs, considering distance ( $< 5$  kpc) and extinction towards the SNRs. In contrast, Boubert et al. (2017) used a Bayesian approach to calculate runaway probabilities for candidates in ten northern SNRs within 2 kpc. They used the simulated velocity distribution of runaway stars from Renzo et al. (2019) and also considered the primary mass  $M_1$ , the mass ratio  $q$  and period  $P_{\text{orb}}$  of the pre-SN binary as well as the age  $t$  of the SNR.  $M_1$ ,  $q$  and  $P_{\text{orb}}$  are predicted by their calculation and used for the prior together with the other parameters. They do not exclude runaway candidates with late spectral types but assign higher probabilities to early-type stars,

### 3.3. Selection of runaway star candidates



(c) Average. Background image from ESO DSS-2-red

FIGURE 3.2: The Vela SNR at 843 MHz (a) and in X-rays (b). The bottom panel (c) shows the GCs from (a) and (b), the Green centre (Green, 2014) as well as the average and its  $1\sigma$  error ellipse.

corresponding to pre-SN mass ratios close to one.

In this work, for each SNR, with *Topcat* or *VizieR* we first listed all *Gaia* stars in the given search radius with  $G \leq 17.0$  mag and a given parallax. We then traced back the projected trajectories of the stars with a *Python* code (see Appendix A), using their positions, proper motions and the age of the SNR to obtain their coordinates ( $RA_{SN}, DEC_{SN}$ ) at the time of the SN. We neglected the Galactic gravitational potential, since the lifetime of a SNR is so short that the potential will not have a significant effect. Gaussian error propagation was used to calculate the uncertainties of the past positions.

The likelihood of a runaway candidate could be naively quantified by the angular distance

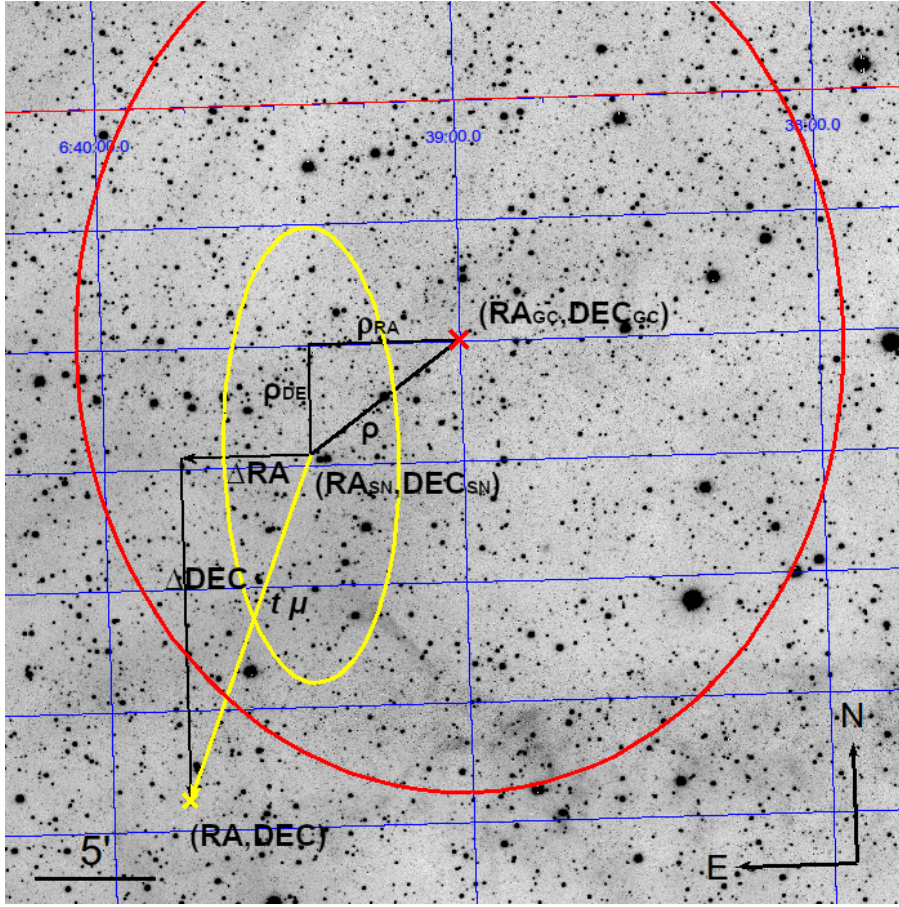


FIGURE 3.3: 2D kinematics of a runaway star candidate, exemplary shown for the star TYC159-251-1 near the centre of the Monoceros Loop. The red labels mark the GC and its error ellipse. The yellow cross marks the current position of the star, which is connected to the position at the time of the SN (surrounded by its error ellipse) by an arrow in proper motion direction. The thick black line marks the angular distance  $\rho$  between the star and the GC at the time of the SN, the thin black lines mark the RA- and DEC-components of  $\rho$  and of the proper motion arrow. The background image was taken by us in  $H\alpha$  with the STK (Mugrauer and Berthold, 2010) at the University Observatory Jena.

$\rho$  of the runaway candidate to the GC  $(RA_{GC}, DEC_{GC})$  at the time of the SN, which is given as

$$\rho = \sqrt{\rho_{RA}^2 + \rho_{DEC}^2} \quad (3.4)$$

$$= \sqrt{\left( (RA_{SN} - RA_{GC}) \cos\left(\frac{DEC_{SN} + DEC_{GC}}{2}\right) \right)^2 + (DEC_{GC} - DEC_{SN})^2}. \quad (3.5)$$

The geometry is illustrated in Fig. 3.3. As an example, we show the motion of TYC159-251-1, identified as a possible runaway candidate in the Monoceros Loop in *Gaia* DR1 TGAS. The yellow cross marks the current position of the star  $(RA, DEC)$ , connected to its position at the time of the SN  $(RA_{SN}, DEC_{SN})$  by an arrow in proper motion direction. The length of the

### 3.3. Selection of runaway star candidates

arrow is given as  $t\mu$ , i.e. the age  $t$  of the SNR times the total proper motion  $\mu = \sqrt{\mu_{\text{RA}}^2 + \mu_{\text{DEC}}^2}$ . The proper motions  $\mu_{\text{RA}}$  given in *Gaia* are already corrected for the curvature of the celestial sphere. The SNR GC ( $\text{RA}_{\text{GC}}, \text{DEC}_{\text{GC}}$ ) is marked by a red cross and its angular distance  $\rho$  to ( $\text{RA}_{\text{SN}}, \text{DEC}_{\text{SN}}$ ) is marked by the thick black line. The RA- and DEC-components of  $\rho$  and  $t\mu$  are illustrated by the thin black lines.

We selected the stars that, at the time of the SN, were located inside the error ellipse of the GC, shown as a red ellipse in Fig. 3.3. For stars from *Gaia* DR1, we used the standard deviations in RA and DEC from the determination of the Vela GC to define the error ellipse, which was then also used for the other SNRs, scaled to the corresponding diameter as given in Green (2014). For stars selected from *Gaia* DR2, we used the error estimate given by Green (2009), which we translate here to

$$\begin{aligned} \Delta\text{GC} &= 0.021^\circ \times 0.017^\circ, \text{ if } 0' \leq \Theta \leq 50', \\ \Delta\text{GC} &= 0.042^\circ \times 0.034^\circ, \text{ if } 50' \leq \Theta \leq 100', \\ \Delta\text{GC} &= 0.063^\circ \times 0.051^\circ, \text{ if } 100' \leq \Theta, \end{aligned} \quad (3.6)$$

where  $\Theta$  is the angular diameter of the SNR. However, if a NS is associated with the SNR, we selected only the stars that could be traced back to a possible common origin with the NS.

Note that the strict limitation of Eqn. 3.6 means that we loose up to  $\sim 33\%$  of runaway star candidates that were located more than  $1\sigma$  from the nominal GC. We made this limitation in order to create feasible observing projects, concentrating on the most promising candidates.

We also checked if the *Gaia* parallaxes of the stars are consistent with the range of possible distances of the SNR. A comparison to the more accurate distances given by Bailer-Jones et al. (2018) yields no significant deviations for the parallax range considered in our work. All candidates are still within the correct range when using their distances from Bailer-Jones et al. (2018).

In *Gaia* DR2, we checked the given values for radius, luminosity and effective temperature, so that post-MS giants could be excluded beforehand. The selection could be made by plotting the candidates into a HRD, shown in Fig. 3.4, where we compare our selected stars to PARSEC isochrones (Bressan et al., 2012)<sup>8</sup>. Reddish colours indicate if a star was classified as a giant. If a star has a higher luminosity than the ZAMS, it can be either a pre-MS star or an evolved star (i.e. terminal-age MS or giant, see Section 5.5). We are looking for young stars, so it might be better to leave a few evolved stars in the sample than excluding too many pre-MS stars. The division was roughly made at the isochrone for 1 Myr. For questionable cases, and since luminosities were not given for all possible targets in *Gaia* DR2, we also checked the

<sup>8</sup>[http://stev.oapd.inaf.it/cgi-bin/cmd\\_3.3](http://stev.oapd.inaf.it/cgi-bin/cmd_3.3)



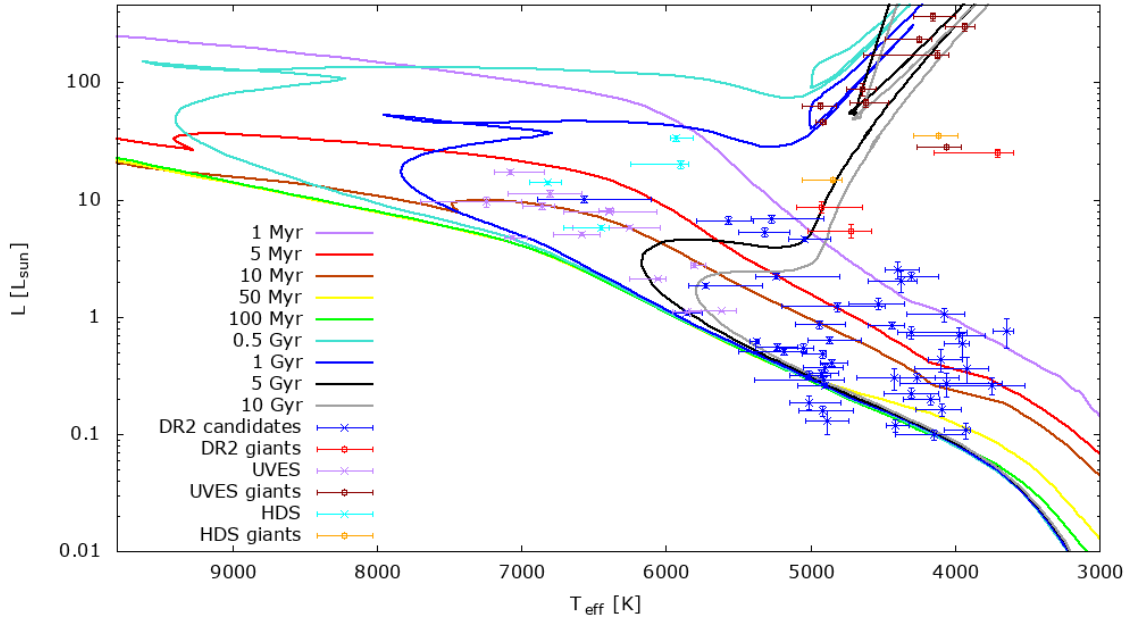


FIGURE 3.4: HRD of the runaway star candidates with effective temperatures and luminosities taken from *Gaia* DR2. In the key, for stars that were observed by us, we give the names of the corresponding spectrographs, UVES and HDS. For comparison, we show isochrones calculated from PARSEC models (Bressan et al., 2012). The stars marked in red, dark-red and orange were considered to be post-MS giants and ruled out from the investigation.

surface gravities  $\log(g)$  of the targets in the *StarHorse* catalogue (Anders et al., 2019). These are plotted versus the effective temperatures in Fig. 3.5. Four targets with  $\log(g) < 3$ , where no luminosity was given, were ruled out. Note that Fig. 3.5 also shows a higher number of UVES targets which are not displayed in Fig. 3.4 because no luminosity was given.

Stars observed with UVES/VLT and HDS/Subaru were selected from *Gaia* DR1, where no radii and luminosities were given. Therefore, the giants in this sample were only rejected after the observation, when their DR2 data became available.

The rejected post-MS stars are listed in Table 3.3, where we show the properties which are relevant for the rejection.

All in all, the stars had to fulfil the following criteria in order to be considered for the further investigation:

- (i) Current position in a cone around the GC according to Eqn. 3.3.
- (ii) Position at the time of the SN within the error ellipse of the GC according to Fig. 3.2 (DR1 TGAS) or Eqn. 3.6 (DR2).
- (iii) *Gaia* parallax distance consistent with SNR distance.
- (iv) Not classified as a giant according to  $T_{\text{eff}}$ ,  $R$ ,  $L$  and  $\log(g)$  (only DR2).

### 3.3. Selection of runaway star candidates

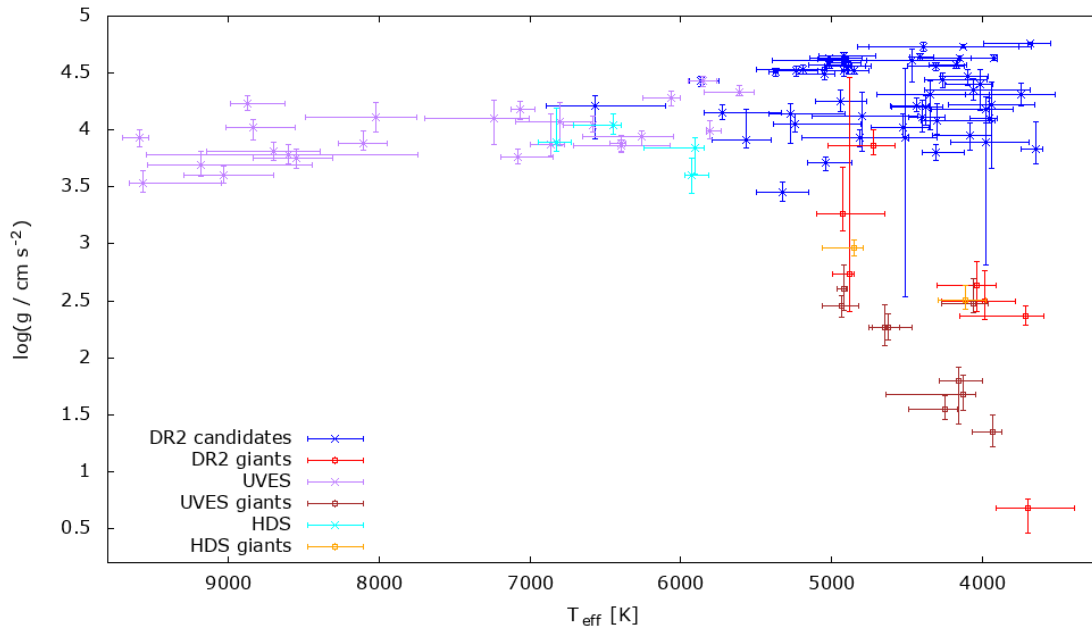


FIGURE 3.5: Here we show surface gravities  $\log(g)$  from the *StarHorse* catalogue (Anders et al., 2019) versus effective temperatures  $T_{\text{eff}}$  from *Gaia* DR2 of the runaway candidates observed with UVES/VLT and HDS/Subaru as well as the stars identified in *Gaia* DR2. The stars marked in red, dark-red and orange were considered to be post-MS giants and ruled out from the investigation.

The remaining targets were then proposed for spectroscopic follow-up observations, which were performed for the targets selected from *Gaia* DR1 TGAS as described in the following chapter.

TABLE 3.3: Post-MS stars rejected from the analysis. We list their name (*Gaia* DR2 identifiers in the last seven rows) and if they were observed with UVES/VLT (U) or HDS/Subaru (H). We give the SNR in which they are located, surface temperature  $T_{\text{eff}}$ , radius  $R$ , luminosity  $L$  (*Gaia* DR2) and  $\log(g)$  (*StarHorse* catalogue, Anders et al. 2019).

Name	Obs.	SNR	$T_{\text{eff}}$ [K]	$R$ [ $R_{\odot}$ ]	$L$ [ $L_{\odot}$ ]	$\log(g/\text{cm s}^{-2})$
HD 261117	U	G205.5+00.5	$4935^{+126}_{-113}$	$10.9^{+0.5}_{-0.5}$	$63.3 \pm 3.5$	$2.45^{+0.10}_{-0.09}$
TYC159-241-1	U	G205.5+00.5	$4645^{+108}_{-98}$	$14.5^{+0.6}_{-0.6}$	$88 \pm 10$	$2.26^{+0.20}_{-0.16}$
TYC159-2006-1	U	G205.5+00.5	$4921^{+45}_{-24}$	$9.36^{+0.09}_{-0.17}$	$46.3 \pm 1.8$	$2.60^{+0.21}_{-0.19}$
TYC159-2408-1	U	G205.5+00.5	$4127^{+511}_{-81}$	$25.8^{+1.1}_{-5.4}$	$174 \pm 14$	$1.68^{+0.17}_{-0.15}$
TYC159-2082-1	U	G205.5+00.5	$4623^{+109}_{-161}$	$12.8^{+0.9}_{-0.6}$	$67 \pm 6$	$2.26^{+0.13}_{-0.10}$
TYC159-892-1	U	G205.5+00.5	$4158^{+128}_{-157}$	$36.9^{+2.9}_{-2.2}$	$366 \pm 29$	$1.79^{+0.13}_{-0.38}$
HD 261527	U	G205.5+00.5	$4248^{+238}_{-84}$	$28.2^{+1.2}_{-2.9}$	$233 \pm 13$	$1.54^{+0.12}_{-0.09}$
TYC159-2962-1	U	G205.5+00.5	$3933^{+135}_{-65}$	$37.3^{+1.3}_{-2.4}$	$299 \pm 23$	$1.35^{+0.16}_{-0.13}$
TYC8152-104-1	U	G266.2-01.2	$4061^{+207}_{-98}$	$10.8^{+0.5}_{-1.0}$	$28.5 \pm 1.3$	$2.48^{+0.21}_{-0.08}$
TYC3344-771-1	H	G160.9+02.6	$4113^{+179}_{-134}$	$11.7^{+0.8}_{-1.0}$	$35.3 \pm 1.4$	$2.50^{+0.13}_{-0.08}$
TYC3344-124-1	H	G160.9+02.6	$4850^{+210}_{-63}$	$5.46^{+0.15}_{-0.44}$	$14.9 \pm 0.5$	$2.97^{+0.07}_{-0.07}$
6005337077025170944	-	G330.0+15.0	$4879^{+113}_{-31}$	-	-	$2.73^{+1.73}_{-0.33}$
5972266309936126592	-	G347.3-00.5	$4040^{+262}_{-133}$	-	-	$2.63^{+0.21}_{-0.23}$
5972266408657061760	-	G347.3-00.5	$3710^{+439}_{-115}$	$12.1^{+0.8}_{-2.4}$	$25.2 \pm 1.9$	$2.37^{+0.09}_{-0.09}$
5972266413014327680	-	G347.3-00.5	$4928^{+169}_{-284}$	$4.1^{+0.5}_{-0.3}$	$8.7 \pm 1.0$	$3.26^{+0.40}_{-0.15}$
5972219443242360448	-	G347.3-00.5	$3697^{+212}_{-311}$	-	-	$0.68^{+0.08}_{-0.22}$
5972267890483115392	-	G347.3-00.5	$3981^{+288}_{-200}$	-	-	$2.49^{+0.27}_{-0.15}$
5972220950723591808	-	G347.3-00.5	$4722^{+303}_{-143}$	$3.49^{+0.23}_{-0.40}$	$5.5 \pm 0.7$	$3.87^{+0.13}_{-0.08}$



# Chapter 4

## Observations and data reduction

High-resolution spectroscopic observations of 39 runaway star candidates in six SNRs were performed at the *European Southern Observatory* (ESO) *Very Large Telescope* (VLT) and the *National Astronomical Observatory of Japan* (NAOJ) Subaru telescope between 2017 Oct 8 and 2018 Oct 26. The goals were:

- (Re)determination of the spectral type
- For FGKM-stars: Identification and analysis of the Li 6708 Å absorption line as youth indicator
- Determination of the radial velocity (RV)
- Determination of atmospheric parameters with special emphasis on effective temperature and rotational velocity

For sufficiently precise RV measurements, a spectral resolving power of  $R \gtrsim 30,000$  was required. Furthermore, we set the exposure times to reach signal-to-noise ratios of  $S/N \gtrsim 50$  in the individual spectra. With  $S/N = 55$  we should be able to measure the equivalent width (EW) of the Li 6708 Å line to a precision of about 20 %.

If one or more stars can be found, for which its kinematics and the above mentioned properties strongly indicate a runaway nature, a further test will have to be done to obtain a final proof: The identification of SN debris, e.g. heavy- and  $\alpha$ -elements in the stellar atmosphere. However, this requires a spectrum with much higher  $S/N$  and resolution and therefore lies beyond the scope of this thesis.

### 4.1 VLT UVES

For southern targets, we have used the *UV-Visual Echelle Spectrograph* (UVES, Dekker et al. 2000), which is mounted at the *Nasmyth* focus of *Kueyen* (*Unit Telescope 2*) at the ESO VLT,

located on the *Cerro Paranal* in Chile. We observed 33 runaway star candidates, selected from *Gaia* DR1 TGAS, in five SNRs on the southern sky, namely (i) G180.0–01.7 (S147), (ii) G205.5+00.5 (Monoceros Loop), (iii) G260.4–03.4 (Puppis A), (iv) G263.9–03.3 (Vela) and (v) G266.2–01.2 (Vela Jr.). All of them were observed in ESO period 100 (P100) in project 0100.D–0314 in service mode between October and December 2017.

UVES is an *echelle* spectrograph, i.e. the spectral orders that are produced by the first grating are separated by a second grating, the cross-disperser (CD), which is mounted perpendicular to the dispersion direction of the echelle grating. The CD separates the orders by at least 10 arcsec throughout the whole usable wavelength range of 3000–11,000 Å (Sbordone and Ledoux, 2017), so that even higher orders do not overlap. The final detected image consists of separated stripes with moderately varying widths, spacings and sensitivities. The same wavelength usually appears in different orders, but the unneeded parts can be cropped off when the spectral orders are merged during the data reduction.

Further details can be seen in Fig. 4.1, where the schematic layout of the instrument is shown. For this image and a detailed description of the instrument see Sbordone and Ledoux (2017). The upper part rotates with the telescope, while the lower part, contained in the black square, is mounted on the instrument table. The light enters from the telescope or the calibration unit at the top, where an iodine cell (for an additional wavelength reference and higher RV precision) and an image slicer (for higher spectral resolving power) can be inserted. The derotator corrects for field rotation and keeps the slit angle fixed throughout the observation. After entering the instrument table, the light passes the filter wheel, which is mainly used for acquisition in order to avoid saturation of the slit viewer camera in the case of bright targets. Optionally, the light can be corrected for polarisation (depolarizer) and atmospheric dispersion (ADC), before it enters either the red arm (Ra, 4200–11,000 Å), the blue arm (Ba, 3000–5000 Å) or both (Dic#1 or Dic#2).

Both arms have a similar layout. They are the main part of the echelle spectrograph, where several mirrors are used to reflect the light onto the echelle grating and the CD. For each arm, two CDs, mounted back-to-back are available, which determine the wavelength of the central echelle order. We used the red arm, CD3, with a central wavelength of 600 nm. In this standard setting, the filter SHP700 is used below the slit. In the red arm, two CCD detectors are used, each with  $2048 \times 4096$  pixels, covering the spectral ranges 4986–5957 Å and 6036–7003 Å, respectively. Using  $1 \times 1$  binning, which is adequate for the relatively bright targets observed in P100, we chose a slit width of 1.2", yielding a resolving power of  $R = 32,250$ . ADC, depolarizer and image slicer were not used because we would have had to increase the exposure times significantly in order to obtain the same  $S/N$  with these devices. The image rotator was only used if the light of a nearby star could otherwise have fallen into the slit.

The individual exposure times varied between 10 s and 500 s, depending on the brightness

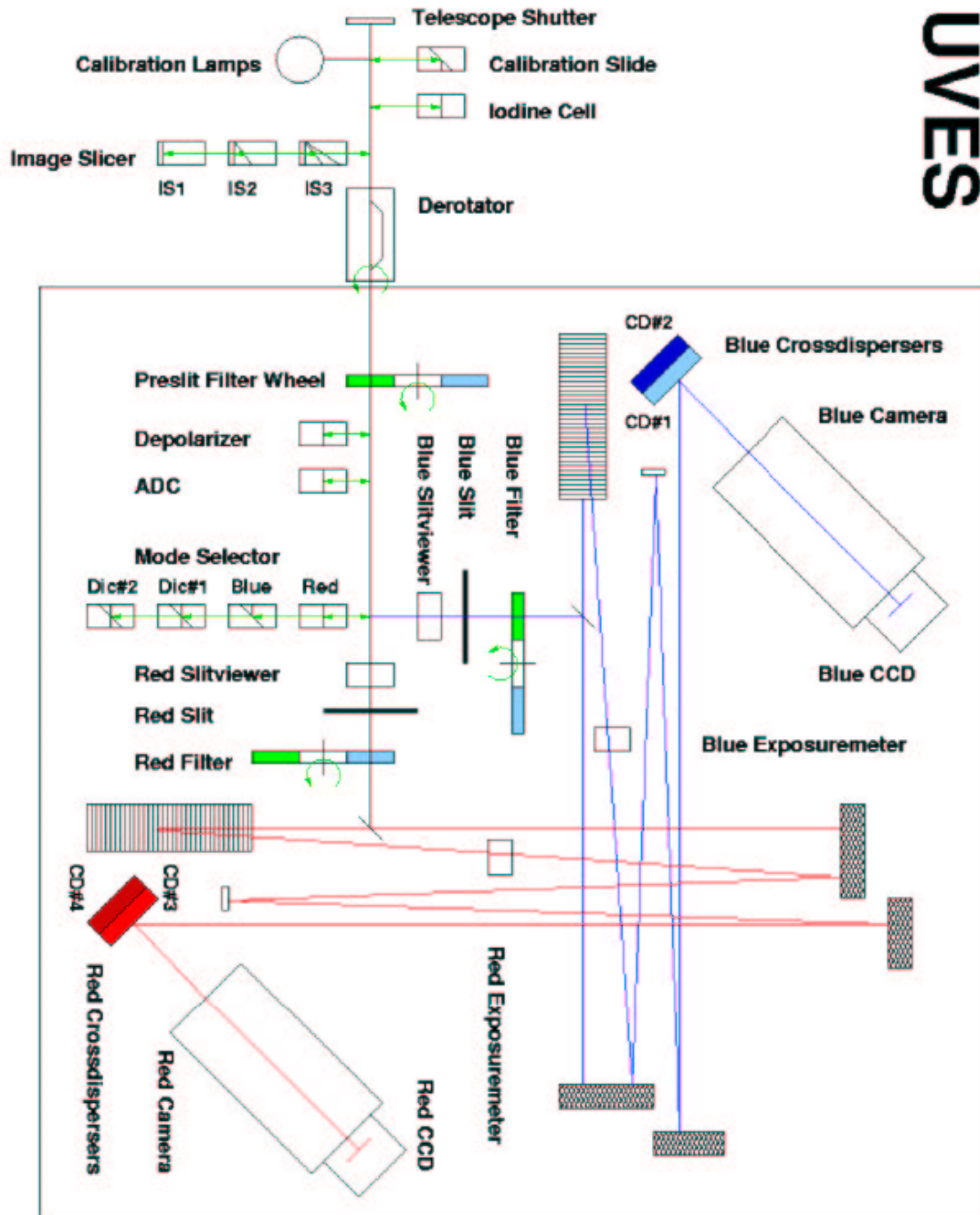


FIGURE 4.1: Schematic layout of UVES. Image taken from the UVES user manual (Sbordone and Ledoux, 2017).

## 4.1. VLT UVES

---

of the star and calculated for the given instrument setting and the required  $S/N$  with the UVES exposure time calculator (ETC)<sup>1</sup>. Two exposures were taken for each star, where an average  $S/N$  of 64.7 was achieved for the single exposures. A VLT project is divided into observation blocks, where in our case one block corresponds to the observation of one star, i.e. the two exposures plus the overheads. For P100, we applied for 10 h in total, where for each observation block we have to consider the following overheads:

- $\sim 240$  s for pointing
- $\sim 120$  s for acquisition
- $\sim 60$  s for setup
- $2 \times 40$  s for readout ( $1 \times 1$  binning)

This gives 500 s overheads for each star or 4 h 35 min in total. The total on-source integration time was 5 h 4 min, yielding 9 h 39 min for the project in P100.

Standard calibrations were used, i.e. bias frames, flatfield images of a halogen lamp and wavelength calibration images of a ThAr lamp which are taken regularly for each standard setup as described in the UVES calibration plan (Sbordone and Ledoux, 2020). Dark frames are not necessary because the dark current in our setup at a detector temperature of  $-120^\circ\text{C}$  is only  $0.5 \text{ e}^-/\text{px}/\text{h}$  (Sbordone and Ledoux, 2017). Data reduction was done with the ESO *Reflex* pipeline for UVES (Bramich and Moehler, 2017). The individual reduction steps are bias subtraction, order detection, flatfielding, wavelength calibration and spectrum extraction. For each star, five bias frames, six flat frames and two arc frames were used. They were recorded on the same day as the science frames. The flats and arcs include one frame each for order detection.

We obtained four reduced spectra for each star; for each of the two exposures, we got one spectrum for the lower and one for the upper wavelength regime. Additional check images were obtained for flux errors, wavelength calibration and its errors, sky background and order extraction. Further details are given in Appendix B.

The two exposures for each star were averaged to one spectrum with *IRAF*. Normalisation was done with *iSpec* (Blanco-Cuaresma et al., 2014).

In Table 4.1 we list the 33 runaway candidates that were observed with UVES/VLT. We obtained the  $S/N$  from the ESO Archive Science Portal. Julian date (JD) and barycentric Julian date (BJD)<sup>2</sup> were calculated with the online tools from AAVSO<sup>3</sup> and Eastman et al.

---

<sup>1</sup><https://www.eso.org/observing/etc/bin/gen/form?INS.NAME=UVES+INS.MODE=spectro>

<sup>2</sup>JD 0 corresponds to 4713 BC Jan 1 (<https://www.aavso.org/about-jd>) and each day changes at noon, 12:00 a.m. The BJD only accounts for a moderate, sinusoidal change reflecting the motion of the Earth around the solar barycentre. The first entry in Table 4.1, BJD = 2458035.85, corresponds to 2017 Oct 09, 08:30 UT.

<sup>3</sup><https://www.aavso.org/jd-calculator>



(2010)<sup>4</sup>, respectively.

While the stars observed in P100, selected from *Gaia* DR1 TGAS, are relatively bright with  $G$  magnitudes between 7.85 and 12.73, the magnitude limit of  $G = 17$  mag, corresponding to  $V = 17.13$  mag, has to be considered for stars selected from *Gaia* DR2. With the given setup we reach  $S/N = 33$  at  $6711 \text{ \AA}$  in one hour integration time, derived with the UVES ETC, version P106.2, for a G0 V star at airmass 1.1, seeing  $1''$  and with  $2 \times 2$  binning. A G0 V star was chosen for this example calculation because it represents a typical target of our selection.

## 4.2 Subaru HDS

Six northern targets, all located in SNR G160.9+02.6 (HB9), were observed in Subaru period S18B in run S18B0195S (service mode) with the *High Dispersion Spectrograph* (HDS), mounted at the Optical *Nasmyth* focus of the Subaru telescope, which is run by the NAOJ and located on the *Mauna Kea*, Big Island, Hawaii. All observations were done on 2018 Oct 26.

HDS provides a total wavelength range of  $3000\text{--}10,000 \text{ \AA}$  and a resolving power of up to  $R = 165,000$  (Aoki et al., 2014), which is the highest among current astronomical spectrographs at 8–10 m-class telescopes. The general structure of the instrument is similar to UVES, including the calibration unit, ADC, image slicers and image rotator in front of the slit. Further similarities are the division into a red and a blue arm, each containing an echelle grating, a cross-disperser and corresponding mirrors. The red arm has two CCD detectors with  $2048 \times 4096$  pixels each, coupled to a  $2 \times 1$  mosaic.

We used the Ra setup, where the filter SC-46 is used below the slit. In this setup, the first CCD covers the wavelength range  $5062\text{--}6446 \text{ \AA}$  and the second one  $6509\text{--}7890 \text{ \AA}$ . With  $2 \times 2$  binning (to improve the  $S/N$ ) and a slit width of  $1.0''$ , we obtain a resolving power of  $R = 36,000$ . As in the case of UVES, ADC, depolarizer and image slicer were not used. The individual exposure times varied between 40 s and 300 s, calculated with the HDS ETC<sup>5</sup>. Two exposures were taken for each target and  $S/N = 105.7$  was reached on average for the single exposures.

For S18B, we initially requested observations of 17 stars in five northern SNRs and a total execution time of 4 h, but only six stars were observed. An observation of a seventh star, TYC4302-833-1 in SNR G119.5+10.2, was started but terminated after the first exposure due to bad weather and high airmass. The six stars in HB9 were observed at airmasses between 1.12 and 1.17 and the exposure times were doubled in order to account for the weather conditions.

<sup>4</sup><http://astrutils.astronomy.ohio-state.edu/time/utc2bjd.html>

<sup>5</sup>[https://www.naoj.org/cgi-bin/hds\\_etc.cgi](https://www.naoj.org/cgi-bin/hds_etc.cgi)

## 4.2. Subaru HDS

TABLE 4.1: List of stars observed with UVES/VLT. The columns give target name, equatorial coordinates (J2000) from *Gaia* DR2, the SNR where the target is located, *Gaia* DR2  $G$  magnitude, barycentric Julian date BJD after the first of the two exposures, total on source integration time  $t_{\text{exp}}$  and the  $S/N$  reached in the fully reduced spectra.

Name	RA [h:m:s]	DEC [d:m:s]	SNR	$G$ [mag]	BJD−2,450,000 [d]	$t_{\text{exp}}$ [s]	$S/N$
TYC1869-1435-1	05:38:15.15	+27:49:18.48	G180.0−01.7	12.20	8056.84606	900	112
TYC1869-1596-1	05:38:23.71	+27:41:33.07	G180.0−01.7	12.16	8060.80811	800	106
TYC1869-1670-1	05:39:03.05	+27:32:35.26	G180.0−01.7	12.57	8058.82311	900	87
TYC159-2540-1	06:37:52.95	+06:39:53.48	G205.5+00.5	12.73	8060.84497	300	48
HD 260990	06:37:57.18	+06:28:47.47	G205.5+00.5	11.63	8075.79833	300	76
HD 261117	06:38:19.74	+06:23:40.70	G205.5+00.5	9.74	8036.85181	60	81
TYC159-241-1	06:38:25.23	+06:11:31.56	G205.5+00.5	10.47	8076.79745	240	104
TYC159-2006-1	06:38:32.24	+06:39:02.91	G205.5+00.5	9.28	8076.80388	60	95
TYC159-2408-1	06:38:32.28	+06:30:22.52	G205.5+00.5	9.94	8076.80850	140	103
TYC159-2771-1	06:38:50.77	+06:35:26.03	G205.5+00.5	12.01	8076.81354	480	69
TYC159-1896-1	06:38:51.46	+06:39:15.88	G205.5+00.5	11.48	8076.82462	360	85
TYC159-2082-1	06:38:59.13	+06:32:37.00	G205.5+00.5	11.08	8076.83232	300	94
HD 261359	06:39:07.47	+06:27:37.99	G205.5+00.5	11.79	8067.76600	720	114
HD 261393	06:39:13.09	+06:37:53.98	G205.5+00.5	10.05	8060.81954	120	110
TYC159-2337-1	06:39:20.12	+06:21:00.47	G205.5+00.5	11.80	8107.61880	800	109
TYC159-2671-1	06:39:24.25	+06:33:08.53	G205.5+00.6	12.25	8076.84023	480	64
TYC159-892-1	06:39:24.38	+06:37:25.98	G205.5+00.5	9.44	8107.65051	100	109
HD 261527	06:39:33.69	+06:06:58.87	G205.5+00.5	8.41	8107.65524	20	83
TYC159-2962-1	06:39:36.43	+06:16:36.10	G205.5+00.5	9.30	8107.65808	100	106
HD 261589	06:39:44.89	+06:27:35.57	G205.5+00.5	11.06	8107.64301	360	99
TYC159-251-1	06:39:47.09	+06:11:16.54	G205.5+00.5	11.51	8107.66221	360	83
TYC159-2564-1	06:40:00.11	+06:17:36.17	G205.5+00.5	11.97	8107.63233	600	80
HD 261715	06:40:13.41	+06:16:45.02	G205.5+00.5	11.25	8107.66940	480	98
TYC159-343-1	06:40:15.57	+06:11:36.61	G205.5+00.5	10.87	8107.67796	180	75
TYC7669-1336-1	08:22:05.66	−42:58:08.41	G260.4−03.4	12.27	8078.79809	1000	100
TYC7669-1414-1	08:22:10.86	−43:04:17.62	G260.4−03.4	11.97	8078.81243	800	94
TYC8150-2802-1	08:34:02.97	−45:32:59.68	G263.9−03.3	12.03	8078.82413	1000	107
TYC8150-3105-1	08:34:35.19	−45:11:37.87	G263.9−03.3	11.94	8078.83783	600	90
TYC8152-120-1	08:52:02.14	−46:23:22.99	G266.2−01.2	11.58	8107.68437	600	80
HD 76060	08:52:02.45	−46:17:19.84	G266.2−01.2	7.85	8035.85245	20	116
TYC8152-1456-1	08:52:05.71	−46:13:37.61	G266.2−01.2	12.47	8077.80900	720	72
TYC8152-104-1	08:52:08.05	−46:12:09.38	G266.2−01.2	11.53	8077.82179	480	91
TYC8152-550-1	08:52:14.68	−46:14:50.00	G266.2−01.2	11.92	8077.83090	480	80

This gives a total exposure time for these stars of 56 min. The overheads for HDS are as follows:

- $\sim 300$  s for pointing and acquisition
- $\sim 60$  s for setup
- $2 \times 44$  s for readout ( $2 \times 2$  binning)

This yields 448 s per star. To the corresponding total execution time of 1 h 41 min we have to add the time spent for calibration frames and a RV standard star, so about 2 h were spent for the project in total.

After the observations were finished, the data were obtained from the *Subaru Telescope Archive System*. Standard calibrations were included, namely five bias frames, eleven flat frames of a halogen lamp and two ThAr wavelength calibration frames for each CCD, which were recorded in the same night as the science frames. The ThAr frames were recorded immediately before and after the science observations, respectively. Data reduction was done manually with *IRAF*. We corrected for the bias level and bad pixels and applied order tracing, flatfielding, spectrum extraction and wavelength calibration, following the procedure described in the manual *Data reduction of echelle spectra with IRAF* (Aoki and Helminiak 2014, see Appendix B for further details). As described for UVES/VLT, also here we obtained four spectra for each star. The last step of the data reduction already included the normalisation of the spectra by fitting a spline to the continuum, before the spectral orders were merged and the two exposures were averaged.

In Table 4.2, we list the six runaway candidates that were observed with Subaru in period S18B. The  $S/N$  was measured in continuum regions between  $6620 \text{ \AA}$  and  $6760 \text{ \AA}$  in the combined spectra with *IRAF*.

For the chosen setup, with the HDS ETC we obtain  $S/N \approx 24$  at  $6697 \text{ \AA}$  for a G0 V star with  $V = 17.13$  mag at airmass 1.1, seeing  $1''$  and an exposure time of one hour.

TABLE 4.2: List of stars observed with HDS/Subaru. The columns give target name, equatorial coordinates (J2000) from *Gaia* DR2, the SNR where the target is located, *Gaia* DR2  $G$  magnitude, barycentric Julian date BJD after the first of the two exposures, total on source integration time  $t_{\text{exp}}$  and the  $S/N$  reached in the fully reduced spectra.

Name	RA [h:m:s]	DEC [d:m:s]	SNR	$G$ [mag]	BJD−2,450,000 [d]	$t_{\text{exp}}$ [s]	$S/N$
TYC3344-235-1	05:00:31.29	+46:33:27.25	G160.9+02.6	11.07	8418.99274	600	145
TYC3344-679-1	05:00:53.98	+46:30:00.61	G160.9+02.6	11.40	8419.00315	600	151
TYC3344-771-1	05:01:10.74	+46:42:11.04	G160.9+02.6	10.60	8419.01078	360	185
TYC3344-683-1	05:01:10.87	+46:27:38.11	G160.9+02.6	12.33	8419.02190	1200	142
TYC3344-124-1	05:01:11.84	+46:47:57.30	G160.9+02.6	10.45	8419.03231	240	136
TYC3344-553-1	05:01:16.00	+46:33:21.68	G160.9+02.6	10.87	8419.03787	360	139

# Chapter 5

## Spectral analysis

In the averaged spectra, we searched for the Li 6707.8 Å absorption line to measure the EW (see Section 5.4). Li was found in ten of our UVES spectra and one of our HDS spectra. Five of these stars were found to be giants (see Fig. 3.4) and are therefore too old to be runaway stars associated to SNRs. Fig. 5.1 shows seven of our VLT spectra around the Li line. While TYC159-1896-1 is only shown for comparison, six of them show Li absorption in their spectra, namely (1) TYC159-251-1 and (2) TYC159-343-1, located in the Monoceros Loop, (3) TYC8150-2802-1 and (4) TYC8150-3105-1 (Vela) as well as (5) TYC8152-1456-1 and (6) TYC8152-550-1 (Vela Jr.). These six stars were analysed further with *iSpec* (Blanco-Cuaresma et al., 2014) to determine their RVs and the atmospheric parameters. We also identified ten runaway candidates with early spectral types, for which we determined the RVs with *IRAF*.

### 5.1 TYC159-251-1 – A new spectroscopic binary

The spectrum of TYC159-251-1 contains additional absorption lines, which are redshifted by  $\sim 1.21\text{--}1.34$  Å compared to the main absorption lines in the red part of the spectrum (see Table D.2). Therefore, the star can be identified as a double-lined spectroscopic binary (SB2), consisting of two almost equally bright components. The system is not yet listed in the 9th Catalogue of Spectroscopic Binary Orbits (SB9, Pourbaix et al. 2009). In the following, we will use the designation *TYC159-251-1A* for the primary component, *TYC159-251-1B* for the secondary component and *TYC159-251-1* for the whole system.

As we would get misleading results from the observed spectrum, which contains light from both stars, we disentangled the two components by subtracting a G0 template spectrum from the observed spectrum to obtain the first component and a F6 template to obtain the second component (both templates taken from Bagnulo et al. 2003). This combination was found after iterating with different combinations of template spectra from Bagnulo et al. (2003) between

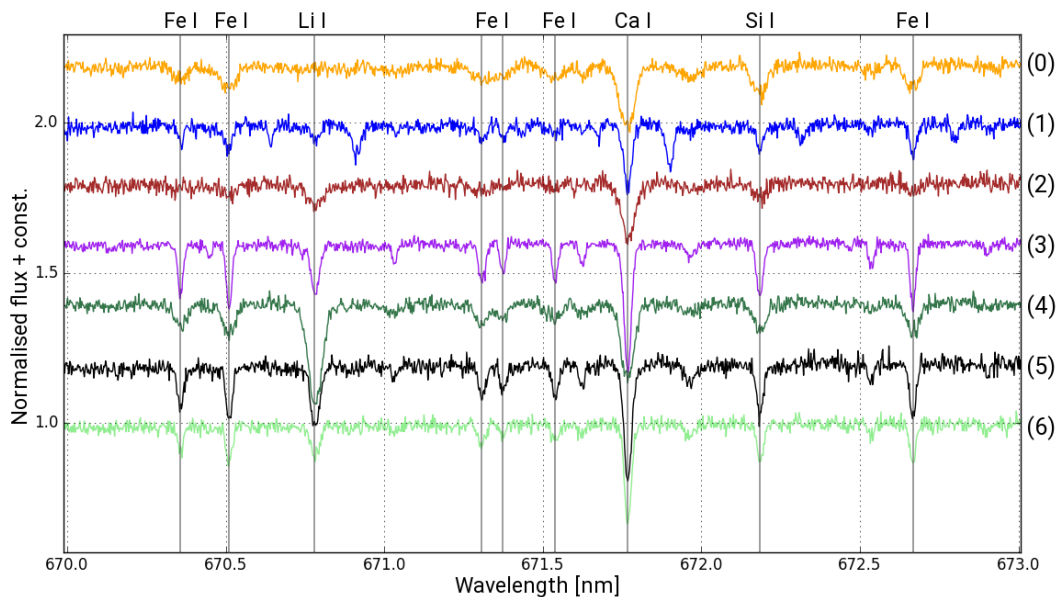


FIGURE 5.1: Normalised, RV corrected and shifted UVES/VLT spectra between  $\sim 6700$  Å and  $6730$  Å. The bottom six spectra show the Li stars, having spectral types between F2 and G2, in particular (1) TYC159-251-1, (2) TYC159-343-1, (3) TYC8150-2802-1, (4) TYC8150-3105-1, (5) TYC8152-1456-1 and (6) TYC8152-550-1. In yellow (0), we show TYC159-1896-1, a mid-F-type star without significant Li absorption, for comparison. The varying strengths of the Li  $6707.8$  Å line can be seen by comparison to the strong, nearby lines: Fe I at  $6704.5$  Å,  $6705.1$  Å,  $6713.1$  Å,  $6713.8$  Å,  $6715.4$  Å and  $6726.7$  Å, Ca I at  $6717.7$  Å and Si I at  $6722.0$  Å.

F6 and G0. We tried the combinations F6+F9, F6+G0, F7+F9, F8+F8, F8+G0 and F9+F9. Other combinations were excluded beforehand. If the residuals between the added templates and the observed spectrum were low (F6+F9, F6+G0, F8+F8, F9+F9), we subtracted the templates from the observed spectrum and determined atmospheric parameters and Li EWs (see Sections 5.3 and 5.4) for the resulting component spectra in order to check if the results are consistent with the choice of template spectra. Consistency was only obtained for the combination F6+G0.

Before adding the templates, their continuum levels were normalised to the flux level of the combined spectrum of TYC159-251-1, multiplied by the factors  $x_1 = 0.661$  and  $x_2 = 0.339$ , respectively, for the two components. These factors result from the luminosities  $\tilde{L}_1 = \log(L_1/L_\odot) = 0.43$  and  $\tilde{L}_2 = \log(L_2/L_\odot) = 0.14$  given in Pecaat and Mamajek (2013, Table 5) for a F6 and G0 star, respectively. The scale factors fulfil the conditions

$$\frac{L_1}{L_2} = \frac{x_1}{x_2} \quad \text{and} \quad x_1 + x_2 = 1. \quad (5.1)$$

Adding up the modified templates F6+G0 yielded the best representation of the observed spectrum (smallest residuals). Fig. 5.2 shows the observed spectrum (blue) as well as the

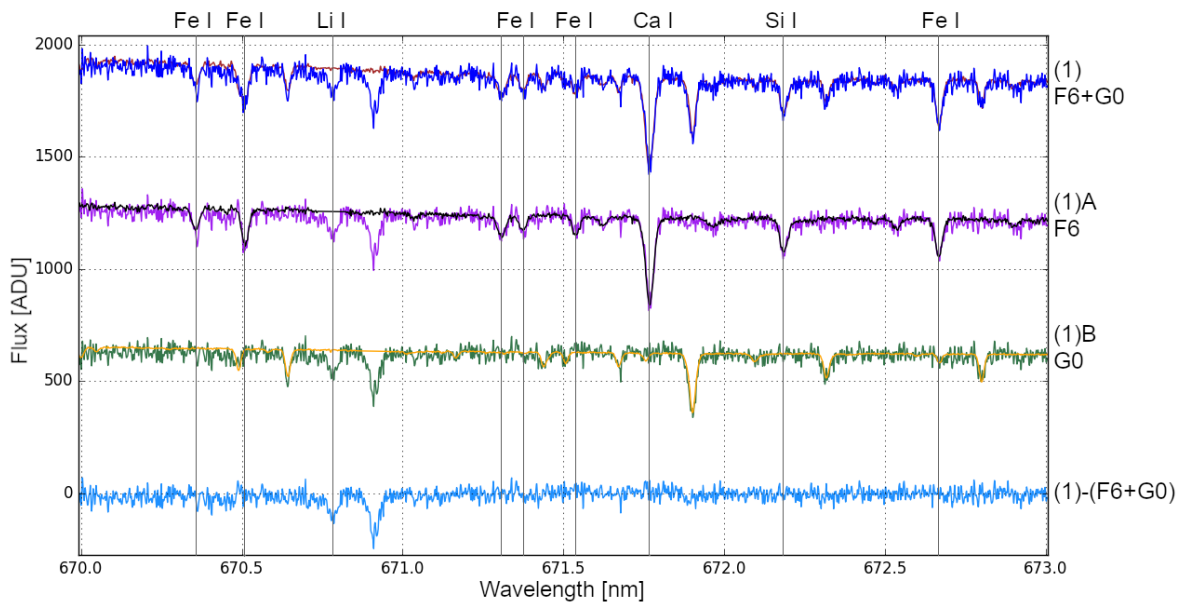


FIGURE 5.2: The spectrum of TYC159-251-1 (blue, 1) and its two components TYC159-251-1 A (purple, 1A) and TYC159-251-1 B (green, 1B) between  $\sim 6700 \text{ \AA}$  and  $6730 \text{ \AA}$ . The primary component is RV-corrected, while the secondary is shifted by  $59.0 \text{ km s}^{-1}$  (see Section 5.2). For comparison, we also show the F6 template spectrum (black), scaled by the factor 0.661, and the G0 template (yellow), scaled by the factor 0.339, which were subtracted from the observed spectrum to obtain the two components. The red spectrum is the addition of the two template spectra, while the residuals between the observed spectrum and the added templates are shown in light-blue. Li was manually removed from the template spectra.

individual components (magenta, green) after subtracting the template spectra (black, yellow). The residuals (light-blue) between the observed spectrum and the added templates (red) only show a significant deviation from zero at the Li lines, which is due to the manual removal of Li in the templates. The removal was necessary because Li had to remain unchanged in the component spectra for reliable measurements of the Li EW. In the following subsections, potential peculiarities in the analysis of this SB2 will be described in additional paragraphs.

## 5.2 Radial and space velocities

Before we could determine the Doppler shift that yields the RV, we had to correct the spectra for the motion of the Earth around the solar barycentre. This barycentric correction (BC) was done with *iSpec*. Then the wavelengths of the spectral lines were compared to an atomic line mask (cross-correlation) to determine the RVs and shift the spectra correspondingly. For the cross-correlation, a line list from a *Narval* solar spectrum (370–1048 nm) was used. For the early-type stars, the RV determination with *iSpec* was not possible due to the fewer and broader lines. We determined their RVs manually with *IRAF* from the positions of the following lines,

## 5.2. Radial and space velocities

if available: He I 5015.7 Å, Fe II 5018.4 Å, He I 5875.6 Å, Si II 6347.1 Å, Si II 6371.4 Å, Fe II 6456.4 Å, H $\alpha$  6562.8 Å. Additionally, for TYC3344-235-1 and TYC3344-683-1 in HB9, we used Mg I 5172.7 Å and Mg I 5183.6 Å. See Appendix D for details.

By combining the RVs  $v_r$  with proper motions  $\mu$  and parallaxes  $\pi$  from *Gaia* DR2 (see Table F.1), the heliocentric space velocities  $v_{\text{space}}$  of the stars were calculated:

$$v_{\text{space}} = \sqrt{v_{\mu}^2 + v_r^2}. \quad (5.2)$$

The transverse velocity  $v_{\mu}$  is given by:

$$v_{\mu} = \frac{149.598 \times 10^6 \text{ km} \times \mu_{\text{tot}}}{3.1557 \times 10^7 \text{ s} \times \pi}, \quad (5.3)$$

where  $149.598 \times 10^6 \text{ km}$  is the Astronomical Unit,  $3.1557 \times 10^7 \text{ s}$  is the length of a year and the total proper motion is given as

$$\mu_{\text{tot}} = \sqrt{\mu_{\text{RA}}^2 + \mu_{\text{DEC}}^2}. \quad (5.4)$$

In order to obtain the peculiar velocity with respect to the LSR, we first calculated the Galactic space velocity components  $(U, V, W)$ , following the equations given in Johnson and Soderblom (1987). Then we corrected for the solar motion with respect to the LSR by adding  $(U_{\odot}, V_{\odot}, W_{\odot}) = (8.5, 13.38, 6.49) \text{ km s}^{-1}$  (Coşkunoğlu et al., 2011). The peculiar velocity is the absolute value of the resulting vector. The calculated velocities of the six Li stars and the early-type runaway candidates are given in Table 5.1. TYC8150-2802-1, TYC8152-1456-1, TYC8152-550-1, TYC3344-235-1, TYC159-2771-1 and HD 76060 have  $v_{\text{pec}} > 25 \text{ km s}^{-1}$  and could therefore be classified as runaway stars according to Tetzlaff (2013).

For the SB2 system TYC159-251-1, we determined the momentary RVs  $v_{r_1}$  and  $v_{r_2}$  of the two components with *IRAF*, measuring the positions of 38 absorption lines of Fe I, Fe II, Ca I, Ni I and Si II. As line list we chose the ILLSS catalogue (Coluzzi, 1999). To obtain the systemic RV  $\gamma$ , we need the mass ratio  $q = M_2/M_1 \leq 1$ . In Section 5.3 we will find the components to have spectral types F6–F7 and F9–G0, respectively, corresponding to  $q = 0.91_{-0.05}^{+0.03}$ . The systemic RV can be calculated as

$$\gamma = v_{r_1} + \frac{q}{1+q} \times (v_{r_2} - v_{r_1}). \quad (5.5)$$



TABLE 5.1: Velocities of the six lithium stars as well as the remaining early-type candidates in HB9, Monoceros Loop and Vela Jr. The barycentric corrections  $BC$  were determined with *iSpec*. The radial velocities  $v_r$  were determined with *iSpec* for the Li-rich stars and with *IRAF* for the early-type stars. For TYC159-251-1, we give the systemic RV  $\gamma$  of the binary, approximated using a mass ratio of  $q = 0.91^{+0.03}_{-0.05}$ . For the spectral types, see Table 5.5. The last two columns give the heliocentric- and peculiar space velocity, respectively (see text).

Name	$BC$ [km s <sup>-1</sup> ]	$v_r$ [km s <sup>-1</sup> ]	$v_{\text{space}}$ [km s <sup>-1</sup> ]	$v_{\text{pec}}$ [km s <sup>-1</sup> ]
Li-rich stars				
TYC159-251-1	5.98	+17.47 <sup>+0.88</sup> <sub>-1.08</sub>	32.17 <sup>+0.73</sup> <sub>-0.80</sub>	19.30 <sup>+1.11</sup> <sub>-1.17</sub>
TYC159-343-1	6.03	+22.27 ± 0.41	25.7 ± 0.4	13.8 ± 0.7
TYC8150-2802-1	15.14	+53.84 ± 0.07	73.2 ± 0.3	58.8 ± 0.6
TYC8150-3105-1	15.01	+20.37 ± 0.29	33.9 ± 0.3	19.7 ± 0.5
TYC8152-1456-1	15.13	-10.59 ± 0.08	37.7 ± 0.8	49.1 ± 1.0
TYC8152-550-1	15.14	+36.12 ± 0.10	42.8 ± 0.2	37.1 ± 0.5
HB9				
TYC3344-235-1	19.15	-31.2 ± 2.8	32.0 ± 2.7	36.0 ± 2.9
TYC3344-679-1	19.18	+8.6 ± 7.3	24.3 ± 2.9	8.2 ± 5.9
TYC3344-683-1	19.19	+9.3 ± 7.3	29.3 ± 2.5	15.3 ± 3.6
TYC3344-553-1	19.18	-14.9 ± 7.3	27.6 ± 4.0	21.9 ± 5.7
Monoceros Loop				
TYC159-2771-1	19.53	+31.8 ± 2.0	40.7 ± 1.8	25.3 ± 2.0
HD261359	22.59	+0.9 ± 5.1	23.2 ± 1.8	17.8 ± 4.5
HD261393	24.55	+31.3 ± 5.8	31.8 ± 5.7	18.5 ± 5.3
TYC159-2337-1	5.94	+22.1 ± 4.7	28.0 ± 4.0	18.0 ± 3.7
TYC159-2671-1	19.57	+23.3 ± 7.3	24.0 ± 7.1	11.4 ± 6.3
Vela Jr.				
HD 76060	9.38	+25.7 ± 7.3	45.2 ± 4.2	31.2 ± 2.7

We obtained the following results:

$$\begin{aligned}
 v_{r_1} &= -10.7 \pm 0.6 \text{ km s}^{-1}, \\
 v_{r_2} &= +48.4 \pm 0.7 \text{ km s}^{-1} \text{ and} \\
 \gamma &= +17.5^{+0.9}_{-1.1} \text{ km s}^{-1}.
 \end{aligned}$$

The systemic RV  $\gamma$  is then used to determine the space motion ( $v_{\text{space}}$  and  $v_{\text{pec}}$  in Table 5.1). Extensive follow-up RV monitoring is needed to fit a RV curve and determine the orbital parameters. Only then the systemic and space velocity of the system can be given reliably.

### 5.3 Atmospheric parameters

We determined the atmospheric parameters of the six Li stars with the synthetic spectral fitting technique provided by *iSpec*. The routine computes synthetic spectra and compares them

to the observed spectra by nonlinear least-squares fitting, minimising the  $\chi^2$ . We used the continuum-normalised and RV-corrected spectra. The routine fits the following parameters: (i) Effective temperature  $T_{\text{eff}}$ , (ii) Surface gravity  $\log(g)$ , (iii) Metallicity  $[M/H]$ , (iv) Microturbulence velocity  $v_t^{\text{mic}}$ , (v) Macroturbulence velocity  $v_t^{\text{mac}}$ , (vi) Rotation  $v_{\text{rot}} \sin(i)$  and (vii) Limb darkening coefficient, taking into account the resolving power  $R = 32,250$ . The metallicity  $[M/H]$  is related to the metal fraction  $Z$  by the relation

$$[M/H] = \log(Z/X) - \log(Z/X)_{\odot}, \quad (5.6)$$

where  $X$  is the H fraction, and with  $\log(Z/X)_{\odot} = 0.0207$  (Bressan et al., 2012).

To create the synthetic spectra, we had to choose a radiative transfer code. The following codes are available in *iSpec* (Blanco-Cuaresma, 2019):

- *SPECTRUM* (Gray and Corbally, 1994)
- *Turbospectrum* (Plez, 2012)
- *SME* (Valenti and Piskunov, 1996)
- *MOOG* (Snedden et al., 2012)
- *WIDTH9/SYNTH* (Kurucz, 1993; Sbordone et al., 2004)

We chose *SPECTRUM* because it provides a low computing time for spectral synthesis. We furthermore used the *ATLAS9.Kurucz* model atmosphere (Kurucz, 2005), solar abundances from Kurucz and the line list *GESv5\_atom\_hfs\_iso.420\_92* (from the *Gaia-ESO Survey*, Heiter et al. 2015, and taking into account hyperfine-structure, hfs).

For the fitting, we chose the red part of the spectrum (6036–7003 Å) because it yields a higher  $S/N$ <sup>1</sup>. We chose a large number (> 100) of Fe I, Fe II, Ca I, Ca II, Ni I, Si I and Si II lines as well as the wings of the H $\alpha$  absorption line, which are good temperature indicators. After the automatic selection of the lines we checked by eye if they were suitable for fitting, i.e. they should reach back to the continuum within the segments that were drawn around each line. In some cases the segments were modified in order to reach that. In Fig. 5.3, we show examples of selected lines for TYC8152-550-1. The synthetic spectra are created in the grey segments while the differences to the observed spectrum are only computed within the yellow line masks. If no continuum regions were available around a line, or if strong deviations between spectrum and fit were recognised within the line mask, the corresponding line was rejected. The selection

---

<sup>1</sup>For optimal results for the surface gravity, we should have also included the blue part of the spectrum, containing the Mg triplet (5167.3–5183.6 Å), which is sensitive to  $\log(g)$  (Blanco-Cuaresma, 2019). However, as we are especially interested in the effective temperature, it was justified to abstain from this additional effort.

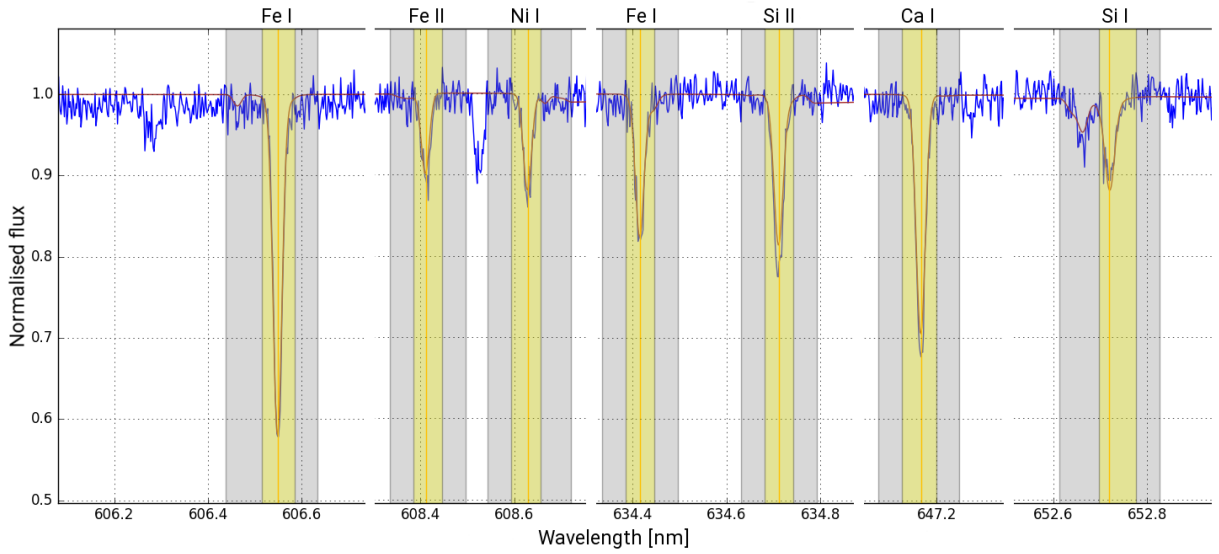


FIGURE 5.3: Different example lines of TYC8152-550-1 (blue) that were used to fit the atmospheric parameters (red). The yellow areas mark the line masks used for the fit, the grey areas show segments of  $0.5 \text{ \AA}$  on each side of each line used for synthesising the spectra. In particular we show Fe I  $6065 \text{ \AA}$ , Fe II  $6084 \text{ \AA}$ , Ni I  $6086 \text{ \AA}$ , Fe I  $6344 \text{ \AA}$ , Si II  $6347 \text{ \AA}$ , Ca I  $6472 \text{ \AA}$  and Si I  $6527 \text{ \AA}$ .

of the  $H\alpha$  wings is shown in the appendix, Fig. E.6. This region has a big effect on the results because it spans a large wavelength range. Therefore, it was important to do the continuum normalisation as precisely as possible. Note that the unwanted downbending of the fits on the right-hand side of the  $H\alpha$  region does not effect the results because it only happens in areas which are not used for the fit. In the segments of the following line it is readjusted to the flux level of the spectrum. The disentangled spectra of the two components of TYC159-251-1 were fitted individually and their  $H\alpha$  regimes are shown separately in Fig. E.7.

As initial parameters for the fits, we used solar parameters as given in Blanco-Cuaresma (2019) and the  $T_{\text{eff}}$  of each star from *Gaia* DR2. In each run, consisting of up to twelve iterations, it can be decided which parameters should be fixed or free. Since all parameters were unknown, we left all of them free, except either macroturbulence or  $v_{\text{rot}} \sin(i)$ , which are strongly correlated with each other. By running the fit several times with different combinations, we guaranteed that the fixed parameter of these two was set to a reasonable value, while the other was left free. The limb darkening coefficient was fixed to 0.6, because changing it did not show any effect.

The resulting atmospheric parameters of the six Li stars are given in Table 5.2. The intrinsic errors are computed from the covariance matrix which connects the errors of the parameters after the least-squares fitting (Blanco-Cuaresma et al., 2014). The flux errors of our spectra were calculated from gain ( $0.52 e^-/\text{ADU}$ ) and read noise ( $2.8 e^-$ ) of UVES with the given setup.

## 5.4. Lithium equivalent widths and abundances

TABLE 5.2: The atmospheric parameters of the six lithium stars determined with *iSpec*. The stars are named as in Fig. 5.1. The effective temperatures from *Gaia* DR2 are also shown for comparison. A missing error indicates that the parameter was kept constant for all iterations. The results for TYC159-251-1 are given for both components individually.

Name	$T_{\text{eff},Gaia}$ [K]	$T_{\text{eff}}$ [K]	$\log(g/\text{cm s}^{-2})$	[M/H]	$v_t^{\text{mic}}$ [km s $^{-1}$ ]	$v_t^{\text{mac}}$ [km s $^{-1}$ ]	$v_{\text{rot}} \sin(i)$ [km s $^{-1}$ ]
(1)A	$6257 \pm 391^*$	$6308 \pm 59$	$4.16 \pm 0.22$	$-0.19 \pm 0.06$	$1.49 \pm 0.24$	0	0
(1)B	$6257 \pm 391^*$	$6032 \pm 73$	$3.94 \pm 0.27$	$-0.16 \pm 0.07$	$1.86 \pm 0.27$	0	0
(2)	$7079 \pm 232$	$6749 \pm 69$	$2.77 \pm 0.35$	$-0.57 \pm 0.08$	$4.9 \pm 0.8$	$16.4 \pm 2.0$	1.5
(3)	$5853 \pm 100$	$5857 \pm 75$	$3.99 \pm 0.20$	$-0.08 \pm 0.06$	$1.28 \pm 0.19$	0	0
(4)	$5614 \pm 228$	$5956 \pm 73$	$4.78 \pm 0.21$	$-0.19 \pm 0.09$	$1.6 \pm 0.5$	4.8	$13.0 \pm 0.9$
(5)	$5806 \pm 77$	$5955 \pm 73$	$4.14 \pm 0.23$	$-0.09 \pm 0.07$	$1.26 \pm 0.26$	$0.8 \pm 1.9$	0
(6)	$6061 \pm 192$	$6165 \pm 63$	$4.26 \pm 0.24$	$-0.27 \pm 0.06$	$1.50 \pm 0.29$	0	0

\* *Gaia* DR2 value for the unresolved system

For comparison, we also show  $T_{\text{eff}}$  from *Gaia* DR2. We give the results for both components of TYC159-251-1, for which the fits were done individually after disentangling the spectra. Note that the disentangled spectra have lower  $S/N$ . The resulting  $T_{\text{eff}}$  for TYC159-251-1 B corresponds to SpT F9 but is also consistent with G0, which was used to disentangle the observed spectrum. The resulting  $T_{\text{eff}}$  for TYC159-251-1 A is fully consistent with the assumption of an F6 template spectrum.  $v_t^{\text{mac}} = 0 \text{ km s}^{-1}$  and  $v_{\text{rot}} \sin(i) = 0 \text{ km s}^{-1}$  were obtained for both components in all iterations, also when one or both of these parameters were left free.

## 5.4 Lithium equivalent widths and abundances

The Li equivalent widths  $EW_{\text{Li}}$  of the six Li stars were measured with *IRAF* by integrating over the area of the Li 6708 Å line with respect to the local continuum. The errors were calculated by adding the uncertainty in fitting the continuum and the error from read-noise and gain of the instrument. The continuum error was derived by varying the flux level of the local continuum for the integration. The  $EW_{\text{Li}}$  was measured three times with three different continuum levels and the maximum deviation from the median value was taken as the error.

If we do not disentangle the spectrum of a binary system, the EWs will be underestimated due to the additional continuum flux from the other component. Therefore, we measured the  $EW_{\text{Li}}$  for both components of TYC159-251-1 individually after disentangling. The absorption line is even stronger for the secondary component. Since the F6 and G0 template spectra also show Li absorption, we removed the lines manually with *IRAF* before subtracting the templates from the observed spectrum. So we made sure that the Li lines of both components remained in the disentangled spectra, where we could then measure the corresponding  $EW_{\text{Li}}$ .

The  $EW_{\text{Li}}$  were converted to abundances by using the curves of growth given by Soderblom

et al. (1993, Table 2). The abundance scale is based on  $\log(N_{\text{H}}) = 12$ . The curves of growth are calculated for  $T_{\text{eff}} = 4000\text{--}6500$  K in steps of 250 K,  $\log(EW_{\text{Li}}) = 0.0\text{--}3.0$  in steps of 0.05 dex (for  $EW_{\text{Li}}$  in mÅ) and local thermodynamic equilibrium. Soderblom et al. (1993) checked these conventional curves of growth by comparison to abundances calculated from spectral synthesis, using the *MOOG* code. The average difference between abundances determined by these two methods was found to be  $0.025 \pm 0.129$  dex.

TABLE 5.3: Parameters of the quadratic fits to extrapolate curves of growth for Li 6708 Å from Soderblom et al. (1993, Table 2)(see Eqn. 5.7 and Fig. 5.4) for three different values of  $\log(EW_{\text{Li}})$ , 1.50, 1.55 and 1.60. The RMS is 0.029 for all three cases.

Parameter	Value	Unit
$a_{1.50}$	$-1.34 \pm 0.16$	$10^{-7} \text{ K}^{-2}$
$b_{1.50}$	$+2.52 \pm 0.17$	$10^{-3} \text{ K}^{-1}$
$c_{1.50}$	$-8.00 \pm 0.43$	$10^0$
$a_{1.55}$	$-1.35 \pm 0.16$	$10^{-7} \text{ K}^{-2}$
$b_{1.55}$	$+2.52 \pm 0.17$	$10^{-3} \text{ K}^{-1}$
$c_{1.55}$	$-7.96 \pm 0.44$	$10^0$
$a_{1.60}$	$-1.35 \pm 0.16$	$10^{-7} \text{ K}^{-2}$
$b_{1.60}$	$+2.52 \pm 0.17$	$10^{-3} \text{ K}^{-1}$
$c_{1.60}$	$-7.90 \pm 0.43$	$10^0$

We determined its Li abundance for  $T_{\text{eff}} = 6750$  K and the three  $EW_{\text{Li}}$  steps  $\log(EW_{\text{Li}}) = 1.50, 1.55$  and  $1.60$ , corresponding to the closest values in Soderblom et al. (1993, Table 2), taking into account the  $EW_{\text{Li}}$  errors<sup>2</sup>. The fits can be seen in Fig. 5.4 and the fit parameters  $a$ ,  $b$  and  $c$  for the three values of  $\log(EW_{\text{Li}})$  are given in Table 5.3. The resulting abundance error of  $\Delta \log(N_{\text{Li}}) = {}_{-0.08}^{+0.07}$  contains the error from varying the value of  $EW_{\text{Li}}$  ( $\Delta_{\text{var}} = {}_{-0.048}^{+0.045}$ ) and the RMS of the fit ( $\Delta_{\text{RMS}} = 0.029$  in all three cases). For the other Li-rich stars, the errors only come from the variation of  $EW_{\text{Li}}$  and/or  $T_{\text{eff}}$ . The Li EWs and abundances of our Li-rich targets are listed in Table 5.4.

In the next section we will describe how the Li content, besides two further methods, can be used to estimate stellar ages.

We estimated the Li abundances of our targets by choosing the values from Soderblom et al. (1993) which best represent the effective temperatures and logarithmic EWs of the Li stars. The upper/lower abundance errors were determined by using the highest/lowest possible values of  $T_{\text{eff}}$  and  $\log(EW_{\text{Li}})$  according to their errors and picking the corresponding abundance from the table.

With  $T_{\text{eff}} = 6749 \pm 69$  K, TYC159-343-1 is not covered by the  $T_{\text{eff}}$  range in Soderblom et al. (1993). Here, we extrapolated the given abundances with a quadratic function

$$\log(N_{\text{Li}}) = aT_{\text{eff}}^2 + bT_{\text{eff}} + c. \quad (5.7)$$

<sup>2</sup>Due to the small  $T_{\text{eff}}$  error of 69 K,  $T_{\text{eff}} = 6750$  K is always the closest value for TYC159-343-1, adopting the step width from Soderblom et al. (1993, Table 2).

## 5.4. Lithium equivalent widths and abundances

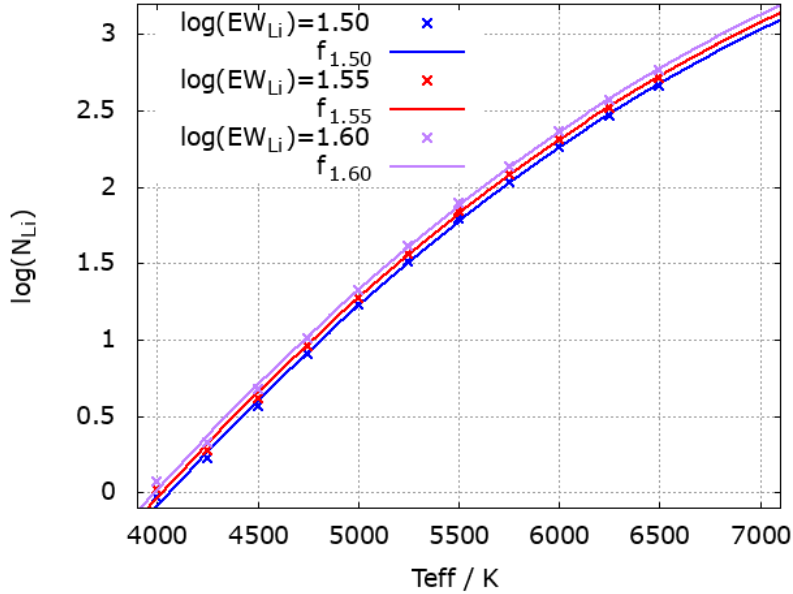


FIGURE 5.4: Quadratic fits to extrapolate curves of growth for Li 6708 Å from Soderblom et al. (1993, Table 2)(see Eqn. 5.7 and Table 5.3). The points represent the values given in the paper, the curves are our fits to these data for three values of  $\log(EW_{\text{Li}})$ . The fit parameters are given in Table 5.3.

TABLE 5.4: Li equivalent widths  $EW_{\text{Li}}$  and abundances  $\log(N_{\text{Li}})$  of the six Li stars. The abundance errors correspond to the minimum and maximum possible abundance from Soderblom et al. (1993), taking into account the uncertainties in  $EW_{\text{Li}}$  and  $T_{\text{eff}}$ . For TYC159-251-1, we give the values for the unresolved system as well as for the individual components. The stars are labeled as (1) TYC159-251-1, (2) TYC159-343-1, (3) TYC8150-2802-1, (4) TYC8150-3105-1, (5) TYC8152-1456-1 and (6) TYC8152-550-1.

Name	$EW_{\text{Li}}$ [mÅ]	$\log(N_{\text{Li}})$
(1)	$17 \pm 2$	$2.15^{+0.30}_{-0.05}$
(1)A	$22 \pm 4$	$2.31^{+0.06}_{-0.11}$
(1)B	$97 \pm 9$	$2.88^{+0}_{-0.08}$
(2)	$35 \pm 5$	$2.91^{+0.07}_{-0.08}$
(3)	$50 \pm 3$	$2.25^{+0.03}_{-0.06}$
(4)	$177 \pm 7$	$3.37 \pm 0$
(5)	$66 \pm 4$	$2.59^{+0.07}_{-0}$
(6)	$33 \pm 4$	$2.47^{+0.05}_{-0.26}$

## 5.5 Stellar ages

Knowing the ages of stars is an important tool to connect observations of stars with model expectations of their evolution. Runaway stars in SNRs have to be young, namely not older than the age of the SN progenitor when it exploded (up to  $\sim 32$  Myr, see Section 1), plus the age of the SNR (up to  $\sim 0.1$  Myr). So we need methods to check if this criterion is fulfilled.

The Sun is the only star for which the age is precisely known. However, it is revealed not by its light, but from measurements of radioactive decay in solar-system material like meteorites (Soderblom, 2010). For the other stars, several (semi-)fundamental, model-dependent and empirical methods have been established, e.g. the detection of the MS turnoff-point in the HRD to determine ages of clusters, or measurements of activity and astroseismology to estimate the ages of individual stars.

While for a broad review about the various methods we refer to Soderblom (2010) and Soderblom et al. (2014), here we focus on the two methods that are needed for the analysis in this work, namely (i) placement of isochrones in the HRD and (ii) the Li depletion test. Additionally, we will describe the concept of kinematic ages, yielding precise ages for safely identified runaway stars and associated objects like SNRs or NSs.

### 5.5.1 HRD isochrone placement

Increasing theoretical understanding of stellar evolution has led to a large variety of models describing the evolution of stellar parameters like mass, temperature, luminosity and composition (e.g. Schaller et al. 1992; Baraffe et al. 1998; Siess et al. 2000; Lejeune and Schaerer 2001; Ekström et al. 2012; Bressan et al. 2012; Marigo et al. 2013; Baraffe et al. 2015; Pastorelli et al. 2019), from the pre-MS evolution (Siess et al., 2000) to the late AGB phase (Pastorelli et al., 2019). These models require detailed knowledge of nuclear energy generation, radiative transfer, opacities, convection physics and the equation of state. Furthermore, rotation, magnetic fields, mass loss and, in the case of binaries, accretion activity affect stellar evolution (Soderblom et al., 2014).

Isochrones can be plotted either in HRDs or CMDs (see Section 2.1). However, when observational data should be plotted into a HRD, one has to know the effective temperature (e.g. from the spectral type), and to obtain the luminosity, one has to know the distance, the extinction and the photometric system to apply the bolometric correction. When using a CMD, the same caveats occur vice-versa for the conversion of the isochrones. We use a simplified HRD with  $T_{\text{eff}}$  vs.  $M_G$ , i.e. we do not need a bolometric correction, while the isochrones can be obtained in the required format (see next paragraph).

The ages of clusters can be determined quite accurately by plotting a large number of ob-

served stars into a CMD or HRD and comparing the MS turnoff-point to isochrones from stellar evolution models. Estimating ages of individual stars in a HRD is, however, rather uncertain, especially on the ZAMS, where the isochrone-density is very high. If the star is located above the ZAMS, it is often difficult to decide if it is pre-MS or evolved. Fig. 5.6 shows a HRD with PARSEC-isochrones (Bressan et al., 2012) representing the stellar evolution up to the first thermal pulse. For the calculation, we used the web interface by Léo Girardi<sup>3</sup> with solar metal fraction,  $Z = 0.0152$ . The other parameters in the web interface (see references therein) were kept on their standard values. The ZAMS is characterised by a higher density of isochrones and limits the possible ranges of effective temperature  $T_{\text{eff}}$  and absolute magnitude (here:  $M_G$ ) to the upper right part of the HRD (except for compact remnants). Pre-MS stars start their lives  $\sim 2-3$  mag brighter than ZAMS stars with similar  $T_{\text{eff}}$  before contracting on the *Hayashi* and/or the *Heney* line (see Section 2.1). For decreasing  $T_{\text{eff}}$ , Fig. 5.6 clearly shows how the turnoff point moves to higher ages. The RGB and AGB are located in the upper right part of the HRD.

An age estimate of an individual star from the HRD requires knowledge of the metallicity and, since large areas in the HRD are consistent with both, pre- and post-MS, an independent measure of the rough evolutionary state. If a star is located on the ZAMS, no further age constraint can be drawn from the HRD. Further caveats are that (i) stellar variability, e.g. from starspots, can temporarily change the stellar brightness. The variability of a star has to be known well in order to correct for this effect. (ii) Unresolved binarity makes stars appear brighter than they are, which can also affect the results for clusters. Furthermore, (iii) the differences between various stellar evolution models are large, and (iv) the derivations of  $T_{\text{eff}}$  and brightness used for the HRD (atmospheric parameter fits, extinction maps, conversion between different photometric systems etc.) are model dependent as well.

### 5.5.2 The lithium test

In stellar interiors, lithium (as well as other elements like boron or beryllium) is burned at temperatures of  $\gtrsim 2.5 \times 10^6$  K. If the Li-depleted material is transported to the photosphere by convection or other mixing-mechanisms, a decreasing Li abundance will be observed with increasing age (e.g. Bodenheimer 1965; D’Antona and Mazzitelli 1984; Sestito and Randich 2005). Since the standard mixing mechanism, convection, only works in late-type stars, Li depletion is mainly expected to be observed in stars with  $M \lesssim 1.2 M_{\odot}$ , corresponding to spectral types F7 to late-M (D’Antona and Mazzitelli, 1984; Soderblom, 2010). However, Li depletion works very differently within this range, depending on the evolutionary timescales, the temperature distribution, the convectivity and non-standard mixing mechanisms like diffusion, gravity

---

<sup>3</sup>[http://stev.oapd.inaf.it/cgi-bin/cmd\\_3.3](http://stev.oapd.inaf.it/cgi-bin/cmd_3.3)



waves, rotation and angular momentum loss. E.g., total depletion usually occurs already on the pre-MS for stars with  $M \lesssim 0.6 M_{\odot}$  due to their high convectivity, whereas for stars with  $M \gtrsim 1 M_{\odot}$  a radiative core develops more quickly, accounting for a lower temperature at the base of the convection zone, so that almost no Li depletion occurs during the pre-MS. In any case, the depletion is not a continuous process. Sestito and Randich (2005) found the four following qualitative epochs for late-F- and G-type stars: (i) A small amount of pre-MS Li destruction, (ii) plateau during the early MS, (iii) MS depletion, (iv) plateau at old ages.

Little or no Li depletion is expected for very young stars ( $\lesssim 10$  Myr), due to the time until a sufficient interior temperature is reached, the burning timescale and the mixing timescale. Furthermore, the initial Li abundance has to be considered. While regular Population I stars have  $\log(N_{\text{Li}}) = 3.1-3.3$  (Jeffries and Oliveira, 2005; Sestito and Randich, 2005), on a scale based on  $\log(N_{\text{H}}) = 12$ , stars with a lower metallicity have a lower initial Li abundance (Lambert and Reddy, 2004), i.e. less time would have been needed to reach a presently observed Li abundance.

By measuring the EW of the  ${}^7\text{Li}$  resonance absorption line at  $6707.8 \text{ \AA}$  (e.g. Covino et al. 1997; Neuhäuser 1997), and the effective temperature  $T_{\text{eff}}$ , a rough age estimate of a star can be obtained, when compared to the data of clusters with known ages. Eric Mamajek fitted polynomials to the data of ten open clusters (Fig. 5.5), which can be used as isochrones to obtain a rough age scale. A similar type of diagram can be plotted for Li abundances. However, this adds additional uncertainty because the curves of growth that are used to convert Li EWs to abundances (Soderblom et al., 1993), are very temperature-sensitive.

**The lithium depletion gap.** Another interesting feature is the Li depletion gap observed in several clusters of  $t \gtrsim 200$  Myr. While from standard mixing theory it is expected that the rate of Li depletion decreases for F dwarfs with increasing  $T_{\text{eff}}$ , in clusters like the 625 Myr old Hyades, stars of  $T_{\text{eff}} \approx 6600 \pm 300 \text{ K}$  show Li depletions which are enhanced by a factor  $\sim 100$  compared to neighbouring hotter and cooler stars (Boesgaard and Tripicco 1986; Thorburn et al. 1993; Deliyannis et al. 2019). In a weaker extent, this feature can also be seen in younger clusters like M35 ( $\sim 175$  Myr), where the gap is just forming (Steinhauer, 2003; Steinhauer and Deliyannis, 2004). It is caused by non-standard mixing on the MS, acting predominantly in the above stated  $T_{\text{eff}}$  regime. Slow mixing, e.g. by rotational and/or gravitational instabilities, and diffusion can play a role, but the exact physical processes are not yet well understood (Steinhauer and Deliyannis, 2004). Recent works (Steinhauer and Deliyannis, 2021) show that rotational mixing plays an important role for the formation of the gap. The authors find that cluster stars with a high  $v_{\text{rot}} \sin(i)$  have a more strongly decreasing Li abundance with age, so by measuring Li abundances and  $v_{\text{rot}} \sin(i)$  of stars within the Li depletion gap, their ages can be inferred by comparison to clusters of known ages, when the initial abundance is

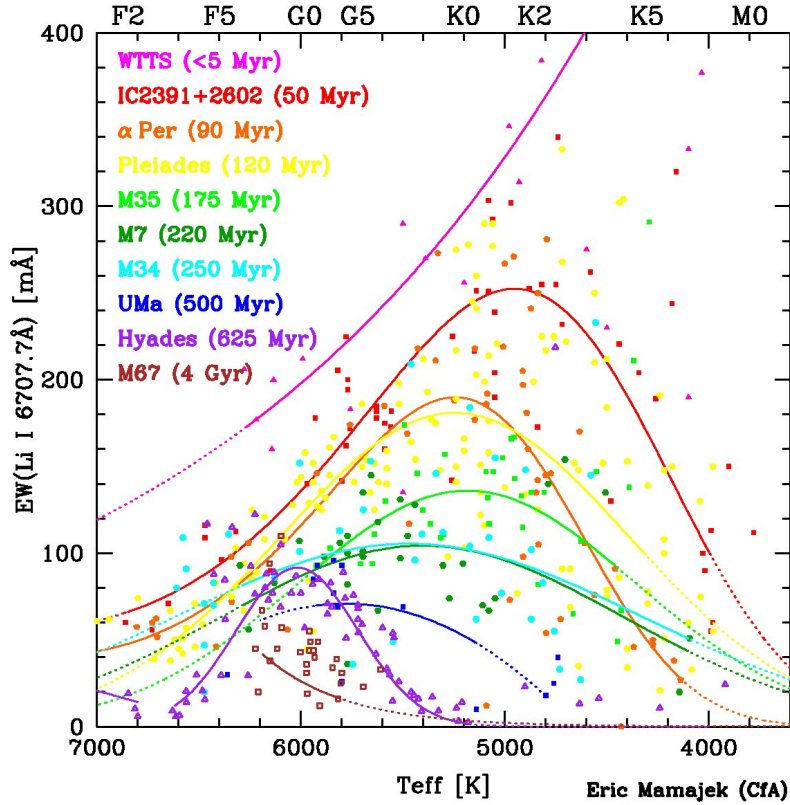


FIGURE 5.5: Lithium equivalent widths  $EW_{\text{Li}}$  vs. effective temperatures  $T_{\text{eff}}$  for stars in clusters with known ages. Eric Mamajek fitted polynomials to these data which can be interpreted as isochrones. The dotted parts of the curves indicate where the fits were extrapolated. The plot was obtained from Eric Mamajek’s homepage<sup>4</sup>.

known. However, this method is not applicable for us due to the insignificant measurements of  $v_{\text{rot}} \sin(i)$  (see Table 5.2) and the unknown initial Li abundances. Additionally, the method only works for stars within the Li depletion gap and only for ages of  $\sim 100$ – $650$  Myr. Nevertheless, comparing stellar Li abundances to clusters of known ages can yield an estimate of their ages, which is most significant for stars within the gap but also works for cooler stars.

While providing an order-of-magnitude estimate and allowing to sort stars of similar spectral type by age, care has to be taken when using the Li test for obtaining absolute ages of individual stars. The big scatter, especially observed for K dwarfs (e.g. in the Pleiades, see Fig. 5.5), the unknown initial Li abundances, different metallicities and rotational velocities and the not well understood physical processes involved in Li depletion add a high degree of uncertainty which has to be considered when we apply the Li test in Section 5.6. Still, the method can be a valuable tool when we want to decide if a runaway star candidate in a SNR can be young enough to be ejected from the SN.

<sup>4</sup><http://www.pas.rochester.edu/~emamajek/images/li.jpg>

### 5.5.3 Kinematic ages

Kinematic ages yield a model-independent age estimate. For a 2D kinematic age, only the position and proper motion of an object have to be known. However, to exclude chance alignments, knowledge of parallax and radial velocity is desired in order to infer a 3D kinematic age. In both cases, the place of origin has to be known, e.g. an open cluster, an OB association, the centre of a SNR or associated individual objects like a NS as its former companion.

Kinematic ages were determined for regular stars, runaway stars and NSs. Noutsos et al. (2013) and Lux (2013) determined kinematic ages of NSs by assuming a range of  $\pm 100$  pc around the Galactic plane as their birth place. The backtracing was performed in 3D, despite the mostly unknown RVs of the NSs, which were considered by Monte Carlo simulations and the velocity distribution by Hobbs et al. (2005). While allowing age determinations for a high number of NSs, the large allowed birth region causes large relative errors, especially for young objects. Tetzlaff et al. (2009; 2010; 2011a; 2012; 2013; 2014a; 2014b) determined kinematic ages of 18 young NSs by tracing them back to local birth associations like OB associations and potential runaway companions. While this method is not applicable to NSs much older than  $\sim 5$  Myr, due to the increasing positional uncertainties of the backtracing, the method allows much more precise age determinations due to the precisely localised birth sites.

Kramer et al. (2003) traced back PSR J0538+2817 to the GC of SNR S147 and found a kinematic age of  $30 \pm 4$  kyr, much less than the characteristic age,  $\tau_c = 620$  kyr. Obviously, the assumption  $P_0 \ll P$  (see Section 2.4.1) does not hold in this case. Further evidence for the PSR association was given by the discovery of the B0.5 V runaway star HD 37424 (Dinçel et al., 2015). Its travel time since the SN,  $30 \pm 4$  kyr, is identical to the kinematic age of the pulsar. HD 37424 flies towards south-east with a peculiar velocity of  $v_{\text{pec}} = 74 \pm 8 \text{ km s}^{-1}$ , while PSR J0538+2817 has a transverse velocity (2D, unknown RV) of  $v_{\text{tra}} = 357_{-43}^{+59} \text{ km s}^{-1}$  to the north.

Note that the travel time of a runaway star since the SN is of course smaller than its actual age. From the known mass of HD 37424,  $\sim 13 M_{\odot}$ , and the pre-SN orbital velocity ( $v_{\text{orb}} = v_{\text{pec}}$ ), Dinçel et al. (2015) could constrain the SN progenitor mass to  $\sim 13-20 M_{\odot}$ , yielding a lifetime of  $\sim 5.6-16.4$  Myr, according to Eqn. 1.1. This should then also be the age of the runaway star, since binaries are almost always born at the same time and location.

When searching for runaway stars in SNRs, the method is not applicable until we have a clear association. Therefore, it is not used in Section 5.6.

Another possibility to infer the age of a runaway star, from both BES and DES, is to identify a birth association or -cluster, which age could be known e.g. from the turnoff point in the HRD and is usually assumed to be equal for all present and former cluster members.

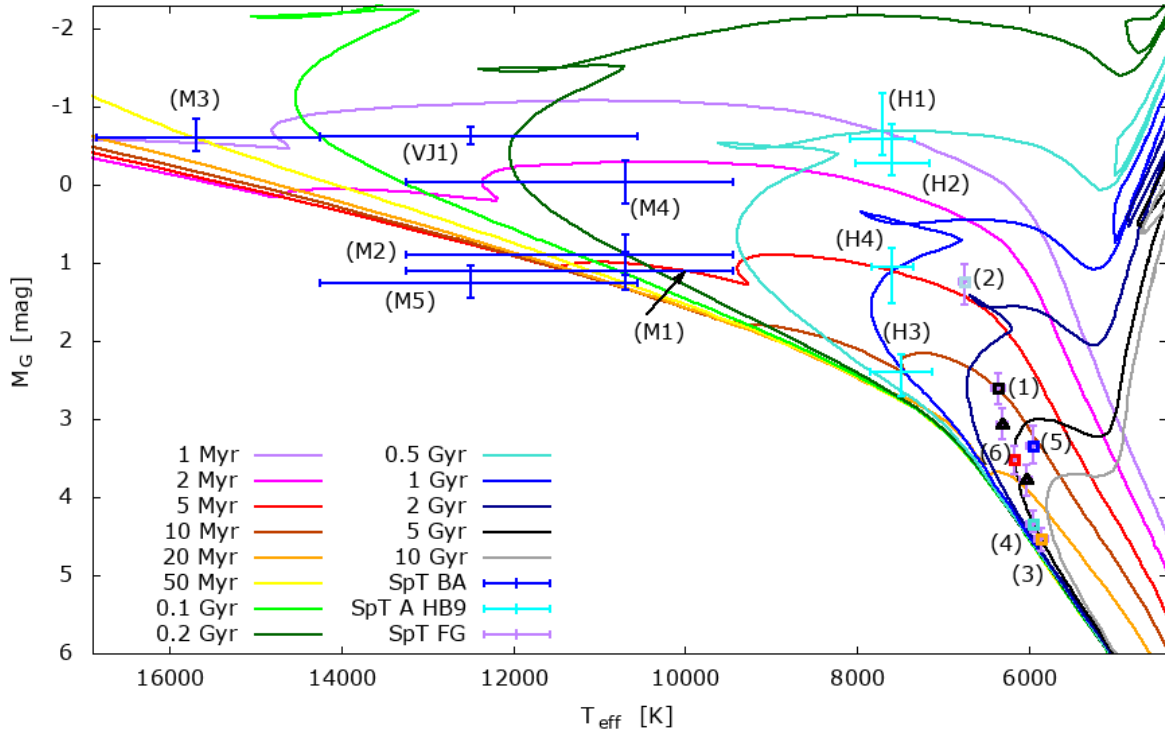


FIGURE 5.6: HRD with absolute  $G$ -band magnitudes of runaway candidate stars and Li-rich stars observed with UVES/VLT and HDS/ Subaru. For an age estimate, we show PARSEC isochrones (Bressan et al., 2012) with metal fraction  $Z = 0.0152$ , corresponding to the solar value. For the early-type stars (blue) in the Monoceros Loop (M) and Vela Jr. (VJ), we used spectral types from the *Skiff* catalogue (Skiff 2009; Voroshilov et al. 1985; Houk 1978) and corresponding  $T_{\text{eff}}$  ranges from Pecaut and Mamajek (2013, Table 5). For stars located in HB9, marked in cyan, we checked the  $T_{\text{eff}}$  from Bai et al. (2019), which are used here for the stars with spectral type late-A. For the Li-rich stars (SpT FG), marked with coloured squares, we show the  $T_{\text{eff}}$  from our parameter fits. TYC159-251-1 is a binary and the HRD positions of the individual components correspond to the black triangles. The stars are labeled as in Table 5.5.

## 5.6 Age estimation

In the following, we will apply two of the methods described in Section 5.5 to estimate the ages of the Li stars. Firstly, we will use the positions of the stars in the HRD, where we can compare them to isochrones (Figs. 5.6, 5.7). Then we make the Li test by using the determined  $T_{\text{eff}}$  and  $EW_{\text{Li}}$  to compare them to stars of clusters with known ages (Fig. 5.8). As a consistency check for the Li test, we can also compare the Li abundances to Pleiades and Hyades stars (see Fig. 5.9, where also the Li depletion gap is illustrated). For the early-type candidates (no Li), we can only obtain a rough estimate from the HRD.

TABLE 5.5: Temperatures, spectral types and magnitudes of the six Li-rich stars and the remaining observed early-type runaway candidates. The effective temperatures  $T_{\text{eff}}$  were taken from the sources given in the table notes, where conversion between  $T_{\text{eff}}$  and the spectral type SpT was done with Pecaut and Mamajek (2013, Table 5).  $G$ ,  $BP$  and  $RP$  magnitudes are from *Gaia* DR2, absolute  $G$  magnitudes  $M_G$  were calculated from *Gaia*  $G$ , extinction  $A_G$  and parallax and  $G$  band extinctions  $A_G$  are from the *StarHorse* catalogue (Anders et al., 2019). For TYC159-251-1, we give the values for the unresolved system as well as for the individual components, assuming that TYC159-251-1 A contributes 66.1 % of the flux and TYC159-251-1 B 33.9 %. The stars are labeled as (1) TYC159-251-1, (2) TYC159-343-1, (3) TYC8150-2802-1, (4) TYC8150-3105-1, (5) TYC8152-1456-1, (6) TYC8152-550-1, (H1) TYC3344-235-1, (H2) TYC3344-679-1, (H3) TYC3344-683-1, (H4) TYC3344-553-1, (M1) TYC159-2771-1, (M2) HD 261359, (M3) HD 261393, (M4) TYC159-2337-1, (M5) TYC159-2671-1 and (VJ1) HD 76060.

Name	$T_{\text{eff}}$ [K]	SpT	$G$ [mag]	$BP$ [mag]	$RP$ [mag]	$M_G$ [mag]	$A_G$ [mag]
Li-rich stars <sup>1</sup>							
(1)	$6351 \pm 78$	F5–F7	11.51	11.78	11.09	$+2.61^{+0.20}_{-0.19}$	$0.14^{+0.20}_{-0.18}$
(1A)	$6308 \pm 59$	F6–F7	11.96	12.23	11.54	$+3.06^{+0.20}_{-0.19}$	$0.14^{+0.20}_{-0.18}$
(1B)	$6032 \pm 73$	F9–G0	12.68	12.96	12.26	$+3.78^{+0.20}_{-0.19}$	$0.14^{+0.20}_{-0.18}$
(2)	$6749 \pm 69$	F2–F4	10.87	11.08	10.54	$+1.24^{+0.29}_{-0.23}$	$0.33^{+0.28}_{-0.22}$
(3)	$5857 \pm 75$	G0–G2	12.03	12.36	11.55	$+4.53^{+0.16}_{-0.13}$	$0.04^{+0.15}_{-0.13}$
(4)	$5956 \pm 73$	F9.5–G1	11.94	12.26	11.42	$+4.34^{+0.11}_{-0.16}$	$0.22^{+0.11}_{-0.16}$
(5)	$5955 \pm 73$	F9.5–G1	12.47	12.81	11.97	$+3.35^{+0.21}_{-0.26}$	$0.22^{+0.21}_{-0.25}$
(6)	$6165 \pm 63$	F7–F9	11.92	12.21	11.48	$+3.52^{+0.19}_{-0.17}$	$0.33^{+0.19}_{-0.17}$
HB9 <sup>2</sup>							
(H1)	$7707 \pm 377$	A5–F0	11.07	11.38	10.61	$-0.60^{+0.21}_{-0.57}$	$1.45^{+0.19}_{-0.57}$
(H2)	$7591 \pm 435$	A6–F0	11.40	11.72	10.92	$-0.28^{+0.16}_{-0.51}$	$1.69^{+0.09}_{-0.49}$
(H3)	$7490 \pm 360$	A7–F0	12.33	12.58	11.94	$+2.40^{+0.30}_{-0.24}$	$0.35^{+0.29}_{-0.23}$
(H4)	$7588 \pm 249$	A7–A9	10.87	11.08	10.53	$+1.06^{+0.46}_{-0.24}$	$0.73^{+0.45}_{-0.24}$
Monoceros Loop <sup>3</sup>							
(M1)	$10700^{+2550}_{-1250}$	B8–A0	12.01	12.13	11.78	$+1.11^{+0.23}_{-0.25}$	$0.29^{+0.20}_{-0.22}$
(M2)	$10700^{+2550}_{-1250}$	B8–A0	11.79	11.87	11.62	$+0.89^{+0.26}_{-0.26}$	$-0.04^{+0.20}_{-0.20}$
(M3)	$15700^{+1150}_{-1450}$	B4–B6	10.05	10.07	10.02	$-0.61^{+0.17}_{-0.24}$	$0.16^{+0.12}_{-0.20}$
(M4)	$10700^{+2550}_{-1250}$	B8–A0	11.80	11.88	11.61	$-0.04^{+0.27}_{-0.27}$	$0.27^{+0.12}_{-0.13}$
(M5)	$12500^{+1750}_{-1950}$	B7–B9	12.25	12.31	12.08	$+1.25^{+0.19}_{-0.22}$	$0.18^{+0.15}_{-0.19}$
Vela Jr. <sup>4</sup>							
(VJ1)	$12500^{+1750}_{-950}$	B7–B9	7.85	7.83	7.92	$-0.63^{+0.11}_{-0.11}$	$0.05^{+0.10}_{-0.10}$

<sup>1</sup>  $T_{\text{eff}}$  from the atmospheric parameter fits (see Section 5.3); <sup>2</sup>  $T_{\text{eff}}$  from Bai et al. (2019); <sup>3</sup> SpT from Voroshilov et al. (1985); <sup>4</sup> SpT from Houk (1978).

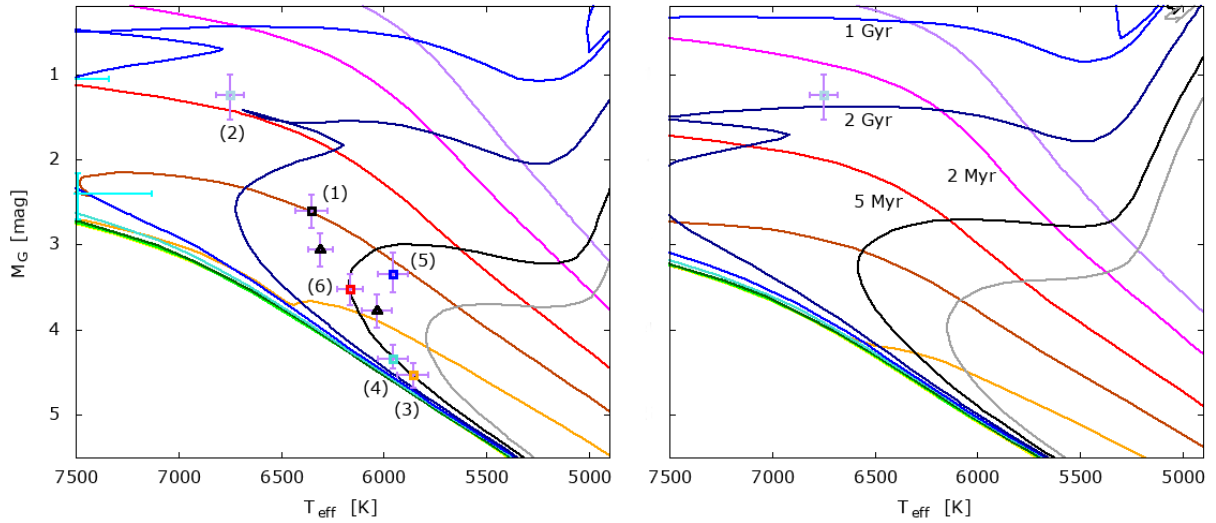


FIGURE 5.7: Left: Zoom-in of Fig. 5.6, centred on the Li-rich stars. Right: HRD with absolute  $G$ -band magnitudes of TYC159-343-1. For an age estimate, we show PARSEC isochrones (Bressan et al., 2012) with metallicity  $[M/H] = -0.57$ . This value and the  $T_{\text{eff}}$  were determined from our parameter fits. The axis scales are similar in both panels. For the key, see Fig. 5.6.

### 5.6.1 HRD isochrone placement

In the HRD (Fig. 5.6, for a zoom-in of the Li-rich stars see Fig. 5.7), we show the remaining early-type runaway candidates as well as the Li-rich stars observed with UVES/VLT and HDS/Subaru, using  $T_{\text{eff}}$  either from their spectral type as given in the *Skiff* catalogue<sup>5</sup> (Skiff 2009; Voroshilov et al. 1985; Houk 1978), from Bai et al. (2019) or from our atmospheric parameter fits. A collection of different possible  $T_{\text{eff}}$  from different sources is given in Appendix G. Using *Gaia* DR2 parallaxes and *StarHorse* extinctions  $A_G$  (Anders et al., 2019), we transformed the apparent magnitudes  $G$  to absolute magnitudes  $M_G$ . For the  $G$ -band extinctions, no errors are given in the *StarHorse* catalogue. Therefore, we converted the  $V$  band extinction errors with the relation  $\Delta A_G = 0.77\Delta A_V$  (Mugrauer, 2019), whereupon  $\Delta M_G$  was determined with Gaussian error propagation. The relevant stellar parameters, i.e. temperatures, spectral types, magnitudes and extinctions are given in Table 5.5.

We compare our stars to isochrones calculated from PARSEC models (Bressan et al., 2012), reflecting the whole stellar evolution until the first thermal pulse, an instability of the He-burning shell during the AGB, caused by a thermonuclear runaway (Pols et al., 2001; Schwarzschild and Härm, 1965). These instabilities lead to sudden changes of the stellar parameters, so that many regular stellar evolution models terminate at the first thermal pulse. However, there are also models for the late AGB evolution after the first thermal pulse (e.g.

<sup>5</sup>*VizieR* online data catalogue that compiles stellar spectral classifications of  $\sim 900,000$  stars from various authors.

Pastorelli et al. 2019).

TABLE 5.6: Estimated HRD ages (see Figs. 5.6 and 5.7) for the six Li-rich stars as well as for the remaining observed runaway star candidates in HB9, Monoceros Loop and Vela Jr. If a star is consistent with the ZAMS, only a lower limit is given in column 2. Otherwise, the values in column 2 represent the case that the star is on its pre-MS and the values in column 3 represent the case that the star is on its terminal-age- or post-MS.

Abbr.	Name	$t_{\text{HRD}}$ [Myr] if (pre-)MS	$t_{\text{HRD}}$ [Myr] if post-MS
Li-rich stars			
(1)A	TYC159-251-1 A	11–16	3200–4500
(1)B	TYC159-251-1 B	14–30	4800–7500
(2)	TYC159-343-1*	2.1–3.8	1600–2300
(3)	TYC8150-2802-1	> 30	–
(4)	TYC8150-3105-1	> 25	–
(5)	TYC8152-1456-1	8–16	5000–8000
(6)	TYC8152-550-1	13–20	3800–6000
HB9			
(H1)	TYC3344-235-1	< 1.6	380–650
(H2)	TYC3344-679-1	2.0	490–800
(H3)	TYC3344-683-1	> 9	–
(H4)	TYC3344-553-1	3.7–7.0	850–1300
Monoceros Loop			
(M1)	TYC159-2771-1	> 4.2	–
(M2)	HD 261359	> 3.5	–
(M3)	HD 261393	< 110	–
(M4)	TYC159-2337-1	1.6–3.3	50–490
(M5)	TYC159-2671-1	> 5	–
Vela Jr.			
(VJ1)	HD 76060	1.1–1.8	90–350

\* HRD ages determined with isochrones for  $[M/H] = -0.57$ .

individual components yield lower effective temperatures. The two individual components differ by 276 K and 0.72 mag.

Before plotting the early-type stars into the HRD, we have to consider that *Gaia* temperatures are trained only up to  $T_{\text{eff}} = 10,000$  K and tend to be underestimated when approaching this limit. Therefore, for the early-type stars observed with UVES, we adopted the spectral

We used the solar metal fraction,  $Z = 0.0152$ , corresponding to  $[M/H] = 0$  (see Equation 5.6 and Bressan et al. 2012). This is close to  $[M/H] = -0.20 \pm 0.13$ , the average metallicity of our targets as given in the *StarHorse* catalogue. The corresponding isochrone shift is relatively small compared to the temperature and magnitude errors for early- and late-type stars, respectively. However, TYC159-343-1 has a significantly lower metallicity of  $[M/H] = -0.57 \pm 0.08$ . Therefore, for this star we plotted separate isochrones to determine its age more precisely (see Fig. 5.7).

While the RGB is located at the upper right in Fig. 5.6, the Li-rich stars are mostly located relatively close to the ZAMS, only TYC159-343-1 lies close to the isochrone for 5 Myr due to its high brightness.

TYC159-251-1 was discovered by us to be a SB2. Photometrically unresolved binarity changes the positions in the HRD. The brightness is then overestimated and the star is located significantly above the ZAMS. We corrected for this effect by assuming that the primary component contributes 66.1 % and the secondary 33.9 % of the flux (see Section 5.1). This adds 0.45 mag and 1.17 mag, respectively, to their  $M_G$  magnitude, shifting them back towards the ZAMS. Furthermore, the revised atmospheric parameter fits for the

types from the *Skiff* catalogue (Skiff 2009). Only one reference is given for each star (Houk 1978 for HD 76060, Voroshilov et al. 1985 for the ten other early-type stars) and no error ranges are provided, so we assume  $\pm 1$  subclass. The corresponding temperatures were inferred from Pecaut and Mamajek (2013, Table 5). Unfortunately, the spectra we obtained for these stars were not suited for determining the spectral type, because we focused on analysing late-type stars, in particular their Li absorption line. Our spectral range of 5000–7000 Å is quite narrow and misses most spectral lines that are usually taken for the analysis of early-type stars. Additionally, the few lines we found are often affected by strong rotational broadening.

Nevertheless, we checked the *Skiff* spectral types for consistency by comparing our spectra to standard star spectra observed with the *Fibre Linked ECHelle Astronomical Spectrograph* (FLECHAS), operated at the 0.9-m telescope of the University Observatory Jena. FLECHAS covers a wavelength range of 3900–8100 Å and achieves a resolving power of  $R \approx 9300$  (Mugrauer et al., 2014). We mainly used the He I line at 5015.7 Å (visible up to B9) and the Fe lines at 5018.0–5018.4 Å (visible from A0 on). Our results are largely consistent with the spectral types given by Voroshilov et al. (1985), with deviations of up to four subclasses (see Fig. C.2).

For the stars observed with HDS/Subaru, from comparison with the spectra we found that the  $T_{\text{eff}}$  from *Gaia* DR2 are underestimated. These targets are not listed in the *Skiff* catalogue; instead we use the values given in Bai et al. (2019) which fit best to our spectra. Using Pecaut and Mamajek (2013, Table 5), these temperatures translate to spectral types A5–F0. However, their absolute magnitudes differ a lot from each other, indicating different ages.

HD 261393, suggested by Boubert et al. (2017) as the best candidate in the Monoceros Loop, has  $T_{\text{eff}} = 14,250\text{--}16,850$  K (Voroshilov et al., 1985) and  $M_G \approx -0.6$  mag. Therefore, it is probably an evolved but still young star of  $\lesssim 110$  Myr, consistent with being the ejected companion of a SN-progenitor ( $t \lesssim 32$  Myr).

### 5.6.2 The lithium test

Fig. 5.8 shows  $T_{\text{eff}}$  and  $EW_{\text{Li}}$  for stars in several open clusters of different ages. The data were obtained from Eric Mamajek<sup>6</sup>, who fitted polynomials to the data of cluster stars, allowing a rough localisation of ages in the  $T_{\text{eff}}\text{--}EW_{\text{Li}}$  space. By comparing the values of the Li stars, with  $T_{\text{eff}}$  from our parameter fits, to these curves, we obtained the age ranges displayed in Table 5.7. These should be seen as an upper limit, because of the unknown initial Li abundances of our targets. If the initial abundance was lower than in the case of the cluster stars, less time would have been necessary to reach the current abundance.

We summarise the ages inferred from the two diagrams in Tables 5.6 and 5.7. TYC8150-2802-1 and TYC8150-3105-1 are consistent with the ZAMS in Fig. 5.6. For TYC8150-2802-1,

<sup>6</sup><http://www.pas.rochester.edu/~emamajek/images/li.jpg>



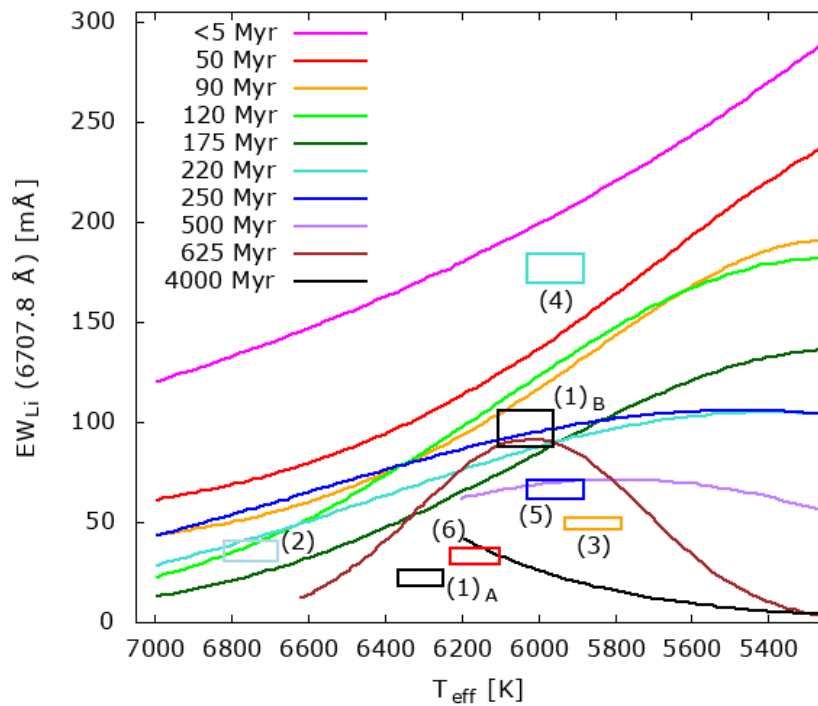


FIGURE 5.8:  $T_{\text{eff}}$  versus  $EW_{\text{Li}}$  for the six lithium stars, shown with coloured error boxes and labeled as in Fig. 5.6. For TYC159-251-1, we only show the individual components. The curves represent open clusters with different ages, which were fitted by Eric Mamajek to the data of the individual cluster stars (see Fig. 5.5, from which the curves were digitised by Richard Bischoff in order to use them for own figures). So the curves can be used as isochrones and rough ages of our stars can be estimated.

## 5.6. Age estimation

the low Li content indicates that it is an evolved star, at least a few hundred Myr old. TYC8150-3105-1, however, shows very strong Li absorption indicating that it is young. From combining both results, we obtain an age of 25–50 Myr, so we suggest that it has just reached the ZAMS. In the SB2 system TYC159-251-1, the primary is slightly above the MS while the secondary is consistent with it. Still, their ages are consistent with each other. A young age of 15–20 Myr could be possible, but we consider it more likely that the binary is on its early post-MS having  $t_{\text{HRD}} \approx 2\text{--}4$  Gyr because their Li content is too small for a young age. TYC159-343-1 is a difficult case: The Li abundance,  $\log(N_{\text{Li}}) = 2.91^{+0.07}_{-0.08}$ , is not a good age tracer in this case, because of two caveats: (i) The low metallicity also means that the star probably had a low initial Li abundance, e.g.  $\log(N_{\text{Li}}) = 2.64 \pm 0.07$  according to Lambert and Reddy (2004, Table 2). This value is even below the measured abundance, which could indicate that the metallicity of TYC159-343-1, as determined with the atmospheric parameter fits, is underestimated. A low initial abundance reduces the time which is necessary to reach the current abundance and therefore the age. (ii) TYC159-343-1 has spectral type F2–F4, meaning that no significant Li depletion is expected from standard mixing mechanisms (D’Antona and Mazzitelli, 1984). In Fig. 5.8, the star lies significantly below the 5 Myr curve and the age can be given as  $t_{\text{Li}} = 90\text{--}625$  Myr. However, due to the caveats stated above, we rather rely on the age ranges estimated from Fig. 5.7.

TABLE 5.7: Ages of the six lithium stars, including both components of the SB2 TYC159-251-1, estimated from Fig. 5.8.

Name	$t_{\text{Li}}$ [Myr]
TYC159-251-1 A	> 625
TYC159-251-1 B	90–4000
TYC159-343-1	90–625
TYC8150-2802-1	625–4000
TYC8150-3105-1	5–50
TYC8152-1456-1	250–4000
TYC8152-550-1	> 625

check of the ages given in Tables 5.6 and 5.7. This comparison works most efficiently for stars within the Li depletion gap, while it also suffers from the caveats described for the Li test in Section 5.5.2, e.g. the large scatter of the  $\log(N_{\text{Li}})$ .

In Fig. 5.9 we compare our Li targets to data of the clusters Pleiades (Boesgaard et al. 1988; Butler et al. 1987; Pilachowski et al. 1987; Soderblom et al. 1993) and Hyades (Boesgaard and Tripicco, 1986; Thorburn et al., 1993). The Li depletion gap of the Hyades is indicated by the brown arrow and the attached horizontal bar at  $T_{\text{eff}} = 6300\text{--}6900$  K. Note that the hot

The HRD positions of TYC8152-1456-1 and TYC8152-550-1 also allow both possibilities, i.e. they could be either pre- or post-MS. Applying the Li test for them excludes that they are very young. So they are probably evolved stars, unrelated to the birth association of the Vela Jr. progenitor, whereas TYC8150-3105-1 could be from the same stellar group that gave birth to the Vela progenitor.

By comparing the measured abundances to cluster data we can obtain a consistency

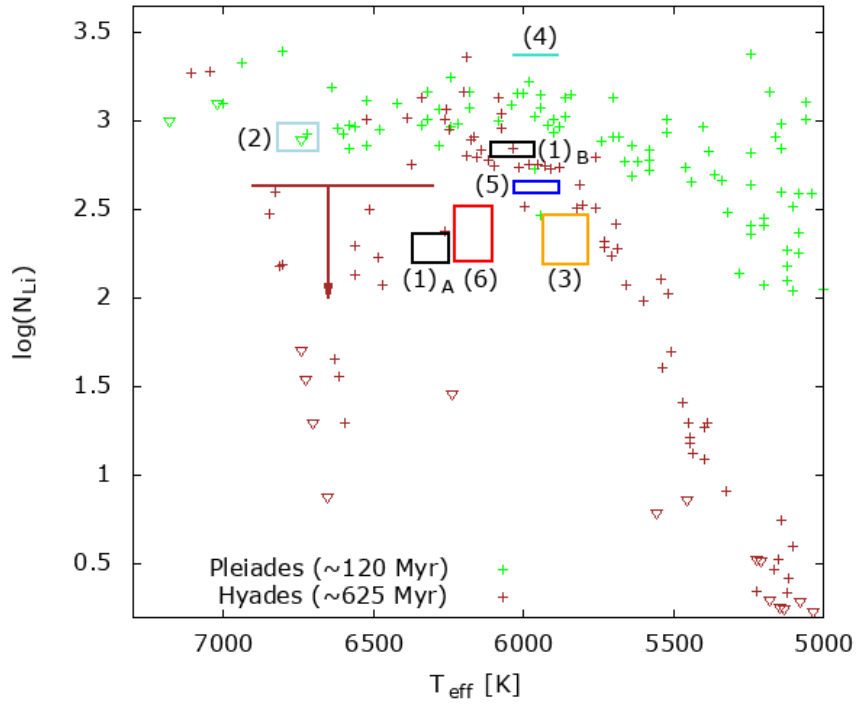


FIGURE 5.9: Lithium abundances of Pleiades and Hyades stars. The data for the Pleiades (green) were taken from Soderblom et al. (1993, Table 1), which also includes data from Butler et al. (1987), Pilachowski et al. (1987) and Boesgaard et al. (1988). The data for the Hyades (brown) were taken from Boesgaard and Tripicco (1986) and Thorburn et al. (1993). Inverted triangles show upper limits in the case of non-detections. Our Li targets, shown with coloured squares representing the error boxes, are labeled as in Fig. 5.8. The stars (1)<sub>A</sub> TYC159-251-1 A and (2) TYC159-343-1 are consistent with the Li depletion gap, which is marked by the brown arrow and the attached horizontal bar.

edge of the gap is steeper than the cold edge, where a larger scatter is observed. The  $T_{\text{eff}}$  of TYC159-251-1 A and TYC159-343-1 are consistent with the Li gap. TYC159-251-1 A lies at the cold edge of the gap and its Li abundance is lower than of Hyades stars with the same  $T_{\text{eff}}$ . Therefore, the Hyades age could be seen as a lower limit for the SB2 TYC159-251-1. TYC159-343-1 has one of the highest Li abundances among our sample, despite its low metallicity. Its Li abundance is comparable to Pleiades stars in this  $T_{\text{eff}}$ -region, so the Pleiades age ( $\sim 125$  Myr) can be seen as an upper limit. Possibly the star is younger than the range inferred from Fig. 5.8 (Table 5.7), where we did not consider the metallicity.

The other four Li-rich targets have lower  $T_{\text{eff}}$  and do not fall in the Li depletion gap. The abundances of TYC8150-2802-1, TYC8152-1456-1 and TYC8152-550-1 are consistent with the Hyades or older, whereas TYC8150-3105-1 has more Li than comparable Pleiades stars. Therefore, it is very young, consistent with what we found from Fig. 5.8.



# Chapter 6

## Discussion

Here, we first want to give an overview of the runaway star candidates identified in this work. After that, we present the individual SNRs in more detail and compare our findings to theoretical models of BES runaway star production.

### 6.1 Overview of the candidates

We list in Table 6.1 the SNRs with their corresponding numbers of runaway star candidates from the different selection steps and if they were already observed, as well as additional information (e.g. the best candidates). A list of the individual candidate stars is given in Table 6.2, where the spectral types were estimated from the *Gaia* DR2  $T_{\text{eff}}$  if available, with the following exceptions: HD 37424 was observed, described and confirmed as a runaway star by Dinçel et al. (2015). The stars in SNR G205.5+00.5 as well as HD 76060 in G266.2–01.2 were observed by us with UVES and their spectral types were adopted from the *Skiff* catalogue (Skiff 2009; Voroshilov et al. 1985; Houk 1978). The stars in G160.9+02.6 (except the faintest one) were observed by us with HDS and their spectral types were adopted from the  $T_{\text{eff}}$  given in Bai et al. (2019).

Note that for the candidates selected from *Gaia* DR2 the allowed locations around the SNR centres at the time of the SN were reduced from an error estimate based on the determination of the Vela SNR centre to a smaller error based on the description in Green (2009) (see Section 3.3). This was necessary to limit the high number of stars from DR2 more strictly, in order to create feasible projects for follow-up observations. In both cases the errors scale with the size of the SNR. Trajectories of associated NSs were considered for the DR2 selection.

In S147, we can confirm the B0.5 V star HD 37424 based on DR2 data. Its position at the time of the SN, with a distance to the GC of  $\rho = 4.8' \pm 7.0'$ , is well within the  $1\sigma$  error ellipse of the GC used for the DR1 selection and only slightly outside (by 8.5 %) of the more strict

## 6.1. Overview of the candidates

TABLE 6.1: Numbers of runaway star candidates with  $G < 17$  mag in the SNRs covered in this work. Columns 2 and 3 give the numbers of runaway star candidates identified in *Gaia* DR1 TGAS and DR2, respectively. Column 4 gives the number of observed stars and if they were observed with UVES/VLT (U) or with HDS/Subaru (H). These observations are all based on the DR1 selection, whereupon *Gaia* DR2 was used for the further characterisation of the targets. Column 5 gives the names of associated NSs and column 6 the numbers of remaining candidates that were not excluded during the analysis.

SNR Name	DR1	DR2	Obs.	PSR	Rem. cand.	Additional info
G074.0–08.5	16	19	0	–	19	
G160.9+02.6	6	1	6 (H)	SGR 0501+4516(?)	5	SGR & PSR prob. unrelated
G180.0–01.7	3	–	3 (U)	J0538+2817	1	HD 37424 confirmed <sup>1</sup>
G205.5+00.5	21	116**	21 (U)	–	5	incl. HD 261393 <sup>2</sup>
G260.4–03.4	2	9	2 (U)	–	9	J0821–4300 prob. unrelated
G263.9–03.3	2	1	2 (U)	J0835–4510	1	
G266.2–01.2	5	12	5 (U)	–	13	J0855–4644 prob. unrelated
G330.0+15.0	6	3	0	–	3	
G111.7–02.1*	0	0	0	CCO J2323+5848	0	
G130.7+03.1*	0	0	0	J0205+6449	0	No cand. consistent with PSR
G184.6–05.8*	0	0	0	J0534+2200	0	
G347.3–00.5*	2	18	0	CCO(?)	18	

\* Historical SNR; \*\* not suggested for observations, more precise constraints required; <sup>1</sup> Dinçel et al. (2015);

<sup>2</sup> Boubert et al. (2017)

error ellipse used for the DR2 selection. We also checked for the possibility that more than one star might be ejected from a SN in a multiple system. But the three other runaway star candidates besides HD 37424, which projected trajectories could originate from the GC, are neither consistent with the associated PSR J0538+2817 nor with HD 37424.

Two of the DR2 candidates in the Lupus Loop are particularly promising. Their positions at the time of the SN were  $1.1' \pm 6.3'$  and  $1.7' \pm 6.6'$  off the GC, respectively (see Table 6.2) and both have very high proper motions clearly directing away from the centre. Spectroscopic follow-up observations are highly suggested for them.

The historical SNRs generally have very small diameters due to their low age. This reduces the number of stars in the cone search. Just as Kochanek (2018) and Fraser and Boubert (2019), for Cas A and the Crab Nebula we did not find any candidates. For SNR G130.7+03.1 (from SN 1181) we found one star with  $G < 17.0$  mag to be consistent with the GC, but it was ruled out due to the missing kinematical consistency with PSR J0205+6449. SNR G347.3–00.5 probably originates from SN 393 and is much larger than the other three historical SNRs ( $\Theta = 65' \times 55'$ ). Here we found 18 candidates to be consistent with the GC.

The twelve SNRs are described in more detail in the following section.

TABLE 6.2: List of detected runaway star candidates. Equatorial coordinates (J2000) and  $G$  magnitudes are taken from *Gaia* DR2. The fifth column shows the angular distance  $\rho$  to the geometric centre at the time of the SN, except for the candidate in G263.9–03.3, where the distance to the location of the Vela pulsar at the time of the SN is given. The last column shows the spectral types SpT.

Gaia DR2	RA [h:m:s]	DEC [d:m:s]	SNR	$\rho$ [arcmin]	$G$ [mag]	SpT
1859462217726265728	20:50:22.2	+30:30:17	G074.0–08.5	$2.3 \pm 4.4$	16.23	K2–K3.5
1859461771049581952	20:50:47.8	+30:30:44	G074.0–08.5	$3.4 \pm 7.1$	16.88	K5–K6
1859469532044083968	20:50:54.6	+30:39:07	G074.0–08.5	$3.5 \pm 4.6$	15.20	K2–K3
1859469364551815040	20:50:54.7	+30:37:30	G074.0–08.5	$3.4 \pm 6.6$	15.65	K2.5–K3.5
1859469467631489920	20:50:55.6	+30:38:14	G074.0–08.5	$1.1 \pm 3.0$	15.47	K2–K3.5
1858709945619185664	20:50:56.7	+30:26:28	G074.0–08.5	$4.9 \pm 8.4$	15.06	G9–K2
1859471357406309120	20:50:57.4	+30:42:39	G074.0–08.5	$2.6 \pm 6.1$	14.44	–
1859471254338021120	20:50:58.7	+30:40:52	G074.0–08.5	$0.6 \pm 2.5$	16.67	K1.5–K3.5
1859471288697195136	20:50:59.1	+30:41:01	G074.0–08.5	$1.1 \pm 6.1$	14.22	G9
1859471082528259840	20:51:00.8	+30:40:48	G074.0–08.5	$1.7 \pm 6.1$	15.94	G9–K3.5
1859470975153131904	20:51:01.9	+30:39:18	G074.0–08.5	$2.0 \pm 4.6$	14.04	G0–G3
1859474823444598144	20:51:02.4	+30:44:37	G074.0–08.5	$3.7 \pm 4.2$	15.67	K2–K3.5
1859471185617972864	20:51:03.1	+30:41:43	G074.0–08.5	$3.5 \pm 5.4$	16.27	K2.5–K3.5
1859471872812767104	20:51:04.1	+30:43:48	G074.0–08.5	$1.9 \pm 6.2$	15.72	K1.5–K3
1859471219977693056	20:51:09.3	+30:42:11	G074.0–08.5	$1.7 \pm 6.1$	16.88	K5–M0
1858715683695452800	20:51:10.1	+30:26:54	G074.0–08.5	$1.7 \pm 8.7$	13.01	G2–K0
1858719291463059840	20:51:17.4	+30:36:47	G074.0–08.5	$1.7 \pm 3.1$	16.95	F2–K6
1858719085309596672	20:51:30.7	+30:36:48	G074.0–08.5	$4.0 \pm 3.9$	13.84	G9–K3.5
1859572714338261504	20:51:35.7	+30:58:15	G074.0–08.5	$6.8 \pm 7.2$	15.02	K3–K6
206966712992657792 <sup>1</sup>	05:00:31.3	+46:33:27	G160.9+02.6	$8 \pm 12$	11.07	A5–F0
206918781157635072 <sup>2</sup>	05:00:54.0	+46:30:01	G160.9+02.6	$10 \pm 24$	11.40	A6–F0
206994059046621824	05:00:55.1	+46:40:38	G160.9+02.6	$1.7 \pm 3.0$	16.27	K5.5–K7
206938263129288704 <sup>3</sup>	05:01:10.9	+46:27:38	G160.9+02.6	$12 \pm 23$	12.33	A7–F0
206942519437580416 <sup>4</sup>	05:01:16.0	+46:33:22	G160.9+02.6	$7 \pm 16$	10.87	A7–A9
3442490264261174528 <sup>5</sup>	05:39:44.4	+27:46:51	G180.0–01.7	$4.8 \pm 6.8$	8.91	B0.5
3133462316432771200 <sup>6</sup>	06:38:50.8	+06:35:26	G205.5+00.5	$12 \pm 33$	12.01	B8–A0
3133412018076162560 <sup>7</sup>	06:39:07.5	+06:27:38	G205.5+00.5	$3 \pm 20$	11.79	B8–A0
3133486093371718656 <sup>8</sup>	06:39:13.1	+06:37:54	G205.5+00.5	$10 \pm 30$	10.05	B4–B6
3133407104633600512 <sup>9</sup>	06:39:20.1	+06:21:01	G205.5+00.5	$11 \pm 24$	11.80	B8–A0
3133414491977266816 <sup>10</sup>	06:39:24.3	+06:33:09	G205.5+00.5	$7 \pm 19$	12.25	B7–B9
5526325078219949440	08:22:00.3	–42:59:34	G260.4–03.4	$1.6 \pm 2.0$	13.58	G2–G9
5526328136236654208	08:22:00.5	–42:57:27	G260.4–03.4	$2.1 \pm 2.8$	13.17	K1.5–K3
5526325112579690496	08:22:05.1	–42:58:43	G260.4–03.4	$0.9 \pm 2.5$	16.86	K7–M0
5526324803342055168	08:22:05.6	–43:01:23	G260.4–03.4	$1.8 \pm 4.1$	16.92	M1–M2
5526324906421263744	08:22:06.3	–42:59:24	G260.4–03.4	$0.5 \pm 2.1$	15.47	K3.5–K5.5
5526325284378390784	08:22:10.1	–42:59:29	G260.4–03.4	$0.3 \pm 2.4$	14.87	K5.5–K7
5526324833397363840	08:22:10.5	–43:00:50	G260.4–03.4	$1.2 \pm 4.0$	15.99	K5.5–M0
5526325250018655616	08:22:15.6	–42:58:32	G260.4–03.4	$1.7 \pm 2.4$	13.56	G9–K3
5526325353097874176	08:22:17.6	–42:58:40	G260.4–03.4	$1.9 \pm 2.4$	13.00	F2–F9
5521967782363042432	08:35:48.5	–45:18:46	G263.9–03.3	$5.1 \pm 3.6$	15.85	K3.5–M1.5
5329655463417782528	08:51:46.0	–46:21:01	G266.2–01.2	$2.1 \pm 3.4$	16.38	K4.5–K7
5329655257259343232	08:51:47.1	–46:21:18	G266.2–01.2	$2.6 \pm 4.1$	16.87	K6–K9

<sup>1</sup> TYC3344-235-1; <sup>2</sup> TYC3344-679-1; <sup>3</sup> TYC3344-683-1; <sup>4</sup> TYC3344-553-1; <sup>5</sup> HD 37424;

<sup>6</sup> TYC159-2771-1; <sup>7</sup> HD 261359; <sup>8</sup> HD 261393; <sup>9</sup> TYC159-2337-1; <sup>10</sup> TYC159-2671-1

## 6.2. Individual supernova remnants

Continued.

Gaia DR2	RA [h:m:s]	DEC [d:m:s]	SNR	$\rho$ [arcmin]	$G$ [mag]	SpT
5329655845686016256	08:51:50.0	-46:20:20	G266.2-01.2	$1.7 \pm 3.3$	15.13	K4-K5.5
5329655983110009856	08:51:53.7	-46:18:19	G266.2-01.2	$1.7 \pm 3.8$	16.57	K6-K9
5329655776966532864	08:51:54.7	-46:19:38	G266.2-01.2	$0.7 \pm 3.8$	15.24	K2.5-K3.5
5329657563672287872	08:51:55.4	-46:16:42	G266.2-01.2	$2.8 \pm 6.1$	16.26	K5-K8
5329656017469763456	08:51:59.1	-46:18:09	G266.2-01.2	$1.0 \pm 4.5$	15.30	K2-K4
5329655811325638272	08:51:59.7	-46:19:02	G266.2-01.2	$0.7 \pm 4.2$	14.91	G8-K2
5329657288780088704	08:52:00.4	-46:17:58	G266.2-01.2	$1.8 \pm 5.7$	16.62	K2.5-K6.5
5329654849253600896	08:52:00.6	-46:21:49	G266.2-01.2	$2.9 \pm 6.1$	14.97	K1.5-K5
5329654849241704320	08:52:00.6	-46:21:49	G266.2-01.2	$2.5 \pm 6.0$	16.82	-
5329657490638374272 <sup>11</sup>	08:52:02.5	-46:17:20	G266.2-01.2	$2.2 \pm 4.8$	7.85	B8 IV,V
5329654883601436032	08:52:05.1	-46:22:19	G266.2-01.2	$2.5 \pm 5.3$	14.91	K0.5-K2.5
6005336183671977344	15:09:15.5	-40:00:55	G330.0+15.0	$1.1 \pm 6.3$	16.31	K7-M0
6005322405417134848	15:09:22.2	-40:17:51	G330.0+15.0	$4.3 \pm 6.0$	15.95	K3.5-M1
6005309932830763648	15:09:27.2	-40:24:26	G330.0+15.0	$1.7 \pm 6.6$	15.70	K9-M2.5
5972266305587974656	17:13:45.2	-39:46:12	G347.3-00.5	$1.3 \pm 2.4$	14.71	K1.5-K3.5
5972266443017191680	17:13:47.2	-39:44:37	G347.3-00.5	$0.7 \pm 2.4$	15.97	K5.5-M0.5
5972266683540067328	17:13:47.5	-39:43:15	G347.3-00.5	$1.9 \pm 3.9$	16.84	K6-M0.5
5972266443017192960	17:13:47.5	-39:44:29	G347.3-00.5	$0.7 \pm 2.5$	16.65	K6-M1.5
5972266447337050496	17:13:49.4	-39:44:01	G347.3-00.5	$1.1 \pm 4.0$	16.98	K6-M1
5972266447374127872	17:13:49.6	-39:44:03	G347.3-00.5	$1.0 \pm 4.1$	15.01	K4-K6
5972266378654585856	17:13:50.5	-39:45:35	G347.3-00.5	$0.5 \pm 3.6$	16.59	K6.5-K9
5972266477376942848	17:13:51.1	-39:43:28	G347.3-00.5	$1.8 \pm 4.0$	14.81	K1-K4.5
5972219340115696512	17:13:51.2	-39:46:40	G347.3-00.5	$1.7 \pm 3.9$	16.54	-
5972266378617336832	17:13:51.4	-39:45:25	G347.3-00.5	$0.5 \pm 2.5$	16.40	K3.5-K6.5
5972266481696795008	17:13:52.4	-39:43:28	G347.3-00.5	$1.6 \pm 3.7$	16.92	K3.5-K9
5972266408657455872	17:13:53.3	-39:44:22	G347.3-00.5	$0.9 \pm 2.4$	16.88	K5-M1
5972266413014335616	17:13:53.5	-39:44:41	G347.3-00.5	$0.7 \pm 2.4$	16.59	K7-M2.5
5972219374522872576	17:13:54.5	-39:46:45	G347.3-00.5	$1.9 \pm 2.9$	15.04	K4.5-K6
5972219477602131840	17:13:55.2	-39:45:22	G347.3-00.5	$1.0 \pm 2.5$	13.47	G8-K1.5
5972266413014326528	17:13:55.5	-39:44:37	G347.3-00.5	$1.3 \pm 2.2$	15.62	K5-K9
5972267886141988864	17:13:56.1	-39:44:03	G347.3-00.5	$1.6 \pm 2.2$	13.94	M3.5
5972267890445877120	17:13:57.0	-39:43:57	G347.3-00.5	$1.8 \pm 2.2$	16.91	K4.5-K9

<sup>11</sup> HD 76060

## 6.2 Individual supernova remnants

### 6.2.1 Cygnus Loop (G074.0-08.5)

The well-studied Cygnus Loop, also known as Cirrus Loop or Veil Nebula, is one of the largest SNRs on the sky, with  $\Theta = 230' \times 160'$ . A wide range of possible distances, from 300 pc to 1800 pc, is given in the literature (Fesen et al., 2018a). For our study, we adopt the range 576–1000 pc given in the UofM catalogue, based on the values found by Blair et al. (2009,  $576 \pm 61$  pc) and Fesen et al. (2018a,  $1000 \pm 200$  pc). The latest published value,  $735 \pm 25$  pc (Fesen et al., 2018b), based on *Gaia* DR2 parallax measurements of six stars, is close to 788 pc, the central value of our adopted range, while the small error,  $\Delta d = 25$  pc seems too optimistic, considering the large range of literature values. The age of the Cygnus Loop was taken to be



between 10 kyr (Katsuda and Tsunemi, 2008) and 20 kyr (Welsh et al., 2002).

Since no NS is firmly associated with the Cygnus Loop (for a possible pulsar wind nebula association see Katsuda et al. 2012), we searched for runaway candidates around the GC in a range defined by Eqn. 3.6 and found 19 objects with  $G < 17$  mag, mostly with spectral type K according to their  $T_{\text{eff}}$  from *Gaia* DR2. They are displayed in Fig. 6.3 (a), where it can be seen that the error ellipse of the target at the north-western edge is just touching the error ellipse of the GC. We still consider it as a promising candidate because it shows a high proper motion directing away from the GC.

TYC2688-2556-1, suggested as a runaway candidate in the Cygnus Loop by Boubert et al. (2017), has  $G = 11.36$  mag and with  $T_{\text{eff}} = 6370_{-89}^{+91}$  K (*Gaia* DR2) or  $6926_{-464}^{+508}$  K (Anders et al., 2019) it has a spectral type between A9 and F6 (Pecaut and Mamajek, 2013, Table 5). From the assumed association, Boubert et al. (2017) gave a SNR distance of  $d = 570 \pm 70$  pc, consistent with the range given above. However, while TYC2688-1556-1 was also part of our earlier selection from *Gaia* DR1 TGAS, its distance of  $427 \pm 6$  pc according to the *Gaia* DR2 parallax and consistent with Anders et al. (2019), is significantly closer than the adopted SNR distance, as also noted by Fesen et al. (2018b). Boubert et al. (2017) further suggested that TYC2688-1556-1 could have a very large ejection velocity of  $\sim 700 \text{ km s}^{-1}$ , which would make it a *hyperrunaway star*. While such a high ejection velocity is very unlikely (Renzo et al., 2019; Tauris, 2015), the scenario is excluded by the *Gaia* DR2 RV of  $-42.6 \pm 1.0 \text{ km s}^{-1}$  which yields  $v_{\text{pec}} = 47.1 \pm 1.2 \text{ km s}^{-1}$ .

While we would exclude TYC2688-2556-1 due to its proximity, we found 19 fainter runaway candidates from *Gaia* DR2, for which we suggest spectroscopic follow-up observations.

### 6.2.2 HB 9 (G160.9+02.6)

HB9 is a  $140' \times 120'$  SNR on the northern hemisphere, where we observed six runaway star candidates around the GC from *Gaia* DR1 with HDS/Subaru. The adopted SNR distance and age are  $d = 0.8 \pm 0.4$  kpc and  $t = 5.5 \pm 1.5$  kyr, respectively (Leahy and Tian, 2007). Among the observed candidates, we found two giants. The other four were introduced in Chapter 5. They have a large range of effective temperatures in the literature. E.g., in the case of TYC3344-679-1, the values reach from 5904 K (*Gaia* DR2) over 7591 K (Bai et al., 2019) to 10,822 K (Anders et al., 2019). The *Gaia* DR2 values are probably underestimated, as can be seen from comparison with our spectra. Unfortunately, the chosen spectral range was not convenient for spectral type determination. Therefore, we rely on the  $T_{\text{eff}}$  given by Bai et al. (2019), corresponding to spectral type late-A. The RVs were calculated from the positions of individual absorption lines (see Section 5.2), where the uncertainties are large due to the low number of available lines. The most precise value is given for TYC3344-235-1, which also

shows the most promising kinematics. Although the proper motion is moderate, its high radial velocity (pointing towards us) gives it the largest peculiar velocity among all early-type stars. If it is the ejected companion, its distance of  $d = 1103_{-45}^{+48}$  pc would require that the SNR lies at the upper edge of its distance range. TYC3344-235-1 and TYC3344-679-1 have high luminosities of  $34 L_{\odot}$  and  $20 L_{\odot}$ , respectively. From their spectra it is clear that they are not giants. They could be very young A-type stars but it is more likely that they are evolved, with ages between  $\sim 0.2$  Gyr and 2 Gyr, especially since TYC3344-235-1 is even located above the isochrone for 1 Myr in Fig. 5.6.

There are two NSs in the vicinity of HB9. PSR J0502+4654 is located  $\sim 17'$  to the northeast of the centre. No stars from *Gaia* DR2 were found to be consistent with a common origin. Its high characteristic age of  $\tau_c = 1.81$  Myr and its proper motion indicate that it is unrelated. The magnetar SGR 0501+4516 is located  $1.38^{\circ}$  to the south of the centre. Since the proper motion is unknown, we cannot draw useful constraints on the search area, but obtain more than 1500 possible candidates. If the location of the GC is close to the explosion site, an association with SGR 0501+4516 is unlikely, because the large angular distance requires an unreasonably high projected velocity of more than  $3400 \text{ km s}^{-1}$  (for  $t \approx 5.5$  kyr,  $d \approx 0.8$  kpc and an explosion at the present GC). This would be more than twice as high as the largest 2D velocities of any other known pulsar (Hobbs et al., 2005).

From *Gaia* DR2, we found one fainter object consistent with the GC. Since both NSs are probably unrelated, we suggest that this is the most probable candidate. It has  $G = 16.27$  mag and was located  $1.7' \pm 3.0'$  from the GC at the time of the SN. Its spectral type is K5.5–K7 according to its *Gaia* DR2  $T_{\text{eff}} = 4172_{-67}^{+184}$  K. From its position in Fig. 3.4 ( $L = 0.199 \pm 0.021 L_{\odot}$ ) it should have a young age of  $\sim 15$ – $50$  Myr, so it could indeed be the ejected companion of the HB9 progenitor.

### 6.2.3 S147 (G180.0–01.7)

S147 is a large northern SNR with  $\Theta = 180'$ . Its distance was adopted from the parallax of the associated radio pulsar, J0538+2817, as  $d = 1.3 \pm 0.2$  kpc (Verbiest et al., 2012). Dinçel et al. (2015) discovered the runaway star HD 37424, a B0.5 V star with  $G = 8.91$  mag, to have a common origin with the pulsar and with the GC of S147. The travel time of pulsar and runaway star, and therefore the age of S147, is  $30 \pm 4$  kyr (Dinçel et al., 2015; Kramer et al., 2003) and the inferred distance is  $d = 1330_{-110}^{+100}$  pc (Dinçel et al., 2015), fully consistent with the range given by Verbiest et al. (2012).

Although a runaway star is already known for S147, we tried to find further candidates in *Gaia*, because it is principally possible that more than one runaway star could be ejected from the BES. Dinçel et al. (2015) only considered OB-type stars, so they might have missed late-

type stars. However, it would be required that we can trace back the trajectory to a common origin with HD 37424 and PSR J0538+2817. We found three stars in *Gaia* DR1 TGAS to be consistent with the GC, but none of those is consistent with the positions of HD 37424 or PSR J0538+2817  $30 \pm 4$  kyr ago. The same applies to the stars from *Gaia* DR2, where we searched both around the GC and around the past position of the pulsar. Therefore, in Fig. 6.3 (c) we only show the motions of PSR J0538+2817 and HD 37424, while the red ellipses mark regions of  $1\sigma$  and  $2\sigma$  around the GC (according to Eqn. 3.6).

We found HD 37424 to have been located at an angular distance from the GC of  $4.8' \pm 7.0'$  at the time of the SN, so we can verify it based on *Gaia* DR2 data. This is also consistent with the predicted offset between the GC and the explosion site of  $4.2'_{-0.6'}^{+0.8'}$  (Dinçel et al., 2015). While the peculiar velocity of the star was found to be  $74 \pm 8$  km s<sup>-1</sup> by Dinçel et al. (2015), we find an even larger value of  $102 \pm 10$  km s<sup>-1</sup>. The difference mainly arises from the increased *Gaia* DR2 proper motion of  $(\mu_{RA}, \mu_{DEC}) = (12.05 \pm 0.16, -9.52 \pm 0.11)$  mas yr<sup>-1</sup> and a slightly increased distance of  $d = 1521_{-141}^{+172}$  pc from the *Gaia* DR2 parallax. The RV of  $9.2 \pm 6.5$  km s<sup>-1</sup> was adopted from Dinçel et al. (2015). Either way it is faster than any other runaway candidate in our sample.

## 6.2.4 Monoceros Loop (G205.5+00.5)

The Monoceros Loop is one of the largest ( $\Theta = 220'$ ) and probably the oldest SNR of our sample, although the age determination is very uncertain (30–150 kyr, Welsh et al. 2001). From Ferrand and Safi-Harb (2012), we adopted  $d = 1.44 \pm 0.54$  kpc, since recent works place it at  $d = 0.941_{-0.094}^{+0.096}$  kpc or  $d = 1.257_{-0.101}^{+0.092}$  kpc (Yu et al., 2019) and  $d = 1.98$  kpc (Zhao et al., 2018), respectively. The discrepancy connects to the question if the Monoceros Loop interacts with the Rosette Nebula (3C 163), an H II region bordering the SNR at the south-western edge.

We observed 21 stars with UVES/VLT in the Monoceros Loop, where no associated NS is known. Eight of those were ruled out because they were found to be giants. Among the others, the most interesting cases are (i) HD 261393, a B5 V star according to Voroshilov et al. (1985), which was proposed as the most likely runaway companion by Boubert et al. (2017), (ii) TYC159-251-1, which was newly discovered by us to be a SB2 and (iii) TYC159-343-1, an F2–F4 star. TYC159-343-1 and both components of TYC159-251-1 show Li absorption. However, the ages inferred in Section 5.6 are higher than what we expect for a BES runaway star. Also, from the updated distance to the Monoceros Loop and from using proper motions and parallaxes from *Gaia* DR2, TYC159-343-1 ( $d = 0.723_{-0.021}^{+0.023}$  kpc) and TYC159-251-1 ( $d = 0.564_{-0.014}^{+0.013}$  kpc) turn out to be foreground stars, even when the lower limit of the SNR distance given by Yu et al. (2019) is extended to  $2\sigma$  ( $0.941$  kpc  $- 2 \times 0.094$  kpc =  $0.753$  kpc).

Boubert et al. (2017) did not have the possibility to use *Gaia* DR2, so we can still ask

the question why HD 261393 gained a higher probability in their work than TYC159-343-1. There are two reasons: (i) It is/was located closer to the GC. Boubert et al. (2017) used a prior to describe the location of the centre as a 2D-Gaussian with a *full width at half maximum* (FWHM) of  $\tilde{\Theta} = \max(5', 0.05 \Theta)$ . This corresponds to  $\tilde{\Theta} = 11'$  in the case of the Monoceros Loop. The angular distance between TYC159-343-1 and the Green centre at the time of the SN was  $21' \pm 22'$ , almost twice the FWHM. This compares to  $10' \pm 25'$  for HD 261393. (ii) It is more massive. Multiplicity studies (e.g. Pinsonneault and Stanek 2006) have shown that massive stars tend to form binaries with similar masses. Therefore, Boubert et al. (2017) assign higher runaway probabilities to more massive, early-type stars. However, in wide systems the companions can form more independently and the distribution of mass ratios  $q$  becomes almost consistent with random pairings from the IMF (Moe and Di Stefano, 2017). Either way, the existence of late-type runaway stars cannot be excluded (see Section 2.5).

Among the other observed stars in the Monoceros Loop, there is TYC159-1896-1 which has spectral type F3–F9 (according to its  $T_{\text{eff}}$  as listed in *Gaia* DR2) and which does not show Li, hence is too old, and nine stars of spectral types mid-B to mid-A. For the latter, we can only obtain a rough age estimate from the HRD. Five of them turn out to be spatially inconsistent with the GC after reevaluating them with DR2 data. Among the others, for TYC159-2771-1, HD 261359 and TYC159-2671-1 we can only give lower limits of 3.5–5 Myrs. Therefore, they are all potentially young enough to be runaway stars ejected from the BES. For TYC159-2337-1, we obtain two possible ranges, where 50–490 Myr is more likely than 1.6–3.3 Myr. 50 Myr would already be too old, but we do not exclude the younger solution.

So in total, we have five good runaway star candidates in the Monoceros Loop, including HD 261393 and four stars of spectral types B7–A1, which trajectories are displayed in Fig. 6.3 (d). We determined their radial velocities  $v_r$  from the positions of individual absorption lines (see Section 5.2). The  $v_r$  in Table 5.1 correspond to average and standard deviation from these measurements. For TYC159-2671-1, H $\alpha$  was the only visible absorption line, so here the error was adopted from the highest error among the other stars. Their spectral types were adopted from Voroshilov et al. (1985), where the given range comes from our error estimate of  $\pm 1$  subclass.

A search for further targets in the DR2 catalogue yields more than 100 candidates with  $G < 17$  mag. We abstain from listing them all in Table 6.2, because it is not realistic to observe them all in the near future. Until more reliable and precise distance and age are known for the Monoceros Loop, it appears more fruitful to first concentrate on the brighter candidates observed with UVES/VLT.

### 6.2.5 Puppis A (G260.4–03.4)

The Vela region, located on the southern sky in the Vela constellation, is a very extended and complex region with several stellar clusters, star-forming regions and three SNRs.

The most distant SNR in this region, with  $d = 1.3 \pm 0.3$  kpc (Reynoso et al., 2017), is Puppis A. Here, two runaway star candidates were observed with UVES, namely TYC7669-1336-1 and TYC7669-1414-1, which could both originate from the GC in projection. According to their  $T_{\text{eff}}$  from *Gaia* DR2, their spectral types are F3–F6 and F1–F2, respectively. No Li was found in the spectra. After reevaluating them with the DR2 parallax, it was found that they are too close to be consistent with the distance given for Puppis A.

A search in *Gaia* DR2 yields nine candidates with  $G < 17$  mag, where eight of them have proper motions pointing to north-west, similar to most other stars in this region of the sky. Only one candidate, a K1.5–K3 star with  $G = 13.2$  mag, has a higher proper motion and a slightly different direction compared to the other stars, pointing to west-north-west. It might, therefore, be the best candidate. It was located  $2.1' \pm 2.7'$  from the GC at the time of the SN. With  $T_{\text{eff}} = 5042_{-180}^{+115}$  K and  $L = 4.64 \pm 0.21 L_{\odot}$ , from Fig. 3.4 it could be consistent with a young age of  $\sim 1$ –2 Myr, although it is more likely an evolved star with 4.5–11 Gyr.

PSR J0821–4300 is located within Puppis A (in projection) and is consistent with the GC at the time of the SN. If this is the associated NS, the runaway star candidates would have to be ruled out because none of them shows a common origin with PSR J0821–4300. However, the PSR distance  $d = 2.2 \pm 0.3$  kpc indicates that it is in the background of Puppis A and the characteristic age  $\tau_c = 1.93 \times 10^8$  yr is almost five orders of magnitude higher than the SNR age ( $t = 4075 \pm 375$  yr). Therefore, the association is very unlikely.

### 6.2.6 Vela (G263.9–03.3)

With  $d = 0.275 \pm 0.025$  kpc, Vela is the closest SNR, therefore having a large diameter of  $\Theta = 255'$ . Its age is only poorly constrained to  $t = 18 \pm 9$  kyr (Ferrand and Safi-Harb, 2012). The characteristic age of the Vela pulsar (J0835–4510),  $\tau_c = 11.3$  kyr, indicates that the SNR age could be close to the lower limit.

Two stars were observed, TYC8150-2802-1 and TYC8150-3105-1, both showing Li in their spectra. Their spectral types are G0–G2 and F9.5–G1, respectively, corresponding to their  $T_{\text{eff}}$  as determined in the atmospheric parameter fits. From the Li content and the position in the HRD, we can conclude that TYC8150-3105-1 has a relatively young age of 25–50 Myr, while TYC8150-2802-1 is probably a further evolved MS star. However, both cannot be associated runaway stars, because their trajectories are not consistent with the past position of the Vela pulsar (J0835–4510). TYC8150-3105-1 could be a member of the young association to which

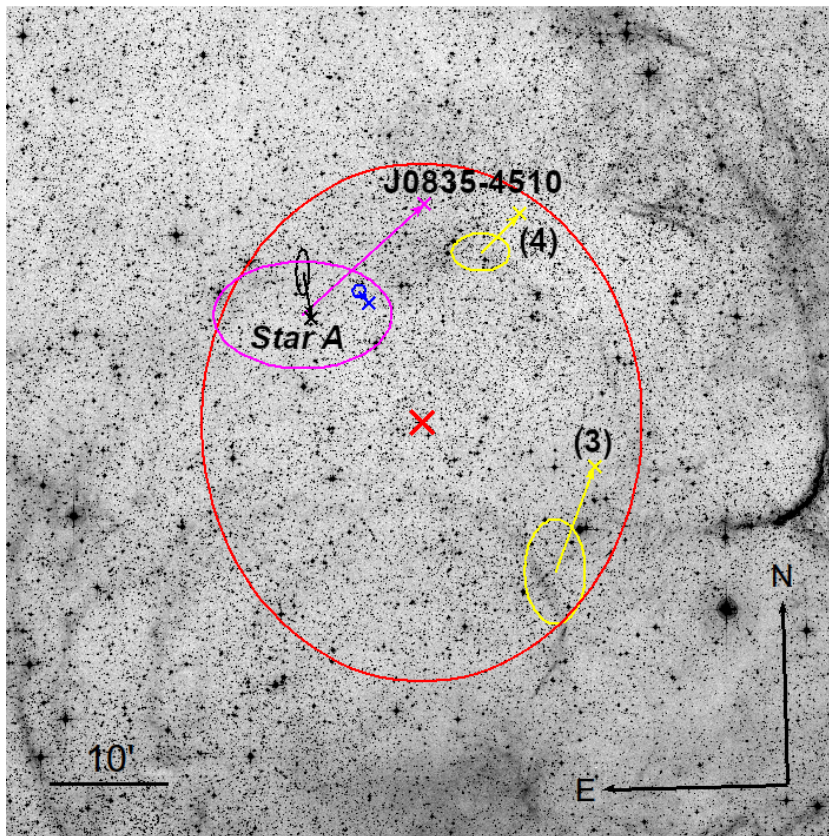


FIGURE 6.1: The central  $70' \times 70'$  of the Vela SNR. The red labels mark the geometric centre and its error ellipse, the yellow labels the Li stars observed in ESO P100, namely (3) TYC8150-2802-1 and (4) TYC8150-3105-1. The crosses mark the current positions, connected to the positions at the time of the SN (with error ellipse) by an arrow in proper motion direction. The motion of the Vela PSR is shown in magenta, our runaway candidate from *Gaia* DR2 in blue and the candidate identified by Fraser and Boubert (2019) in black. Background image from ESO DSS-2-red.

also the Vela progenitor belonged, whereas TYC8150-2802-1 is probably an interloper.

Fig. 6.1 shows the motion of the Li stars in yellow and the Vela pulsar in magenta. Two further candidates are marked, found in *Gaia* DR2, which are consistent with the Vela pulsar: The star marked in blue was found by us and could be observed in the near future. The star marked in black was found by Fraser and Boubert (2019), therein denoted as *Star A*. It is closer to the nominal past position of the Vela pulsar, but with  $G = 20.1$  mag, it is much too faint to obtain a spectrum with sufficient  $S/N$ . Fraser and Boubert (2019) note that it is unlikely that the ejected companion of the Vela SN progenitor would be such faint (absolute magnitude  $M_G = 12.7$  mag), so probably *Star A* is an unrelated background star. Fraser and Boubert (2019) used the distribution of runaway star velocities given by Renzo et al. (2019) (see Fig. 6.2) to constrain their search radius, which limits their selection more strictly than the  $v_{\max} = 1000 \text{ km s}^{-1}$  used by us. Therefore, the star marked in blue in Fig. 6.1 was not found by them.

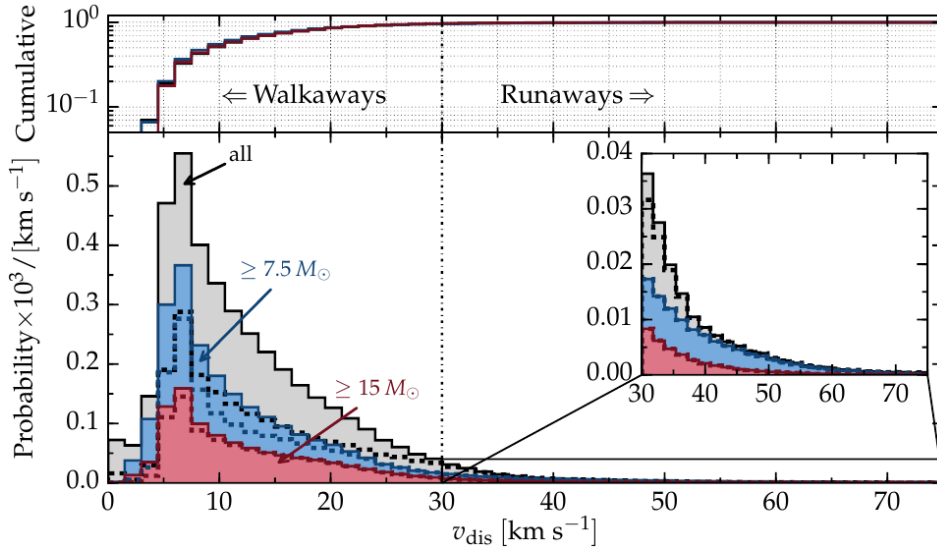


FIGURE 6.2: The runaway star velocity distribution from the population synthesis made by Renzo et al. (2019). The red, blue and grey histograms show the velocity distribution of MS stars ejected from the BES with  $M > 15 M_{\odot}$ ,  $M > 7.5 M_{\odot}$  and all stars, respectively. The dashed distributions show the stars that have experienced Roche-lobe overflow or common-envelope evolution. The inset magnifies the regime of stars ejected with  $v > 30 \text{ km s}^{-1}$ .

### 6.2.7 Vela Junior (G266.2–01.2)

Vela Jr. is located about  $3^{\circ}$  east of Vela. With an age between 2.4 kyr and 5.1 kyr it is younger than Vela and its distance is between 0.5 kpc and 1.0 kpc (Allen et al., 2015).

Five stars were observed with UVES: TYC8152-120-1 is a mid-F star, where no Li was discovered. TYC8152-104-1 is a K giant, and TYC8152-1456-1 (F9.5–G1) and TYC8152-550-1 (F7–F9) show Li absorption in their spectra. However, the measured abundances indicate that they are much too old to be runaway stars associated with the Vela Jr. progenitor (see Fig. 5.8, Table 5.7). HD 76060 is the brightest star of our observed sample ( $G = 7.85 \text{ mag}$ ). Its spectral type is B8 IV-V, according to Houk (1978). From its *Gaia* DR2 parallax, we infer a distance of  $d = 0.486_{-0.010}^{+0.011} \text{ kpc}$ , which could still be consistent with the lower distance limit of Vela Jr. Its position at the time of the SN is consistent with Eqn. 3.6 and its peculiar velocity of  $31.2 \pm 2.7 \text{ km s}^{-1}$  (see Table 5.1 for further parameters) is relatively high. Its age, according to Fig. 5.6, is either 1.1–1.8 Myr (if pre-MS) or 90–350 Myr (if post-MS). Although the post-MS age, which would be too high, is more likely, the pre-MS cannot be excluded. Furthermore, with  $2\sigma$  error bars it could also be young enough if it is post-MS. Therefore, we still consider HD 76060 as a promising candidate.

PSR J0855–4644 is located at the edge of Vela Jr., but located  $\sim 44'$  from the GC. The proper motion of the pulsar is unknown, but its dispersion measure distance of 5.64 kpc (Yao et al., 2017) shows that it is in the background.

A search for DR2 candidates which trace back to a position around the GC according to Eqn. 3.6 yields twelve objects with  $G < 17$  mag, which are listed in Table 6.2.

### 6.2.8 Lupus Loop (G330.0+15.0)

The Lupus Loop on the southern hemisphere has a diameter of  $\Theta = 180'$  and an age of  $23 \pm 8$  kyr (Ferrand and Safi-Harb, 2012; Toor, 1980; Winkler et al., 1979). With a distance of  $0.33 \pm 0.18$  kpc (Betoya-Nonesa et al., 2009; Toor, 1980) it is one of the closest SNRs, but the large deviations between the literature values lead to large uncertainties in the calculation of runaway candidate trajectories.

Six candidates were found in *Gaia* DR1 TGAS, but no observations were obtained. Later, we found three very promising candidates from *Gaia* DR2, which were located close to the GC at the time of the SN and which are moving away from it with a high velocity. The closest of them had an angular distance of only  $1.1' \pm 4.4'$  and is moving to the west, while the fastest one, moving to the south, has a total proper motion of  $\sim 65$  mas yr $^{-1}$  which corresponds to a 2D projected velocity of  $\sim 62$  km s $^{-1}$  at its distance of  $\sim 0.20$  kpc.

These three candidates (see Fig. 6.4 (c)), which have  $G = 15.70$ – $16.31$  mag and spectral types between K3.5 and M2.5 according to their  $T_{\text{eff}}$  from *Gaia* DR2, are highly suggested for follow-up spectroscopic observations. One or possibly even two of them could become the first discovered late-type runaway stars associated with a SNR.

### 6.2.9 Cassiopeia A (G111.7–02.1)

We call Cassiopeia A a historical SNR due to its young age of  $334 \pm 18$  yr (Ferrand and Safi-Harb, 2012), although it is still a matter of debate if the SN was observed by the Astronomer Royal John Flamsteed on 1680 Aug 16, when he reported the sighting of a 5th to 6th magnitude star that he never observed again (Ashworth, 1980; Thorstensen et al., 2001). Fesen et al. (2006) investigated the proper motions of individual knots in the expanding shell and found an age of  $339 \pm 19$  yr, assuming some degree of deceleration by shock heating. This would be consistent with the Flamsteed sighting.

With  $d = 3.5 \pm 0.2$  kpc (Alarie et al., 2014; Reed et al., 1995), Cassiopeia A is the most distant SNR of our sample and therefore we can only observe stars down to spectral type  $\sim$ F9. Nevertheless, we searched for runaway candidates. Due to the well known age, finding a runaway star would yield a very precise localisation of the explosion site. However, no *Gaia* DR2 stars with  $G < 17$  mag were found within a radius of  $0.36'$  around the GC, which is the maximum possible angular distance a star could have travelled in the time since the SN according to Eqn. 3.3. If we add the error of the GC from Eqn. 3.6 to the search radius, we



obtain one star that is consistent with the GC, but from *Gaia* DR2  $T_{\text{eff}}$ , radius and luminosity it can be seen that it is a giant. Therefore, we can exclude runaway stars with  $G < 17$  mag associated with Cassiopeia A, consistent with the works by Kochanek (2018) and Fraser and Boubert (2019).

### 6.2.10 3C58 (SN 1181, G130.7+03.1)

3C58 is a pulsar wind nebula powered by the radio pulsar J0205+6449, which was formed during the historical SN observed in 1181 AD. Its size is  $9' \times 5'$  and its distance is  $2.6 \pm 0.6$  kpc, where the lower limit comes from Kothes (2013) and the upper limit from Wallace et al. (1994). Its age can be precisely given as 839 yr.

Since PSR J0205+6449 is firmly associated with the SNR, the trajectories of possible runaway companions are strictly constrained. No *Gaia* DR2 objects were found to be consistent with PSR J0205+6449, even down to  $G = 20$  mag and even if the error of the pulsar position in 1181 AD is extended to  $2\sigma$ .

### 6.2.11 Crab Nebula (M1, SN 1054, G184.6–05.8)

The Crab Nebula is probably the most extensively studied celestial object beyond the solar system. As 3C58, it is a PWN, powered by the Crab pulsar (J0534+2200) and originating from the SN observed in 1054 AD in Taurus. The PWN has a size of  $7' \times 5'$ , a distance of  $1.85 \pm 0.35$  kpc and an age of 966 yr. For the distance, we adopt here the range given in the review by Davidson and Fesen (1985), based on the works by *Virginia Trimble* (Trimble 1968; Trimble 1973). Note however that Fraser and Boubert (2019) recently gave a larger value of  $3.37^{+4.04}_{-0.97}$  kpc.

As for 3C58, the spatial origin of potential runaway stars is already known quite accurately from the motion of the pulsar, and similarly we can exclude runaway former companions of the Crab pulsar down to  $G = 20$  mag, which is also consistent with Kochanek (2018) and Fraser and Boubert (2019).

### 6.2.12 SN 393 (G347.3–00.5)

G347.3–00.5 is very probably the remnant of the SN that was observed 393 AD by Chinese astronomers in Scorpion (Wang et al., 1997). Since the SN happened longer ago and more nearby, with  $\Theta = 65' \times 55'$  the SNR appears much larger on the sky than the other historical SNRs. For the distance, we adopt  $1.3 \pm 0.4$  kpc given by Cassam-Chenaï et al. (2004), consistent with 1 kpc listed in the UofM catalogue. Assuming that the association to SN 393 is correct, the age is 1627 yr.

G347.3–00.5 contains the central compact object 1WGA J1713.4–3949, but the association is not clear and no proper motion is given for the object. Therefore, we searched for runaway candidates around the GC according to Eqn. 3.6 and found 18 promising objects with  $13.47 \text{ mag} < G < 16.98 \text{ mag}$  and spectral types between G8 and M3.5. We suggest to take high-resolution spectra to search for the Li 6708 Å line.

## 6.3 Constraints on runaway star production

Here, we want to give an estimate on how the findings of this work fit model populations of runaway stars in the literature (Boubert et al., 2017; Renzo et al., 2019). We investigated twelve SNRs and can exclude runaway stars with  $G < 17 \text{ mag}$  in three of them. For SNR S147, we can confirm HD 37424 with *Gaia* DR2 data. Based on this association, we find no further runaway stars within S147. In each of the remaining eight SNRs, we find one or more candidates, but none of those can be confirmed yet.

So the minimum number of BES runaway stars within the twelve investigated SNRs is one, while the maximum number is nine, corresponding to a fraction of ejected runaway stars per SNR of 8–75 %. The upper limit could be even higher if we also count the cases where more than one runaway star could have been ejected. In three of the investigated SNRs (Cygnus Loop, Vela Jr., Lupus Loop), two of the remaining candidates could have a common origin. Although many more error ellipses of the runaway star candidates are overlapping, it was considered that for a certain age of the SNR the error regimes would shrink correspondingly.

This compares to theoretical values for runaway stars ejected from core-collapse SNe between 32.5 % (Boubert et al., 2017) and 68 % (Renzo et al., 2019). The latter value comes from  $78_{-22}^{+9}$  % of binary systems that do not merge before the first SN, multiplied by  $86_{-22}^{+10}$  % that get disrupted during the SN, which gives  $67_{-26}^{+17}$  % of high-mass binary systems that eject a runaway star. Boubert et al. (2017) state that  $\sim 1.22$  core-collapse SNe happen in each high-mass binary system, so we get  $55_{-21}^{+13}$  % of core-collapse SNe that eject a runaway star.

Both values are consistent with our findings. We need follow-up observations of our best candidates to search for SN debris as well as more precise estimates for the ages, distances and explosion sites of the SNRs to further constrain the numbers of ejected runaway stars in SNRs. From the theoretical values, we expect to verify three to seven of our runaway star candidates within the eleven SNRs besides S147 in the future.

Note that the average peculiar velocity of our ten observed runaway star candidates in HB9, Monoceros Loop and Vela Jr. is  $\overline{v_{\text{pec}}} = 20 \pm 9 \text{ km s}^{-1}$ , which is significantly higher than  $\sim 6 \text{ km s}^{-1}$ , the peak of the velocity distribution found by Renzo et al. (2019). Including HD 37424, for which we calculated  $v_{\text{pec}} = 102 \pm 10 \text{ km s}^{-1}$ , would further increase the average

velocity. Since we did not apply any selection criteria regarding the velocities of the stars, and since most of our candidates will turn out not to be BES-ejected runaway stars, this might indicate that the BES runaway star velocities simulated by Renzo et al. (2019) are underestimated. However, we need a much higher number of peculiar velocities as well as clear identifications of runaway stars in order to attain to a sound conclusion.

### 6.3. Constraints on runaway star production

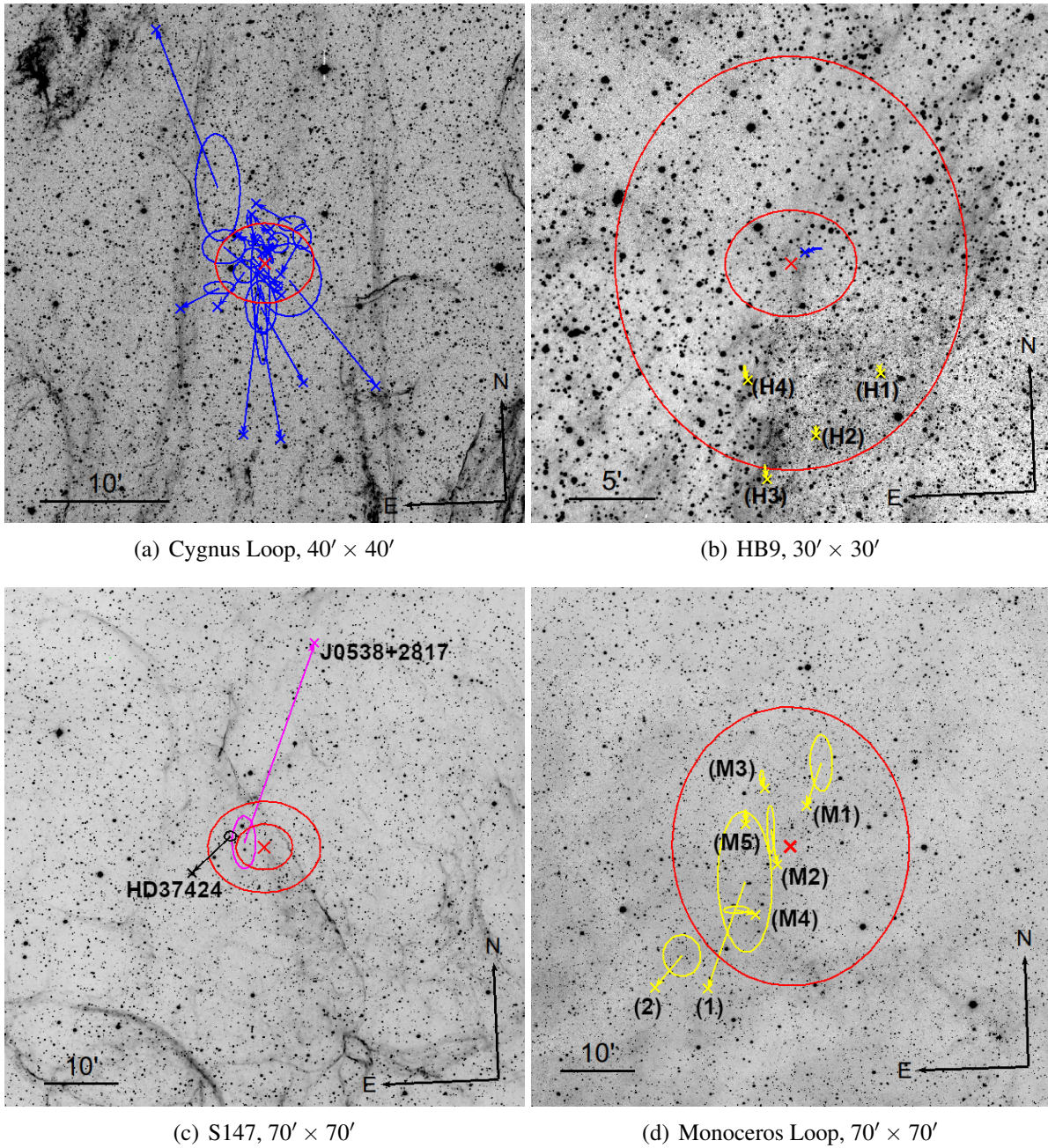


FIGURE 6.3: The runaway star candidates in the investigated SNRs. As shown for Vela in Fig. 6.1, the GC and its error ellipse are shown in red. For cases where both selection steps were relevant for the corresponding SNR, the outer ellipse corresponds to the error for the DR1-selection and the inner ellipse to the DR2-selection (Eqn. 3.6). An exception is S147, where the outer ellipse represents the  $2\sigma$ -range according to Eqn. 3.6. Observed runaway candidates are shown in yellow and labeled at their current position as in Table 5.5, runaway candidates identified in *Gaia* DR2 are shown in blue, runaway candidates identified by other authors are shown in black and associated NSs are shown in magenta. The background images were observed in  $H\alpha$  with the STK (Mugrauer and Berthold, 2010) at the University Observatory Jena.

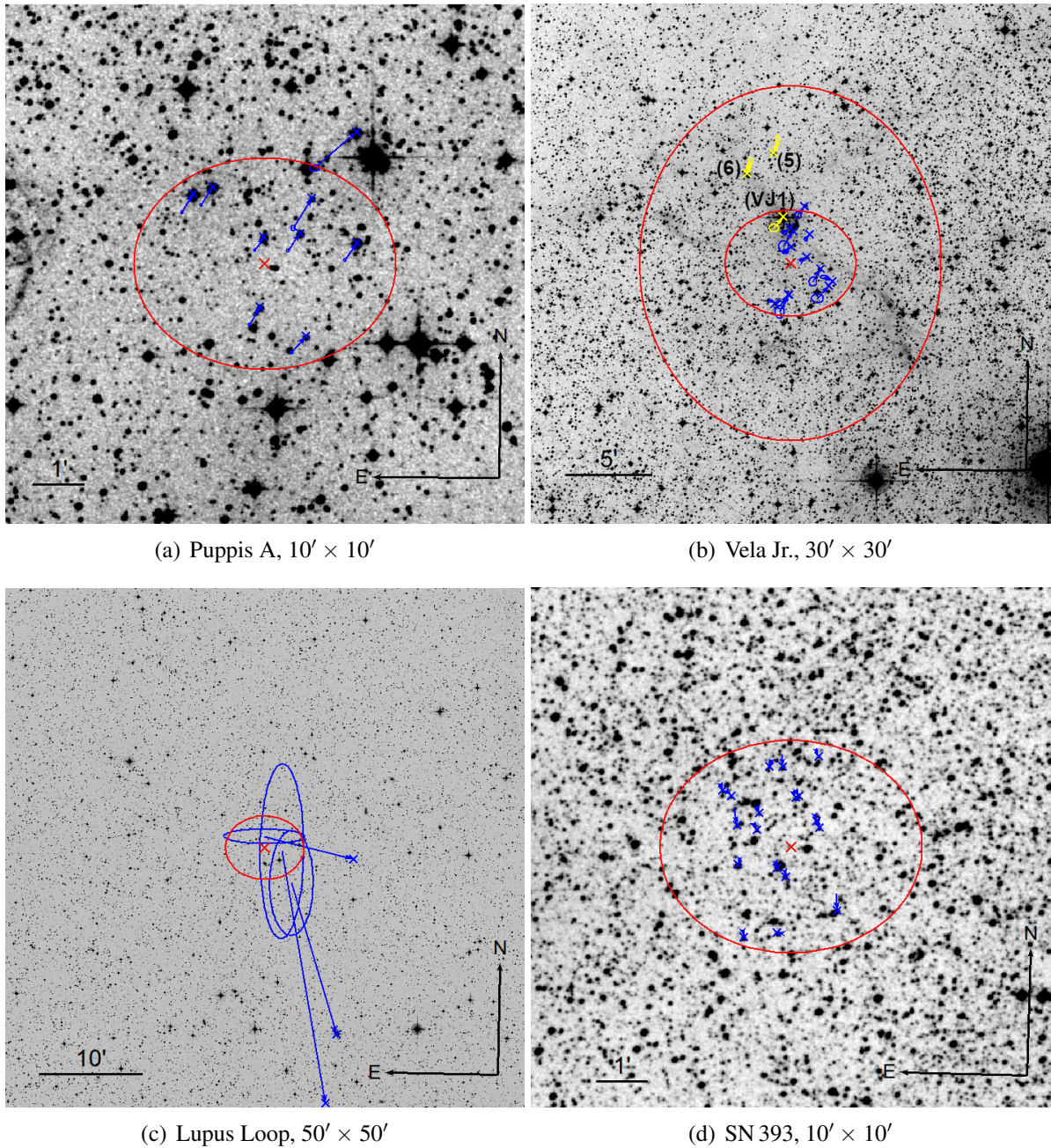


FIGURE 6.4: The runaway star candidates in the investigated SNRs. As shown for Vela in Fig. 6.1, the GC and its error ellipse are shown in red. For cases where both selection steps were relevant for the corresponding SNR, the outer ellipse corresponds to the error for the DR1-selection and the inner ellipse to the DR2-selection (Eqn. 3.6). observed runaway candidates are shown in yellow and labeled as in Table 5.5, runaway candidates identified in *Gaia* DR2 are shown in blue. The background images for (a), (b) and (d) are taken from ESO DSS-2-red, the one for (c) from ESO DSS-1 due to a better image quality. The SNRs Cassiopeia A, 3C58 and Crab nebula, where no candidates were found, are not shown here.



# Chapter 7

## Conclusions

### 7.1 Summary

As the main result of our search for runaway stars in twelve Galactic SNRs, we present a list of 74 promising candidate stars, including HD 37424 in SNR S147, which was discovered to be the former companion of the S147 progenitor by Dinçel et al. (2015) and now confirmed with *Gaia* DR2 data. The other 73 candidates are suggested for spectroscopic follow-up observations. Ten of these stars were already observed with UVES/VLT and Subaru/HDS. For these we suggest to take spectra with high  $S/N$  and high resolution in order to search for SN debris in the stellar atmospheres. For the remaining candidates, found in *Gaia* DR2, we first need to estimate the ages. Most of them have spectral type K, so the Li 6708 Å absorption line will be a useful age indicator for them.

We started the project with data from *Gaia* DR1 TGAS (before DR2 became available) and selected stars that were located close to the SNR GC at the time of the SN, with an error ellipse drawn from the scaled standard deviation of the Vela GC (see Fig. 3.2). For this selection, we used 23 SNRs, located at distances of up to 1.6 kpc. We then obtained spectra of 39 stars in six SNRs with VLT/UVES (33 stars in five SNRs) and HDS/Subaru (six stars in HB9). After *Gaia* DR2 became available, eleven of these were excluded because they were found to be giants (see Figs. 3.4, 3.5 and Table 3.3) and 18 were found to be too old or spatially inconsistent with the SNR or the NS (according to DR2 parallax distance or the position at the time of the SN). We found a significant amount of lithium in ten of the stars observed with UVES and one of the stars observed with HDS, but all of them were ruled out. Five of them are post-MS giants, while the other six, for which we present the spectral analysis in Section 5, were ruled out for the following reasons: (i) The two Li stars in Monoceros were found to be too close, (ii) the two Li stars in Vela were found to be spatially inconsistent with the position of the Vela pulsar at the time of the SN and (iii) the two Li stars in Vela Jr. were found to be too old to be associated

runaway stars. Their Li abundances indicate ages of more than 32 Myr, which we consider as the maximum age of a SN progenitor (Ekström et al., 2012) and therefore also as the maximum age of a runaway star in a SNR.

Nevertheless, we also determined radial velocities and atmospheric parameters of the Li-rich stars and made some interesting discoveries. (i) TYC159-251-1 (Monoceros Loop) was discovered by us to be a double-lined spectroscopic binary. We disentangled the spectrum and found that the primary has spectral type F6–F7 and the secondary F9–G0. Their brightness difference of  $\sim 0.76$  mag is moderate, but the secondary shows stronger Li absorption because the primary lies in the Li depletion gap (e.g. Steinhauer and Deliyannis 2004). (ii) TYC159-343-1 (Monoceros Loop) might be a young star. We obtained 90–625 Myr from Fig 5.8, but its Li signal is hard to interpret due to the early spectral type ( $F3 \pm 1$ ) (D’Antona and Mazzitelli, 1984), and its low metallicity of  $[M/H] = -0.57 \pm 0.08$  (Lambert and Reddy, 2004). Even 2.1–3.8 Myr, the pre-MS solution from Fig. 5.6, is possible. (iii) TYC8150-3105-1 (Vela) shows the strongest Li absorption among all observed stars ( $EW_{\text{Li}} = 177 \pm 7 \text{ m\AA}$ ), so it was found to be younger than  $\sim 50$  Myr. It could be a member of the same OB association from which the SNR formed.

Among the observed stars, there were also seven stars of spectral types F and G that did not show Li absorption, hence they are too old, and 15 stars of spectral types B and A. Among the latter, five were excluded due to spatial inconsistency with the geometric centre of the Monoceros Loop, where they are all located. We were left with ten stars of spectral types B and A, four in HB9, five in Monoceros and one in Vela Jr., that could not be excluded. Since Li cannot be used as an age indicator for them, their ages were only roughly constrained from the HRD (see Table 5.6). The B-type star HD 261393, already suggested by Boubert et al. (2017), is the most likely candidate in the Monoceros Loop. We suggest to take a spectrum with high resolution and high  $S/N$  in order to search for SN debris in its atmosphere.

After *Gaia* DR2 became available, we extended our search and found 63 additional runaway candidates which were not yet observed. However, the creation of feasible observing projects was a main goal and therefore, the selection criteria were adjusted as follows: (i) The maximum SNR distance was reduced from 1.6 kpc to 0.5 kpc, within the errors. Exceptions were only made for SNRs where targets from DR1 were already observed, and for the historical SNRs. (ii) The error ellipses around the SNR GCs, where the targets had to be located at the time of the SN, were reduced to the range defined by Eqn. 3.6. (iii) The magnitude was limited to  $G \leq 17$  mag. (iv) Trajectories of associated NSs were considered, namely for Vela, 3C58 and the Crab nebula. In Vela, we point out two stars which are consistent with the motion of the Vela PSR. The star marked in blue in Fig. 6.1 is suggested for observations, while *Star A* (Fraser and Boubert, 2019) is too faint to be investigated spectroscopically.

TYC2688-2556-1, suggested by Boubert et al. (2017) as the ejected former companion of



the Cygnus Loop progenitor, was excluded by us. *Gaia* DR2 data show that it is probably too nearby, if the adopted distance to the Cygnus Loop (576–1000 pc) is not strongly overestimated.

Note that we might miss some stars with  $G > 17$  mag which would mainly be spectral type M. Due to missing observations of such late-type stars around high-mass primaries, we do not know how many M-type runaway stars we could expect. Furthermore, we might miss some *Gaia* DR2 candidates due the reduced allowed angular distance to the GC at the time of the SN, especially if there is a significant offset between the GC and the actual explosion site.

The complete list of 74 promising runaway candidates is presented in Table 6.2, with further details listed in the appendix, Tables F.5–F.8. Among the twelve investigated SNRs, nine SNe could have ejected a runaway star, while only HD 37424 in S147 is confirmed. Three of these SNe could possibly have ejected two runaway stars.

Although these numbers are yet very imprecise due to the lack of clear identifications, they fit to model expectations (Boubert et al., 2017; Renzo et al., 2019, see Section 6.3). According to these, we expect to verify three to seven of our runaway candidates in the future. Extending this estimate to the 294 known SNRs in the Galaxy, among which  $\sim 83\%$  should originate from core-collapse SNe (Mannucci et al., 2005), we expect a total number of 83–166 BES-ejected runaway stars.

Our method showed that we can constrain the ages of individual stars by combining HRD isochrone placement and the Li test. Although all of our Li-rich targets were rejected, the detection of a sufficient amount of Li in one of the candidate stars identified with *Gaia* DR2 would be a strong indication, especially since most of these have late spectral types and are therefore older on average.

## 7.2 Future prospects

Our analysis of runaway candidates selected from *Gaia* DR1 showed that rough age estimates can help to constrain the sample of possible runaway stars. As the next step for this project, spectroscopic observations are required for the runaway candidates identified in *Gaia* DR2, in order to determine atmospheric parameters and search for the Li 6708 Å absorption line. Many of these candidates have spectral type K, where the Li 6708 Å line is a useful age indicator. High priority should be given to the three promising candidates in the Lupus Loop, which show a high transverse velocity, directing away from the GC.

In order to finally proof a BES origin, we need to observe the best candidates with very high resolution and  $S/N$  to be able to detect SN debris, e.g. heavy- and  $\alpha$ -elements, in the stellar atmospheres. This applies to the B- and A-type candidates in Table 6.2, e.g. HD 261393

and also HD 37424.

Our project will soon be updated with the new data from *Gaia* EDR3, providing more precise positions, proper motions, parallaxes and photometric data. The final *Gaia* data release (DR3), which will be provided in 2022, will also contain RVs and effective temperatures of a large number of sources. These data will allow to consider a larger number of candidates and yield more precise constraints.

We also emphasise that it is important to exactly know the explosion site. The case of HD 37424 in SNR S147 is rather exceptional because both, the pulsar and the runaway star, trace back to the Green centre and meet it within just a few arcminutes. We did not find other cases where a pair of a pulsar and a runaway candidate was located so close to the GC. In general, the explosion site will not coincide with the GC, due to the motion of the LSR and due to asymmetries of the SNR expansion (e.g. Meyer et al. 2015; Meyer et al. 2020). A careful analysis of the time-dependent SNR morphology is needed to locate the explosion site.

In Appendix H we present a new approach to determine SNR light centres from the  $H\alpha$  observations that we performed at the University Observatory Jena. In the future, this method could be applied to SNR images in different wavelengths. Averaging the results for different wavelengths could then yield the best model-independent estimate for the SN explosion site.

A much higher number of runaway stars ejected from the BES (and the DES) can potentially be found outside of SNRs. Here, *Gaia* EDR3 provides valuable data to trace back the trajectories of runaway candidates and NSs, but also the motion of the stellar associations and clusters in which they were born. Although the identification of a runaway star is almost always a probabilistic approach (except SN debris can be found in the atmosphere), the full set of *Gaia* data will be an excellent tool to divide between chance projections, close but unrelated flybys and actual, physical encounters or common origins.

Finally, the next generation of ground-based telescopes, e.g. the ESO *Extremely Large Telescope* (ELT), will set the ground for spectroscopic observations of much fainter stars, so that it will be possible to observe stars at higher distances and to obtain spectra of better quality. Eventually, this will increase the number of clear runaway star associations and we will obtain the desired insights into the evolution of massive binary systems, SNR expansion and statistical considerations of runaway- and hypervelocity stars from different production channels.

# Appendix A

## *Python* code for the calculation of trajectories

Here, we present the *Python* code that was used to find the *Gaia* stars located within the error range of the GC at the time of the SN. The code requires the catalogue obtained from the cone search for *Gaia* stars (Eqn. 3.3) as input file and creates a *.txt* file listing the candidate stars and the relevant kinematic and photometric properties. Most importantly, it calculates the position at the time of the SN, which is compared to the errors of the GC. Note that the output requires two further, manual selection steps: (i) The routine yields stars contained in a search box (not an ellipse) around the GC, where the edge lengths correspond to twice the values given by Eqn. 3.6 for right ascension and declination. Stars contained in the box, but not in the ellipse, were removed, except they showed a promising proper motion, i.e. directing away from the GC with a high velocity. (ii) Giants could not be identified by the routine and were removed later as described in Section 3.3. The code given below is an example and contains the data of SNR G330.0+15.0 (Lupus Loop). Age, distance and GC error of the SNR have to be defined manually in the code, whereas the GC coordinates are read from the input file. For the Lupus Loop, the code yields six candidates, where two were found to lie outside of the GC error ellipse and one is a giant.

```

import re
import sys
import StringIO
import numpy as np
from numpy import square, sqrt, cos, sin, pi
from math import log10
output=StringIO.StringIO()

SNR=str(raw_input("SNR: "))

def calcrho():

    #open input catalogue from Gaia cone search in VizieR:
    coords = open(SNR+"_Gaiacone_dr2.tsv").readlines()

    #load main data as numpy array:
    data = np.loadtxt(SNR+"_Gaiacone_dr2.tsv", skiprows = 110, usecols =
        ↪ (0,1,2,3,4,5,6,7,8,9,10,11,12,13,14,15,16))

    #define and print coordinates and error of the Geometric center:
    d_Vela = 255 #diameter of Vela SNR in [arcmin], for GC error calculation for DR1 selection
    d_SNR = 180 #diameter of SNR in [arcmin], for GC error calculation for DR1 selection
    ra_GC = float(coords[0]) #[deg], from input cat.
    dec_GC = float(coords[1]) #[deg], from input cat.
    #ra_GC_err = 0.3076 * d_SNR/d_Vela #for DR1: Vela GC RA err, scaled by size of SNR
    #dec_GC_err = 0.3622 * d_SNR/d_Vela #for DR1: Vela GC DEC err, scaled by size of SNR
    ra_GC_err = 0.063 #[deg]
    dec_GC_err = 0.051 #[deg]
    print "# Geometric center (ra, dec, ra_err, dec_err / deg):", ra_GC, dec_GC, ra_GC_err,
        ↪ dec_GC_err

    #print header for output file:
    print "# d_GC(deg) ra(deg) dec(deg) pmra(mas/yr) pmdec(mas/yr) plx(mas) ra_SN(deg)
        ↪ dec_SN(deg) rho_ra(deg) rho_dec(deg) rho_tot(deg) ra_err(mas) dec_err(mas)
        ↪ pmra_err(mas/yr) pmdec_err(mas/yr) plx_err(mas) ra_SN_err(deg) dec_SN_err(deg)
        ↪ rho_ra_err(deg) rho_dec_err(deg) rho_tot_err(deg) rho_tot_min(deg) rho_tot_max(
        ↪ deg) plx_min(mas) plx_max(mas) d(kpc) d_min(kpc) d_max(kpc) ra_SN_min(deg)
        ↪ ra_SN_max(deg) dec_SN_min(deg) dec_SN_max(deg) ra_SN_min_2(deg)

```

```

↪ ra_SN_max_2(deg) dec_SN_min_2(deg) dec_SN_max_2(deg) g_mag(mag)"

#input SNR data from Green and Umanitoba:
age = 23000 #[yr]
age_err = 8000 #[yr]
dist = 0.325 #[kpc]
dist_err = 0.175 #[kpc]

#Scan through input catalogue:
a = 0
b = len(data)-1
i = a

while a<=i<=b:

    #read basic data of the stars inside the cone:
    ra = data[i][2] #[deg]
    dec = data[i][4] #[deg]
    pmra = data[i][9] #[mas/yr]
    pmdec = data[i][11] #[mas/yr]
    plx = data[i][7] #[mas]

    ra_err = data[i][3] #[deg]
    dec_err = data[i][5] #[deg]
    pmra_err = data[i][10] #[mas/yr]
    pmdec_err = data[i][12] #[mas/yr]
    plx_err = data[i][8] #[mas]

    g_mag = data[i][16] #[mag]

    #Calculate the distance to the SNR GC at the time of the SN (rho) and further
    ↪ astrometric data and errors in [deg].
    d_GC = sqrt( pow((ra-ra_GC)*cos((dec+dec_GC)*(pi/180)/2),2) + pow((dec-
    ↪ dec_GC),2) ) #current dist. to the GC
    ra_SN = ra-(pmra/(1000*3600))*age #RA at time of SN
    dec_SN = dec-(pmdec/(1000*3600))*age #DEC at time of SN
    rho_ra = ra-(pmra/(1000*3600))*age-ra_GC #RA dist. to the GC at time of SN
    rho_dec = dec-(pmdec/(1000*3600))*age-dec_GC #DEC dist. to the GC at time of
    ↪ SN

```

```

rho_tot = sqrt( pow((ra_SN-ra_GC) * cos((dec_SN+dec_GC)/2*(pi/180)),2) + pow
↳ ((dec_GC-dec_SN),2) ) #dist. to the GC at time of SN
ra_SN_err = sqrt(pow(ra_err/(1000*3600),2) + pow(age*pmra_err/(1000*3600),2)
↳ + pow(pmra/(1000*3600)*age_err,2))
dec_SN_err = sqrt(pow(dec_err/(1000*3600),2) + pow(age*pmdec_err/(1000*3600)
↳ ,2) + pow(pmdec/(1000*3600)*age_err,2))
rho_ra_err = sqrt(pow(ra_err/(1000*3600),2) + pow(age*pmra_err/(1000*3600),2)
↳ + pow(pmra/(1000*3600)*age_err,2) + ra_GC_err*ra_GC_err)
rho_dec_err = sqrt(pow(dec_err/(1000*3600),2) + pow(age*pmdec_err
↳ /(1000*3600),2) + pow(pmdec/(1000*3600)*age_err,2) + dec_GC_err*
↳ dec_GC_err)
rho_tot_err1 = (pow(ra_SN_err,2)+pow(ra_GC_err,2)) * 4*pow(ra_SN-ra_GC,2) *
↳ pow(cos((dec_SN+dec_GC)/2*(pi/180)),4)
rho_tot_err2 = (pow(dec_SN_err,2)+pow(dec_GC_err,2)) * (8*pow(dec_SN-
↳ dec_GC,2) + 2*pow(ra_SN-ra_GC,4) * pow(sin((dec_SN+dec_GC)/2*(pi
↳ /180)),2) * pow(cos((dec_SN+dec_GC)/2*(pi/180)),2))
rho_tot_err3 = 4*(pow(ra_SN-ra_GC,2) * pow(cos((dec_SN+dec_GC)/2*(pi/180))
↳ ,2) + pow(dec_SN-dec_GC,2) )
rho_tot_err = sqrt((rho_tot_err1 + rho_tot_err2) / rho_tot_err3)
rho_tot_min = rho_tot - rho_tot_err
rho_tot_max = rho_tot + rho_tot_err
plx_min = plx - plx_err #[mas]
plx_max = plx + plx_err #[mas]
d = 1 / plx #[kpc]
d_min = 1 / plx_max #[kpc]
d_max = 1 / plx_min #[kpc]
ra_SN_min = ra_SN - ra_SN_err
ra_SN_max = ra_SN + ra_SN_err
dec_SN_min = dec_SN - dec_SN_err
dec_SN_max = dec_SN + dec_SN_err

#check if runaway candidate criteria are fulfilled (position and distance consistent
↳ with SNR; magnitude limit):
if ra_SN_min <= ra_GC+ra_GC_err and ra_SN_max >= ra_GC-ra_GC_err and
↳ dec_SN_min <= dec_GC+dec_GC_err and dec_SN_max >= dec_GC-
↳ dec_GC_err and d_min <= dist+dist_err and d_max >= dist-dist_err and
↳ g_mag <= 17.0:

#print candidate data for output file:

```

```

print i+1, d_GC, ra, dec, pmra, pmdec, plx, ra_SN, dec_SN, rho_ra,
    ↪ rho_dec, rho_tot, ra_err, dec_err, pmra_err, pmdec_err, plx_err,
    ↪ ra_SN_err, dec_SN_err, rho_ra_err, rho_dec_err, rho_tot_err,
    ↪ rho_tot_min, rho_tot_max, plx_min, plx_max, d, d_min, d_max,
    ↪ ra_SN_min, ra_SN_max, dec_SN_min, dec_SN_max, g_mag

    i+=1

#save the results:
save_stdout = sys.stdout
fh = open(SNR+"_Gaiacheck_dr2.txt","w")
sys.stdout = fh
print >> output, calcrho()
sys.stdout = save_stdout

#directly print a gnuplot script from the results:
def printscript():
    coords = open(SNR+"_Gaiacone_dr2.tsv").readlines()
    ra_GC = float(coords[0])
    dec_GC = float(coords[1])
    clist = np.loadtxt(SNR+"_Gaiacheck_dr2.txt", skiprows=2)
    print "reset"
    print "set title 'Runaway candidates for "+SNR+"'"
    print "set xra[227.7:227.25]"
    print "set yra[-40.45:-39.75]"
    print "set xla 'RA / deg'"
    print "set yla 'DEC / deg'"
    print "unset key"
    print "set zeroaxis"
    print "set parametric"
    print "ra =", ra_GC
    print "dec =", dec_GC
    print "ra_err = 0.063"
    print "dec_err = 0.051"
    print "fra(t) = ra + ra_err * cos(t)"
    print "fdec(t) = dec + dec_err * sin(t)"
    for i in range(0,len(clist)):
        print "set arrow from",clist[i][7],",",clist[i][8],"to",clist[i][2],",",clist[i][3]
    for i in range(0,len(clist)):
        print "ra"+str(i+1), "=",clist[i][7]

```

```

print "dec"+str(i+1),"=",clist[i][8]
print "ra_err"+str(i+1),"=",clist[i][17]
print "dec_err"+str(i+1),"=",clist[i][18]
print "fra"+str(i+1)+"(t) = ra"+str(i+1)," + ra_err"+str(i+1)," * cos(t)"
print "fdec"+str(i+1)+"(t) = dec"+str(i+1)," + dec_err"+str(i+1)," * sin(t)"
print "set term png font 'Verdana,14'"
print "set out '"+SNR+"_test.png'"
print "plot '"+SNR+"_Gaiacheck_dr2.txt' u 3:4 title 'Position now' lc rgb 'blue' ps 1, '"+
    ↪ SNR+"_Gaiacheck_dr2.txt' u 8:9 title 'Position at SN' lc rgb 'purple' ps 1, './'
    ↪ SNR_coords.txt' u 1:2 title 'GC' lc rgb 'red' ps 2, fra(t) lc rgb 'red', fdec(t) lc rgb '
    ↪ red',",
for i in range(0,len(clist)):
    print "fra"+str(i+1)+"(t) lc rgb 'purple',", "fdec"+str(i+1)+"(t) lc rgb 'purple',",
print "\n", "set term wxt"
print "repl"

#save gnuplot script:
save_stdout = sys.stdout
fh = open(SNR+"_script_dr2","w")
sys.stdout = fh
print >> output, printscript()
sys.stdout = save_stdout

```



# Appendix B

## Data reduction

Here, we provide further information about the data reduction. We start with HDS/Subaru, where the reduction was done manually with *IRAF*. Then, for UVES/VLT we display the *Kepler* workflow which is contained in the ESO *Reflex* pipeline. We describe the most important workflow actors and present check images which were used to monitor the success of the automatic data reduction.

### B.1 HDS/Subaru

In the following, we will guide the reader through spectroscopic data reduction with the example of the star TYC3344-124-1, observed with HDS/Subaru. We will show the raw science image and the calibration images, as well as the effects of the calibration steps. The data reduction was done with standard *IRAF* tasks, where for some individual steps we used routines written by NAOJ staff, obtained from the HDS/Subaru webpage<sup>1</sup>. We followed the procedure described in Aoki and Helminiak (2014), to which we refer the reader for further details. Firstly, in Fig. B.1 we show the spectral format for our setup, i.e. which orders with which wavelengths are covered by the two CCDs. The total wavelength range is 5062–7890 Å, where for small wavelengths the orders overlap, while for the largest wavelengths the orders are cropped, so gaps will appear in the merged spectrum. However, these gaps do not occur in wavelength regimes which are relevant for our analysis.

### Overscan correction

Each of the two HDS detectors contains two readout ports in the middle, so the HDS images have an overscan region which yields the bias level for each individual frame. The position is

---

<sup>1</sup><https://www.subarutelescope.org/Observing/Instruments/HDS/>

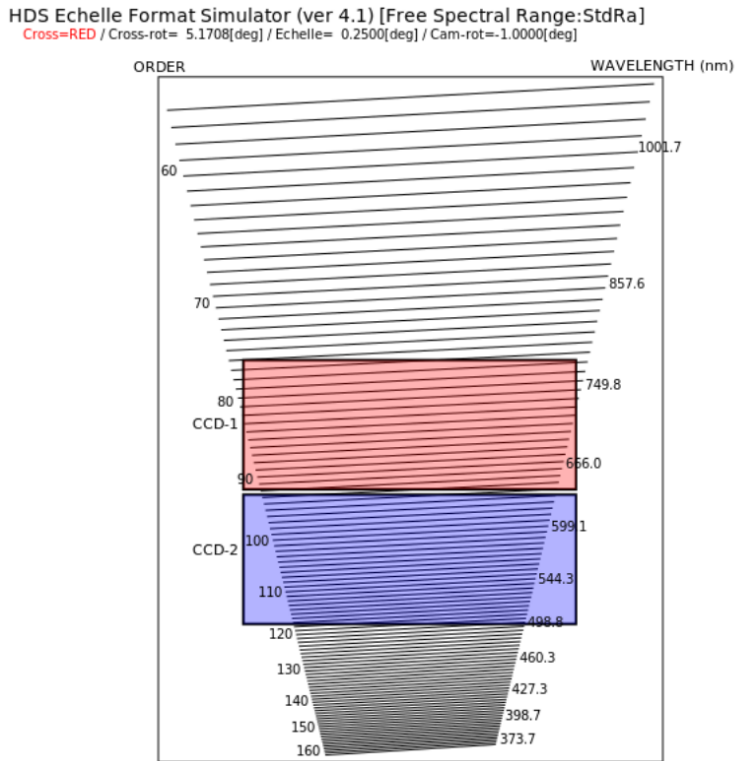


FIGURE B.1: Spectral format for our setup at HDS/Subaru. Image obtained from the HDS echelle format simulator<sup>2</sup>.

TABLE B.1: Gain of HDS/Subaru CCDs. Data taken from Aoki and Helminiak (2014).

Unit of output	Gain [ $e^-$ /ADU]
CCD1, left (long wavelength)	1.628
CCD1, right (short wavelength)	1.615
CCD2, left (long wavelength)	1.782
CCD2, right (short wavelength)	1.665

illustrated in Fig. B.2. Note that we used  $2 \times 2$  binning, i.e. the effective detector size in our case is  $1024 \times 2050$  pixel and the size of the overscan-region is  $(2 \times 50) \times 2050$  pixel. All images that we show in the following are already overscan-corrected, i.e. the average counts in the overscan-region are subtracted from the image, the image is corrected for the different gains of the detector parts (see Table B.1) and the region is cropped from the image. The correction was done with the NAOJ script *overscan.cl*.

## Bias subtraction

Five bias frames were recorded for each CCD. In Fig. B.3, we show example bias frames of the red (left) and the blue (right) detector. One sees that the detectors have bad columns, especially

<sup>2</sup>[https://www.naoj.org/cgi-bin/hds\\_efs.cgi](https://www.naoj.org/cgi-bin/hds_efs.cgi)

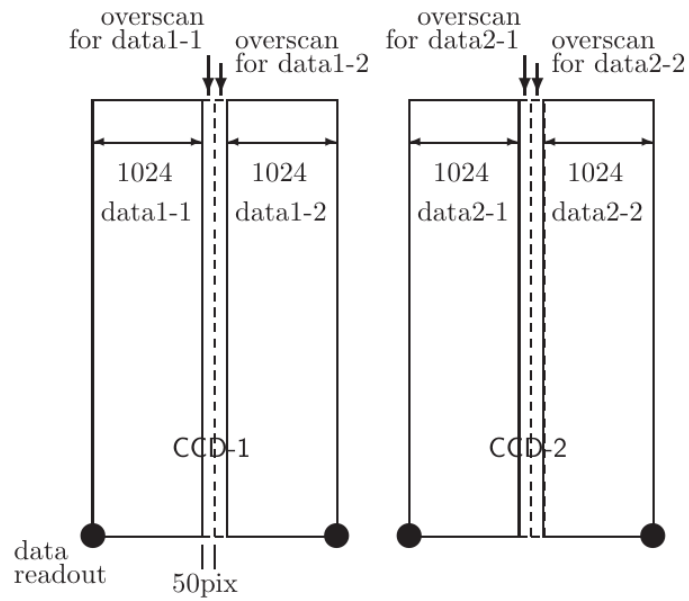


FIGURE B.2: The HDS/Subaru CCDs and their indicated Overscan regions. The orientation of the image is rotated by  $90^\circ$  counter-clockwise compared to Fig. B.1. Image taken from Aoki and Helminiak (2014).

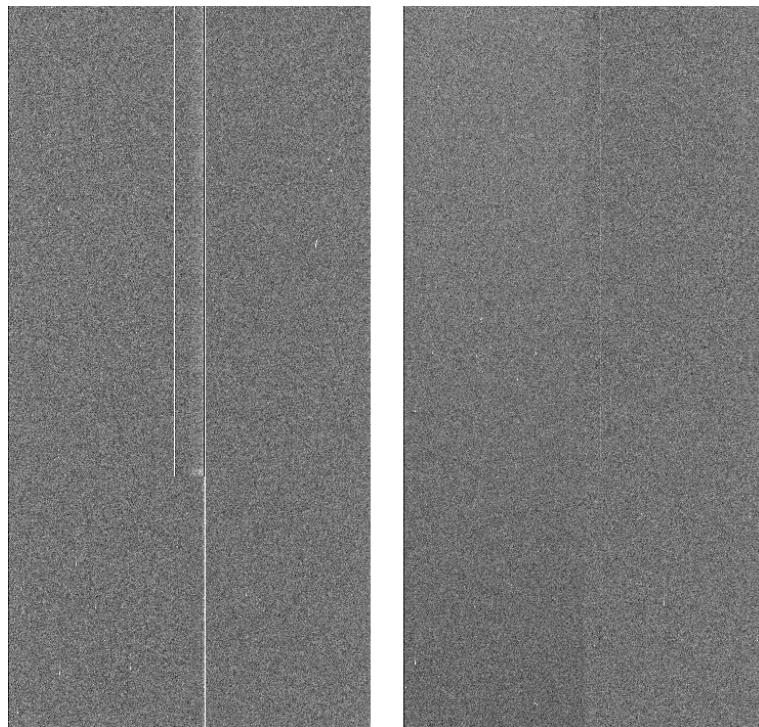


FIGURE B.3: Overscan-corrected bias images for HDS/Subaru. The red detector is on the left and the blue one on the right.

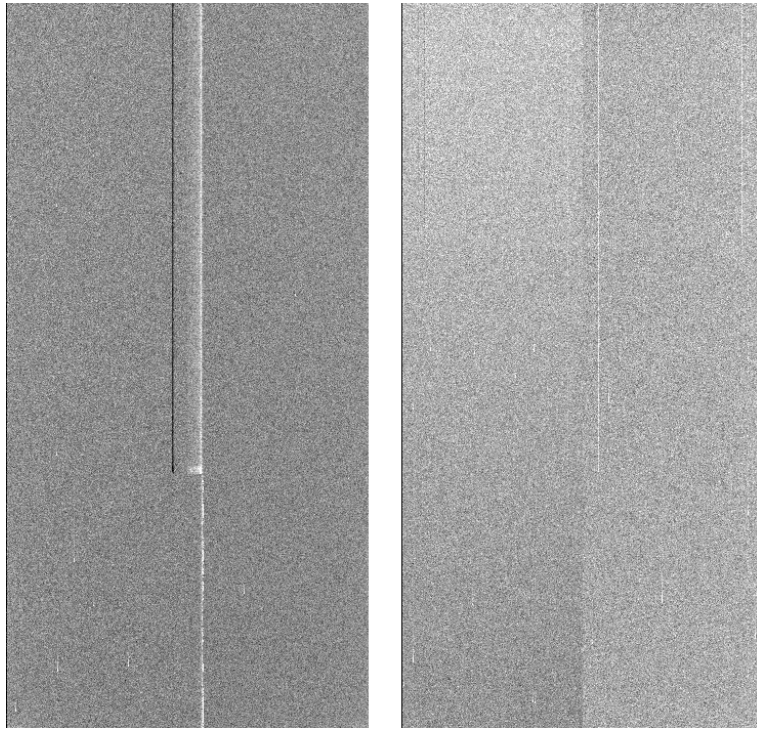


FIGURE B.4: Master bias images for HDS/Subaru. The red detector is on the left and the blue one on the right.

in the red. Bad-pixel masks were created to account for this problem. The overscan-corrected bias images were median-averaged to obtain the master bias for each detector, whereupon the master biases were corrected with the bad-pixel mask (see Fig. B.4). It can be seen that the bad-pixel mask did not work perfectly, so there are still artefacts from the bad columns. However, the flux differences and therefore the effects on the spectra are strongly reduced now.

A subtraction of the master biases from the flatfields, science frames etc. in the subsequent steps was not necessary because the overscan correction, which was performed for each image, already contains a bias subtraction. Corrections for non-linearity and cosmic rays were not done for the science frames because the count-level was relatively low for all targets ( $\lesssim 12,000 e^-$ ) and the pollution with cosmic rays was moderate. However, linearity-correction was done for the flatfields, which have a much higher flux on average.

## Order extraction

A first order extraction was done with a relatively bright target; here we used TYC3344-771-1. The order extraction is needed to define the pixel positions of the spectral orders along the two detector axes. In a first step, the number of orders is identified by scanning horizontally through the image, i.e. in slit direction. In a second step, for each order the positions of the maximum flux are fitted along the dispersion axis (vertical). So the 2D spectra are transformed into 1D

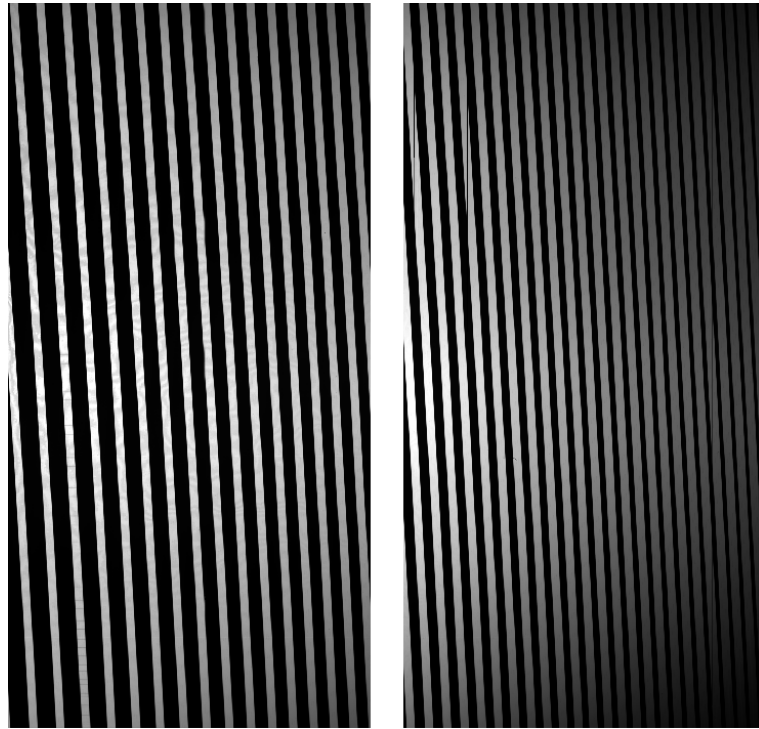


FIGURE B.5: Master flatfields for HDS/Subaru. The red detector is on the left and the blue one on the right.

spectra, where the flux is given depending on the pixel coordinate in dispersion direction for each order. The solution was saved in a file which was later used for the extraction of the flat- and science frames.

## Flatfielding

Flatfielding is necessary to account for the different sensitivities of the CCD pixels. Eleven flatfields were recorded for each CCD. After overscan-correction, masking and linearity-correction (with the NAOJ script *hdslinear.cl*), we median-combined the flatfields, which gave the master-flats shown in Fig. B.5. Then the flatfields were corrected for scattered light in the background and normalised to 1, so that the flatfield correction did not change the general flux level of the science frames. The normalisation was also done for the inter-order regions, as can be seen from the grey areas in Fig. B.6.

The next step was to apply overscan-correction, masking and background-subtraction to the science frames. This is the status shown for the example TYC3344-124-1 in Fig. B.7. After that, the frames were divided by the normalised master flats and extracted to a 1D-spectrum with the reference file created before.

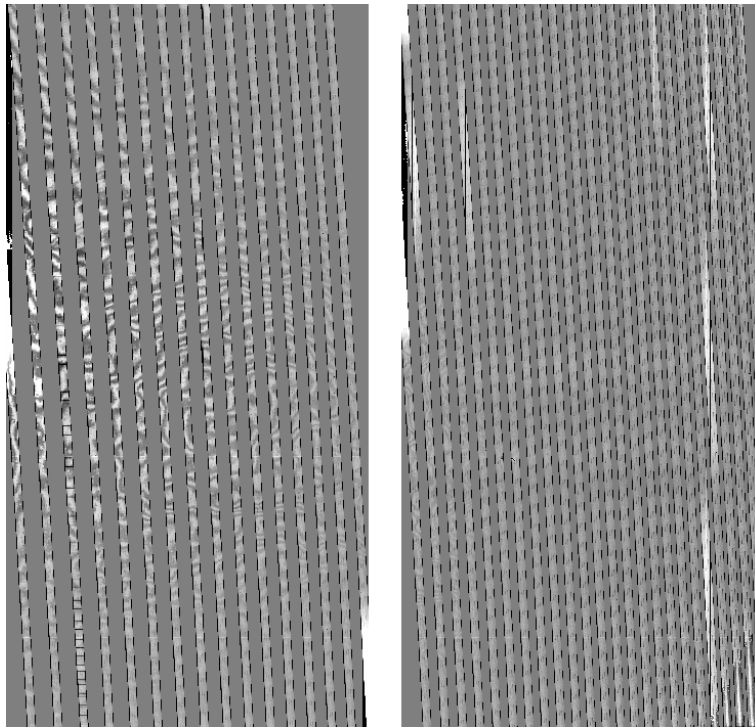


FIGURE B.6: Normalised master flatfields for HDS/Subaru. The red detector is on the left and the blue one on the right.

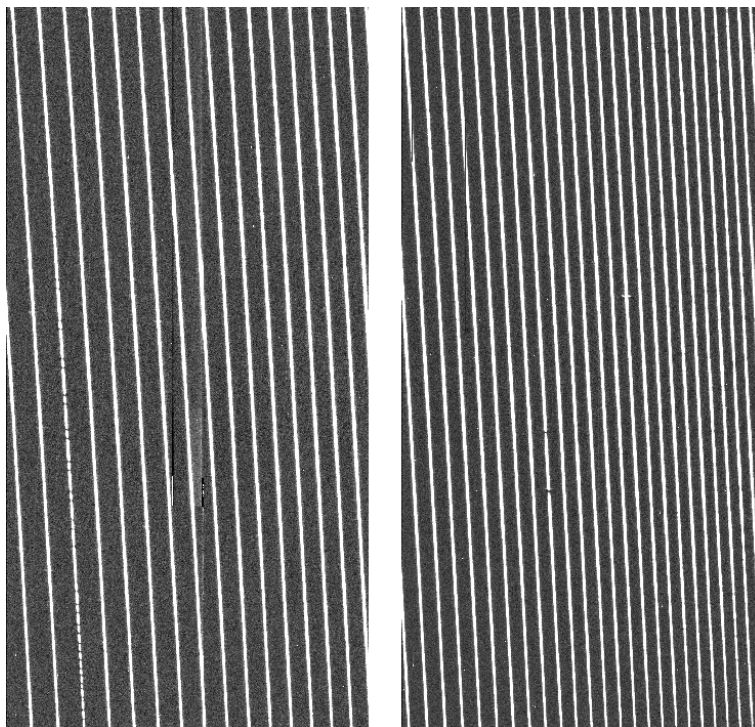


FIGURE B.7: 2D HDS spectrum from the first exposure of TYC3344-124-1 before flatfielding. The spectrum is overscan-corrected, masked and corrected for scattered light in the background. The red detector is on the left and the blue one on the right.

## Continuum normalisation

Despite the corrections for the different pixel sensitivities, the spectra mostly show lower count rates (here: measured in [e<sup>-</sup>]) at the edges of the spectral orders. This effect, also called *ripple*, is caused by the echelle blaze function, which is given as:

$$R(\lambda) = \frac{\sin^2(\pi\alpha X)}{(\pi\alpha X)^2}, \text{ where} \quad (\text{B.1})$$

$$X \equiv m \frac{1 - \lambda_c}{\lambda}. \quad (\text{B.2})$$

Here,  $m$  is the number of the spectral order. It is related to  $\lambda_c$ , the central wavelength of the order, by the echelle constant  $k \equiv m\lambda_c$  (only constant within an order). The constant  $\alpha$  determines the width of the ripple function (Heap and Brown, 1997).

If the count rate is not required for the analysis, which was the case for the targets observed with HDS/Subaru, one possibility to remove the ripple is the continuum normalisation. By fitting spline functions to the individual orders of the spectra, we adjusted the continuum levels to 1. The order of the spline and the rejection parameters (avoiding absorption lines to be included in the fit) were adjusted for the different spectral orders, so that the best possible solution was found.

## Wavelength calibration

Now it was time to convert the pixel coordinates along the dispersion direction to wavelengths. This calibration was done with the two ThAr frames which were recorded for each detector, one at the beginning, one at the end of the night. Fig. B.8 shows the overscan-corrected and masked ThAr frames (first exposure). Note that the strong scattered light is not a problem here because it does not affect the assignment of line positions needed for the calibration.

The images were extracted with the reference file as described above. Then we identified the exact positions of the ThAr emission lines and assigned wavelengths to them by comparison with the ThAr line atlas given by the NAOJ (Honda and Aoki, 2002)<sup>3</sup>. The 89th order is exemplary shown in Fig. B.9.

The manual selection of several evenly distributed lines was sufficient in order to allow the *IRAF* routine *ecidentify* to assign the remaining lines automatically. A fitting function was created and the deviations of the assigned lines from the fit were shown in a check plot (see Fig. B.10). The fit was improved by deleting strongly deviating lines ( $\gtrsim 0.01 \text{ \AA}$ ). It was found that the wavelength solution also fitted to the second ThAr exposure at the end of the night. Finally, the solution was used to convert all science frames to wavelength space. Fig. B.11

<sup>3</sup><https://www.naoj.org/Observing/Instruments/HDS/wavecal.html>

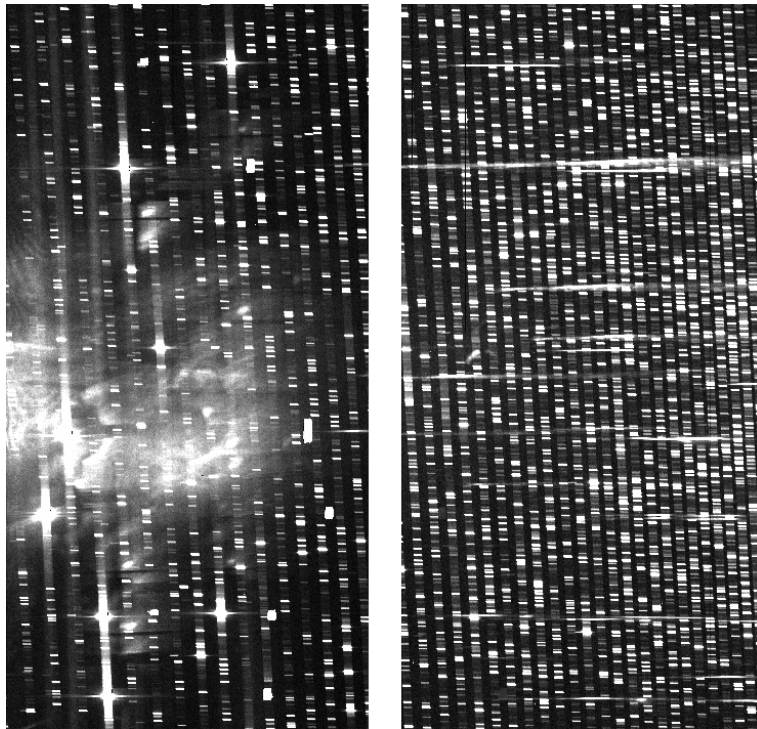


FIGURE B.8: ThAr frame for HDS/Subaru wavelength calibration. The image is overscan-corrected and masked. The red detector is on the left and the blue one on the right.

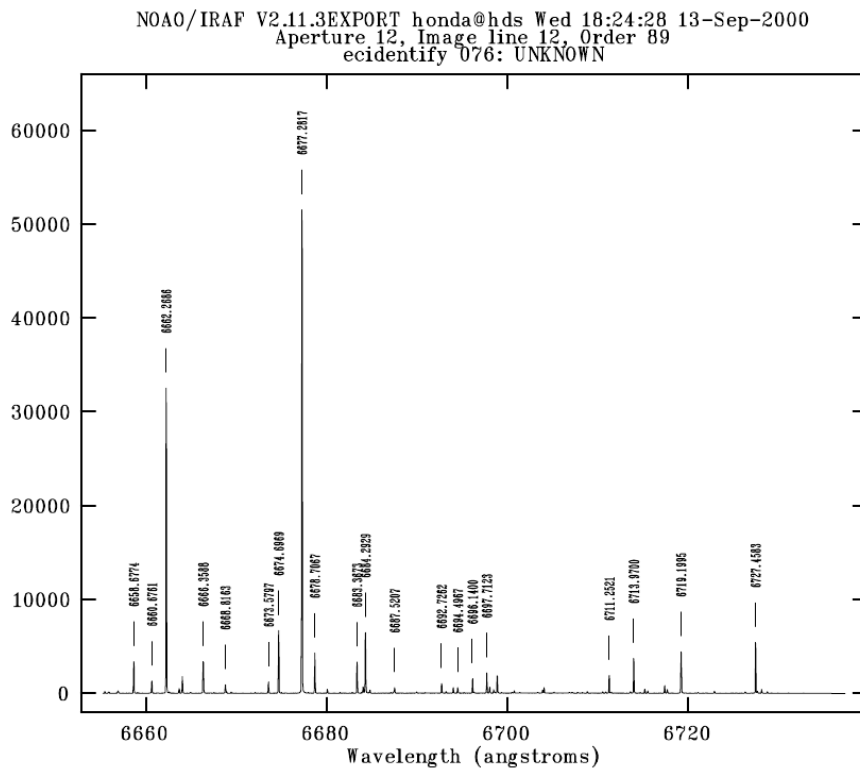


FIGURE B.9: The 89th echelle order from the ThAr line atlas for HDS/Subaru (Honda and Aoki, 2002). The ThAr emission lines are marked with their corresponding exact wavelengths in  $\text{\AA}$ .



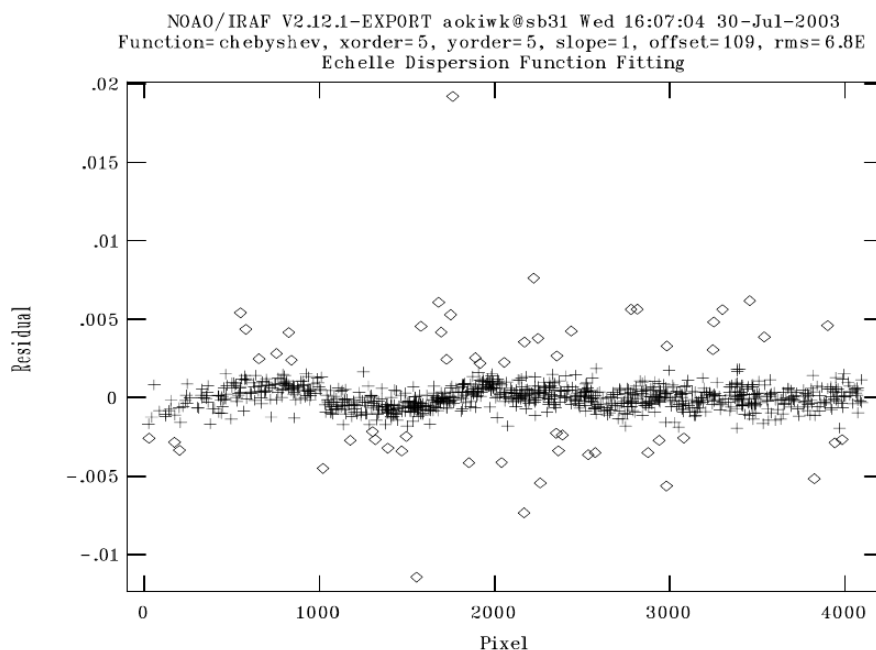


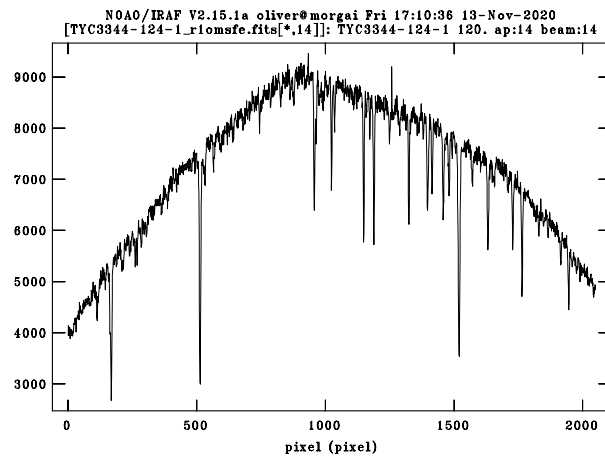
FIGURE B.10: Here we show how the fit for the wavelength calibration is created. The abscissa gives the pixel coordinate along the dispersion axis, the ordinate shows the residuals between the ThAr lines and the fitted wavelength solution. Strongly deviating lines were excluded here and are marked with open diamonds. Figure taken from Aoki and Helminiak (2014).

shows the effects of normalisation and wavelength calibration on an extracted spectrum of TYC3344-124-1 in the 14th aperture of the red detector. This corresponds to the 89th order ( $\sim 6655\text{--}6740\text{ \AA}$ ) shown in Fig. B.9.

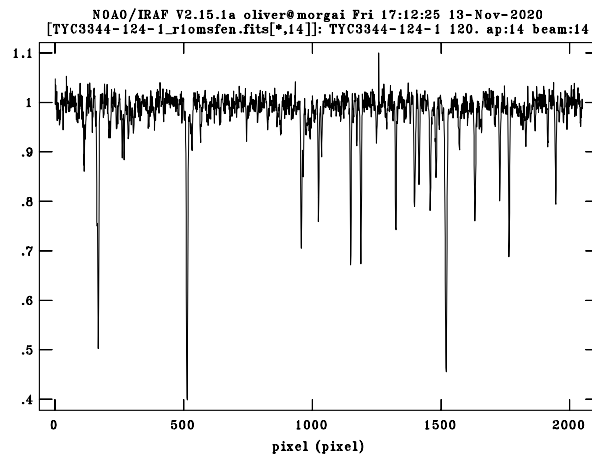
## Combining the spectral orders

For the analysis, it is helpful to have a merged spectrum, where we do not have to switch between the orders when we want to go to another wavelength. In order to avoid degradation at the edges of the orders we used the continuum functions. These were obtained from dividing the original spectra (wavelength-calibrated spectra with instrumental flux) by the normalised spectra in the individual orders. With the *IRAF* task *scombine*, we merged the original spectra as well as the continuum functions. Dividing the merged original spectrum by the merged continuum function yielded a merged, normalised spectrum.

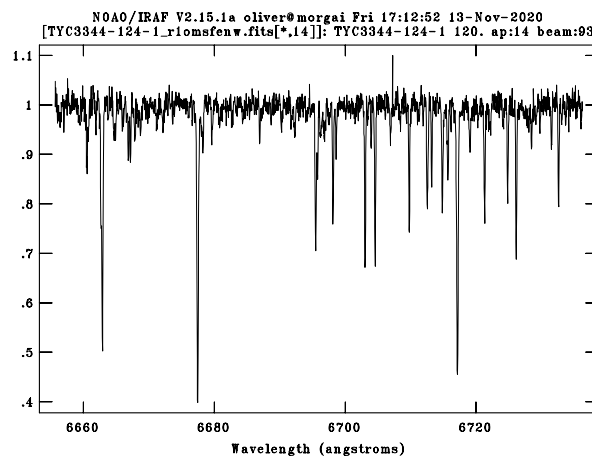
The data reduction was now complete. As a last step before the analysis, we median-averaged the two exposures of each target in order to increase the  $S/N$ . This only works if both exposures have relatively similar individual  $S/N$ , which was the case for all six targets.



(a) Extracted spectrum



(b) Normalised spectrum



(c) Wavelength calibrated spectrum

FIGURE B.11: Normalisation and wavelength calibration for TYC3344-124-1, first exposure, exemplarily for the 89th echelle order (14th aperture).

## B.2 UVES/VLT

Fig. B.12 shows the *Kepler* workflow, contained in the ESO *Reflex* pipeline, which was designed specifically for the reduction of UVES data. The workflow consists of the main steps (1) Data organisation and selection, (2) Creation of master calibration files, (3) Wavelength response and calibration, (4) Spectrum extraction and (5) Output organisation. These steps and the involved actors, which are displayed as turquoise boxes in Fig. B.12, are briefly described in the following subsections, where the names and actions of actors are given in *italics*. We show check images from the data reduction exemplary for the first exposure of HD 261393. For further details we refer the reader to the *Reflex UVES tutorial* (Bramich and Moehler, 2017).

### (1) Data organisation and selection

After *initialising*, the *Data Organiser* scans through the input directories with the raw science and calibration data, identifies the image type (from the FITS file header) and collects all the files which are relevant for the data reduction. In the *Data Set Selection*, the user can interactively choose one or more of the available data sets to be reduced in this run. Thereby, the files can be inspected and e.g. calibration frames of poor quality can be rejected. By *initialising the current dataset*, the pipeline continues with step (2).

### (2) Creation of master calibration files

Each of the actors here uses a pre-defined UVES pipeline recipe. The actors are *Master Bias Creation*, *Master Dark Creation*, which is skipped here because the dark current was neglected, the *Spectrum Locator*, which computes an initial guess of the order positions, taking into account the setup and weather conditions, the *Order Detection*, which uses a flatfield to find the exact order positions, and the *Master Flat Creation*.

Fig. B.13 shows the identification of spectral orders. The bottom right panel shows the spectral format, i.e. the distribution of the spectral orders over the CCD detector. The other panels show the deviations of characteristic positions from model expectations.

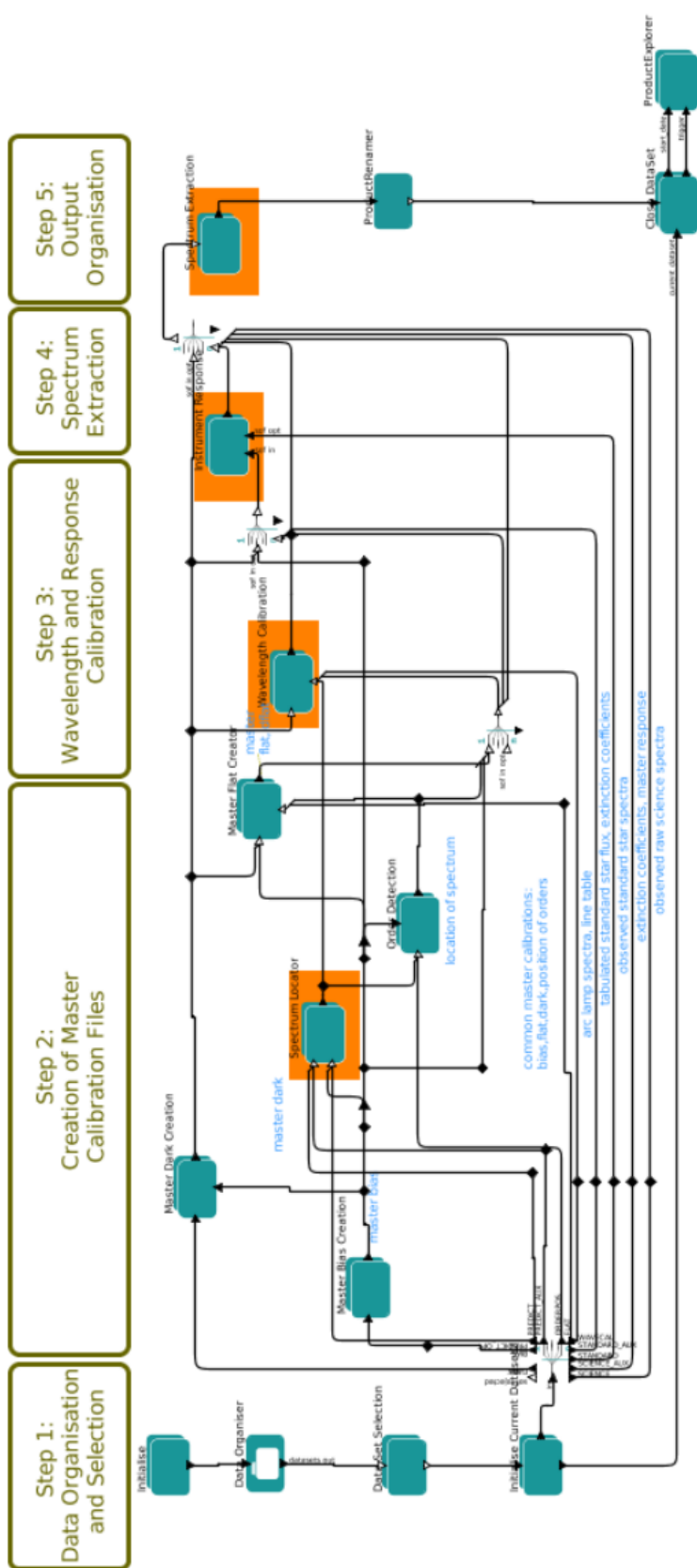


FIGURE B.12: The *Kepler* workflow for the reduction of UVES data, used for the ESO *Reflex* pipeline. Image taken from Bramich and Moehler (2017).

### (3) Wavelength and response calibration

From this step, we only needed the *Wavelength Calibration*, which creates the wavelength solution from the ThAr frames. (see Fig. B.14). The arclines from the ThAr frames are used to assign concrete wavelengths to the pixel values within the spectral orders. The bottom right panel shows again the spectral format, while the top panels show the residuals of the arclines, either for the wavelength (left) or the corresponding spectral order (right). Arclines that deviated too strongly (red) were not used for the fit. The numbers of identified and used lines are given below the image.

The *Instrument Response* actor was skipped because we did not need flux-calibrated spectra. These could be computed here from a standard star observation and the creation of an instrument response curve.

### (4) Spectrum extraction

The *Spectrum Extraction* actor extracts and merges the science spectra. Fig. B.15 shows the extracted complete spectrum, instrumental flux versus wavelength, in the top panel. The other panels show the  $S/N$ , which decreases at the edges of the CCDs, the FWHM, the strength of the ripple and the slit position, for the individual spectral orders.

### (5) Output organisation

The next actor is the *Product Renamer*, where the names of the reduced images and adjacent files can be defined and the data are saved. *Close DataSet* and *ProductExplorer* end the routine and display the produced data.

Besides the reduced science spectrum (merged and with instrumental flux in [ADU]), for each exposure and each detector we obtained a spectrum showing the flux errors, the spectrum of the sky background which was subtracted before the extraction, as well as additional information about the order extraction, the wavelength calibration and its errors.

The reduced science spectra were then median-averaged with *IRAF* in order to improve the  $S/N$  and remove cosmics. In contrast to HDS/Subaru, not all UVES spectra were continuum-normalised but only those where it was required for the analysis (e.g. for the atmospheric parameter fits).

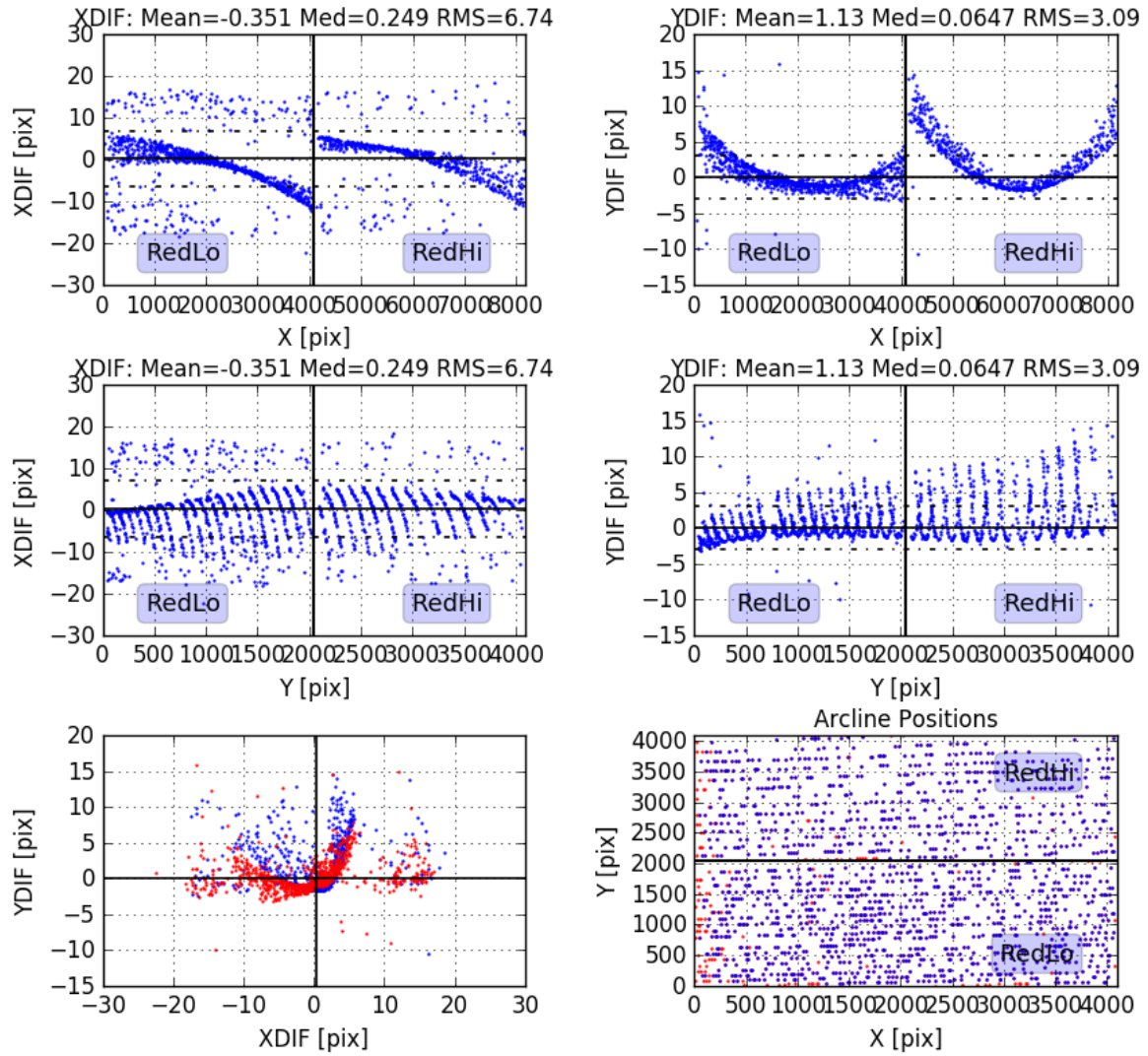
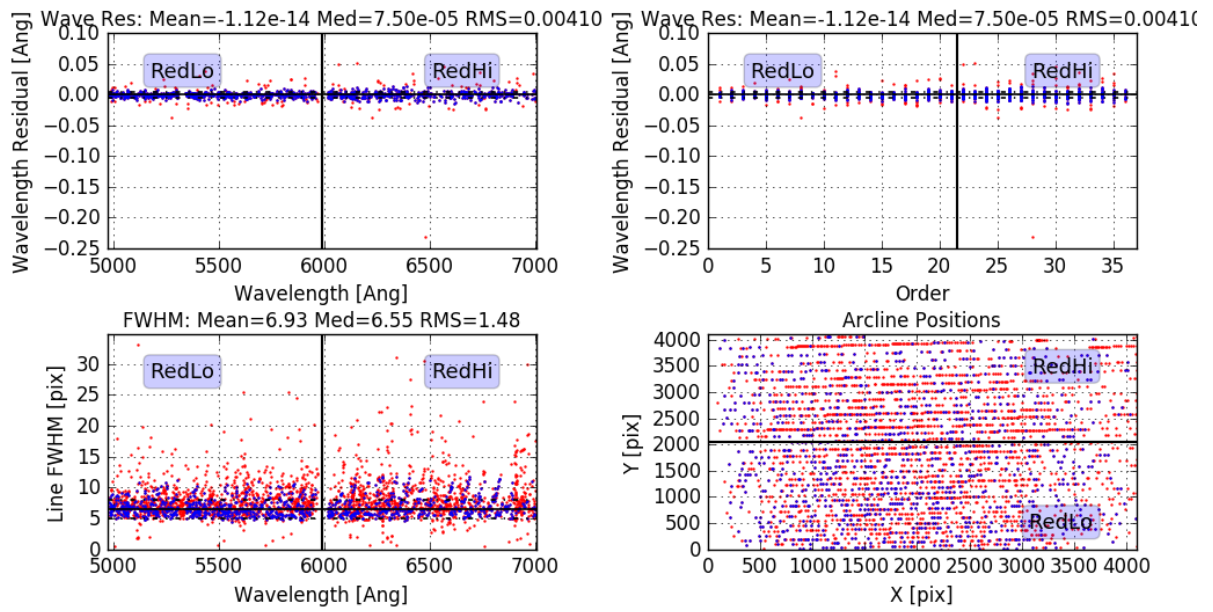


FIGURE B.13: Spectrum location for HD 261393, first exposure.



No. of detected lines = 2877  
 Initial no. of fitted lines = 1099  
 Final no. of fitted lines = 971

FIGURE B.14: Wavelength calibration for HD 261393, first exposure.

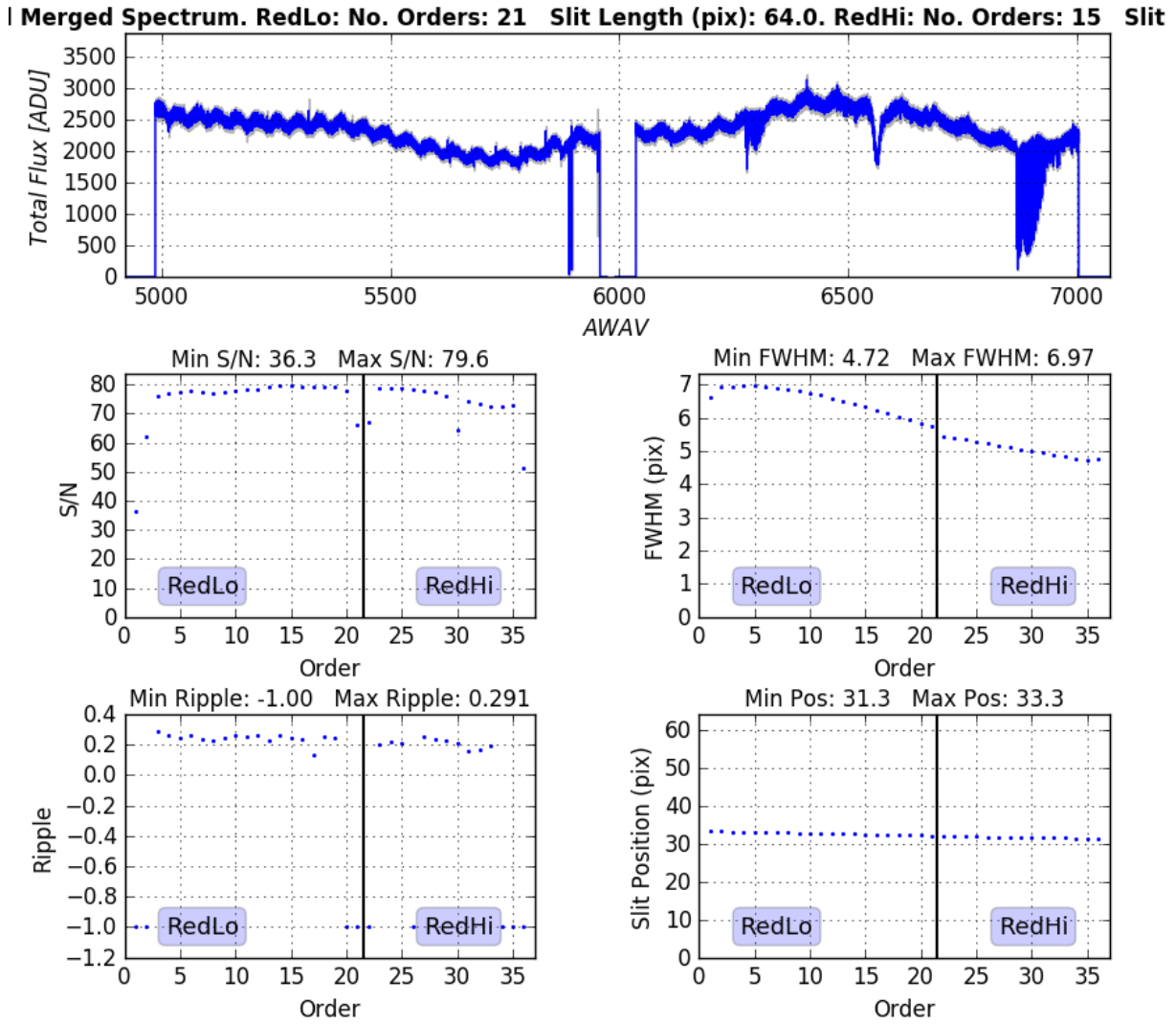


FIGURE B.15: Spectrum extraction for HD 261393, first exposure.



# Appendix C

## Comparison to standard stars

Here, we compare observed spectra to standard stars, namely the Li-rich targets (Fig. C.1) and the early-type candidates in the Monoceros Loop and Vela Jr. (Fig. C.2). The inferred spectral types SpT are given in Table C.1, where we compare them to the spectral types from the atmospheric parameter fits and the *Skiff* catalogue, as they were used in this thesis for Li-rich and early-type UVES stars, respectively. For the ranges of the SpTs from comparison to standard stars we assume the following errors: (i)  $\pm 1$  subclass for the Li-rich stars, (ii)  $\pm 2$  subclasses for the early-type stars. For the ranges of the adopted SpTs we note: (i) The errors for the Li-rich stars are based on the  $T_{\text{eff}}$  errors from the atmospheric parameter fits, converted with Pecaut and Mamajek (2013, Table 5). (ii) The precision of the *Skiff* SpTs was assumed to be  $\pm 1$  subclass.

TABLE C.1: Spectral types SpT of UVES targets in comparison to standard stars. The third column gives the SNR in which the target is located, the fourth column gives the SpTs inferred from Figs. C.1 and C.2, the fifth column the adopted spectral types that were used in Chapter 5 and the sixth column gives the origin of the adopted SpTs:  $T_{\text{eff}}$  from atmospheric parameter fits (APF), Voroshilov et al. (1985) (Vo85), Houk (1978) (Ho78).

	Name	SNR	SpT std	SpT adopted	Reference
(1)	TYC159-251-1	G205.5+00.5	F1–F3	F5–F7	APF
(2)	TYC159-343-1	G205.5+00.5	A9–F3	F2–F4	APF
(3)	TYC8150-2802-1	G263.9–03.3	F9.5–G1	G0–G2	APF
(4)	TYC8150-3105-1	G263.9–03.3	F2–F4	F9.5–G1	APF
(5)	TYC8152-1456-1	G266.2–01.2	F7–F9	F9.5–G1	APF
(6)	TYC8152-550-1	G266.2–01.2	F5–F7	F7–F9	APF
(M1)	TYC159-2771-1	G205.5+00.5	B9–A2	B8–A0	Vo85
(M2)	HD 261359	G205.5+00.5	B8–A1	B8–A0	Vo85
(M3)	HD 261393	G205.5+00.5	B6–B9.5	B4–B6	Vo85
(M4)	TYC159-2337-1	G205.5+00.5	B8–A1	B8–A0	Vo85
(M5)	TYC159-2671-1	G205.5+00.5	B6–B9.5	B7–B9	Vo85
(VJ1)	HD 76060	G266.2–01.2	B5–B9	B7–B9	Ho78

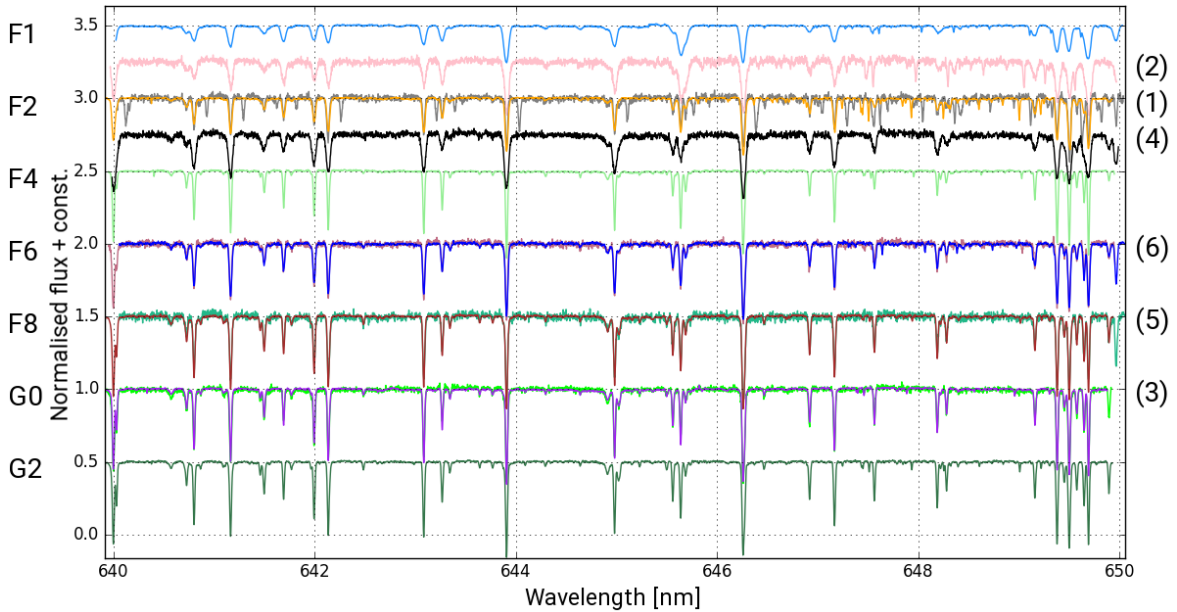


FIGURE C.1: Spectra of our Li stars between  $\sim 6400 \text{ \AA}$  and  $6500 \text{ \AA}$  in comparison to standard stars. The fluxes of the spectra are shifted by adding constant values in order to place them on or between the best fitting standard star spectra, which spectral types are noted on the left-hand side. The standard star spectra were obtained from Bagnulo et al. (2003, ESO DDT Program 266.D-5655)<sup>1</sup>. The six Li stars are numbered as introduced in Chapter 5: (1) TYC159-251-1, (2) TYC159-343-1, (3) TYC8150-2802-1, (4) TYC8150-3105-1, (5) TYC8152-1456-1, (6) TYC8152-550-1.

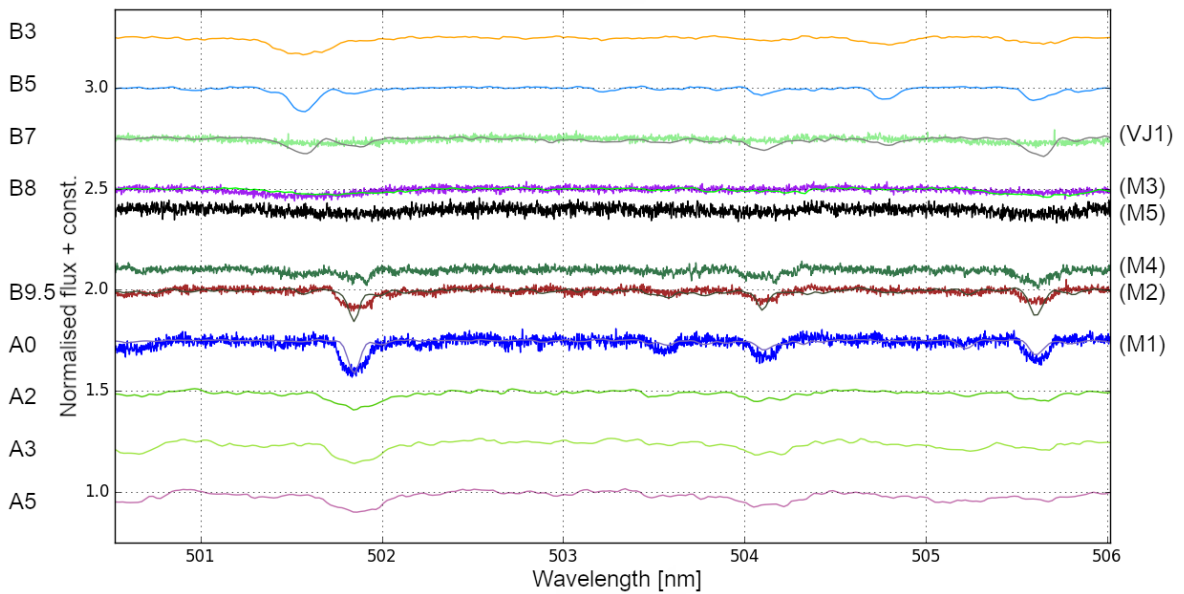


FIGURE C.2: Spectra of the early-type candidates in the Monoceros Loop and Vela Jr. between  $\sim 5005 \text{ \AA}$  and  $5060 \text{ \AA}$  in comparison to standard stars. The fluxes of the spectra are shifted by adding constant values in order to place them on or between the best fitting standard star spectra, which spectral types are noted on the left-hand side. The standard star spectra were observed with the *Fibre Linked ECHelle Astronomical Spectrograph* (FLECHAS, Mugrauer et al. 2014). The candidate stars are numbered as in Chapter 5: (M1) TYC159-2771-1, (M2) HD 261359, (M3) HD 261393, (M4) TYC159-2337-1, (M5) TYC159-2671-1, (VJ1) HD 76060.

<sup>1</sup>[http://www.eso.org/sci/observing/tools/uvespop/field\\_stars\\_uptonow.html](http://www.eso.org/sci/observing/tools/uvespop/field_stars_uptonow.html)



# Appendix D

## Determination of radial velocities with *IRAF*

In the following, we demonstrate how we manually determined the RVs of the early-type stars with *IRAF plot* and provide the results for the individual lines in Table D.1. For the early-type stars, due to the broadening of the lines and the noisy spectra, we measured the central wavelength of each available line three times by Gaussian fitting and used the average as the result for each line. Due to the later spectral type, a much higher number of lines could be used for the SB2 TYC159-251-1, where the RV determination is presented in Table D.2. Here, one measurement per line was sufficient. The RVs were then used for the further analysis as described in Section 5.2.

The measurements for the early-type stars are exemplary illustrated with the Fe II line ( $\lambda_0 = 5018.434 \text{ \AA}$ ) and the H $\alpha$  line ( $\lambda_0 = 6562.817 \text{ \AA}$ ) of TYC159-2771-1 in Fig. D.1. The laboratory wavelengths  $\lambda_0$  were taken from the ILLSS-catalogue (Coluzzi, 1999). The central wavelengths were determined by fitting a Gaussian to the line core at three different positions. The three results were averaged, yielding  $\lambda_{\text{obs}}$  and the RVs calculated with the known formula as

$$v_r = c \frac{\lambda_{\text{obs}} - \lambda_0}{\lambda_0} + BC. \quad (\text{D.1})$$

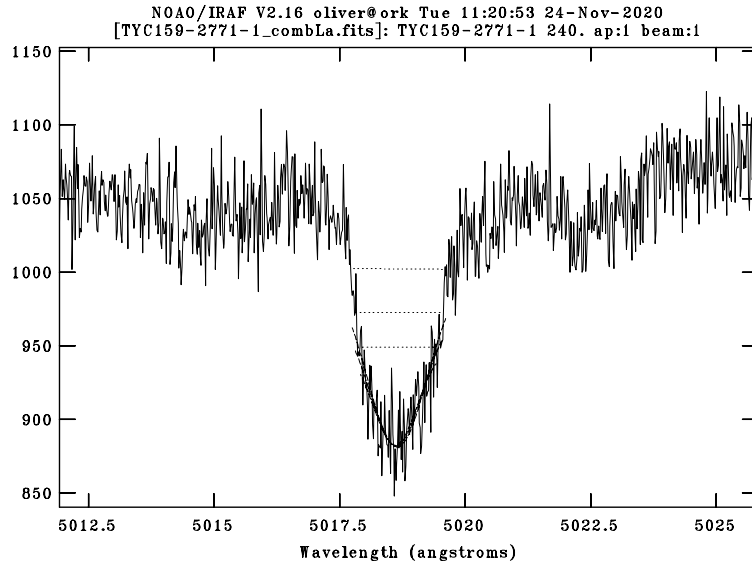
The barycentric corrections  $BC$  were calculated before with *iSpec* (see Table 5.1). The resulting RVs for the individual lines were then averaged, as given in the first row for each star in Table D.1. These values were used for the further analysis in Section 5.2.

TABLE D.1: RV determination for the early-type runaway candidates in the Monoceros Loop (M), Vela Jr. (VJ) and HB9 (H). Indices 1, 2 and 3 correspond to the measurements at the middle, bottom and top position in Fig. D.1, respectively. We list the central wavelengths of the Gaussian fits.  $\lambda_{\text{obs}}$  corresponds to the average of these three measurements. The first row for each star gives mean and standard deviation of the RVs calculated for the individual lines. In the cases where only H $\alpha$  could be used, the error was adopted from the highest standard deviation among the other stars,  $\Delta v_r = 7.3 \text{ km s}^{-1}$ .

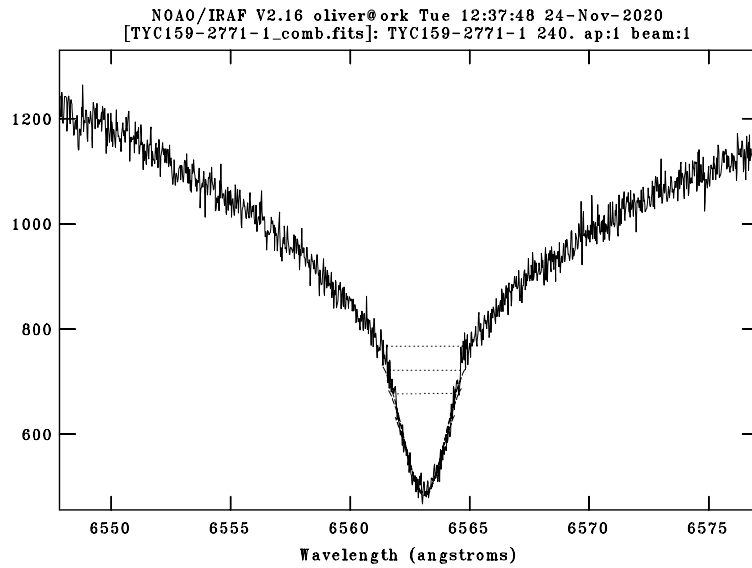
Line	$\lambda_0$ [Å]	$\lambda_{\text{obs},1}$ [Å]	$\lambda_{\text{obs},2}$ [Å]	$\lambda_{\text{obs},3}$ [Å]	$\lambda_{\text{obs}}$ [Å]	$v_r$ [km s $^{-1}$ ]
TYC159-2771-1 (M1)						$+31.8 \pm 2.0$
Fe II	5018.434	5018.628	5018.607	5018.647	5018.627	+31.08
Mg I	5172.684	5172.832	5172.812	5172.845	5172.830	+27.96
Mg I	5183.604	5183.856	5183.866	5183.870	5183.864	+34.56
Si II	6347.091	6347.373	6347.358	6347.379	6347.370	+32.71
Si II	6371.359	6371.636	6371.627	6371.646	6371.636	+32.58
Fe II	6456.376	6456.612	6456.576	6456.647	6456.612	+30.47
H $\alpha$	6562.817	6563.111	6563.112	6563.111	6563.111	+32.98
HD 261359 (M2)						$+0.9 \pm 5.1$
Fe II	5018.434	5018.244	5018.261	5018.235	5018.247	+11.40
Mg I	5172.684	5172.238	5172.230	5172.242	5172.237	-3.35
Mg I	5183.604	5183.283	5183.289	5183.261	5183.278	+3.71
Si II	6347.091	6346.629	6346.668	6346.674	6346.657	+2.09
Si II	6371.359	6370.841	6370.694	6370.835	6370.790	-4.18
Fe II	6456.376	6455.806	6455.793	6455.858	6455.819	-3.27
H $\alpha$	6562.817	6562.314	6562.315	6562.319	6562.316	-0.30
HD 261393 (M3)						$+31.3 \pm 5.8$
He I	5015.675	5015.838	5015.876	5015.824	5015.846	+34.77
He I	5875.618	5875.811	5875.855	5875.819	5875.828	+35.28
He I	5875.650	5875.811	5875.855	5875.819	5875.828	+33.65
H $\alpha$	6562.817	6562.738	6562.748	6562.752	6562.746	+21.31
TYC159-2337-1 (M4)						$+22.1 \pm 4.7$
He I	5875.618	5875.994	5876.018	5876.008	5876.007	+25.77
He I	5875.650	5875.994	5876.018	5876.008	5876.007	+24.14
Si II	6347.091	6347.332	6347.233	6347.333	6347.299	+15.78
Si II	6371.359	6371.561	6371.635	6371.595	6371.597	+17.14
H $\alpha$	6562.817	6563.285	6563.345	6563.243	6563.291	+27.59
TYC159-2671-1 (M5)						$+23.3 \pm 7.3$
H $\alpha$	6562.817	6562.909	6562.900	6562.890	6562.900	+23.35
HD 76060 (VJ1)						$+25.7 \pm 7.3$
H $\alpha$	6562.817	6563.186	6563.162	6563.172	6563.173	+25.66
TYC3344-235-1 (H1)						$-31.2 \pm 2.8$
Mg I	5172.684	5171.775	5171.725	5171.771	5171.757	-34.59
Mg I	5183.604	5182.814	5182.801	5182.798	5182.804	-27.11
Si II	6347.091	6345.993	6345.985	6346.010	6345.996	-32.57
H $\alpha$	6562.817	6561.729	6561.724	6561.735	6561.729	-30.54
TYC3344-679-1 (H2)						$+8.6 \pm 7.3$
H $\alpha$	6562.817	6562.589	6562.605	6562.559	6562.584	+8.55
TYC3344-683-1 (H3)						$+9.3 \pm 7.3$
Mg I	5172.684	5172.339	5172.379	5172.331	5172.350	-0.20
Mg I	5183.604	5183.604	5183.604	5183.582	5183.597	+18.75
Si II	6347.091	6346.782	6346.804	6346.793	6346.793	+5.12
H $\alpha$	6562.817	6562.695	6562.704	6562.679	6562.693	+13.51
TYC3344-553-1 (H4)						$-14.9 \pm 7.3$
H $\alpha$	6562.817	6562.068	6562.075	6562.068	6562.070	-14.93

TABLE D.2: RV determination for the SB2 TYC159-251-1. The primary and secondary are indicated by (A) and (B), respectively. Average and standard deviation are given in the first row.

Line	$\lambda_0$ [Å]	$\lambda_{\text{obs}}$ (A) [Å]	$\lambda_{\text{obs}}$ (B) [Å]	$v_r$ (A) [km s <sup>-1</sup> ]	$v_r$ (B) [km s <sup>-1</sup> ]
TYC159-251-1				$-10.7 \pm 0.6$	$+48.4 \pm 0.7$
FeI	6055.987	6055.668	6056.874	-9.81	+49.89
FeI	6078.496	6078.153	6079.345	-10.94	+47.85
FeI	6079.020	6078.681	6079.875	-10.74	+48.15
NiI	6108.121	6107.774	6108.989	-11.05	+48.58
NiI	6116.181	6115.853	6117.042	-10.10	+48.18
CaI	6122.219	6121.879	6123.088	-10.67	+48.53
FeI	6127.913	6127.560	6128.767	-11.29	+47.76
FeI	6173.343	6172.988	6174.215	-11.26	+48.33
FeI	6180.216	6179.879	6181.074	-10.37	+47.60
FeI	6191.562	6191.219	6192.438	-10.63	+48.40
FeI	6200.323	6199.974	6201.178	-10.89	+47.32
FeI	6213.438	6213.093	6214.313	-10.67	+48.20
FeI	6230.728	6230.384	6231.607	-10.57	+48.27
FeI	6252.561	6252.213	6253.441	-10.71	+48.17
FeI	6256.370	6256.008	6257.233	-11.37	+47.33
FeI	6344.154	6343.782	6345.044	-11.60	+48.04
Si II	6347.091	6346.748	6347.992	-10.22	+48.54
FeI	6355.038	6354.687	6355.937	-10.58	+48.39
FeI	6358.692	6358.318	6359.566	-11.65	+47.19
Si II	6371.359	6371.008	6372.262	-10.54	+48.47
FeI	6400.010	6399.645	6400.898	-11.12	+47.58
FeI	6411.658	6411.295	6412.570	-10.99	+48.62
FeI	6430.851	6430.486	6431.762	-11.04	+48.45
Fe II	6432.654	6432.314	6433.589	-9.87	+49.56
CaI	6439.073	6438.716	6439.986	-10.64	+48.49
CaI	6449.810	6449.459	6450.719	-10.33	+48.23
CaI	6462.566	6462.247	6463.512	-8.82	+49.86
CaI	6499.649	6499.288	6500.561	-10.67	+48.05
FeI	6609.116	6608.755	6610.051	-10.40	+48.39
FeI	6633.760	6633.386	6634.706	-10.92	+48.73
NiI	6643.641	6643.265	6644.575	-10.99	+48.13
FeI	6663.446	6663.059	6664.371	-11.43	+47.60
FeI	6677.960	6677.621	6678.941	-9.24	+50.02
CaI	6717.685	6717.304	6718.633	-11.02	+48.29
FeI	6726.670	6726.294	6727.632	-10.78	+48.85
FeI	6750.152	6749.771	6751.107	-10.94	+48.39
NiI	6767.778	6767.403	6768.743	-10.63	+48.73



(a) Fe II 5018.434 Å



(b) H $\alpha$  6562.817 Å

FIGURE D.1: RV determination for the early-type stars by Gaussian fitting at three positions for each line with *IRAF*, exemplary shown for (a) the Fe II line at  $\lambda_0 = 5018.434 \text{ \AA}$  and (b) the H $\alpha$  line at  $\lambda_0 = 6562.817 \text{ \AA}$  of TYC159-2771-1. The fits at the middle, bottom and top position correspond to indices 1, 2 and 3 in Table D.1, respectively. We used the unnormalised spectra, so the abscissa shows the instrumental flux in [ADU].



# Appendix E

## Spectral analysis with *iSpec*

*iSpec* (Blanco-Cuaresma et al., 2014) was used for the analysis of late-type stars (F and G), while for the early-type stars we used *IRAF splot*. In this section, we show different analysis steps in more detail, namely (i) continuum normalisation (Figs. E.1 and E.2), (ii) barycentric correction (Fig. E.3), (iii) RV determination (Fig. E.4) and (iv) atmospheric parameter fits (Fig. E.5). The steps are demonstrated exemplary for the Li-rich star TYC8150-2802-1 (Vela). The parameters given in the windows are the ones used for TYC8150-2802-1 during the analysis. Figs. E.6 and E.7 show the atmospheric parameter fits for the Li-rich stars in the region of the H $\alpha$  line, as described in Section 5.3.

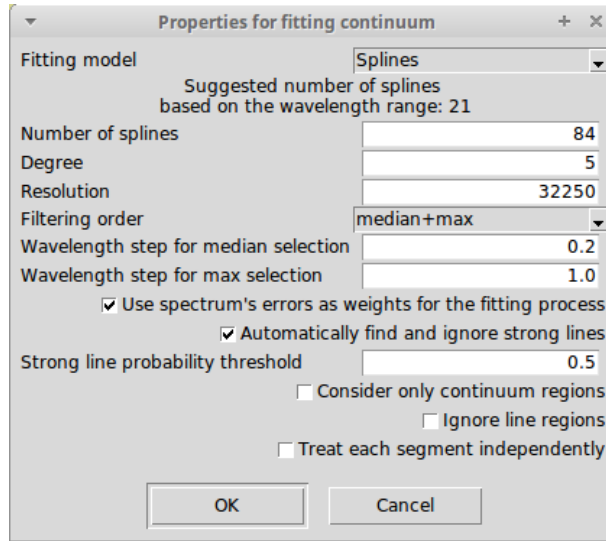


FIGURE E.1: Continuum normalisation with *iSpec*. Parameters for TYC8150-2802-1

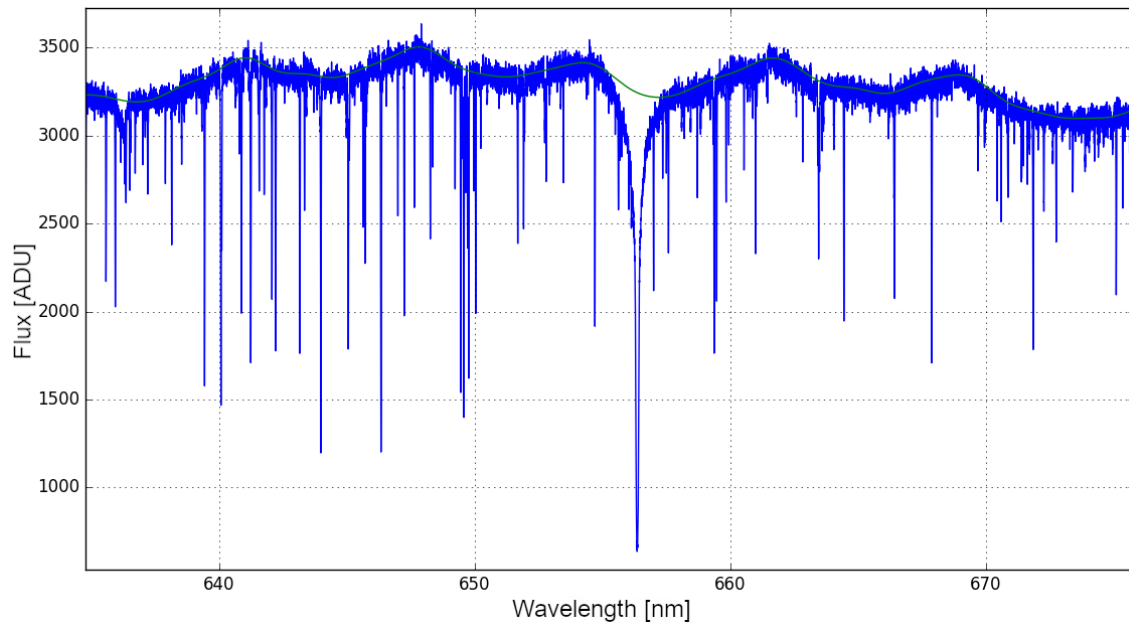


FIGURE E.2: Continuum normalisation for TYC8150-2802-1 with *iSpec* – fitted continuum. The blue line is the original spectrum with instrumental fluxes, the green line is the fitted continuum which was used for normalisation.

Barycentric velocity determination

Date (DD/MM/YYYY) 21/11/2017  
 Time (HH:MM:SS) 07:45:54  
 Epoch J2000.0  
 Right ascension (HH:MM:SS) 08:34:02.90  
 Declination (DD:MM:SS) -45:32:59.10

OK Cancel

FIGURE E.3: Barycentric correction for TYC8150-2802-1 with *iSpec*. The window gives the time stamp (UT of the midpoint of the observation) and the stellar coordinates used for the calculation.

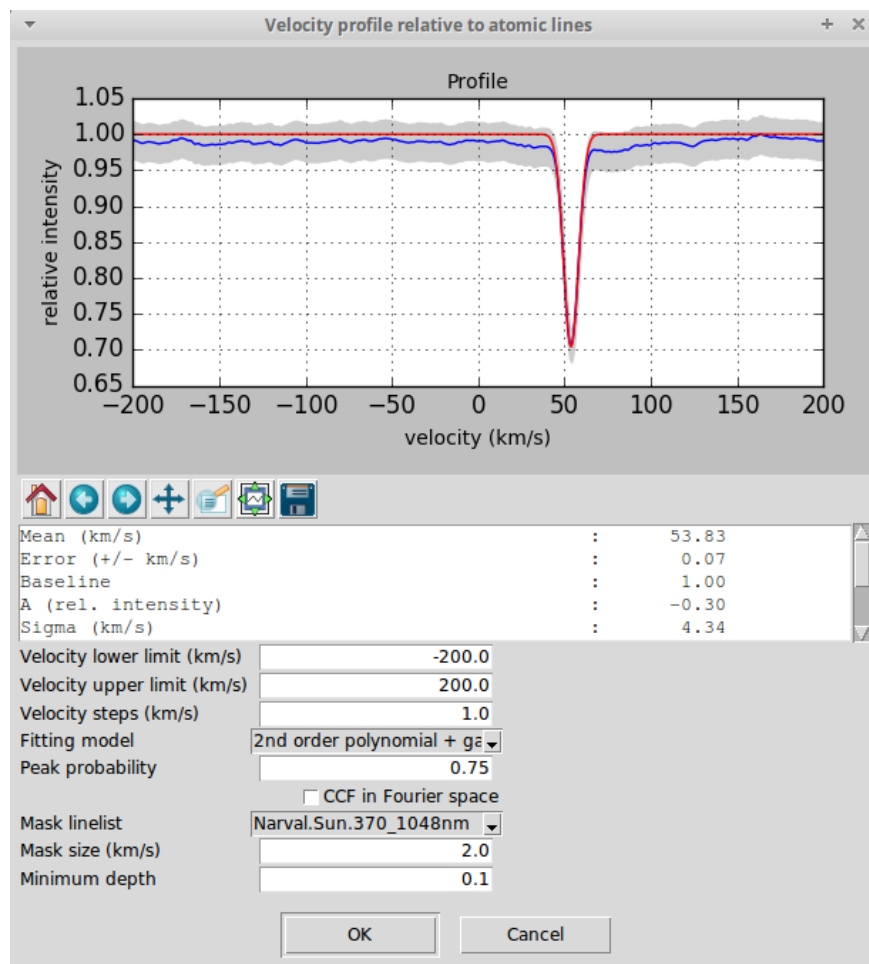


FIGURE E.4: RV determination for TYC8150-2802-1 with *iSpec*. The standard input parameters given here were used for all targets. The result is given in the middle.

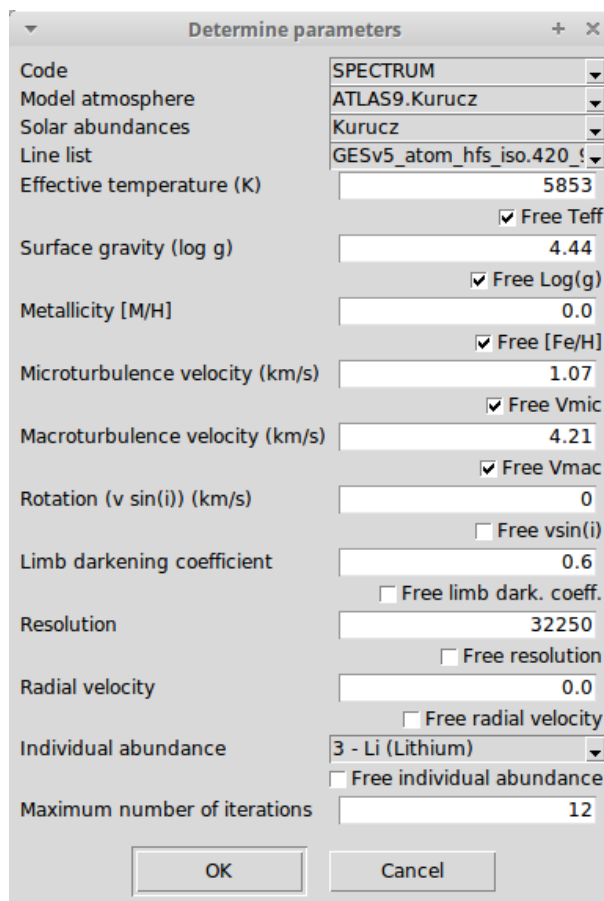


FIGURE E.5: Atmospheric parameter fits for TYC8150-2802-1 with *iSpec*. The window gives the initial parameters used for the target (see Section 5.3). The tick marks indicate if the corresponding parameter was left free. Further iterations were done, where e.g. *Rotation* ( $v \sin(i)$ ) was left free instead of the *Macroturbulence velocity*. The parameter *Radial velocity* was not relevant because we used RV-corrected spectra and the *Individual abundance* was not determined here but with *IRAF splot* and the curves of growth from Soderblom et al. (1993, Table 2). The *Maximum number of iterations* was set to 12 for all targets.

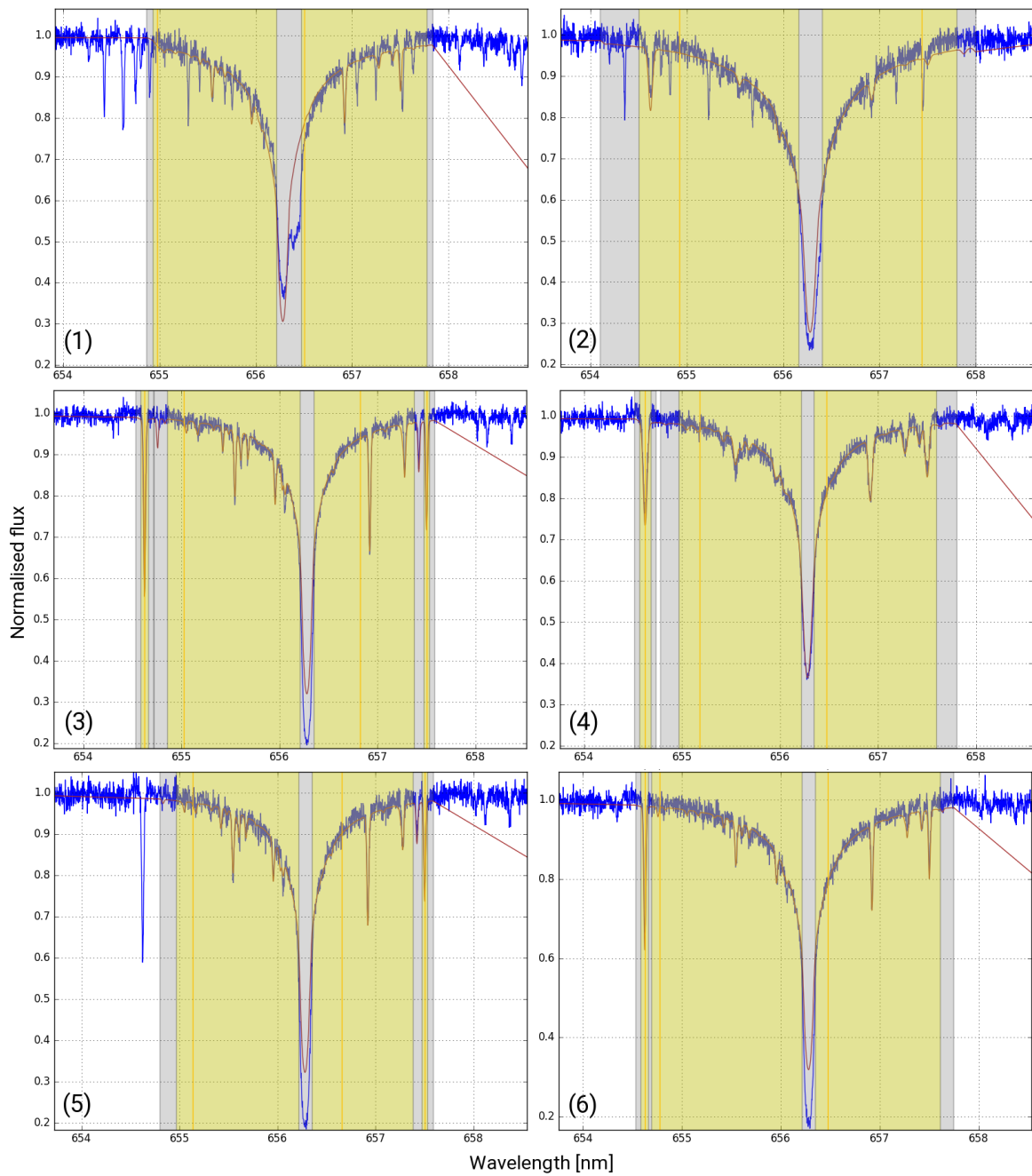


FIGURE E.6: The H $\alpha$  absorption lines of (1) TYC159-251-1, (2) TYC159-343-1, (3) TYC8150-2802-1, (4) TYC8150-3105-1, (5) TYC8152-1456-1 and (6) TYC8152-550-1 that were used to fit the atmospheric parameters. The spectra are shown in blue and the fit in red. The yellow areas mark the H $\alpha$  wings and additional Fe I lines at 6546 and 6575 Å in the cases (3), (4), (5) and (6). The grey areas show segments around the lines used for synthesising the spectra.

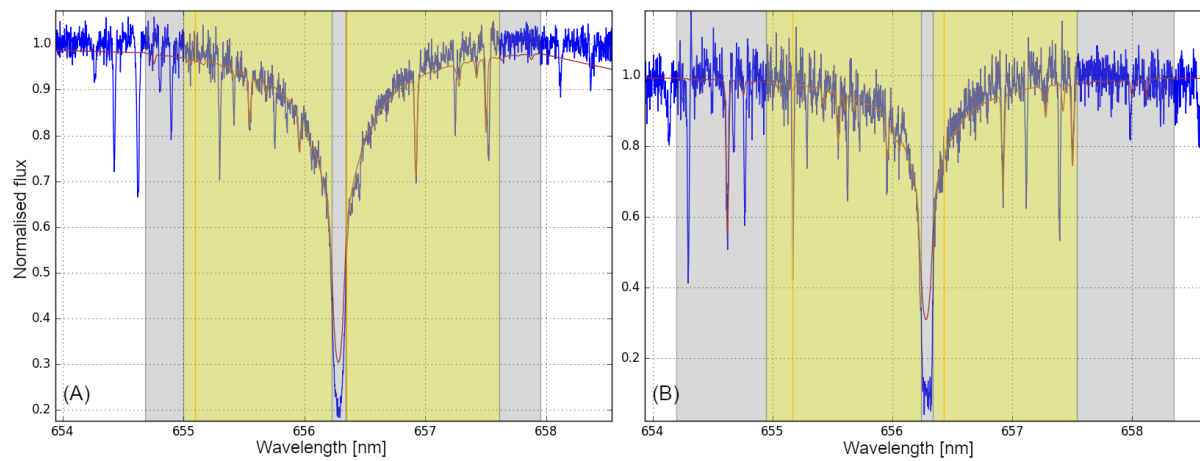


FIGURE E.7: The H $\alpha$  absorption lines of TYC159-251-1 (A) and TYC159-251-1 B (B) that were used to fit the atmospheric parameters. The spectra are shown in blue and the fit in red. The yellow areas mark the H $\alpha$  wings and the grey areas show segments around the lines used for synthesising the spectra.

# Appendix F

## Additional data

In the following tables, we provide additional data for the observed stars (Tables F.1, F.2, F.3, F.4) and the runaway candidates (Tables F.5, F.6, F.7, F.8). Note that the ten stars in HB9, Monoceros and Vela Jr., which were observed by us and remained as runaway candidates, are contained in both groups. They are indicated by numbers 1–4 and 6–11 in the notes of Table F.5. Generally, the entries are sorted by right ascension and numbered correspondingly in column 1. Exception: In Tables F.1–F.4, we first list the stars observed with UVES/VLT, then the six stars observed with HDS/Subaru.

The distances in Tables F.4 and F.8 are simply calculated as  $d = 1/\pi$ , with the parallax  $\pi$ . For a more precise value, the parallax zero-point offset  $\Delta\pi$  should be taken into account. This is given by Anders et al. (2019) as:

$$\begin{aligned}\Delta\pi &= 0.005 \text{ mas} && \text{for } G \leq 14 \text{ mag}, \\ \Delta\pi &= (0.1676 - 0.0084 \times G) \text{ mas} && \text{for } 14 \text{ mag} < G < 16.5 \text{ mag}, \\ \Delta\pi &= 0.029 \text{ mas} && \text{for } G \geq 16.5 \text{ mag},\end{aligned}\tag{F.1}$$

depending on the *Gaia*  $G$  magnitude. Neglecting the zero-point offset leads to overestimating the distances. However, the approximation is justified in the scope of this work, since the targets are relatively nearby ( $\leq 2$  kpc), so the effect of the offset is moderate. The calculated distances are largely consistent with the values given by Bailer-Jones et al. (2018) and Anders et al. (2019), who both used a Bayesian approach for the distance determination.

TABLE F.1: *Gaia* DR2 data of the observed stars – Positions and kinematics. For observational data of these targets, see Tables 4.1 and 4.2. Column 1 gives a running number that is also used for the subsequent tables. Column 2 gives the target name, columns 3 and 4 give right ascension and declination in ICRS (International Celestial Reference System), respectively. The positional coordinates are precise to 0.019–0.097 mas. Column 5 gives the parallax  $\pi$  and columns 6 and 7 give the proper motion  $\mu$  in right ascension and declination.

#	Name	RA <sub>ICRS</sub> [deg]	DEC <sub>ICRS</sub> [deg]	$\pi$ [mas]	$\mu_{\text{RA}}$ [mas/yr]	$\mu_{\text{DEC}}$ [mas/yr]
1	TYC1869-1435-1	84.563148	+27.821778	1.043 ± 0.054	+1.49 ± 0.09	−4.97 ± 0.06
2	TYC1869-1596-1	84.598797	+27.692493	0.938 ± 0.053	+0.44 ± 0.08	−5.83 ± 0.06
3	TYC1869-1670-1	84.762745	+27.543102	0.845 ± 0.067	+3.26 ± 0.09	−5.91 ± 0.07
4	TYC159-2540-1	99.470627	+6.664842	0.763 ± 0.057	−0.71 ± 0.09	−3.24 ± 0.07
5	HD 260990	99.488233	+6.479851	1.373 ± 0.059	−2.80 ± 0.09	−0.45 ± 0.08
6	HD 261117	99.582248	+6.394601	1.295 ± 0.052	−1.26 ± 0.07	−8.68 ± 0.06
7	TYC159-241-1	99.605126	+6.192085	0.816 ± 0.075	−0.03 ± 0.09	−3.65 ± 0.08
8	TYC159-2006-1	99.634302	+6.650805	1.876 ± 0.053	−10.78 ± 0.08	−0.68 ± 0.07
9	TYC159-2408-1	99.634466	+6.506260	0.835 ± 0.047	−7.24 ± 0.08	+1.23 ± 0.07
10	TYC159-2771-1	99.711535	+6.590548	0.753 ± 0.042	+1.46 ± 0.07	−3.78 ± 0.07
11	TYC159-1896-1	99.714443	+6.654405	1.534 ± 0.038	+4.86 ± 0.07	−1.75 ± 0.06
12	TYC159-2082-1	99.746349	+6.543591	0.710 ± 0.040	−3.96 ± 0.07	−4.64 ± 0.06
13	HD 261359	99.781141	+6.460540	0.651 ± 0.050	−0.48 ± 0.08	−3.15 ± 0.07
14	HD 261393	99.804555	+6.631657	0.792 ± 0.046	−0.20 ± 0.09	−0.97 ± 0.07
15	TYC159-2337-1	99.833831	+6.350130	0.485 ± 0.054	−1.70 ± 0.09	−0.45 ± 0.08
16	TYC159-2671-1	99.851046	+6.552367	0.686 ± 0.038	+0.08 ± 0.07	−0.78 ± 0.06
17	TYC159-892-1	99.851596	+6.623874	0.719 ± 0.038	+0.68 ± 0.07	−2.05 ± 0.06
18	HD 261527	99.890413	+6.116339	1.413 ± 0.058	+9.17 ± 0.11	−2.98 ± 0.10
19	TYC159-2962-1	99.901791	+6.276690	0.911 ± 0.052	−0.32 ± 0.08	−1.38 ± 0.07
20	HD 261589	99.937077	+6.459878	0.372 ± 0.062	−1.19 ± 0.11	−0.64 ± 0.10
21	TYC159-251-1	99.946228	+6.187886	1.774 ± 0.041	+3.63 ± 0.07	−9.44 ± 0.06
22	TYC159-2564-1	100.000448	+6.293380	0.701 ± 0.039	−2.13 ± 0.08	−0.26 ± 0.07
23	HD 261715	100.055850	+6.279158	0.821 ± 0.038	−1.18 ± 0.07	−3.35 ± 0.07
24	TYC159-343-1	100.064880	+6.193490	1.383 ± 0.042	+2.51 ± 0.09	−2.76 ± 0.08
25	TYC7669-1336-1	125.523575	−42.968986	1.328 ± 0.025	−3.77 ± 0.04	+3.77 ± 0.04
26	TYC7669-1414-1	125.545233	−43.071570	1.583 ± 0.028	−3.76 ± 0.05	−2.28 ± 0.05
27	TYC8150-2802-1	128.512272	−45.549786	3.226 ± 0.028	−16.94 ± 0.05	+29.17 ± 0.05
28	TYC8150-3105-1	128.646540	−45.193808	3.351 ± 0.028	−16.00 ± 0.05	+10.48 ± 0.04
29	TYC8152-120-1	133.008911	−46.389719	1.456 ± 0.038	−3.17 ± 0.06	−0.01 ± 0.06
30	HD 76060	133.010128	−46.288801	2.058 ± 0.045	−12.42 ± 0.08	+10.31 ± 0.09
31	TYC8152-1456-1	133.023810	−46.227165	1.661 ± 0.037	+5.17 ± 0.06	−11.56 ± 0.07
32	TYC8152-104-1	133.033516	−46.202573	1.015 ± 0.028	−5.07 ± 0.05	+7.20 ± 0.05
33	TYC8152-550-1	133.061215	−46.247268	2.435 ± 0.026	+4.95 ± 0.04	−10.71 ± 0.05
34	TYC3344-235-1	75.130367	+46.557565	0.907 ± 0.038	−0.23 ± 0.09	−1.37 ± 0.06
35	TYC3344-679-1	75.224911	+46.500149	1.005 ± 0.059	+0.74 ± 0.18	−4.76 ± 0.11
36	TYC3344-771-1	75.294801	+46.703038	1.372 ± 0.036	+8.00 ± 0.08	−6.39 ± 0.06
37	TYC3344-683-1	75.295303	+46.460557	1.213 ± 0.035	−1.09 ± 0.07	−7.02 ± 0.05
38	TYC3344-124-1	75.299322	+46.799185	1.944 ± 0.042	−4.29 ± 0.08	−15.41 ± 0.06
39	TYC3344-553-1	75.316643	+46.555993	1.528 ± 0.037	−1.98 ± 0.08	−7.22 ± 0.06



TABLE F.2: *Gaia* DR2 data of the observed stars – Magnitudes and stellar parameters. For observational data of these targets, see Tables 4.1 and 4.2. Column 1 gives the running number, column 2 gives the  $G$ -band magnitude, accurate to 0.2–1.1 mmag. Columns 3 and 4 give the  $BP$  and  $RP$  magnitudes, respectively, accurate to 0.5–4.6 mmag. Column 5 gives the effective temperature  $T_{\text{eff}}$ , column 6 the radius  $R$  and column 7 the luminosity  $L$ . Note that  $R$  and  $L$  are not given for stars with  $T_{\text{eff}} > 8000$  K. Finally, column 8 gives the absolute  $G$ -band magnitude which was not given in *Gaia* DR2 but calculated by us with the distance modulus (Eqn. 2.4) and the  $G$ -band extinctions from the *StarHorse* catalogue (see Table F.3).

#	$G$ [mag]	$BP$ [mag]	$RP$ [mag]	$T_{\text{eff}}$ [K]	$R$ [ $R_{\odot}$ ]	$L$ [ $L_{\odot}$ ]	$M_G$ [mag]
1	12.20	12.43	11.83	6859 <sup>+135</sup> <sub>-84</sub>	2.11 <sup>+0.05</sup> <sub>-0.08</sub>	8.85 ± 0.62	+1.88 <sup>+0.75</sup> <sub>-0.28</sub>
2	12.16	12.38	11.80	6802 <sup>+290</sup> <sub>-217</sub>	2.42 <sup>+0.17</sup> <sub>-0.19</sub>	11.33 ± 0.87	+0.86 <sup>+0.22</sup> <sub>-0.59</sub>
3	12.57	12.79	12.20	7242 <sup>+459</sup> <sub>-238</sub>	1.97 <sup>+0.14</sup> <sub>-0.23</sub>	9.65 ± 0.98	+0.98 <sup>+0.22</sup> <sub>-0.62</sub>
4	12.73	12.86	12.48	8022 <sup>+464</sup> <sub>-271</sub>	–	–	+1.78 <sup>+0.28</sup> <sub>-0.28</sub>
5	11.63	11.71	11.47	8872 <sup>+117</sup> <sub>-250</sub>	–	–	+2.26 <sup>+0.20</sup> <sub>-0.20</sub>
6	9.74	10.28	9.09	4935 <sup>+126</sup> <sub>-113</sub>	10.88 <sup>+0.52</sup> <sub>-0.53</sub>	63.31 ± 3.47	+0.31 <sup>+0.16</sup> <sub>-0.17</sub>
7	10.47	11.10	9.74	4645 <sup>+108</sup> <sub>-98</sub>	14.48 <sup>+0.63</sup> <sub>-0.64</sub>	87.97 ± 10.19	-0.16 <sup>+0.26</sup> <sub>-0.26</sub>
8	9.28	9.79	8.65	4921 <sup>+45</sup> <sub>-24</sub>	9.36 <sup>+0.09</sup> <sub>-0.17</sub>	46.29 ± 1.76	+0.71 <sup>+0.18</sup> <sub>-0.18</sub>
9	9.94	10.79	9.07	4127 <sup>+511</sup> <sub>-81</sub>	25.78 <sup>+1.05</sup> <sub>-5.36</sub>	173.71 ± 13.58	-1.28 <sup>+0.18</sup> <sub>-0.25</sub>
10	12.01	12.13	11.78	8107 <sup>+162</sup> <sub>-158</sub>	–	–	+1.11 <sup>+0.23</sup> <sub>-0.25</sub>
11	11.48	11.76	11.06	6396 <sup>+315</sup> <sub>-327</sub>	2.30 <sup>+0.25</sup> <sub>-0.21</sub>	7.96 ± 0.29	+2.23 <sup>+0.27</sup> <sub>-0.19</sub>
12	11.08	11.72	10.34	4623 <sup>+109</sup> <sub>-161</sub>	12.78 <sup>+0.94</sup> <sub>-0.58</sub>	67.29 ± 5.54	+0.21 <sup>+0.19</sup> <sub>-0.18</sub>
13	11.79	11.87	11.62	8549 <sup>+286</sup> <sub>-243</sub>	–	–	+0.89 <sup>+0.26</sup> <sub>-0.26</sub>
14	10.05	10.07	10.02	9179 <sup>+354</sup> <sub>-735</sub>	–	–	-0.61 <sup>+0.17</sup> <sub>-0.24</sub>
15	11.80	11.88	11.61	9033 <sup>+260</sup> <sub>-334</sub>	–	–	-0.04 <sup>+0.27</sup> <sub>-0.27</sub>
16	12.25	12.31	12.08	8833 <sup>+187</sup> <sub>-277</sub>	–	–	+1.25 <sup>+0.19</sup> <sub>-0.22</sub>
17	9.44	10.26	8.59	4158 <sup>+128</sup> <sub>-157</sub>	36.86 <sup>+2.94</sup> <sub>-2.17</sub>	365.83 ± 28.71	-2.27 <sup>+0.19</sup> <sub>-0.22</sub>
18	8.41	9.17	7.59	4248 <sup>+238</sup> <sub>-84</sub>	28.20 <sup>+1.16</sup> <sub>-2.91</sub>	233.34 ± 12.64	-0.77 <sup>+0.18</sup> <sub>-0.16</sub>
19	9.30	10.26	8.36	3933 <sup>+135</sup> <sub>-65</sub>	37.25 <sup>+1.27</sup> <sub>-2.43</sub>	299.15 ± 23.39	-1.74 <sup>+0.17</sup> <sub>-0.19</sub>
20	11.06	11.06	11.00	9568 <sup>+88</sup> <sub>-523</sub>	–	–	-1.14 <sup>+0.40</sup> <sub>-0.39</sub>
21	11.51	11.78	11.09	6257 <sup>+391</sup> <sub>-211</sub>	2.05 <sup>+0.14</sup> <sub>-0.23</sub>	5.80 ± 0.20	+2.61 <sup>+0.20</sup> <sub>-0.19</sub>
22	11.97	12.04	11.79	8701 <sup>+443</sup> <sub>-309</sub>	–	–	+1.22 <sup>+0.23</sup> <sub>-0.27</sub>
23	11.25	11.26	11.17	9591 <sup>+110</sup> <sub>-61</sub>	–	–	+0.79 <sup>+0.17</sup> <sub>-0.20</sub>
24	10.87	11.08	10.54	7079 <sup>+112</sup> <sub>-232</sub>	2.76 <sup>+0.19</sup> <sub>-0.09</sub>	17.21 ± 0.76	+1.24 <sup>+0.29</sup> <sub>-0.23</sub>
25	12.27	12.51	11.88	6583 <sup>+196</sup> <sub>-126</sub>	1.74 <sup>+0.07</sup> <sub>-0.10</sub>	5.11 ± 0.16	+2.63 <sup>+0.21</sup> <sub>-0.19</sub>
26	11.97	12.17	11.63	7068 <sup>+54</sup> <sub>-103</sub>	1.46 <sup>+0.04</sup> <sub>-0.02</sub>	4.79 ± 0.14	+2.80 <sup>+0.26</sup> <sub>-0.20</sub>
27	12.03	12.36	11.55	5853 <sup>+101</sup> <sub>-90</sub>	1.02 <sup>+0.03</sup> <sub>-0.03</sub>	4.95 ± 2.08	+4.53 <sup>+0.16</sup> <sub>-0.13</sub>
28	11.94	12.26	11.42	5614 <sup>+228</sup> <sub>-102</sub>	1.12 <sup>+0.04</sup> <sub>-0.08</sub>	1.13 ± 0.02	+4.34 <sup>+0.11</sup> <sub>-0.16</sub>
29	11.58	11.83	11.18	6397 <sup>+71</sup> <sub>-33</sub>	2.31 <sup>+0.03</sup> <sub>-0.05</sub>	8.06 ± 0.31	+2.21 <sup>+0.21</sup> <sub>-0.22</sub>
30	7.85	7.83	7.92	8599 <sup>+942</sup> <sub>-854</sub>	–	–	-0.63 <sup>+0.11</sup> <sub>-0.11</sub>
31	12.47	12.81	11.97	5806 <sup>+23</sup> <sub>-77</sub>	1.65 <sup>+0.04</sup> <sub>-0.02</sub>	2.78 ± 0.09	+3.35 <sup>+0.21</sup> <sub>-0.26</sub>
32	11.53	12.42	10.61	4061 <sup>+208</sup> <sub>-98</sub>	10.78 <sup>+0.54</sup> <sub>-1.02</sub>	28.50 ± 1.28	+0.24 <sup>+0.13</sup> <sub>-0.13</sub>
33	11.92	12.21	11.48	6061 <sup>+193</sup> <sub>-59</sub>	1.32 <sup>+0.03</sup> <sub>-0.08</sub>	2.12 ± 0.04	+3.52 <sup>+0.19</sup> <sub>-0.17</sub>
34	11.07	11.38	10.61	5930 <sup>+44</sup> <sub>-112</sub>	5.49 <sup>+0.21</sup> <sub>-0.08</sub>	33.57 ± 2.11	-0.60 <sup>+0.21</sup> <sub>-0.57</sub>
35	11.40	11.72	10.92	5904 <sup>+339</sup> <sub>-60</sub>	4.30 <sup>+0.09</sup> <sub>-0.46</sub>	20.22 ± 1.56	-0.28 <sup>+0.16</sup> <sub>-0.51</sub>
36	10.60	11.43	9.73	4113 <sup>+179</sup> <sub>-134</sub>	11.70 <sup>+0.80</sup> <sub>-0.96</sub>	35.28 ± 1.38	+0.16 <sup>+0.12</sup> <sub>-0.13</sub>
37	12.33	12.58	11.94	6449 <sup>+259</sup> <sub>-56</sub>	1.93 <sup>+0.03</sup> <sub>-0.15</sub>	5.80 ± 0.26	+2.40 <sup>+0.30</sup> <sub>-0.24</sub>
38	10.45	11.01	9.77	4850 <sup>+210</sup> <sub>-63</sub>	5.46 <sup>+0.15</sup> <sub>-0.44</sub>	14.87 ± 0.46	+1.73 <sup>+0.13</sup> <sub>-0.11</sub>
39	10.87	11.08	10.53	6823 <sup>+124</sup> <sub>-95</sub>	2.68 <sup>+0.08</sup> <sub>-0.09</sub>	14.04 ± 0.51	+1.06 <sup>+0.46</sup> <sub>-0.24</sub>



TABLE F.4: Calculated parameters of the observed stars. The distances  $d$  are calculated from the parallaxes  $\pi$  in Table F.1 as  $d = 1/\pi$ , the total proper motions as  $\mu_{\text{tot}} = \sqrt{\mu_{\text{RA}}^2 + \mu_{\text{DEC}}^2}$ , the transverse velocities as  $v_{\mu} = 149.598 \times 10^6 \text{ km} \times \mu_{\text{tot}} / (3.1558 \times 10^7 \text{ s} \times \pi)$ , where  $149.598 \times 10^6 \text{ km}$  is the Astronomical Unit and  $3.1558 \times 10^7 \text{ s}$  is the length of a year. Columns 5 and 6 give right ascension and declination at the time of the SN, calculated as  $\text{RA}_{\text{SN}} = \text{RA} - \mu_{\text{RA}} t$ , where  $t$  is the age of the SNR (analogous for  $\text{DEC}_{\text{SN}}$ ). Column 7 gives the angular distance  $\rho$  to the GC at the time of the SN, according to Eqn. 3.5, where the errors are computed with the GC error from the *Gaia* DR1 selection.

#	$d$ [kpc]	$\mu_{\text{tot}}$ [mas/yr]	$v_{\mu}$ [km s <sup>-1</sup> ]	$\text{RA}_{\text{SN}}$ [deg]	$\text{DEC}_{\text{SN}}$ [deg]	$\rho$ [arcmin]
1	0.959 <sup>+0.052</sup> <sub>-0.047</sub>	5.19 ± 0.06	23.59 ± 1.25	84.5507 ± 0.0018	+27.8632 ± 0.0055	11 ± 12
2	1.066 <sup>+0.064</sup> <sub>-0.057</sub>	5.85 ± 0.06	29.55 ± 1.70	84.5951 ± 0.0008	+27.7411 ± 0.0065	10 ± 15
3	1.184 <sup>+0.101</sup> <sub>-0.087</sub>	6.75 ± 0.08	37.88 ± 3.02	84.7356 ± 0.0037	+27.5924 ± 0.0066	14 ± 22
4	1.311 <sup>+0.105</sup> <sub>-0.091</sub>	3.32 ± 0.07	20.60 ± 1.59	99.4883 ± 0.0120	+6.7458 ± 0.0540	21 ± 22
5	0.728 <sup>+0.033</sup> <sub>-0.030</sub>	2.83 ± 0.09	9.77 ± 0.51	99.5581 ± 0.0466	+6.4910 ± 0.0077	11 ± 16
6	0.772 <sup>+0.032</sup> <sub>-0.030</sub>	8.77 ± 0.06	32.11 ± 1.32	99.6136 ± 0.0210	+6.6116 ± 0.1447	11 ± 22
7	1.225 <sup>+0.124</sup> <sub>-0.103</sub>	3.65 ± 0.08	21.23 ± 2.01	99.6058 ± 0.0022	+6.2834 ± 0.0609	16 ± 24
8	0.533 <sup>+0.015</sup> <sub>-0.015</sub>	10.80 ± 0.08	27.29 ± 0.79	99.9038 ± 0.1797	+6.6678 ± 0.0115	14 ± 23
9	1.197 <sup>+0.071</sup> <sub>-0.063</sub>	7.34 ± 0.08	41.67 ± 2.37	99.8154 ± 0.1206	+6.4756 ± 0.0205	4 ± 19
10	1.328 <sup>+0.079</sup> <sub>-0.071</sub>	4.05 ± 0.07	25.52 ± 1.50	99.6750 ± 0.0244	+6.6851 ± 0.0630	12 ± 26
11	0.652 <sup>+0.017</sup> <sub>-0.016</sub>	5.17 ± 0.07	15.96 ± 0.45	99.5929 ± 0.0810	+6.6982 ± 0.0293	15 ± 23
12	1.409 <sup>+0.084</sup> <sub>-0.075</sub>	6.10 ± 0.07	40.77 ± 2.34	99.8454 ± 0.0661	+6.6596 ± 0.0774	11 ± 25
13	1.536 <sup>+0.126</sup> <sub>-0.108</sub>	3.19 ± 0.07	23.21 ± 1.84	99.7931 ± 0.0082	+6.5393 ± 0.0526	3 ± 22
14	1.262 <sup>+0.078</sup> <sub>-0.069</sub>	0.99 ± 0.07	5.91 ± 0.56	99.8096 ± 0.0041	+6.6558 ± 0.0162	10 ± 25
15	2.061 <sup>+0.260</sup> <sub>-0.208</sub>	1.76 ± 0.09	17.20 ± 2.13	99.8764 ± 0.0285	+6.3614 ± 0.0078	11 ± 22
16	1.458 <sup>+0.086</sup> <sub>-0.077</sub>	0.79 ± 0.06	5.43 ± 0.52	99.8491 ± 0.0022	+6.5719 ± 0.0131	7 ± 20
17	1.390 <sup>+0.078</sup> <sub>-0.070</sub>	2.16 ± 0.06	14.26 ± 0.85	99.8346 ± 0.0114	+6.6752 ± 0.0343	12 ± 25
18	0.708 <sup>+0.030</sup> <sub>-0.028</sub>	9.64 ± 0.11	32.36 ± 1.37	99.6611 ± 0.1529	+6.1909 ± 0.0497	19 ± 26
19	1.098 <sup>+0.067</sup> <sub>-0.060</sub>	1.42 ± 0.07	7.37 ± 0.56	99.9097 ± 0.0056	+6.3112 ± 0.0231	15 ± 23
20	2.689 <sup>+0.535</sup> <sub>-0.383</sub>	1.35 ± 0.11	17.26 ± 3.17	99.9669 ± 0.0201	+6.4758 ± 0.0109	13 ± 16
21	0.564 <sup>+0.013</sup> <sub>-0.013</sub>	10.11 ± 0.07	27.01 ± 0.65	99.8555 ± 0.0605	+6.4238 ± 0.1573	8 ± 22
22	1.426 <sup>+0.084</sup> <sub>-0.075</sub>	2.14 ± 0.08	14.47 ± 0.97	100.0536 ± 0.0355	+6.2998 ± 0.0046	22 ± 20
23	1.218 <sup>+0.060</sup> <sub>-0.054</sub>	3.55 ± 0.07	20.51 ± 1.03	100.0854 ± 0.0198	+6.3629 ± 0.0559	22 ± 18
24	0.723 <sup>+0.023</sup> <sub>-0.021</sub>	3.73 ± 0.08	12.80 ± 0.48	100.0020 ± 0.0420	+6.2625 ± 0.0461	21 ± 22
25	0.753 <sup>+0.014</sup> <sub>-0.014</sub>	5.33 ± 0.04	19.03 ± 0.38	125.5278 ± 0.0004	-42.9732 ± 0.0004	2 ± 7
26	0.632 <sup>+0.011</sup> <sub>-0.011</sub>	4.40 ± 0.05	13.19 ± 0.27	125.5495 ± 0.0004	-43.0690 ± 0.0002	4 ± 7
27	0.310 <sup>+0.003</sup> <sub>-0.003</sub>	33.73 ± 0.05	49.56 ± 0.44	128.5970 ± 0.0423	-45.6956 ± 0.0729	9 ± 29
28	0.298 <sup>+0.003</sup> <sub>-0.002</sub>	19.13 ± 0.05	27.06 ± 0.24	128.7265 ± 0.0400	-45.2462 ± 0.0262	36 ± 30
29	0.687 <sup>+0.018</sup> <sub>-0.017</sub>	3.17 ± 0.06	10.32 ± 0.33	133.0123 ± 0.0012	-46.3897 ± 0.0001	3 ± 14
30	0.486 <sup>+0.011</sup> <sub>-0.010</sub>	16.14 ± 0.08	37.18 ± 0.83	133.0231 ± 0.0047	-46.2995 ± 0.0039	2 ± 13
31	0.602 <sup>+0.014</sup> <sub>-0.013</sub>	12.67 ± 0.07	36.15 ± 0.84	133.0184 ± 0.0019	-46.2151 ± 0.0043	7 ± 14
32	0.985 <sup>+0.028</sup> <sub>-0.026</sub>	8.81 ± 0.05	41.14 ± 1.14	133.0388 ± 0.0019	-46.2101 ± 0.0027	8 ± 14
33	0.411 <sup>+0.004</sup> <sub>-0.004</sub>	11.80 ± 0.05	22.96 ± 0.26	133.0561 ± 0.0019	-46.2361 ± 0.0040	6 ± 14
34	1.103 <sup>+0.049</sup> <sub>-0.045</sub>	1.39 ± 0.06	7.28 ± 0.46	75.1307 ± 0.0002	+46.5597 ± 0.0006	8 ± 14
35	0.995 <sup>+0.062</sup> <sub>-0.055</sub>	4.82 ± 0.11	22.72 ± 1.43	75.2238 ± 0.0004	+46.5074 ± 0.0020	10 ± 17
36	0.729 <sup>+0.019</sup> <sub>-0.018</sub>	10.24 ± 0.07	35.36 ± 0.95	75.2826 ± 0.0033	+46.7128 ± 0.0027	3 ± 15
37	0.824 <sup>+0.025</sup> <sub>-0.023</sub>	7.10 ± 0.05	27.76 ± 0.84	75.2970 ± 0.0005	+46.4713 ± 0.0029	12 ± 17
38	0.514 <sup>+0.011</sup> <sub>-0.011</sub>	16.00 ± 0.06	39.01 ± 0.85	75.3059 ± 0.0018	+46.8227 ± 0.0064	10 ± 16
39	0.655 <sup>+0.016</sup> <sub>-0.016</sub>	7.48 ± 0.06	23.22 ± 0.60	75.3197 ± 0.0008	+46.5670 ± 0.0030	7 ± 16

TABLE F.5: *Gaia* DR2 data of the 74 runaway candidates – Positions and kinematics. For general data of these targets, see Table 6.2. Column 1 gives a running number that is also used for the subsequent tables. Column 2 gives the *Gaia* DR2 name, columns 3 and 4 give right ascension and declination in ICRS (International Celestial Reference System), respectively. The positional coordinates are precise to 0.011–0.475 mas. Column 5 gives the parallax  $\pi$  and column 6 and 7 give the proper motion  $\mu$  in right ascension and declination.

#	Name	RA <sub>ICRS</sub> [deg]	DEC <sub>ICRS</sub> [deg]	$\pi$ [mas]	$\mu_{\text{RA}}$ [mas/yr]	$\mu_{\text{DEC}}$ [mas/yr]
1	1859462217726265728	312.592375	+30.504681	1.308 ± 0.061	−29.35 ± 0.08	−33.48 ± 0.08
2	1859461771049581952	312.699079	+30.512013	1.210 ± 0.071	−14.13 ± 0.11	−23.77 ± 0.11
3	1859469532044083968	312.727618	+30.651875	1.637 ± 0.032	+8.32 ± 0.04	−11.21 ± 0.04
4	1859469364551815040	312.727666	+30.624829	1.179 ± 0.036	−19.73 ± 0.05	−15.57 ± 0.05
5	1859469467631489920	312.731500	+30.637080	1.056 ± 0.038	−8.91 ± 0.05	−8.92 ± 0.05
6	1858709945619185664	312.736018	+30.440852	1.160 ± 0.031	−5.54 ± 0.04	−34.80 ± 0.04
7	1859471357406309120	312.739227	+30.710701	1.161 ± 0.063	−2.34 ± 0.11	+0.33 ± 0.08
8	1859471254338021120	312.744587	+30.681094	0.967 ± 0.062	+1.23 ± 0.09	+2.62 ± 0.10
9	1859471288697195136	312.746193	+30.683502	1.599 ± 0.030	+0.49 ± 0.04	−0.17 ± 0.04
10	1859471082528259840	312.753337	+30.679925	1.104 ± 0.043	+4.01 ± 0.06	−3.19 ± 0.06
11	1859470975153131904	312.757722	+30.654955	1.289 ± 0.022	+5.62 ± 0.03	+4.32 ± 0.03
12	1859474823444598144	312.760013	+30.743593	1.109 ± 0.038	+12.65 ± 0.05	+6.65 ± 0.05
13	1859471185617972864	312.763066	+30.695169	1.416 ± 0.166	−1.78 ± 0.22	−6.69 ± 0.22
14	1859471872812767104	312.767008	+30.730001	1.151 ± 0.039	+9.32 ± 0.05	+9.07 ± 0.05
15	1859471219977693056	312.788710	+30.702950	1.429 ± 0.070	+6.22 ± 0.10	+2.48 ± 0.10
16	1858715683695452800	312.791938	+30.448036	1.576 ± 0.031	+8.28 ± 0.04	−45.93 ± 0.04
17	1858719291463059840	312.822423	+30.613069	1.631 ± 0.216	+10.21 ± 0.27	−10.51 ± 0.30
18	1858719085309596672	312.878151	+30.613298	1.014 ± 0.021	+14.21 ± 0.03	−5.79 ± 0.03
19	1859572714338261504	312.898927	+30.971162	2.013 ± 0.605	+20.08 ± 0.80	+49.24 ± 0.98
20	206966712992657792 <sup>1</sup>	75.130367	+46.557565	0.907 ± 0.038	−0.23 ± 0.09	−1.37 ± 0.06
21	206918781157635072 <sup>2</sup>	75.224911	+46.500149	1.005 ± 0.059	+0.74 ± 0.18	−4.76 ± 0.11
22	206994059046621824	75.229514	+46.677188	1.317 ± 0.066	+11.38 ± 0.13	−1.56 ± 0.10
23	206938263129288704 <sup>3</sup>	75.295303	+46.460557	1.213 ± 0.035	−1.09 ± 0.07	−7.02 ± 0.05
24	206942519437580416 <sup>4</sup>	75.316643	+46.555993	1.528 ± 0.037	−1.98 ± 0.08	−7.22 ± 0.06
25	3442490264261174528 <sup>5</sup>	84.935062	+27.780845	0.658 ± 0.067	+12.05 ± 0.16	−9.52 ± 0.11
26	3133462316432771200 <sup>6</sup>	99.711535	+6.590548	0.753 ± 0.042	+1.46 ± 0.07	−3.78 ± 0.07
27	3133412018076162560 <sup>7</sup>	99.781141	+6.460540	0.651 ± 0.050	−0.48 ± 0.08	−3.15 ± 0.07
28	3133486093371718656 <sup>8</sup>	99.804555	+6.631657	0.792 ± 0.046	−0.20 ± 0.09	−0.97 ± 0.07
29	3133407104633600512 <sup>9</sup>	99.833831	+6.350130	0.485 ± 0.054	−1.70 ± 0.09	−0.45 ± 0.08
30	3133414491977266816 <sup>10</sup>	99.851046	+6.552367	0.686 ± 0.038	+0.08 ± 0.07	−0.78 ± 0.06
31	5526325078219949440	125.501325	−42.992833	0.649 ± 0.019	−4.39 ± 0.03	+5.10 ± 0.03
32	5526328136236654208	125.501993	−42.957411	0.972 ± 0.015	−16.16 ± 0.02	+10.41 ± 0.03
33	5526325112579690496	125.521142	−42.978667	0.625 ± 0.069	−7.30 ± 0.10	+8.68 ± 0.11
34	5526324803342055168	125.523390	−43.023089	0.601 ± 0.082	−5.26 ± 0.13	+4.62 ± 0.12
35	5526324906421263744	125.526356	−42.989947	0.687 ± 0.032	−4.43 ± 0.05	+5.18 ± 0.05
36	5526325284378390784	125.542224	−42.991448	0.725 ± 0.028	−3.46 ± 0.04	+3.82 ± 0.04
37	5526324833397363840	125.543606	−43.013791	0.673 ± 0.042	−3.94 ± 0.07	+5.14 ± 0.07
38	5526325250018655616	125.564853	−42.975399	0.654 ± 0.017	−4.27 ± 0.03	+5.31 ± 0.03
39	5526325353097874176	125.573313	−42.977781	0.672 ± 0.020	−4.29 ± 0.03	+5.22 ± 0.03
40	5521967782363042432	128.952112	−45.312827	3.892 ± 0.035	−3.73 ± 0.07	−3.48 ± 0.06

<sup>1</sup> TYC3344-235-1; <sup>2</sup> TYC3344-679-1; <sup>3</sup> TYC3344-683-1; <sup>4</sup> TYC3344-553-1; <sup>5</sup> HD 37424;

<sup>6</sup> TYC159-2771-1; <sup>7</sup> HD 261359; <sup>8</sup> HD 261393; <sup>9</sup> TYC159-2337-1; <sup>10</sup> TYC159-2671-1

Continued.

#	Name	RA <sub>ICRS</sub> [deg]	DEC <sub>ICRS</sub> [deg]	$\pi$ [mas]	$\mu_{\text{RA}}$ [mas/yr]	$\mu_{\text{DEC}}$ [mas/yr]
41	5329655463417782528	132.941726	-46.350325	1.138 ± 0.051	-10.68 ± 0.09	-3.65 ± 0.10
42	5329655257259343232	132.946147	-46.354851	1.137 ± 0.067	-15.34 ± 0.12	+11.60 ± 0.12
43	5329655845686016256	132.958285	-46.338908	1.012 ± 0.029	-9.71 ± 0.05	+11.64 ± 0.05
44	5329655983110009856	132.973636	-46.305272	1.176 ± 0.264	-4.37 ± 0.46	+4.80 ± 0.52
45	5329655776966532864	132.977995	-46.327171	1.295 ± 0.032	-6.10 ± 0.06	+3.12 ± 0.06
46	5329657563672287872	132.980771	-46.278300	1.050 ± 0.047	-8.46 ± 0.08	+8.42 ± 0.10
47	5329656017469763456	132.996284	-46.302485	1.006 ± 0.032	-12.80 ± 0.06	+14.18 ± 0.06
48	5329655811325638272	132.998752	-46.317179	1.307 ± 0.031	-8.05 ± 0.06	+5.22 ± 0.06
49	5329657288780088704	133.001471	-46.299404	0.993 ± 0.153	-6.38 ± 0.30	+4.49 ± 0.28
50	5329654849253600896	133.002264	-46.363585	0.805 ± 0.283	-11.80 ± 0.49	+16.06 ± 0.51
51	5329654849241704320	133.002598	-46.363528	1.004 ± 0.118	-10.52 ± 0.17	+9.91 ± 0.38
52	5329657490638374272 <sup>11</sup>	133.010128	-46.288801	2.058 ± 0.045	-12.42 ± 0.08	+10.31 ± 0.09
53	5329654883601436032	133.021170	-46.371986	1.281 ± 0.053	-5.31 ± 0.09	-1.39 ± 0.09
54	6005336183671977344	227.314358	-40.015328	1.899 ± 0.136	-29.21 ± 0.17	-5.22 ± 0.17
55	6005322405417134848	227.342296	-40.297512	3.715 ± 0.124	-15.74 ± 0.14	-37.81 ± 0.12
56	6005309932830763648	227.363310	-40.407551	4.925 ± 0.070	-15.79 ± 0.13	-62.94 ± 0.09
57	5972266305587974656	258.438306	-39.769985	1.125 ± 0.035	-1.75 ± 0.07	-11.54 ± 0.04
58	5972266443017191680	258.446795	-39.743588	0.858 ± 0.061	-1.16 ± 0.11	-3.97 ± 0.07
59	5972266683540067328	258.447837	-39.720764	0.817 ± 0.099	-2.08 ± 0.20	-4.69 ± 0.13
60	5972266443017192960	258.447971	-39.741474	0.537 ± 0.089	-0.76 ± 0.16	-2.11 ± 0.10
61	5972266447337050496	258.455627	-39.733732	0.526 ± 0.107	-2.49 ± 0.19	-3.42 ± 0.12
62	5972266447374127872	258.456833	-39.734190	0.700 ± 0.068	-1.86 ± 0.11	-2.71 ± 0.08
63	5972266378654585856	258.460201	-39.759748	0.785 ± 0.084	-0.88 ± 0.16	-3.90 ± 0.10
64	5972266477376942848	258.462750	-39.724512	0.914 ± 0.037	-0.11 ± 0.06	-8.25 ± 0.05
65	5972219340115696512	258.463250	-39.777651	0.867 ± 0.125	+0.58 ± 0.23	+0.03 ± 0.15
66	5972266378617336832	258.464085	-39.757037	0.950 ± 0.093	-0.69 ± 0.19	-2.49 ± 0.11
67	5972266481696795008	258.468230	-39.724511	0.580 ± 0.097	+0.56 ± 0.18	-1.66 ± 0.12
68	5972266408657455872	258.471906	-39.739502	0.881 ± 0.100	-0.91 ± 0.20	-2.21 ± 0.14
69	5972266413014335616	258.472737	-39.744801	1.144 ± 0.092	-0.36 ± 0.18	-0.49 ± 0.12
70	5972219374522872576	258.476952	-39.779260	0.615 ± 0.049	-0.94 ± 0.08	-4.08 ± 0.05
71	5972219477602131840	258.480085	-39.756075	0.776 ± 0.029	+0.46 ± 0.06	-1.96 ± 0.03
72	5972266413014326528	258.481037	-39.743528	0.890 ± 0.049	-3.34 ± 0.09	-11.79 ± 0.06
73	5972267886141988864	258.483729	-39.734184	1.063 ± 0.166	-4.01 ± 0.26	-3.12 ± 0.18
74	5972267890445877120	258.487333	-39.732551	0.561 ± 0.109	-1.75 ± 0.23	-3.73 ± 0.15

<sup>11</sup> HD 76060

TABLE F.6: *Gaia* DR2 data of the runaway candidates – Magnitudes and stellar parameters. For general data of these targets, see Table 6.2. Column 1 gives the running number, column 2 gives the  $G$ -band magnitude, accurate to 0.2–6.4 mmag. Columns 3 and 4 give the  $BP$  and  $RP$  magnitudes, respectively, accurate to 0.4–64 mmag. Column 5 gives the effective temperature  $T_{\text{eff}}$ , column 6 the radius  $R$  and column 7 the luminosity  $L$ . Note that  $R$  and  $L$  are not given for stars with  $T_{\text{eff}} > 8000$  K. Finally, column 8 gives the absolute  $G$ -band magnitude which was not given in *Gaia* DR2 but calculated by us with the distance modulus (Eqn. 2.4) and the  $G$ -band extinctions from the *StarHorse* catalogue (see Table F.7).

#	$G$ [mag]	$BP$ [mag]	$RP$ [mag]	$T_{\text{eff}}$ [K]	$R$ [ $R_{\odot}$ ]	$L$ [ $L_{\odot}$ ]	$M_G$ [mag]
1	16.23	16.83	15.49	4920 <sup>+166</sup> <sub>-215</sub>	0.55 <sup>+0.05</sup> <sub>-0.04</sub>	0.158 ± 0.016	+6.36 <sup>+0.18</sup> <sub>-0.16</sub>
2	16.88	17.58	16.08	4413 <sup>+68</sup> <sub>-89</sub>	0.59 <sup>+0.03</sup> <sub>-0.02</sub>	0.120 ± 0.015	+7.34 <sup>+0.15</sup> <sub>-0.16</sub>
3	15.20	15.71	14.53	4905 <sup>+183</sup> <sub>-19</sub>	0.71 <sup>+0.00</sup> <sub>-0.05</sub>	0.261 ± 0.012	+6.11 <sup>+0.10</sup> <sub>-0.14</sub>
4	15.65	16.13	15.02	4924 <sup>+91</sup> <sub>-117</sub>	0.79 <sup>+0.04</sup> <sub>-0.03</sub>	0.329 ± 0.023	+6.25 <sup>+0.17</sup> <sub>-0.19</sub>
5	15.47	15.99	14.82	4920 <sup>+139</sup> <sub>-26</sub>	0.96 <sup>+0.01</sup> <sub>-0.05</sub>	0.485 ± 0.040	+5.28 <sup>+0.16</sup> <sub>-0.18</sub>
6	15.06	15.47	14.48	5232 <sup>+152</sup> <sub>-144</sub>	0.91 <sup>+0.05</sup> <sub>-0.06</sub>	0.553 ± 0.035	+5.28 <sup>+0.17</sup> <sub>-0.13</sub>
7	14.44	–	–	–	–	–	+5.08 <sup>+1.18</sup> <sub>-1.40</sub>
8	16.67	17.24	15.95	5014 <sup>+131</sup> <sub>-220</sub>	0.57 <sup>+0.06</sup> <sub>-0.02</sub>	0.188 ± 0.026	+6.37 <sup>+0.19</sup> <sub>-0.18</sub>
9	14.22	14.63	13.66	5373 <sup>+45</sup> <sub>-14</sub>	0.91 <sup>+0.00</sup> <sub>-0.02</sub>	0.619 ± 0.029	+4.99 <sup>+0.14</sup> <sub>-0.13</sub>
10	15.94	16.43	15.29	4907 <sup>+487</sup> <sub>-140</sub>	0.74 <sup>+0.05</sup> <sub>-0.12</sub>	0.289 ± 0.025	+5.94 <sup>+0.16</sup> <sub>-0.14</sub>
11	14.04	14.36	13.57	5864 <sup>+80</sup> <sub>-116</sub>	1.00 <sup>+0.05</sup> <sub>-0.02</sub>	1.076 ± 0.049	+4.66 <sup>+0.12</sup> <sub>-0.09</sub>
12	15.67	16.20	15.00	4902 <sup>+148</sup> <sub>-129</sub>	0.84 <sup>+0.05</sup> <sub>-0.04</sub>	0.370 ± 0.029	+5.86 <sup>+0.18</sup> <sub>-0.11</sub>
13	16.27	16.82	15.56	4888 <sup>+146</sup> <sub>-150</sub>	0.50 <sup>+0.04</sup> <sub>-0.03</sub>	0.130 ± 0.031	+6.51 <sup>+0.29</sup> <sub>-0.28</sub>
14	15.72	16.28	15.03	5014 <sup>+136</sup> <sub>-148</sub>	0.75 <sup>+0.05</sup> <sub>-0.04</sub>	0.320 ± 0.025	+5.79 <sup>+0.15</sup> <sub>-0.14</sub>
15	16.88	17.71	15.95	4149 <sup>+262</sup> <sub>-224</sub>	0.61 <sup>+0.07</sup> <sub>-0.07</sub>	0.099 ± 0.010	+7.28 <sup>+0.90</sup> <sub>-0.20</sub>
16	13.01	13.35	12.51	5725 <sup>+122</sup> <sub>-390</sub>	1.39 <sup>+0.21</sup> <sub>-0.06</sub>	1.872 ± 0.080	+3.79 <sup>+0.19</sup> <sub>-0.14</sub>
17	16.95	16.95	15.78	5096 <sup>+1842</sup> <sub>-837</sub>	–	–	–
18	13.84	14.22	13.29	5240 <sup>+142</sup> <sub>-438</sub>	1.81 <sup>+0.35</sup> <sub>-0.09</sub>	2.229 ± 0.121	+3.37 <sup>+0.19</sup> <sub>-0.18</sub>
19	15.02	15.49	14.09	4509 <sup>+374</sup> <sub>-212</sub>	–	–	+5.71 <sup>+0.79</sup> <sub>-0.70</sub>
20	11.07	11.38	10.61	5930 <sup>+44</sup> <sub>-112</sub>	5.49 <sup>+0.21</sup> <sub>-0.08</sub>	33.566 ± 2.106	–0.60 <sup>+0.21</sup> <sub>-0.57</sub>
21	11.40	11.72	10.92	5904 <sup>+339</sup> <sub>-60</sub>	4.30 <sup>+0.09</sup> <sub>-0.46</sub>	20.218 ± 1.559	–0.28 <sup>+0.16</sup> <sub>-0.51</sub>
22	16.27	17.06	15.41	4172 <sup>+184</sup> <sub>-68</sub>	0.85 <sup>+0.03</sup> <sub>-0.07</sub>	0.199 ± 0.021	+5.50 <sup>+0.23</sup> <sub>-0.54</sub>
23	12.33	12.58	11.94	6449 <sup>+259</sup> <sub>-56</sub>	1.93 <sup>+0.03</sup> <sub>-0.15</sub>	5.799 ± 0.256	+2.40 <sup>+0.30</sup> <sub>-0.24</sub>
24	10.87	11.08	10.53	6823 <sup>+124</sup> <sub>-95</sub>	2.68 <sup>+0.08</sup> <sub>-0.09</sub>	14.039 ± 0.513	+1.06 <sup>+0.46</sup> <sub>-0.24</sub>
25	8.91	8.98	8.79	8712 <sup>+292</sup> <sub>-1614</sub>	–	–	–2.84 <sup>+0.23</sup> <sub>-0.23</sub>
26	12.01	12.13	11.78	8107 <sup>+162</sup> <sub>-158</sub>	–	–	+1.11 <sup>+0.23</sup> <sub>-0.25</sub>
27	11.79	11.87	11.62	8549 <sup>+286</sup> <sub>-243</sub>	–	–	+0.89 <sup>+0.26</sup> <sub>-0.26</sub>
28	10.05	10.07	10.02	9179 <sup>+354</sup> <sub>-735</sub>	–	–	–0.61 <sup>+0.17</sup> <sub>-0.24</sub>
29	11.80	11.88	11.61	9033 <sup>+260</sup> <sub>-334</sub>	–	–	–0.04 <sup>+0.27</sup> <sub>-0.27</sub>
30	12.25	12.31	12.08	8833 <sup>+187</sup> <sub>-277</sub>	–	–	+1.25 <sup>+0.19</sup> <sub>-0.22</sub>
31	13.58	13.92	13.05	5569 <sup>+225</sup> <sub>-173</sub>	2.77 <sup>+0.18</sup> <sub>-0.21</sub>	6.670 ± 0.530	+1.74 <sup>+0.67</sup> <sub>-0.30</sub>
32	13.17	13.74	12.46	5042 <sup>+115</sup> <sub>-180</sub>	2.82 <sup>+0.22</sup> <sub>-0.12</sub>	4.640 ± 0.211	+1.93 <sup>+0.20</sup> <sub>-0.20</sub>
33	16.86	17.74	15.92	3952 <sup>+127</sup> <sub>-48</sub>	1.64 <sup>+0.04</sup> <sub>-0.10</sub>	0.593 ± 0.139	+4.14 <sup>+0.26</sup> <sub>-0.25</sub>
34	16.92	17.93	15.89	3642 <sup>+98</sup> <sub>-43</sub>	2.18 <sup>+0.05</sup> <sub>-0.11</sub>	0.752 ± 0.213	+4.00 <sup>+0.46</sup> <sub>-0.35</sub>
35	15.47	16.18	14.64	4530 <sup>+207</sup> <sub>-180</sub>	1.85 <sup>+0.15</sup> <sub>-0.16</sub>	1.294 ± 0.143	+3.06 <sup>+0.24</sup> <sub>-0.52</sub>
36	14.87	15.64	14.00	4308 <sup>+92</sup> <sub>-191</sub>	2.68 <sup>+0.25</sup> <sub>-0.11</sub>	2.227 ± 0.210	+2.35 <sup>+0.22</sup> <sub>-0.21</sub>
37	15.99	16.82	15.07	4080 <sup>+254</sup> <sub>-141</sub>	2.05 <sup>+0.15</sup> <sub>-0.23</sub>	1.051 ± 0.147	+3.26 <sup>+0.27</sup> <sub>-0.21</sub>
38	13.56	13.94	13.01	5269 <sup>+143</sup> <sub>-358</sub>	3.16 <sup>+0.47</sup> <sub>-0.17</sub>	6.916 ± 0.524	+0.74 <sup>+0.12</sup> <sub>-0.60</sub>
39	13.00	13.23	12.60	6570 <sup>+325</sup> <sub>-467</sub>	2.46 <sup>+0.40</sup> <sub>-0.22</sub>	10.191 ± 0.724	+0.78 <sup>+0.11</sup> <sub>-0.71</sub>
40	15.85	16.90	14.82	4129 <sup>+696</sup> <sub>-458</sub>	–	–	+8.73 <sup>+0.07</sup> <sub>-0.06</sub>

Continued.

#	$G$ [mag]	$BP$ [mag]	$RP$ [mag]	$T_{\text{eff}}$ [K]	$R$ [ $R_{\odot}$ ]	$L$ [ $L_{\odot}$ ]	$M_G$ [mag]
41	16.38	17.12	15.54	$4305^{+190}_{-186}$	$0.85^{+0.08}_{-0.07}$	$0.225 \pm 0.022$	$+5.88^{+0.23}_{-0.17}$
42	16.87	17.67	15.96	$4094^{+182}_{-136}$	$0.80^{+0.06}_{-0.07}$	$0.162 \pm 0.020$	$+4.73^{+0.18}_{-0.16}$
43	15.13	15.77	14.36	$4438^{+168}_{-84}$	$1.56^{+0.06}_{-0.11}$	$0.852 \pm 0.060$	$+4.21^{+0.08}_{-0.09}$
44	16.57	17.35	15.58	$4014^{+233}_{-86}$	–	–	$+4.82^{+0.52}_{-0.54}$
45	15.24	15.75	14.57	$4853^{+79}_{-104}$	$0.90^{+0.04}_{-0.03}$	$0.406 \pm 0.024$	$+5.29^{+0.18}_{-0.17}$
46	16.26	16.96	15.24	$4263^{+124}_{-291}$	$1.01^{+0.15}_{-0.06}$	$0.302 \pm 0.030$	$+4.79^{+0.23}_{-0.27}$
47	15.30	15.88	14.55	$4873^{+149}_{-225}$	$1.12^{+0.11}_{-0.06}$	$0.638 \pm 0.049$	–
48	14.91	15.34	14.32	$5187^{+313}_{-159}$	$0.88^{+0.05}_{-0.10}$	$0.503 \pm 0.029$	$+5.18^{+0.14}_{-0.17}$
49	16.62	17.07	15.24	$4469^{+458}_{-301}$	–	–	–
50	14.97	15.48	14.12	$4800^{+329}_{-375}$	–	–	$+1.60^{+0.76}_{-1.41}$
51	16.82	–	–	–	–	–	$+7.54^{+1.48}_{-1.52}$
52	7.85	7.83	7.92	$8599^{+942}_{-854}$	–	–	$-0.63^{+0.11}_{-0.11}$
53	14.91	15.34	14.27	$5049^{+189}_{-71}$	$0.96^{+0.03}_{-0.07}$	$0.541 \pm 0.049$	$+5.17^{+0.15}_{-0.18}$
54	16.31	17.20	15.38	$3927^{+146}_{-27}$	$0.71^{+0.01}_{-0.05}$	$0.108 \pm 0.016$	$+7.47^{+0.18}_{-0.18}$
55	15.95	16.62	14.76	$4391^{+363}_{-637}$	–	–	$+7.48^{+0.19}_{-0.26}$
56	15.70	16.82	14.64	$3685^{+309}_{-139}$	–	–	$+9.18^{+0.07}_{-0.06}$
57	14.71	15.27	13.98	$4940^{+169}_{-176}$	$1.27^{+0.09}_{-0.09}$	$0.861 \pm 0.063$	$+3.78^{+0.33}_{-0.23}$
58	15.97	16.79	15.04	$3978^{+362}_{-185}$	$1.76^{+0.18}_{-0.28}$	$0.699 \pm 0.106$	$+3.52^{+0.27}_{-0.26}$
59	16.84	17.73	15.81	$3923^{+356}_{-156}$	$1.30^{+0.11}_{-0.21}$	$0.361 \pm 0.090$	–
60	16.65	17.45	15.55	$3937^{+285}_{-284}$	–	–	$+1.70^{+0.40}_{-1.92}$
61	16.98	17.76	15.82	$3973^{+239}_{-281}$	–	–	$+3.39^{+0.63}_{-0.77}$
62	15.01	15.70	14.15	$4379^{+225}_{-117}$	$2.48^{+0.14}_{-0.23}$	$2.042 \pm 0.411$	$+1.44^{+0.24}_{-0.31}$
63	16.59	17.35	15.62	$4101^{+87}_{-151}$	$1.31^{+0.10}_{-0.05}$	$0.437 \pm 0.097$	$+3.97^{+0.39}_{-0.53}$
64	14.81	15.39	14.05	$4812^{+386}_{-325}$	$1.59^{+0.24}_{-0.22}$	$1.228 \pm 0.114$	$+3.76^{+0.25}_{-0.19}$
65	16.54	–	–	–	–	–	$+6.68^{+1.38}_{-1.60}$
66	16.40	17.02	15.43	$4419^{+263}_{-282}$	$0.94^{+0.13}_{-0.11}$	$0.301 \pm 0.061$	–
67	16.92	17.64	15.99	$4346^{+354}_{-396}$	–	–	$+4.02^{+1.21}_{-0.62}$
68	16.88	17.69	15.83	$4060^{+324}_{-381}$	$1.05^{+0.23}_{-0.15}$	$0.272 \pm 0.063$	$+4.20^{+0.30}_{-0.28}$
69	16.59	17.52	15.47	$3746^{+362}_{-229}$	$1.21^{+0.17}_{-0.20}$	$0.261 \pm 0.043$	$+4.42^{+0.24}_{-0.22}$
70	15.04	15.70	14.22	$4401^{+85}_{-151}$	$2.74^{+0.20}_{-0.10}$	$2.542 \pm 0.444$	$+1.44^{+0.25}_{-0.36}$
71	13.47	13.87	12.88	$5322^{+178}_{-172}$	$2.70^{+0.19}_{-0.17}$	$5.281 \pm 0.473$	$+2.59^{+0.15}_{-0.17}$
72	15.62	16.32	14.54	$4302^{+100}_{-384}$	$1.55^{+0.32}_{-0.07}$	$0.743 \pm 0.091$	$+3.41^{+0.36}_{-0.30}$
73	13.94	18.45	12.19	$3283^{+41}_{-11}$	–	–	–
74	16.91	17.58	15.79	$4412^{+139}_{-494}$	–	–	–





Continued.

#	$d$ [kpc]	$A_V$ [mag]	$A_G$ [mag]	$T_{\text{eff}}$ [K]	$\log(g/\text{cm s}^{-2})$	$Z$	$M$ [ $M_{\odot}$ ]
41	0.843 <sup>+0.050</sup> <sub>-0.042</sub>	0.96 <sup>+0.27</sup> <sub>-0.19</sub>	0.79 <sup>+0.21</sup> <sub>-0.14</sub>	4977 <sup>+258</sup> <sub>-169</sub>	4.56 <sup>+0.03</sup> <sub>-0.04</sub>	+0.28 <sup>+0.15</sup> <sub>-0.26</sub>	0.83 <sup>+0.06</sup> <sub>-0.04</sub>
42	0.872 <sup>+0.066</sup> <sub>-0.061</sub>	3.02 <sup>+0.17</sup> <sub>-0.13</sub>	2.42 <sup>+0.13</sup> <sub>-0.10</sub>	6292 <sup>+224</sup> <sub>-165</sub>	4.47 <sup>+0.06</sup> <sub>-0.08</sub>	-1.22 <sup>+0.51</sup> <sub>-0.80</sub>	0.81 <sup>+0.09</sup> <sub>-0.07</sub>
43	0.952 <sup>+0.043</sup> <sub>-0.039</sub>	1.13 <sup>+0.05</sup> <sub>-0.08</sub>	0.94 <sup>+0.04</sup> <sub>-0.06</sub>	5606 <sup>+144</sup> <sub>-117</sub>	4.21 <sup>+0.07</sup> <sub>-0.05</sub>	+0.20 <sup>+0.19</sup> <sub>-0.20</sub>	1.00 <sup>+0.04</sup> <sub>-0.07</sub>
44	1.810 <sup>+2.065</sup> <sub>-0.012</sub>	2.61 <sup>+0.25</sup> <sub>-0.29</sub>	2.11 <sup>+0.19</sup> <sub>-0.22</sub>	6132 <sup>+395</sup> <sub>-405</sub>	4.40 <sup>+0.13</sup> <sub>-0.23</sub>	-0.41 <sup>+0.29</sup> <sub>-0.39</sub>	0.93 <sup>+0.16</sup> <sub>-0.12</sub>
45	0.738 <sup>+0.031</sup> <sub>-0.029</sub>	0.61 <sup>+0.23</sup> <sub>-0.21</sub>	0.52 <sup>+0.18</sup> <sub>-0.16</sub>	5418 <sup>+278</sup> <sub>-223</sub>	4.53 <sup>+0.03</sup> <sub>-0.04</sub>	-0.08 <sup>+0.28</sup> <sub>-0.30</sub>	0.85 <sup>+0.07</sup> <sub>-0.07</sub>
46	0.926 <sup>+0.055</sup> <sub>-0.056</sub>	1.94 <sup>+0.27</sup> <sub>-0.32</sub>	1.58 <sup>+0.21</sup> <sub>-0.25</sub>	5747 <sup>+315</sup> <sub>-304</sub>	4.44 <sup>+0.06</sup> <sub>-0.07</sub>	-0.09 <sup>+0.29</sup> <sub>-0.29</sub>	0.93 <sup>+0.09</sup> <sub>-0.07</sub>
47	-	-	-	-	-	-	-
48	0.743 <sup>+0.034</sup> <sub>-0.026</sub>	0.37 <sup>+0.17</sup> <sub>-0.21</sub>	0.31 <sup>+0.13</sup> <sub>-0.17</sub>	5621 <sup>+215</sup> <sub>-240</sub>	4.53 <sup>+0.04</sup> <sub>-0.04</sub>	-0.26 <sup>+0.29</sup> <sub>-0.22</sub>	0.85 <sup>+0.05</sup> <sub>-0.06</sub>
49	-	-	-	-	-	-	-
50	2.144 <sup>+1.829</sup> <sub>-1.270</sub>	3.24 <sup>+0.07</sup> <sub>-1.54</sub>	2.90 <sup>+0.05</sup> <sub>-1.19</sub>	12869 <sup>+1593</sup> <sub>-6465</sub>	4.12 <sup>+0.20</sup> <sub>-0.31</sub>	-0.28 <sup>+0.28</sup> <sub>-0.34</sub>	2.91 <sup>+1.12</sup> <sub>-1.81</sub>
51	1.007 <sup>+0.190</sup> <sub>-0.126</sub>	-0.83 <sup>+1.89</sup> <sub>-1.95</sub>	-0.71 <sup>+1.46</sup> <sub>-1.50</sub>	4274 <sup>+1055</sup> <sub>-672</sub>	4.68 <sup>+0.15</sup> <sub>-0.10</sub>	-0.27 <sup>+0.30</sup> <sub>-0.36</sub>	0.61 <sup>+0.18</sup> <sub>-0.18</sub>
52	0.476 <sup>+0.011</sup> <sub>-0.013</sub>	0.05 <sup>+0.13</sup> <sub>-0.14</sub>	0.05 <sup>+0.10</sup> <sub>-0.10</sub>	11314 <sup>+1406</sup> <sub>-999</sub>	3.78 <sup>+0.09</sup> <sub>-0.08</sub>	-0.15 <sup>+0.32</sup> <sub>-0.33</sub>	3.25 <sup>+0.33</sup> <sub>-0.38</sub>
53	0.740 <sup>+0.068</sup> <sub>-0.044</sub>	0.32 <sup>+0.16</sup> <sub>-0.20</sub>	0.28 <sup>+0.13</sup> <sub>-0.15</sub>	5406 <sup>+204</sup> <sub>-220</sub>	4.49 <sup>+0.05</sup> <sub>-0.06</sub>	+0.11 <sup>+0.27</sup> <sub>-0.23</sub>	0.89 <sup>+0.06</sup> <sub>-0.05</sub>
54	0.515 <sup>+0.042</sup> <sub>-0.008</sub>	0.29 <sup>+0.13</sup> <sub>-0.12</sub>	0.24 <sup>+0.10</sup> <sub>-0.09</sub>	4123 <sup>+117</sup> <sub>-40</sub>	4.63 <sup>+0.03</sup> <sub>-0.02</sub>	+0.13 <sup>+0.28</sup> <sub>-0.12</sub>	0.68 <sup>+0.03</sup> <sub>-0.03</sub>
55	0.274 <sup>+0.015</sup> <sub>-0.013</sub>	1.66 <sup>+0.23</sup> <sub>-0.32</sub>	1.32 <sup>+0.18</sup> <sub>-0.25</sub>	4507 <sup>+228</sup> <sub>-269</sub>	4.73 <sup>+0.04</sup> <sub>-0.04</sub>	-0.70 <sup>+0.30</sup> <sub>-0.41</sub>	0.56 <sup>+0.04</sup> <sub>-0.01</sub>
56	0.210 <sup>+0.002</sup> <sub>-0.004</sub>	-0.03 <sup>+0.08</sup> <sub>-0.06</sub>	-0.02 <sup>+0.06</sup> <sub>-0.05</sub>	3553 <sup>+39</sup> <sub>-22</sub>	4.76 <sup>+0.01</sup> <sub>-0.01</sub>	-0.00 <sup>+0.03</sup> <sub>-0.11</sub>	0.50 <sup>+0.00</sup> <sub>-0.01</sub>
57	0.858 <sup>+0.061</sup> <sub>-0.045</sub>	1.42 <sup>+0.41</sup> <sub>-0.29</sub>	1.19 <sup>+0.32</sup> <sub>-0.22</sub>	6199 <sup>+711</sup> <sub>-396</sub>	4.25 <sup>+0.09</sup> <sub>-0.09</sub>	-0.22 <sup>+0.33</sup> <sub>-0.31</sub>	1.05 <sup>+0.19</sup> <sub>-0.12</sub>
58	1.127 <sup>+0.129</sup> <sub>-0.104</sub>	2.62 <sup>+0.28</sup> <sub>-0.28</sub>	2.12 <sup>+0.22</sup> <sub>-0.21</sub>	6285 <sup>+475</sup> <sub>-387</sub>	4.19 <sup>+0.10</sup> <sub>-0.12</sub>	-0.28 <sup>+0.29</sup> <sub>-0.23</sub>	1.06 <sup>+0.18</sup> <sub>-0.14</sub>
59	-	-	-	-	-	-	-
60	2.344 <sup>+0.746</sup> <sub>-0.548</sub>	4.27 <sup>+0.21</sup> <sub>-2.45</sub>	3.60 <sup>+0.17</sup> <sub>-1.88</sub>	10941 <sup>+2592</sup> <sub>-5925</sub>	4.22 <sup>+0.20</sup> <sub>-0.56</sub>	-0.31 <sup>+0.39</sup> <sub>-0.38</sub>	2.17 <sup>+0.78</sup> <sub>-1.14</sub>
61	3.371 <sup>+3.542</sup> <sub>-0.963</sub>	2.74 <sup>+0.59</sup> <sub>-0.82</sub>	2.19 <sup>+0.46</sup> <sub>-0.63</sub>	5960 <sup>+932</sup> <sub>-1032</sub>	3.89 <sup>+0.29</sup> <sub>-1.07</sub>	-0.20 <sup>+0.33</sup> <sub>-0.33</sub>	1.21 <sup>+0.33</sup> <sub>-0.24</sub>
62	1.370 <sup>+0.336</sup> <sub>-0.194</sub>	3.31 <sup>+0.15</sup> <sub>-0.29</sub>	2.80 <sup>+0.12</sup> <sub>-0.22</sub>	9320 <sup>+716</sup> <sub>-949</sub>	4.20 <sup>+0.10</sup> <sub>-0.16</sub>	-0.23 <sup>+0.24</sup> <sub>-0.30</sub>	1.90 <sup>+0.32</sup> <sub>-0.24</sub>
63	1.276 <sup>+0.236</sup> <sub>-0.161</sub>	2.59 <sup>+0.40</sup> <sub>-0.61</sub>	2.10 <sup>+0.31</sup> <sub>-0.47</sub>	6303 <sup>+652</sup> <sub>-561</sub>	4.35 <sup>+0.10</sup> <sub>-0.13</sub>	-0.32 <sup>+0.43</sup> <sub>-0.40</sub>	1.02 <sup>+0.20</sup> <sub>-0.12</sub>
64	1.080 <sup>+0.089</sup> <sub>-0.067</sub>	1.03 <sup>+0.31</sup> <sub>-0.22</sub>	0.85 <sup>+0.24</sup> <sub>-0.17</sub>	5473 <sup>+340</sup> <sub>-293</sub>	3.93 <sup>+0.07</sup> <sub>-0.08</sub>	-0.22 <sup>+0.31</sup> <sub>-0.20</sub>	0.94 <sup>+0.08</sup> <sub>-0.05</sub>
65	1.247 <sup>+0.342</sup> <sub>-0.225</sub>	-0.52 <sup>+1.74</sup> <sub>-2.03</sub>	-0.44 <sup>+1.34</sup> <sub>-1.57</sub>	4851 <sup>+1002</sup> <sub>-921</sub>	4.63 <sup>+0.10</sup> <sub>-0.16</sub>	-0.27 <sup>+0.30</sup> <sub>-0.36</sub>	0.70 <sup>+0.22</sup> <sub>-0.17</sub>
66	-	-	-	-	-	-	-
67	2.029 <sup>+0.736</sup> <sub>-0.547</sub>	2.11 <sup>+1.50</sup> <sub>-0.65</sub>	1.72 <sup>+1.15</sup> <sub>-0.50</sub>	6158 <sup>+3290</sup> <sub>-836</sub>	4.31 <sup>+0.12</sup> <sub>-0.30</sub>	-0.19 <sup>+0.40</sup> <sub>-0.43</sub>	1.14 <sup>+0.58</sup> <sub>-0.21</sub>
68	1.116 <sup>+0.150</sup> <sub>-0.136</sub>	3.02 <sup>+0.21</sup> <sub>-0.17</sub>	2.41 <sup>+0.16</sup> <sub>-0.13</sub>	6252 <sup>+343</sup> <sub>-286</sub>	4.35 <sup>+0.10</sup> <sub>-0.09</sub>	-0.50 <sup>+0.30</sup> <sub>-0.41</sub>	0.94 <sup>+0.13</sup> <sub>-0.10</sub>
69	0.832 <sup>+0.105</sup> <sub>-0.091</sub>	3.12 <sup>+0.21</sup> <sub>-0.18</sub>	2.46 <sup>+0.16</sup> <sub>-0.14</sub>	5812 <sup>+272</sup> <sub>-229</sub>	4.31 <sup>+0.09</sup> <sub>-0.10</sub>	-0.12 <sup>+0.24</sup> <sub>-0.38</sub>	0.90 <sup>+0.08</sup> <sub>-0.06</sub>
70	1.514 <sup>+0.306</sup> <sub>-0.196</sub>	3.02 <sup>+0.23</sup> <sub>-0.41</sub>	2.54 <sup>+0.18</sup> <sub>-0.32</sub>	8741 <sup>+900</sup> <sub>-1004</sub>	4.11 <sup>+0.15</sup> <sub>-0.13</sub>	-0.21 <sup>+0.33</sup> <sub>-0.29</sub>	1.86 <sup>+0.25</sup> <sub>-0.24</sub>
71	1.232 <sup>+0.070</sup> <sub>-0.062</sub>	0.39 <sup>+0.17</sup> <sub>-0.19</sub>	0.33 <sup>+0.13</sup> <sub>-0.15</sub>	5312 <sup>+221</sup> <sub>-211</sub>	3.45 <sup>+0.09</sup> <sub>-0.08</sub>	-0.68 <sup>+0.31</sup> <sub>-0.49</sub>	0.98 <sup>+0.16</sup> <sub>-0.13</sub>
72	1.085 <sup>+0.098</sup> <sub>-0.082</sub>	2.42 <sup>+0.45</sup> <sub>-0.35</sub>	1.96 <sup>+0.34</sup> <sub>-0.27</sub>	6142 <sup>+750</sup> <sub>-508</sub>	4.08 <sup>+0.15</sup> <sub>-0.12</sub>	-0.13 <sup>+0.25</sup> <sub>-0.37</sub>	1.12 <sup>+0.25</sup> <sub>-0.15</sub>
73	-	-	-	-	-	-	-
74	-	-	-	-	-	-	-

TABLE F.8: Calculated parameters of the runaway candidates. The distances  $d$  are calculated from the parallaxes  $\pi$  in Table F.5 as  $d = 1/\pi$ , the total proper motions as  $\mu_{\text{tot}} = \sqrt{\mu_{\text{RA}}^2 + \mu_{\text{DEC}}^2}$ , the transverse velocities as  $v_{\mu} = 149.598 \times 10^6 \text{ km} \times \mu_{\text{tot}} / (3.1558 \times 10^7 \text{ s} \times \pi)$ , where  $149.598 \times 10^6 \text{ km}$  is the Astronomical Unit and  $3.1558 \times 10^7 \text{ s}$  is the length of a year. Columns 5 and 6 give right ascension and declination at the time of the SN, calculated as  $\text{RA}_{\text{SN}} = \text{RA} - \mu_{\text{RA}} t$ , where  $t$  is the age of the SNR (analogous for  $\text{DEC}_{\text{SN}}$ ). Column 7 gives the angular distance  $\rho$  to the GC at the time of the SN, according to Eqn. 3.5, where the errors are mainly computed with the GC error from Eqn. 3.6, except for the ten observed runaway candidates in HB9, Monoceros and Vela Jr (see Table F.4).

#	$d$ [kpc]	$\mu_{\text{tot}}$ [mas/yr]	$v_{\mu}$ [km s <sup>-1</sup> ]	$\text{RA}_{\text{SN}}$ [deg]	$\text{DEC}_{\text{SN}}$ [deg]	$\rho$ [arcmin]
1	0.765 <sup>+0.037</sup> <sub>-0.034</sub>	44.53 ± 0.08	161.4 ± 7.5	312.71468 ± 0.04077	+30.64419 ± 0.04651	2.3 ± 4.7
2	0.827 <sup>+0.052</sup> <sub>-0.046</sub>	27.65 ± 0.11	108.4 ± 6.4	312.75795 ± 0.01963	+30.61104 ± 0.03301	3.4 ± 5.1
3	0.611 <sup>+0.012</sup> <sub>-0.012</sub>	13.96 ± 0.04	40.4 ± 0.8	312.69294 ± 0.01156	+30.69859 ± 0.01557	3.5 ± 3.7
4	0.848 <sup>+0.027</sup> <sub>-0.025</sub>	25.13 ± 0.05	101.1 ± 3.1	312.80989 ± 0.02741	+30.68969 ± 0.02162	3.4 ± 3.8
5	0.947 <sup>+0.035</sup> <sub>-0.033</sub>	12.61 ± 0.05	56.6 ± 2.0	312.76861 ± 0.01237	+30.67426 ± 0.01240	1.1 ± 3.5
6	0.862 <sup>+0.024</sup> <sub>-0.022</sub>	35.23 ± 0.04	144.0 ± 3.8	312.75912 ± 0.00770	+30.58583 ± 0.04833	4.9 ± 5.9
7	0.861 <sup>+0.050</sup> <sub>-0.044</sub>	2.36 ± 0.11	9.6 ± 0.7	312.74896 ± 0.00328	+30.70934 ± 0.00057	2.6 ± 4.3
8	1.035 <sup>+0.071</sup> <sub>-0.063</sub>	2.90 ± 0.10	14.2 ± 1.0	312.73945 ± 0.00176	+30.67017 ± 0.00367	0.6 ± 3.4
9	0.625 <sup>+0.012</sup> <sub>-0.012</sub>	0.52 ± 0.04	1.5 ± 0.1	312.74416 ± 0.00070	+30.68419 ± 0.00028	1.1 ± 4.3
10	0.906 <sup>+0.036</sup> <sub>-0.034</sub>	5.12 ± 0.06	22.0 ± 0.9	312.73665 ± 0.00557	+30.69321 ± 0.00444	1.7 ± 4.2
11	0.776 <sup>+0.014</sup> <sub>-0.013</sub>	7.09 ± 0.03	26.1 ± 0.5	312.73429 ± 0.00781	+30.63698 ± 0.00599	2.0 ± 4.2
12	0.902 <sup>+0.032</sup> <sub>-0.030</sub>	14.29 ± 0.05	61.1 ± 2.1	312.70729 ± 0.01758	+30.71590 ± 0.00923	3.7 ± 4.1
13	0.706 <sup>+0.094</sup> <sub>-0.074</sub>	6.92 ± 0.22	23.2 ± 2.8	312.77049 ± 0.00264	+30.72305 ± 0.00934	3.5 ± 4.3
14	0.869 <sup>+0.030</sup> <sub>-0.028</sub>	13.00 ± 0.05	53.6 ± 1.8	312.72817 ± 0.01295	+30.69223 ± 0.01259	1.9 ± 4.1
15	0.700 <sup>+0.036</sup> <sub>-0.032</sub>	6.70 ± 0.10	22.2 ± 1.1	312.76279 ± 0.00865	+30.69262 ± 0.00347	1.7 ± 4.2
16	0.635 <sup>+0.013</sup> <sub>-0.012</sub>	46.67 ± 0.04	140.4 ± 2.7	312.75745 ± 0.01150	+30.63942 ± 0.06379	1.7 ± 6.8
17	0.613 <sup>+0.093</sup> <sub>-0.072</sub>	14.65 ± 0.29	42.6 ± 5.7	312.77989 ± 0.01422	+30.65684 ± 0.01464	1.7 ± 3.5
18	0.986 <sup>+0.020</sup> <sub>-0.020</sub>	15.35 ± 0.03	71.8 ± 1.5	312.81893 ± 0.01974	+30.63742 ± 0.00804	4.0 ± 3.6
19	0.497 <sup>+0.213</sup> <sub>-0.115</sub>	53.18 ± 0.96	125.2 ± 37.7	312.81527 ± 0.02809	+30.76598 ± 0.06852	6.8 ± 6.5
20	1.103 <sup>+0.049</sup> <sub>-0.045</sub>	1.39 ± 0.06	7.3 ± 0.5	75.13072 ± 0.00017	+46.55966 ± 0.00058	8.1 ± 14.1
21	0.995 <sup>+0.062</sup> <sub>-0.052</sub>	4.82 ± 0.11	22.7 ± 1.4	75.22379 ± 0.00041	+46.50742 ± 0.00199	9.6 ± 16.8
22	0.759 <sup>+0.040</sup> <sub>-0.036</sub>	11.49 ± 0.13	41.3 ± 2.1	75.21213 ± 0.00475	+46.67958 ± 0.00067	1.7 ± 3.0
23	0.824 <sup>+0.025</sup> <sub>-0.023</sub>	7.10 ± 0.05	27.8 ± 0.8	75.29697 ± 0.00047	+46.47128 ± 0.00293	11.9 ± 16.7
24	0.655 <sup>+0.016</sup> <sub>-0.016</sub>	7.48 ± 0.06	23.2 ± 0.6	75.31967 ± 0.00084	+46.56702 ± 0.00301	6.6 ± 15.5
25	1.521 <sup>+0.173</sup> <sub>-0.141</sub>	15.36 ± 0.14	110.7 ± 11.3	84.83461 ± 0.01346	+27.86019 ± 0.01062	4.8 ± 7.0
26	1.328 <sup>+0.079</sup> <sub>-0.071</sub>	4.05 ± 0.07	25.5 ± 1.5	99.67501 ± 0.02442	+6.68507 ± 0.06304	12.0 ± 25.8
27	1.536 <sup>+0.126</sup> <sub>-0.108</sub>	3.19 ± 0.07	23.2 ± 1.8	99.79309 ± 0.00821	+6.53934 ± 0.05256	3.5 ± 21.6
28	1.262 <sup>+0.078</sup> <sub>-0.069</sub>	0.99 ± 0.07	5.9 ± 0.6	99.80963 ± 0.00406	+6.65583 ± 0.01622	10.0 ± 25.4
29	2.061 <sup>+0.260</sup> <sub>-0.208</sub>	1.76 ± 0.09	17.2 ± 2.1	99.87638 ± 0.02846	+6.36140 ± 0.00780	11.2 ± 22.4
30	1.458 <sup>+0.086</sup> <sub>-0.077</sub>	0.79 ± 0.06	5.4 ± 0.5	99.84907 ± 0.00217	+6.57192 ± 0.01313	7.3 ± 20.2
31	1.542 <sup>+0.045</sup> <sub>-0.043</sub>	6.73 ± 0.03	49.2 ± 1.4	125.50629 ± 0.00046	-42.99861 ± 0.00053	1.6 ± 1.8
32	1.029 <sup>+0.016</sup> <sub>-0.015</sub>	19.22 ± 0.02	93.8 ± 1.4	125.52028 ± 0.00168	-42.96920 ± 0.00108	2.1 ± 2.7
33	1.600 <sup>+0.200</sup> <sub>-0.160</sub>	11.34 ± 0.11	86.0 ± 9.6	125.52940 ± 0.00077	-42.98849 ± 0.00091	0.9 ± 2.5
34	1.665 <sup>+0.262</sup> <sub>-0.199</sub>	7.00 ± 0.13	55.3 ± 7.6	125.52934 ± 0.00057	-43.02832 ± 0.00050	1.8 ± 2.8
35	1.455 <sup>+0.071</sup> <sub>-0.064</sub>	6.81 ± 0.05	47.0 ± 2.2	125.53137 ± 0.00046	-42.99581 ± 0.00054	0.5 ± 2.1
36	1.379 <sup>+0.055</sup> <sub>-0.051</sub>	5.16 ± 0.04	33.7 ± 1.3	125.54614 ± 0.00036	-42.99578 ± 0.00040	0.3 ± 2.5
37	1.486 <sup>+0.098</sup> <sub>-0.086</sub>	6.47 ± 0.07	45.6 ± 2.9	125.54806 ± 0.00042	-43.01961 ± 0.00054	1.2 ± 2.8
38	1.530 <sup>+0.042</sup> <sub>-0.040</sub>	6.82 ± 0.03	49.4 ± 1.3	125.56969 ± 0.00045	-42.98141 ± 0.00055	1.7 ± 2.4
39	1.487 <sup>+0.045</sup> <sub>-0.042</sub>	6.75 ± 0.03	47.6 ± 1.4	125.57816 ± 0.00045	-42.98369 ± 0.00054	1.9 ± 2.2
40	0.257 <sup>+0.002</sup> <sub>-0.002</sub>	5.10 ± 0.07	6.2 ± 0.1	128.97074 ± 0.00932	-45.29544 ± 0.00870	5.1 ± 5.4

Continued.

#	$d$ [kpc]	$\mu_{\text{tot}}$ [mas/yr]	$v_{\mu}$ [km s $^{-1}$ ]	RA $_{\text{SN}}$ [deg]	DEC $_{\text{SN}}$ [deg]	$\rho$ [arcmin]
41	0.879 $^{+0.041}_{-0.038}$	11.29 $\pm$ 0.09	47.0 $\pm$ 2.1	132.95286 $\pm$ 0.00401	-46.34652 $\pm$ 0.00137	2.1 $\pm$ 2.9
42	0.880 $^{+0.055}_{-0.049}$	19.23 $\pm$ 0.12	80.2 $\pm$ 4.8	132.96213 $\pm$ 0.00575	-46.36693 $\pm$ 0.00435	2.6 $\pm$ 3.8
43	0.988 $^{+0.030}_{-0.028}$	15.16 $\pm$ 0.05	71.0 $\pm$ 2.1	132.96840 $\pm$ 0.00364	-46.35104 $\pm$ 0.00437	1.7 $\pm$ 3.4
44	0.850 $^{+0.246}_{-0.156}$	6.49 $\pm$ 0.49	26.2 $\pm$ 6.2	132.97818 $\pm$ 0.00171	-46.31028 $\pm$ 0.00188	1.7 $\pm$ 3.9
45	0.772 $^{+0.019}_{-0.018}$	6.85 $\pm$ 0.06	25.1 $\pm$ 0.6	132.98435 $\pm$ 0.00229	-46.33042 $\pm$ 0.00117	0.7 $\pm$ 2.8
46	0.952 $^{+0.044}_{-0.040}$	11.93 $\pm$ 0.09	53.9 $\pm$ 2.4	132.98958 $\pm$ 0.00317	-46.28707 $\pm$ 0.00316	2.8 $\pm$ 4.3
47	0.994 $^{+0.033}_{-0.031}$	19.10 $\pm$ 0.06	90.0 $\pm$ 2.9	133.00961 $\pm$ 0.00480	-46.31726 $\pm$ 0.00532	1.0 $\pm$ 4.1
48	0.765 $^{+0.019}_{-0.018}$	9.59 $\pm$ 0.06	34.8 $\pm$ 0.9	133.00714 $\pm$ 0.00302	-46.32262 $\pm$ 0.00196	0.7 $\pm$ 4.1
49	1.007 $^{+0.184}_{-0.135}$	7.80 $\pm$ 0.30	37.3 $\pm$ 5.9	133.00812 $\pm$ 0.00241	-46.30408 $\pm$ 0.00171	1.8 $\pm$ 4.3
50	1.242 $^{+0.673}_{-0.323}$	19.93 $\pm$ 0.50	117.3 $\pm$ 41.3	133.01455 $\pm$ 0.00445	-46.38031 $\pm$ 0.00604	2.9 $\pm$ 4.3
51	0.996 $^{+0.132}_{-0.104}$	14.45 $\pm$ 0.29	68.2 $\pm$ 8.1	133.01355 $\pm$ 0.00395	-46.37385 $\pm$ 0.00374	2.5 $\pm$ 4.3
52	0.486 $^{+0.011}_{-0.010}$	16.14 $\pm$ 0.08	37.2 $\pm$ 0.8	133.02307 $\pm$ 0.00466	-46.29954 $\pm$ 0.00387	2.2 $\pm$ 4.1
53	0.781 $^{+0.034}_{-0.031}$	5.48 $\pm$ 0.09	20.3 $\pm$ 0.9	133.02670 $\pm$ 0.00199	-46.37054 $\pm$ 0.00053	2.5 $\pm$ 4.0
54	0.527 $^{+0.041}_{-0.035}$	29.67 $\pm$ 0.17	74.1 $\pm$ 5.3	227.50096 $\pm$ 0.06492	-39.98199 $\pm$ 0.01165	1.1 $\pm$ 4.4
55	0.269 $^{+0.009}_{-0.009}$	40.95 $\pm$ 0.13	52.3 $\pm$ 1.8	227.44283 $\pm$ 0.03498	-40.05595 $\pm$ 0.08403	4.3 $\pm$ 6.9
56	0.203 $^{+0.003}_{-0.003}$	64.89 $\pm$ 0.09	62.5 $\pm$ 0.9	227.46417 $\pm$ 0.03509	-40.00545 $\pm$ 0.13986	1.7 $\pm$ 4.1
57	0.889 $^{+0.029}_{-0.027}$	11.68 $\pm$ 0.04	49.2 $\pm$ 1.6	258.43910 $\pm$ 0.00003	-39.76477 $\pm$ 0.00002	1.3 $\pm$ 2.5
58	1.166 $^{+0.089}_{-0.077}$	4.14 $\pm$ 0.07	22.9 $\pm$ 1.7	258.44732 $\pm$ 0.00005	-39.74180 $\pm$ 0.00003	0.7 $\pm$ 2.4
59	1.223 $^{+0.168}_{-0.132}$	5.13 $\pm$ 0.14	29.8 $\pm$ 3.7	258.44878 $\pm$ 0.00009	-39.71865 $\pm$ 0.00006	1.9 $\pm$ 2.8
60	1.862 $^{+0.370}_{-0.265}$	2.24 $\pm$ 0.11	19.8 $\pm$ 3.4	258.44831 $\pm$ 0.00007	-39.74052 $\pm$ 0.00005	0.7 $\pm$ 2.6
61	1.900 $^{+0.484}_{-0.321}$	4.23 $\pm$ 0.15	38.1 $\pm$ 7.8	258.45675 $\pm$ 0.00008	-39.73219 $\pm$ 0.00006	1.1 $\pm$ 2.9
62	1.428 $^{+0.154}_{-0.127}$	3.29 $\pm$ 0.09	22.3 $\pm$ 2.2	258.45767 $\pm$ 0.00005	-39.73297 $\pm$ 0.00004	1.0 $\pm$ 2.9
63	1.274 $^{+0.124}_{-0.124}$	4.00 $\pm$ 0.11	24.2 $\pm$ 2.7	258.46060 $\pm$ 0.00007	-39.75799 $\pm$ 0.00005	0.5 $\pm$ 2.8
64	1.094 $^{+0.045}_{-0.042}$	8.25 $\pm$ 0.05	42.8 $\pm$ 1.7	258.46280 $\pm$ 0.00003	-39.72079 $\pm$ 0.00002	1.8 $\pm$ 2.9
65	1.153 $^{+0.195}_{-0.146}$	0.58 $\pm$ 0.23	3.2 $\pm$ 1.4	258.46299 $\pm$ 0.00011	-39.77767 $\pm$ 0.00007	1.7 $\pm$ 2.9
66	1.053 $^{+0.114}_{-0.094}$	2.58 $\pm$ 0.12	12.9 $\pm$ 1.4	258.46440 $\pm$ 0.00008	-39.75592 $\pm$ 0.00005	0.5 $\pm$ 2.6
67	1.723 $^{+0.346}_{-0.247}$	1.75 $\pm$ 0.12	14.3 $\pm$ 2.6	258.46798 $\pm$ 0.00008	-39.72376 $\pm$ 0.00005	1.6 $\pm$ 2.8
68	1.135 $^{+0.145}_{-0.116}$	2.39 $\pm$ 0.15	12.9 $\pm$ 1.7	258.47232 $\pm$ 0.00009	-39.73851 $\pm$ 0.00006	0.9 $\pm$ 2.5
69	0.875 $^{+0.076}_{-0.065}$	0.60 $\pm$ 0.14	2.5 $\pm$ 0.6	258.47290 $\pm$ 0.00008	-39.74458 $\pm$ 0.00005	0.7 $\pm$ 2.1
70	1.627 $^{+0.140}_{-0.119}$	4.19 $\pm$ 0.05	32.3 $\pm$ 2.6	258.47738 $\pm$ 0.00004	-39.77742 $\pm$ 0.00003	1.9 $\pm$ 2.7
71	1.289 $^{+0.050}_{-0.046}$	2.02 $\pm$ 0.04	12.3 $\pm$ 0.5	258.47988 $\pm$ 0.00003	-39.75519 $\pm$ 0.00002	1.0 $\pm$ 2.0
72	1.124 $^{+0.066}_{-0.059}$	12.26 $\pm$ 0.06	65.3 $\pm$ 3.6	258.48255 $\pm$ 0.00004	-39.73821 $\pm$ 0.00003	1.3 $\pm$ 2.2
73	0.941 $^{+0.174}_{-0.127}$	5.09 $\pm$ 0.24	22.7 $\pm$ 3.7	258.48554 $\pm$ 0.00012	-39.73277 $\pm$ 0.00008	1.6 $\pm$ 2.4
74	1.782 $^{+0.428}_{-0.289}$	4.12 $\pm$ 0.17	34.8 $\pm$ 6.9	258.48812 $\pm$ 0.00011	-39.73087 $\pm$ 0.00007	1.8 $\pm$ 2.4



# Appendix G

## Effective temperatures

Here, we provide effective temperatures of the Li-rich stars and the early-type runaway candidates, obtained from different references, as well as the corresponding mean values. Transformations from colour indices or spectral types were done with Pecaut and Mamajek (2013, Table 5). Besides the different methods and references mentioned in the main part of this thesis, we add here the temperatures inferred from the colour indices  $J - H$  (2MASS) and  $B - V$  (APASS).

TABLE G.1: Effective temperatures of the Li-rich stars and the remaining early-type candidates, obtained from the resources given in the table notes. The stars are labeled as introduced in Table 5.5. The last column gives the mean values and standard deviations of all available temperatures. The values that were used for the analysis in Section 5 are marked with an asterisk. All values are given in K.

Name	<i>Gaia</i> DR2 <sup>1</sup>	APF <sup>2</sup>	Skiff <sup>3</sup>	std-stars <sup>4</sup>	2MASS <i>J</i> – <i>H</i> <sup>5</sup>	<i>StarHorse</i> <sup>6</sup>	Bai+2019 <sup>7</sup>	APASS <i>B</i> – <i>V</i> <sup>8</sup>	Mean
1	6257 <sup>+391</sup> <sub>-211</sub>	*6351 ± 78	–	6875 ± 155	6055 ± 285	6438 <sup>+403</sup> <sub>-394</sub>	6316 ± 119	6340 ± 170	6376 ± 232
2	7079 <sup>+112</sup> <sub>-232</sub>	*6749 ± 69	–	7080 ± 360	6780 ± 440	7326 <sup>+722</sup> <sub>-545</sub>	7051 ± 205	6875 ± 155	6991 ± 188
3	5853 <sup>+101</sup> <sub>-90</sub>	*5857 ± 75	–	5940 ± 60	5795 ± 205	5951 <sup>+300</sup> <sub>-251</sub>	5814 ± 150	5840 ± 160	5864 ± 55
4	5614 <sup>+228</sup> <sub>-102</sub>	*5956 ± 73	–	6725 ± 85	5500 ± 220	5962 <sup>+234</sup> <sub>-282</sub>	5830 ± 192	5790 ± 130	5911 ± 368
5	5806 <sup>+23</sup> <sub>-77</sub>	*5955 ± 73	–	6150 ± 90	5610 ± 270	5927 <sup>+430</sup> <sub>-422</sub>	5885 ± 212	5630 ± 290	5852 ± 176
6	6061 <sup>+193</sup> <sub>-59</sub>	*6165 ± 63	–	6375 ± 135	6255 ± 255	6599 <sup>+440</sup> <sub>-369</sub>	6110 ± 125	6120 ± 120	6241 ± 176
H1	5930 <sup>+44</sup> <sub>-112</sub>	–	–	–	6635 ± 395	9789 <sup>+1938</sup> <sub>-2591</sub>	*7707 ± 377	6110 ± 230	7234 ± 1420
H2	5904 <sup>+339</sup> <sub>-60</sub>	–	–	–	7040 ± 400	10822 <sup>+1007</sup> <sub>-3064</sub>	*7591 ± 435	6110 ± 230	7494 ± 1774
H3	6449 <sup>+259</sup> <sub>-56</sub>	–	–	–	6780 ± 440	6954 <sup>+731</sup> <sub>-491</sub>	*7490 ± 360	6195 ± 315	6773 ± 444
H4	6823 <sup>+124</sup> <sub>-93</sub>	–	–	–	7515 ± 485	8145 <sup>+3746</sup> <sub>-675</sub>	*7588 ± 249	6685 ± 345	7351 ± 536
M1	8107 <sup>+192</sup> <sub>-138</sub>	–	*10700 <sup>+2550</sup> <sub>-1250</sub>	9770 ± 930	8170 ± 670	8013 <sup>+577</sup> <sub>-589</sub>	8181 ± 145	7720 ± 280	8666 ± 1033
M2	8549 <sup>+286</sup> <sub>-243</sub>	–	*10700 <sup>+2550</sup> <sub>-1250</sub>	10850 ± 1650	7305 ± 495	7609 <sup>+548</sup> <sub>-544</sub>	8195 ± 267	8175 ± 375	8769 ± 1324
M3	9179 <sup>+354</sup> <sub>-735</sub>	–	*15700 <sup>+1150</sup> <sub>-1450</sub>	12450 ± 2050	10385 ± 2115	10352 <sup>+1192</sup> <sub>-1408</sub>	7431 ± 599	10525 ± 1975	10860 ± 2424
M4	9033 <sup>+260</sup> <sub>-334</sub>	–	*10700 <sup>+2550</sup> <sub>-1250</sub>	10850 ± 1650	7885 ± 665	8164 <sup>+450</sup> <sub>-414</sub>	8176 ± 261	8175 ± 375	8997 ± 1172
M5	8833 <sup>+187</sup> <sub>-277</sub>	–	*12500 <sup>+1750</sup> <sub>-1950</sub>	12450 ± 2050	8750 ± 950	8368 <sup>+592</sup> <sub>-566</sub>	8182 ± 379	8035 ± 235	9588 ± 1845
VJ1	8599 <sup>+942</sup> <sub>-854</sub>	–	*12500 <sup>+1750</sup> <sub>-950</sub>	13200 ± 2500	15150 ± 5450	11314 <sup>+1406</sup> <sub>-999</sub>	7765 ± 525	–	11421 ± 2568

<sup>1</sup> *Gaia* DR2 (Gaia Collaboration et al., 2018); <sup>2</sup> APF: Our atmospheric parameter fits (see Section 5.3); <sup>3</sup> Skiff: The *Skiff* catalogue, in particular Voroshilov et al. (1985) for the stars in the Monoceros Loop (M1–M5) and Houk (1978) for HD 76060; <sup>4</sup> std-stars: Comparison to standard stars (see Section C); <sup>5</sup> 2MASS *J* – *H* (Cutri et al., 2003); <sup>6</sup> *StarHorse* catalogue (Anders et al., 2019); <sup>7</sup> Bai+2019 (Bai et al., 2019); <sup>8</sup> APASS *B* – *V* (Henden et al., 2015); \* Value was used for the analysis in Section 5

# Appendix H

## H $\alpha$ observations of supernova remnants

As described in Section 2.3.1, SNRs emit H $\alpha$  radiation when the shock front interacts with the surrounding ISM. Therefore, H $\alpha$  emission is a good tracer for the SNR morphology, except for the youngest SNRs which did not yet sweep up enough ISM material. We made H $\alpha$  observations of 15 northern SNRs with the *Schmidt Teleskop Kamera* (STK, Mugrauer and Berthold 2010) at the University Observatory Jena (Pfau, 1984). An overview of the targets is given in Table H.1. The purpose of the project was to produce high-quality images, to measure the 2D geometry and to determine the centre of light of the targets with a *Python* code. The centre of light might be a better indicator for the 2D explosion site than the geometric centre (GC), because brighter ejecta indicate a higher ISM density and therefore a slower expansion velocity of the corresponding filaments. However, the procedure should be repeated in as many different wavelength regimes as possible in order to obtain more reliable results. This was e.g. done by Xue and Schaefer (2015) for the Tycho SNR. They determined the GC by drawing baselines from one edge of the SNR shell to the opposite at nine positions, plus the corresponding perpendicular lines, yielding 36 edge points. They obtained the GC by averaging the results from the nine intersections and performed this procedure for images in eight different wavelengths.

Our results presented in this chapter are preliminary and mostly without errors. A complete analysis of the topic will be presented in a forthcoming paper. Wolfgang Stenglein is working on a *Python* code to determine the GCs of the observed SNRs, based on the method presented by Xue and Schaefer (2015), but using more baselines. These results can then be compared to the light centres and to the GCs as given by Green (2014).

Targets which are in common with the sample used for the search for runaway stars are Cygnus Loop, Cassiopeia A, G130.7+03.1 (SN 393), HB9, the Crab Nebula and the Monoceros Loop. An H $\alpha$  image of S147 was already created by Dinçel et al. (2015) with the same instrument. The images are used throughout this thesis as background images to display the movement of the runaway candidates in the central parts of the SNRs.

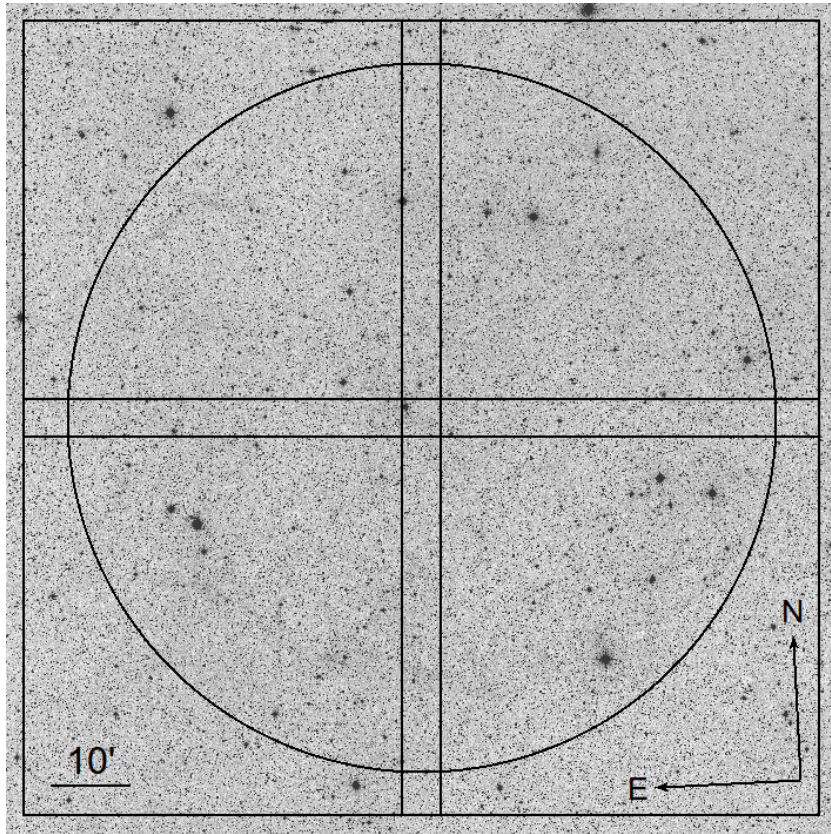


FIGURE H.1: The image shows  $105' \times 105'$  around the Green centre of SNR G119.5+10.2. The overlapping black squares, each with an edge length of  $52.8'$ , corresponding to the STK FOV, show the four different pointings that were used to construct the mosaic image. The black circle represents the rough size of the SNR ( $90' \times 90'$  according to Green 2014), which is very faint in the optical. The background image was taken from ESO DSS-1.

## H.1 Observations

The STK uses the 90-cm tube of the University Observatory Jena, where the *Schmidt* plate has a diameter of 60 cm. The configuration yields a field of view (FOV) of  $52.8' \times 52.8'$ . The targets were observed in 39 nights between 2017 Jun 08 and 2019 Jul 25. Each frame was observed three times with individual integration times of 600 s and with a CCD temperature of  $\sim -22^\circ\text{C}$ . The airmass limit was set to  $X < 1.8$ . In the case of SNRs larger than the FOV, multiple adjacent fields were observed and the resulting images were stacked to mosaics. Fig. H.1 shows the arrangement of observing frames in the case of a  $2 \times 2$  mosaic, exemplary for SNR G119.5+10.2.

In several cases, SNRs or their individual frames were observed multiple times, mainly due to two reasons: (i) An earlier observation suffered from low quality, e.g. an enhanced background flux if the moon was too bright or nearby. (ii) Due to the long exposure times, an afterglow from previous observations could occur. Taking six instead of three images of one



TABLE H.1: Overview of SNRs observed in H $\alpha$ . The columns give name, coordinates (J2000), size, morphological type, distance, age and number of frames. Positions, sizes and types were taken from Green (2014), distances and ages were taken from the UofM catalogue (Ferrand and Safi-Harb, 2012) and references therein.

SNR Name	RA [h:m:s]	DEC [d:m]	$\Theta$ [arcmin]	Type	$d$ [kpc]	$t$ [kyr]	Frames
G073.9+00.9	20:14:15	+36:12	$27 \times 27$	S?	$2.25 \pm 1.75$	$11.5 \pm 0.5$	$1 \times 1$
G074.0-08.5	20:51:00	+30:40	$230 \times 160$	S	$0.79 \pm 0.21$	$15 \pm 5$	$5 \times 5$
G089.0+04.7	20:45:00	+50:35	$120 \times 90$	S	$0.8 \pm 2.2$	$11.4 \pm 6.6$	$3 \times 3$
G114.3+00.3	23:37:00	+61:55	$90 \times 55$	S	0.7	7.7	$2 \times 2$
G116.5+01.1	23:53:40	+63:15	$80 \times 60$	S	1.6	$32.5 \pm 17.5$	$2 \times 2$
G116.9+00.2	23:59:10	+62:26	$34 \times 34$	S	$2.55 \pm 0.95$	$12.75 \pm 5.25$	$1 \times 1$
G119.5+10.2	00:06:40	+72:45	$90 \times 90$	S	$1.4 \pm 0.3$	13	$2 \times 2$
G132.7+01.3	02:17:40	+62:45	$80 \times 80$	S	$2.05 \pm 0.15$	$29 \pm 4$	$2 \times 2$
G160.9+02.6	05:01:00	+46:40	$140 \times 120$	S	$0.80 \pm 0.40$	$5.5 \pm 1.5$	$4 \times 4$
G189.1+03.0	06:17:00	+22:34	$45 \times 45$	C	$1.35 \pm 0.65$	$16.5 \pm 13.5$	$1 \times 1$
G205.5+00.5	06:39:00	+06:30	$220 \times 220$	S	$1.44 \pm 0.54$	$90 \pm 60$	$5 \times 5$
G111.7-02.1*	23:23:26	+58:48	$5 \times 5$	S	$3.50 \pm 0.20$	$0.334 \pm 0.018$	$1 \times 1$
G120.1+01.4*	00:25:18	+64:09	$8 \times 8$	S	$3.25 \pm 1.75$	448	$1 \times 1$
G130.7+03.1*	02:05:41	+64:49	$9 \times 5$	F	$2.60 \pm 0.60$	0.839	$1 \times 1$
G184.6-05.8*	05:34:31	+22:01	$7 \times 5$	F	$1.85 \pm 0.35$	0.966	$1 \times 1$

\* Historical SNR

frame guaranteed that the afterglow in the three latest images was sufficiently reduced. The total on-source integration time for the project was 70 h, 35 min, including multiple observations of the same frame but excluding calibrations. Table H.2 lists the observers that contributed to the observations at the University Observatory Jena.

Table I.1 gives an overview of the observed SNR frames, including date and weather. If frames were observed multiple times, we only list the observations yielding the best quality (i.e. low background, high  $S/N$ , no afterglow, good focus). Besides the 15 SNRs listed here, we also observed SNR G040.5-00.5 and G127.1+00.5. However, due to a lack of visible H $\alpha$  emission and low relevance for this work they were not considered for the analysis.

## H.2 Data reduction

For calibration, 600 s dark frames as well as H $\alpha$  skyflats were taken every few weeks. While it was tried to record the skyflats as often as possible, in the data reduction more priority was given to have a large set of skyflats with high quality. Therefore, temporal offsets of a few weeks between calibration and observation were acceptable. Domeflats were regularly taken but not used for the data reduction.

Data reduction was done with *ESO Eclipse*, either manually or with the pipeline written by Dr. Markus Mugrauer. Master darks and -flats were created from the closest available dataset

### H.3. Image corrections and astrometric calibration

---

TABLE H.2: Overview of the observers who contributed to the SNR observations. The times refer to on-source integration times of the SNRs, rounded to minutes, including multiple observations of the same frame but excluding calibrations.

Observer	Time	Observer	Time
Lux	39 h 05 min	Wagner	7 h 00 min
Bischoff	19 h 50 min	Heyne	3 h 50 min
Stenglein	18 h 00 min	Hartung	1 h 30 min
Zehe	13 h 30 min	Blümcke	1 h 30 min
Gilbert	11 h 10 min	Trepanovski	40 min
Hildebrandt	10 h 30 min	Munz	30 min
Mugrauer	7 h 50 min	Dadalauri	30 min
Geymeier	7 h 15 min	Schubert	20 min
Hoffmann	7 h 10 min	Zielke	20 min

with the required quality. The master darks were subtracted from the individual science frames and the result was divided through the master flat. Then, for each frame the reduced images of the three exposures were averaged by taking the median to increase the  $S/N$  and to get rid of artefacts like airplane- or satellite trails and bright cosmics. The further processing of the combined images is described in the following.

## H.3 Image corrections and astrometric calibration

The next step was to remove further artefacts like blooming around bright stars, bad pixels and possible remaining satellite trails. This was done with *MaxIm DL* by replacing the problematic pixels with a randomised average of neighbouring pixels.

For larger SNRs, the individual mosaic frames were stacked together with *MaxIm DL* (up to  $3 \times 3$ ) or with a *C* code written by Dr. Markus Mugrauer (larger than  $3 \times 3$ ). In *MaxIm DL*, the overlapping edges of neighbouring frames (see Fig. H.1) can be dragged on top of each other, so that the common stars are recognised and the background levels are adjusted to each other. The procedure is repeated for the remaining frames, whereupon the stacked mosaic can be saved as a new file. Due to the curvature of the sky, this procedure does not work for very large mosaics, because *MaxIm DL* can only apply moderate rotations for the stacking. Therefore, the largest mosaics were created by Dr. Markus Mugrauer with a *C* code.

The astrometric calibration was done with *GAIA* - the *Graphical Astronomy and Image Analysis Tool*, by loading *Gaia* DR2 catalogue data for selected stars in the corresponding image area. With *GAIA*, the individual stars in our images could be matched to the coordinates given by *Gaia* DR2, from which pixel scale in x and y, orientation and RMS are calculated. The calibrated image then contains the information of the sky coordinate of each pixel value.

## H.4 Analysis

The calibrated images could be used to measure the 2D geometry, in particular their sizes. For the determination of the light centres, first the stars had to be removed from the image. This was done with the *object detection* in *GAIA*, which creates an additional *.fits* image with only the stars, which is then subtracted from the original image. The thresholds for the object detection were given such that no SNR filaments were accidentally detected. Remaining smaller stars, or artefacts around brighter stars could then be removed by manual patching. Possibly remaining very faint background stars, which are distributed almost isotropically, do not have a significant effect on the result. The patched images were then refurbished by smoothing with an adequate mesh size (4–10), in order to smear out artefacts from the patching and possible remaining faint stars. The smoothing, which averages the pixels in the corresponding mesh size, does not significantly affect the result for the light centre. The steps described here, i.e. image corrections, calibration, removal of stars and smoothing, were partly done by Wolfgang Stenglein and Markus Mugrauer.

### Geometry and sizes

In *ds9*, we measured the sizes of the SNRs in two perpendicular directions in the calibrated images. For each SNR, we first measured the length  $\Theta_a$  of the major axis and then drew a perpendicular line close to the midpoint of the major axis, yielding the minor axis with the length  $\Theta_b$ . Note that the lengths measured here are only a rough estimate, since the endpoints of the axes were only selected visually, which could depend on the flux scaling of the image. The corresponding values are given in Table H.3 and can be compared to the sizes given by Green (2014), listed in Table H.1. Only in the case of regularly shaped shell-type SNRs, we drew an ellipse for which the axis lengths and rotation were taken from the previously measured axes. Note that the position of the ellipse could still be slightly shifted compared to the axes. The midpoint of the ellipse can be seen as a rough estimate for the GC.

### Light centres

The light centre of an SNR yields an estimate of the explosion site. It might be closer to the actual explosion site than the GC, because the light centre will be closer to the brightest regions of the SNR, which usually correspond to regions of higher ISM-density. In these regions, the emission is higher due to a higher number of excitations of ISM-particles. However, the higher number of collisions also slows down the expansion of the SNR shell. Therefore, we expect the explosion site to be closer to brighter regions of the SNR. Note that this consideration does not take into account the past variation of ISM-density along the expansion path. Also, the

SNR morphology can look very different in other wavelengths. Therefore, the approach as presented here is very preliminary. A thorough analysis of SNR explosion sites from imaging observations requires images in as many wavelengths as possible, as well as a theoretical study on the question of how accurately the light centre really represents the explosion site.

In the following, we demonstrate the determination of a SNR light centre exemplary for IC 443 (G189.1+03.0). This is a bright SNR of medium size ( $\Theta = 45'$ , observation of one frame was sufficient). In the UofM catalogue (Ferrand and Safi-Harb, 2012), the distance  $d = 0.7\text{--}2.0$  kpc and the age  $t = 3\text{--}30$  kyr are rather poorly constrained. Due to its high brightness, the edge of the *mixed morphology* SNR IC 443 is easy to see, except in the south, where it interacts with a molecular cloud. In this region, also a NS and a PWN are known. However, an association of the NS with the SNR is unlikely because its proper motion is not pointing back towards the GC (Swartz et al., 2015).

Fig. H.2 shows the main steps in processing the image of IC 443. After obtaining raw images like in panel (a), we obtained the image shown in (b) after data reduction, median-combination of the three exposures and calibration and the image shown in (c) after removing the stars and smoothing with a mesh size of four as described above. For determining the light centre, we only want to consider the emission from the SNR. Besides removing the stars, this was achieved by cropping off the image regions outside the SNR: We defined a polygon in *ds9*, from which a mask and a corresponding new image were created within the *Python* code that was also used for the calculation of the light centre (see Appendix J). All flux values outside the SNR were set to zero. The cropped image shown in panel (d) also contains a simple background subtraction: For the correct weighting of the light centre, the lowest flux value of all pixels in the calibrated image was identified (406 ADU in this case) and subtracted from the whole image, so that a minimum flux of 0–1 ADU was achieved. For defining the polygon, we had to divide between emission regions belonging to the SNR and emission regions associated to unrelated or interacting objects like the molecular cloud at the southern edge of IC 443. This can be quite arbitrary and the transitions can also be fluent. Therefore, it is recommended to repeat the analysis with further possible polygons as well as with images from different wavelengths.

The calculation of the SNR light centre was then performed by adding the flux-weighted pixel coordinates and dividing the result through the sum of the flux values. The result is the flux-weighted mean position of the pixel coordinates,  $(x_{lc}, y_{lc})$ , which is then transformed to right ascension and declination ( $RA_{lc}, DEC_{lc}$ ) by using the astrometric calibration of the image. For most of the SNRs, we defined only one polygon, so the results are given without errors. However, the code presented in Appendix J could easily be adjusted in order to incorporate several polygons and calculate mean and standard deviation for the corresponding results.

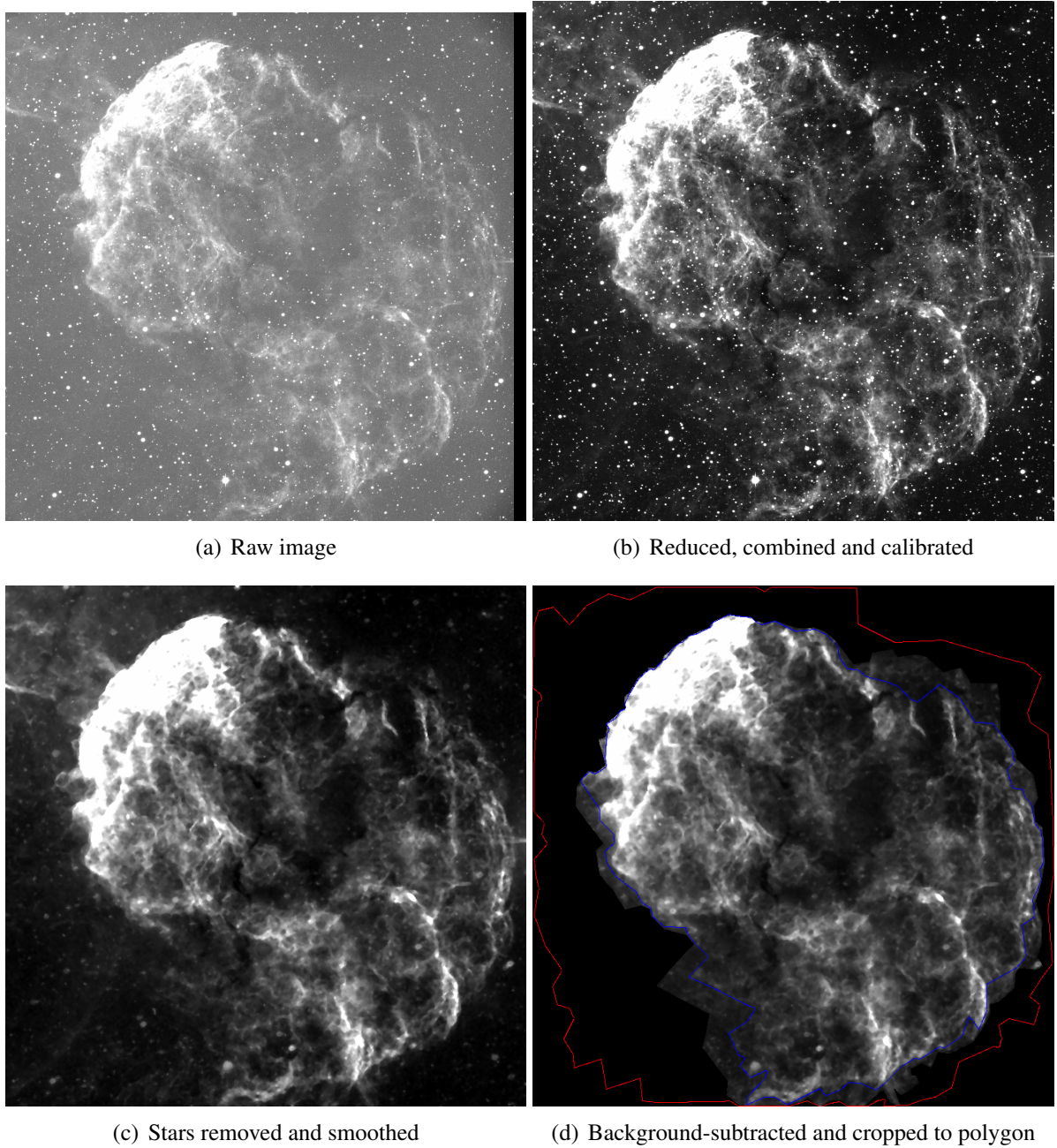


FIGURE H.2: The main steps in processing the  $H\alpha$  image of IC 443. We show (a) the raw image (unreduced, single 600 s exposure), (b) the image after data reduction, combination of the three exposures (median) and calibration, (c) the image after removing the stars and smoothing with a mesh size of four and (d) the image after background subtraction and cropped to a polygon representing the shape of the SNR. The blue and red contours represent two further possible polygon shapes that were defined for IC 443.

## H.5 Results

In Table H.3 and Figs. H.4–H.7 we summarise the results for the observed SNRs. We were able to determine the light centre for nine of the SNRs. The analysis could not be done if the SNR was too faint or if the visible emission could not be safely associated with the SN ejecta. In the following, we briefly describe our preliminary results for the individual SNRs.

**G189.1+03.0 (IC 443)** was the only SNR where we defined three different polygons and averaged the results. In the following, index 1 refers to the regular polygon, index 2 to a narrower polygon where only the brightest filaments were considered and index 3 to a wide polygon where also faint and diffuse emission, e.g. at the north-east, were considered. The additional polygons are indicated by the blue and red contours in Fig. H.2. We obtained the following coordinates (the resulting pixel coordinates are only given for the first polygon):

$$\begin{aligned} (x_{\text{lc}}^1, y_{\text{lc}}^1) &= (964.78, 907.93) \text{ px}, \\ (\text{RA}_{\text{lc}}^1, \text{DEC}_{\text{lc}}^1) &= (94.2794, 22.5633) \text{ deg}, \\ (\text{RA}_{\text{lc}}^2, \text{DEC}_{\text{lc}}^2) &= (94.2825, 22.5692) \text{ deg}, \\ (\text{RA}_{\text{lc}}^3, \text{DEC}_{\text{lc}}^3) &= (94.3093, 22.5743) \text{ deg}. \end{aligned}$$

From these values, we can calculate average and standard deviation:

$$\text{RA}_{\text{lc}}^{\text{av}}, \text{DEC}_{\text{lc}}^{\text{av}} = (94.290 \pm 0.016, 22.569 \pm 0.006) \text{ deg}.$$

This result is also given in Table H.3, where it can be compared to the *Green* centre.

The results for IC 443 are illustrated together with the SNR geometry in Fig. H.3, where it can be seen that the light centre, as compared to the GC given by Green (2014), is shifted towards the east by  $\sim 2.3'$ . This is expected because the strongest emission is visible at the north-eastern edge of the SNR. Our light centre for the third polygon has a larger right ascension than the other two, because it incorporates more emission especially on the eastern side. Nevertheless, the error ellipse is relatively small compared to the distance to the *Green* centre.

**G073.9+00.9.** No analysis could be done for this SNR. It is interacting with a molecular cloud (Zdziarski et al., 2016), so no SNR shell is visible in our  $\text{H}\alpha$  image, although it is indicated as possible shell type in Green (2014). The visible emission has an irregular shape and we cannot decide which parts belong to the SNR and which to the molecular cloud. Since the SNR is not detected in X-rays (Zdziarski et al., 2016), the radio observations (e.g. Kothes et al. 2006) might be the only possibility to obtain the light centre.

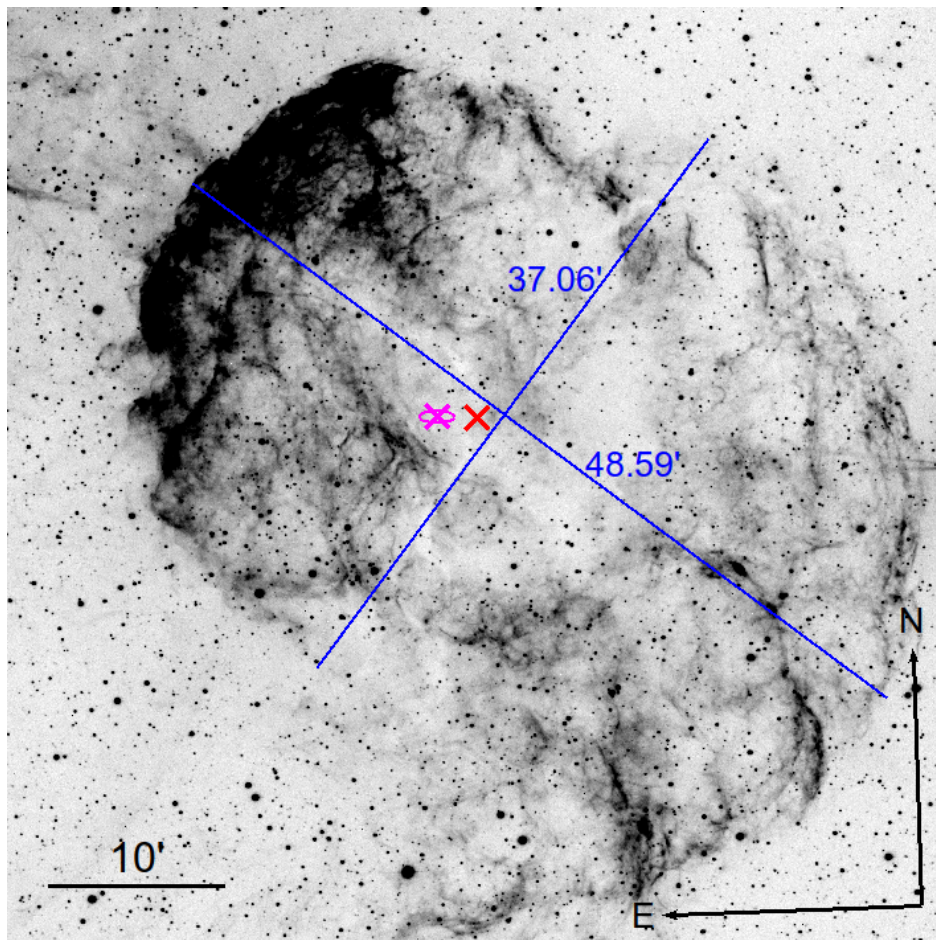


FIGURE H.3: The image shows the SNR IC 443 (G189.1+03.0) as observed by us in  $H\alpha$ . The total FOV is  $52.8' \times 52.8'$ . The blue lines mark the major and minor axis of the SNR, where the measured lengths in [arcmin] are indicated. The red cross marks the GC as given by Green (2014), the magenta cross marks the average light centre as calculated by us and the corresponding error ellipse. Note that the colour scale is inverted compared to Fig. H.2.

## H.5. Results

TABLE H.3: Results of the analysis of SNR  $H\alpha$  images. The columns give SNR name, length of the major- and minor axis, respectively, and the central coordinates according to Green (2014) (index GC), our fitted ellipses (ec) and our calculated light centres (lc). No results could be found for SNRs with very weak emission or with an irregular shape.

SNR	$\Theta_a$ [arcmin]	$\Theta_b$ [arcmin]	$RA_{GC}$ [deg]	$DEC_{GC}$ [deg]	$RA_{ec}$ [deg]	$DEC_{ec}$ [deg]	$RA_{lc}$ [deg]	$DEC_{lc}$ [deg]
G073.9+00.9	–	–	303.5625	36.2000	–	–	–	–
G074.0–08.5	221.6	166.9	312.7500	30.6667	–	–	312.7389	30.8230
G089.0+04.7	132.1	128.4	311.2500	50.5833	311.0897	50.4745	310.9287	50.3730
G114.3+00.3	–	–	354.2500	61.9167	–	–	–	–
G116.5+01.1	–	–	358.4167	63.2500	–	–	–	–
G116.9+00.2	33.74	33.39	359.7917	62.4333	359.8193	62.4463	359.8247	62.4426
G119.5+10.2	86.00	85.35	1.6667	72.7500	–	–	1.5923	72.6784
G132.7+01.3	92.44	87.96	34.4167	62.7500	–	–	34.8538*	62.6125*
G160.9+02.6	134.1	109.9	75.2500	46.6667	–	–	75.1532	46.5558
G189.1+03.0	48.59	37.06	94.2500	22.5667	–	–	94.2904	22.5689
G205.5+00.5	214.6	189.9	99.7500	6.5000	99.6137	6.4540	99.6827	6.4089
G111.7–02.1	–	–	350.8583	58.8000	–	–	–	–
G120.1+01.4	–	–	6.3250	64.1500	–	–	–	–
G130.7+03.1	6.38	5.25	31.4208	64.8167	–	–	–	–
G184.6–05.8	7.00	5.27	83.6292	22.0167	83.6327	22.0140	83.6321	22.0110

\* Affected by molecular cloud interaction

**G074.0–08.5 (Cygnus Loop).** The image of this large SNR contains 25 frames, among which five frames were re-observed to improve the  $S/N$ . However, these are not incorporated into the mosaic shown in Fig. H.4 (b), so the quality is not optimal. Nevertheless, the bright filaments are clearly visible. The Cygnus Loop shows the largest major axis among our sample, due to the blowout region in the south. It is suggested (e.g. Meyer et al. 2015; Meyer et al. 2020) that the progenitor could have been a massive runaway star and that the southern filaments are related to wind mass-loss of the progenitor. Due to this irregularity, we did not fit an ellipse to the SNR edge. The light centre is shifted to the north compared to the *Green* centre, due to the bright emission in the north.

**G089.0+04.7 (HB21).** In this  $3 \times 3$  mosaic, the SNR emission is clearly visible. However, it appears rather diffuse, without a clearly pronounced limb brightening. Further emission might be located outside the image, towards the west and the south. Therefore, our light centre and especially our ellipse centre might have to be shifted towards these directions. The fact that the *Green* centre lies even more towards north-east, indicates that the SNR has a different morphology in the radio regime.

**G114.3+00.3.** This SNR is very faint in  $H\alpha$ , which could be caused by strong interstellar absorption in the line of sight (Yar-Uyaniker et al., 2004). The bright nebula to the left of the



GC is not part of the SNR but an H II region. Due to the very faint emission, we could not safely identify the edge, so we did not fit an ellipse. The determination of a light centre would be too much affected by the H II region, even if we would remove it from the image.

**G116.5+01.1** is even fainter in H $\alpha$  than G114.3+00.3, therefore we could not do any analysis. For the radio properties, see Yar-Uyaniker et al. (2004). Note that both of these SNRs were detected in the optical by Fesen et al. (1997).

**G116.9+00.2 (CTB 1)**. This is the most spherical SNR of our sample. Its bright, circular shell is clearly visible in H $\alpha$ , as indicated by the yellow ellipse in Fig. H.5 (b). The measured major- and minor axes, 33.74' and 33.39', are almost identical. The bright shell of the SNR is only interrupted by the north-eastern blowout region. Another peculiarity is a small gap in the south-western shell, caused by dust-cloud absorption according to Fesen et al. (1997). The centres determined from our two methods, as well as the one given by Green (2014), are located very close to each other. For a more illustrative image of CTB 1, see Fig. 2.7.

**G119.5+10.2 (CTA 1)** is classified as shell-type in Green (2014) but actually shows a mixed morphology. It has a clearly pronounced southern shell, while the northern parts are faint and diffuse. Also note that Slane et al. (2004) describe the NS RX J0007.0+7302, close to the centre of CTA 1. We measured similar lengths for major- and minor axis of this medium-sized SNR (86.00'  $\times$  85.35'), but did not fit an ellipse due to the missing northern shell. The light centre is shifted southward compared to the *Green* centre, as expected from the bright southern shell.

**G132.7+01.3 (HB3)**. This shell-type, medium-sized SNR shows pronounced H $\alpha$  filaments at the eastern and western shell, while the northern and southern emission is rather diffuse. We did not fit an ellipse because further emission might be located beyond the southern edge of our image. HB3 is interacting with the molecular cloud/H II region W3 in the south-east (Zhou et al., 2016), demonstrating the limitations of our approach to determine the light centre: The magenta cross in Fig. H.5 (d) is strongly shifted towards the molecular cloud, as compared to the *Green* centre. Although the parts outside the SNR were cropped off before the calculation, further emission from the molecular cloud is visible inside the SNR. A careful estimate of the additional emission and a corresponding subtraction of the flux values could help to obtain a more reliable result for the light centre.

**G160.9+02.6 (HB9)**. For this large shell-type SNR we created a 4  $\times$  4 mosaic. While in our H $\alpha$  image it appears like the northern parts were cropped off, in radio the SNR looks more

circular (Leahy and Tian, 2007). This difference also explains the shift between the light centre and the *Green* centre. The nebula in the north does not affect our calculation.

**G205.5+00.5 (Monoceros Loop).** This old SNR is also the largest of our sample when adding major- and minor axis (214.6' and 189.9'). Green (2014) even give 220'  $\times$  220'. The SNR is accompanied by two molecular clouds, NGC 2264 in the north and the very bright Rosette nebula in the south-west. It is not clear if the Monoceros Loop interacts with the Rosette nebula (Zhao et al. 2018; Yu et al. 2019). The SNR shell is well visible at most parts of its circumference, also where it is bordering the nebulae. The bright emission that was visually associated to the Rosette nebula was cropped off for the calculation of the light centre. Therefore, the light centre is not significantly shifted to the south-west, as we would otherwise expect.

**G111.7–02.1 (Cassiopeia A).** The youngest SNR of our sample is almost invisible in  $H\alpha$ . Guided by the *Green* centre, one can only see some very faint spots of emission. See Fig. 2.6 for a multi-wavelength view of this shell-type SNR, where one can also see optical emission recorded by the HST. The general faintness in optical bands is expected due to the strong interstellar absorption, which also avoided a clear naked-eye detection of the SN around 1680 AD (see Ashworth (1980); Thorstensen et al. (2001) for the possible sighting by John Flamsteed). We also suffer from a bad image quality due to an afterglow from previous observations, visible as faint diagonal stripes in Fig. H.6 (c). A further  $H\alpha$  observation under perfect conditions and with a much longer exposure time might yield enough flux to estimate the size of the SNR, but it appears more fruitful to concentrate on other wavelengths.

**G120.1+01.4 (Tycho).** The remnant of the SN that was observed by Tycho Brahe in 1572 AD is only slightly older than Cas A and also very faint. Some faint shell filaments are visible at the north and the east. Note that in Fig. H.6 (d) we show the complete STK FOV of 52.8'  $\times$  52.8', so the SNR, having  $\Theta = 8'$  (Green, 2014), appears very small. The same applies to Cas A. The visible emission was not sufficient to do any analysis. In Fig. H.6 (d), we also show in blue the GC determined by Xue and Schaefer (2015) from images of different wavelengths.

**G130.7+03.1 (3C58).** Similar problems as noted for Cas A and the Tycho SNR also arise for the probable remnant of the historical SN from 1181 AD. This SNR, displayed in Fig. H.7 (a), is a PWN powered by PSR J0205+6449. Only very faint spots of  $H\alpha$  emission are visible. With the help of a different flux scaling, we estimated a size of 6.38'  $\times$  5.25', but we could not fit an ellipse or determine the light centre. We note that the visible  $H\alpha$  emission looks very

different compared to its shape in X-ray and radio (e.g. Bietenholz 2006; Gotthelf et al. 2007; Kothes 2013), where it is more strongly elongated along the right ascension axis.

**G184.6–05.8 (Crab nebula).** We end our discussion with the famous Crab nebula, which has the highest peak brightness of all SNRs on the sky. As 3C58, it is a PWN, powered by the Crab pulsar (J0534+2200). It is surprising, how much brighter the Crab nebula is compared to 3C58, especially in the optical, although they share a similar history (originating from a core-collapse SN and powered by a compact object). Since the Crab nebula is so bright, we can clearly identify its edge in Fig. H.7 (b). Consequently, the centre from our ellipse fit, the light centre, and the GC from Green (2014) are all very close to each other. Therefore, in Fig. H.7 (b) we do not show the complete FOV but a zoom-in to the central  $20' \times 20'$ . The measured size of  $7.00' \times 5.27'$  is consistent with Green (2014). Illustrative views on the Crab nebula are presented in Figs. 2.7 (b) and H.8. Fig. 2.7 (b) gives a multi-colour image based on HST observations. Fig. H.8 (a) presents our  $H\alpha$  observation in a different flux scaling, so that the bright filaments become visible. Fig. H.8 (b) presents a colour-image which we recorded in the broadband optical filters B, V and R. As for the  $H\alpha$  images, this was done with the STK at the University Observatory Jena. We made exposures of  $3 \times 30$  s in each of the three filters. The reduced and averaged images for each band were then stacked with *MaxIm DL* to obtain the final colour image.

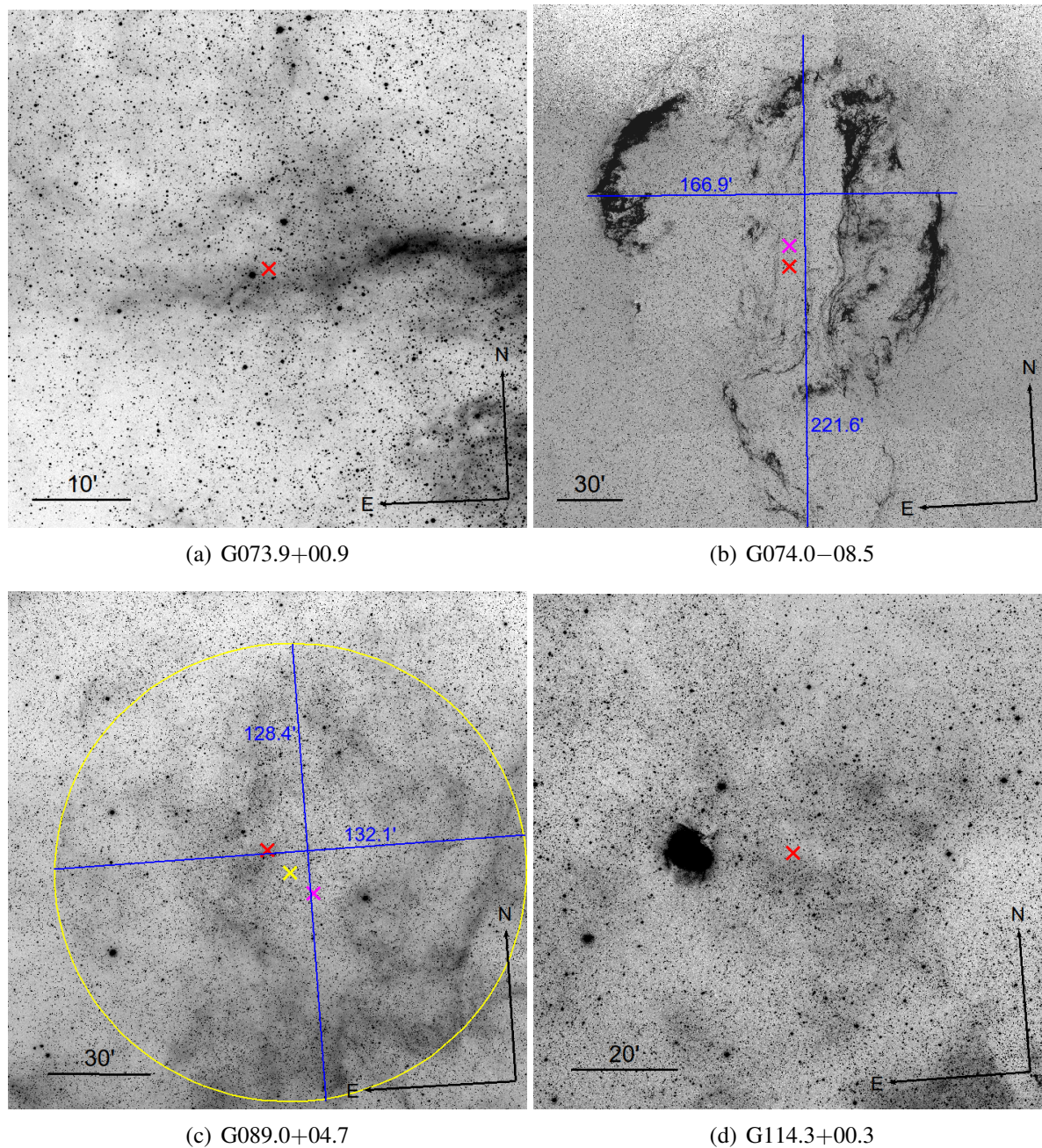


FIGURE H.4: Results of the analysis of the  $H\alpha$  images – Part 1. Here we show (a) G073.9+00.9, (b) G074.0–08.5 (Cygnus Loop), (c) G089.0+04.7 (HB21) and (d) G114.3+00.3. The red cross marks the GC as given by Green (2014) and if the corresponding analysis steps were possible, the blue lines mark the major and minor axis of the SNR, the yellow ellipse roughly marks the edge of the SNR, the yellow cross the centre of the ellipse and the magenta cross the light centre as determined with our *Python* code. Note the different sizes as indicated by the scale. The images are shown in full size, only cropped to a box in the case of mosaics.

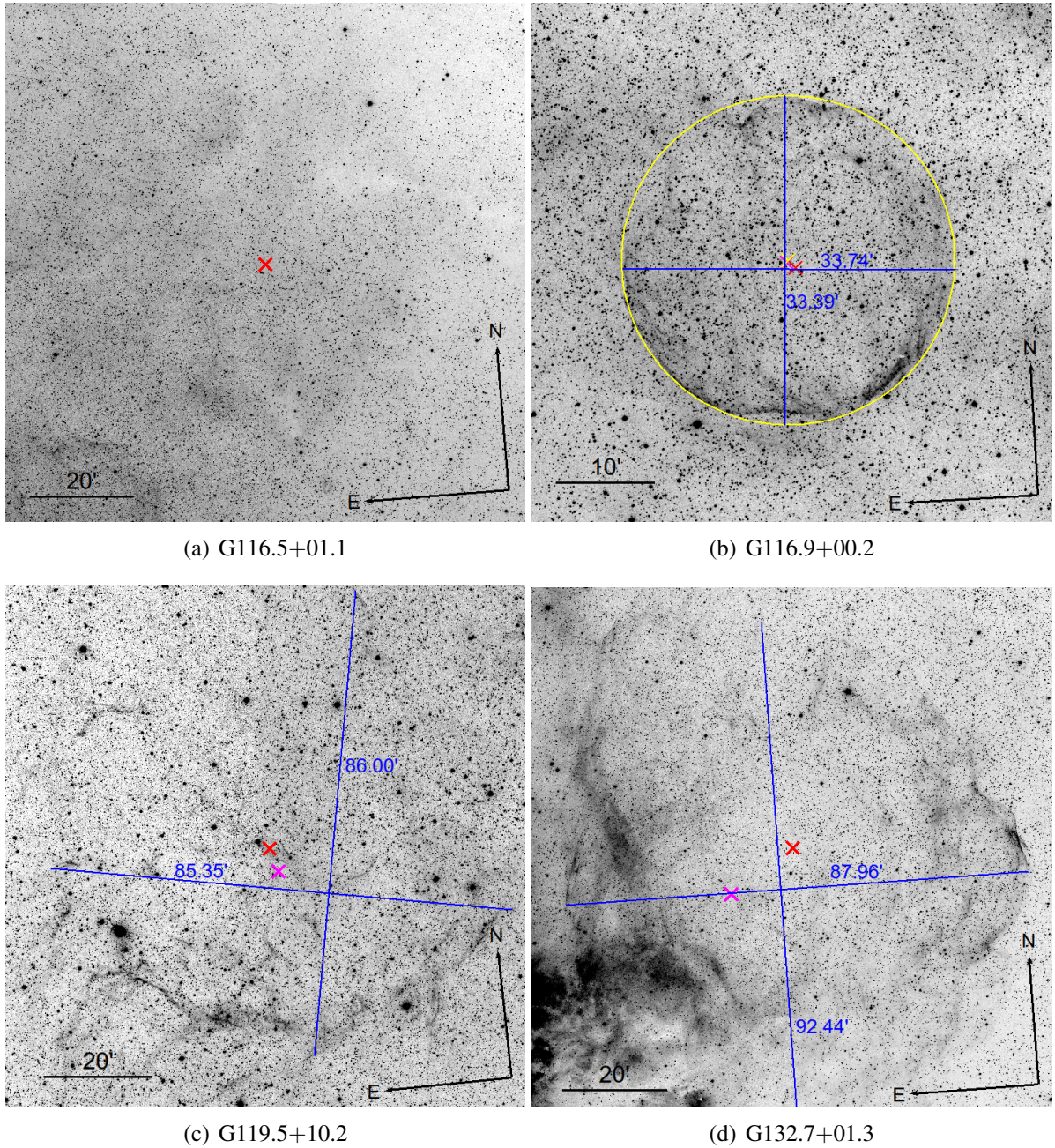


FIGURE H.5: Results of the analysis of the  $H\alpha$  images – Part 2. Here we show (a) G116.5+01.1, (b) G116.9+00.2 (CTB 1), (c) G119.5+10.2 (CTA 1) and (d) G132.7+01.3 (HB3). The red cross marks the GC as given by Green (2014) and if the corresponding analysis steps were possible, the blues lines mark the major and minor axis of the SNR, the yellow ellipse roughly marks the edge of the SNR, the yellow cross the centre of the ellipse and the magenta cross the light centre as determined with our *Python* code. Note the different sizes as indicated by the scale. The images are shown in full size, only cropped to a box in the case of mosaics.

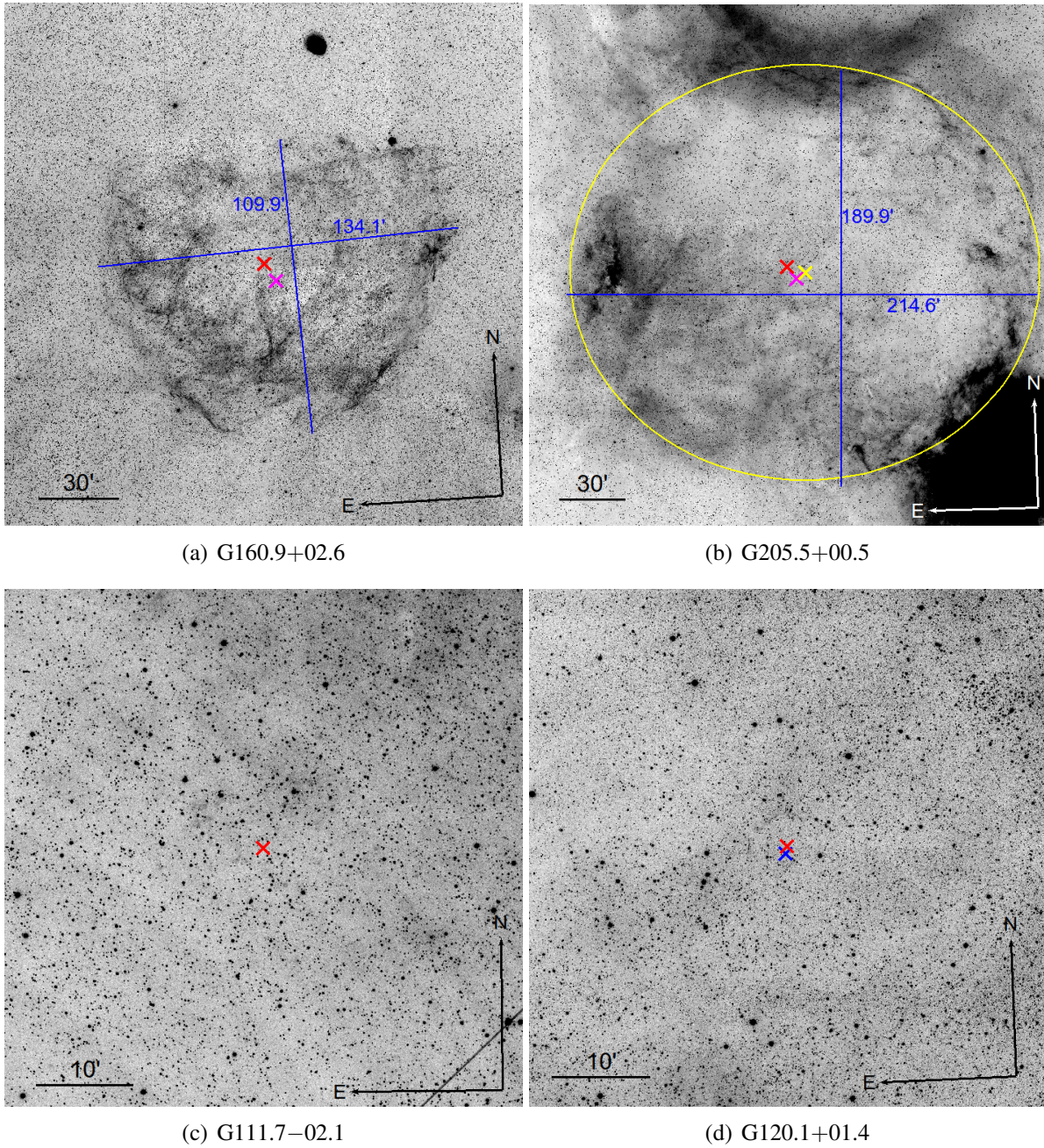


FIGURE H.6: Results of the analysis of the  $H\alpha$  images – Part 3. Here we show (a) G160.9+02.6 (HB9), (b) G205.5+00.5 (Monoceros Loop), (c) G111.7-02.1 (Cassiopeia A) and (d) G120.1+01.4 (Tycho). The red cross marks the GC as given by Green (2014) and if the corresponding analysis steps were possible, the blue lines mark the major and minor axis of the SNR, the yellow ellipse roughly marks the edge of the SNR, the yellow cross the centre of the ellipse and the magenta cross the light centre as determined with our *Python* code. For G120.1+01.4, the blue cross marks the GC as determined by Xue and Schaefer (2015). Note the different sizes as indicated by the scale. The images are shown in full size, only cropped to a box in the case of mosaics.

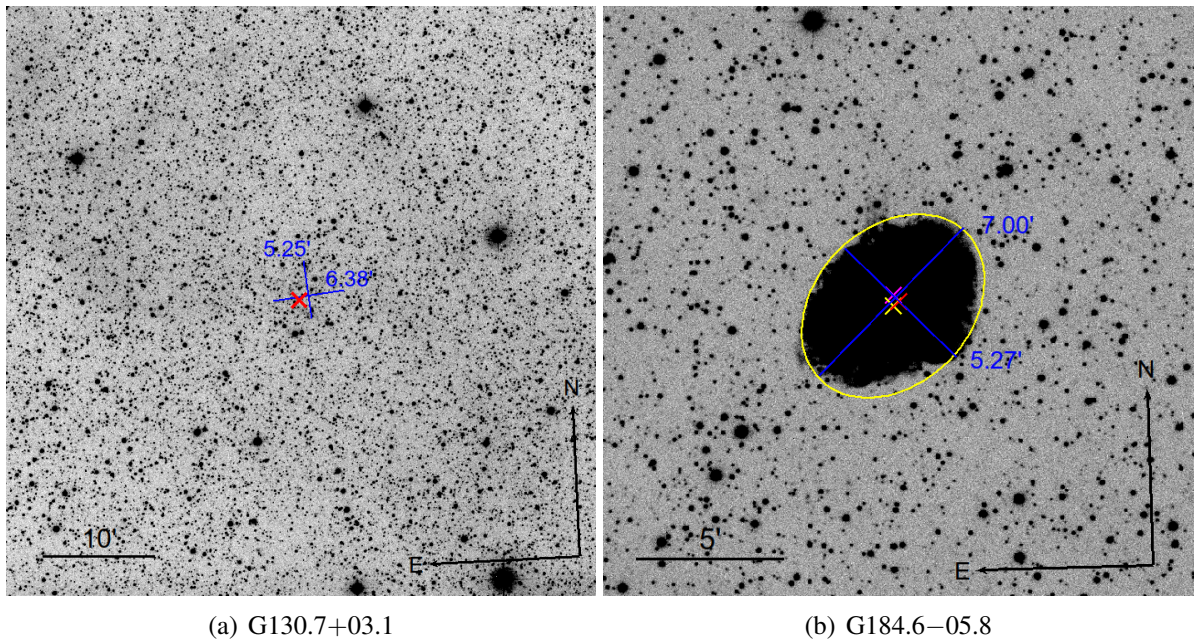


FIGURE H.7: Results of the analysis of the  $H\alpha$  images – Part 4. Here we show (a) G130.7+03.1 (SN 1181) and (b) G184.6–05.8 (Crab nebula). The red cross marks the GC as given by Green (2014) and if the corresponding analysis steps were possible, the blues lines mark the major and minor axis of the SNR, the yellow ellipse roughly marks the edge of the SNR, the yellow cross the centre of the ellipse and the magenta cross the light centre as determined with our *Python* code. Note the different sizes as indicated by the scale. Image (a) is shown in full size ( $52.8' \times 52.8'$ ), image (b) shows the central  $20' \times 20'$  around the centre of the Crab nebula, so that the results can be distinguished from each other.

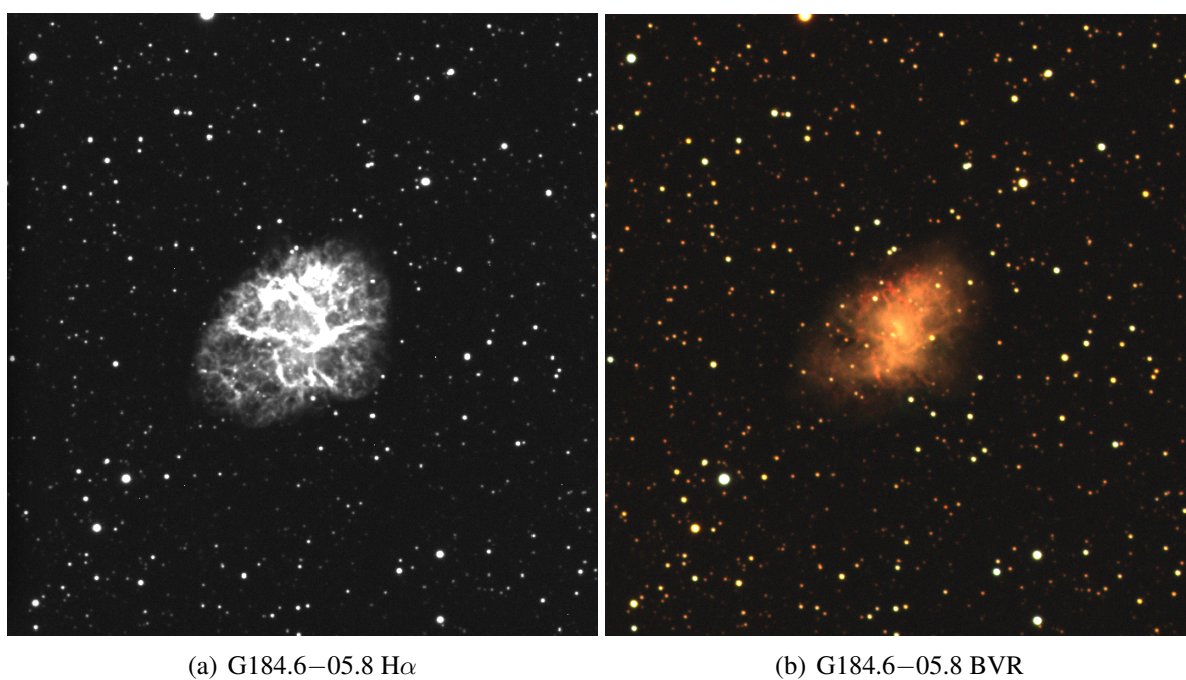


FIGURE H.8: Here we show a further view on the Crab nebula in (a) H $\alpha$  and (b) BVR for illustrative purposes. The images sizes are about  $20' \times 20'$ . The colour scale is inverted compared to the previous figures and more details are visible due to a different flux scaling.



# Appendix I

## Overview of the $H\alpha$ observations

All observed SNR frames are listed with their corresponding central coordinates, the date (consistent with the GSH nightlog), the weather conditions and the illumination of the moon, if it was above the horizon. Peculiarities are given as footnotes. For frames that were observed more than once, we only list the observations that yielded the resulting image of best quality (high  $S/N$ , low background, good focus, good autoguiding etc.).

TABLE I.1: Overview of observed SNR frames. Besides the name (incl. frame number if applicable) we give the central coordinates (J2000), the observation date (consistent with nightlog), approximate weather conditions and the degree of moon illumination. Special remarks are given as footnotes. We only list the observations that yielded the image with the best quality for the corresponding frame.

Frame	RA [h:m:s]	DEC [d:m]	Date	Weather	Moon
G073.9+00.9	20:14:15.0	+36:12:00	2017 Jun 08	clear	99 %
G074.0−08.5 f01	20:58:30.6	+32:15:48	2019 Apr 24	clear	78 %
G074.0−08.5 f02	20:54:43.8	+32:16:06	2019 Apr 29	clear	−
G074.0−08.5 f03	20:50:56.8	+32:15:60	2017 Aug 14	few cirrus	−
G074.0−08.5 f04	20:47:09.9	+32:15:28	2019 Apr 29	clear	−
G074.0−08.5 f05	20:43:23.2	+32:14:30	2019 Apr 29	clear	−
G074.0−08.5 f06	20:58:28.3	+31:27:49	2017 Aug 21	clear, little hazy	−
G074.0−08.5 f07	20:54:43.5	+31:28:07	2017 Aug 21	clear, little hazy	−
G074.0−08.5 f08	20:50:58.4	+31:27:59	2017 Aug 21	clear, little hazy	−
G074.0−08.5 f09	20:47:13.4	+31:27:28	2017 Aug 21	clear, little hazy	−
G074.0−08.5 f10	20:43:28.5	+31:26:31	2017 Aug 21	clear, little hazy	−
G074.0−08.5 f11	20:58:26.2	+30:39:50	2017 Aug 21	clear, little hazy	−
G074.0−08.5 f12	20:54:43.2	+30:40:07	2017 Aug 21	clear, little hazy	−
G074.0−08.5 f13	20:51:00.0	+30:40:00	2017 Aug 21	clear, little hazy	−
G074.0−08.5 f14	20:47:16.8	+30:39:29	2017 Aug 21	clear, little hazy	−
G074.0−08.5 f15	20:43:33.8	+30:38:34	2017 Aug 21	clear, little hazy	−
G074.0−08.5 f16	20:58:24.0	+29:51:53	2017 Aug 21	clear, little hazy	−
G074.0−08.5 f17	20:54:42.8	+29:52:08	2017 Aug 22	few cirrus, little hazy	−
G074.0−08.5 f18	20:51:01.5	+29:52:00	2017 Aug 22	few cirrus, little hazy	−
G074.0−08.5 f19	20:47:20.2	+29:51:30	2017 Aug 22	few cirrus, little hazy	−
G074.0−08.5 f20	20:43:39.0	+29:50:36	2017 Aug 22	few cirrus, little hazy	−
G074.0−08.5 f21	20:58:21.9	+29:03:55	2017 Aug 22	few cirrus, little hazy	−
G074.0−08.5 f22	20:54:42.4	+29:04:09	2017 Aug 22	few cirrus, little hazy	−
G074.0−08.5 f23	20:51:03.0	+29:04:02	2017 Aug 22	few cirrus, little hazy	−
G074.0−08.5 f24	20:47:23.5	+29:03:31	2017 Aug 22	few cirrus, little hazy	−
G074.0−08.5 f25	20:43:44.0	+29:02:38	2019 Jul 25	few cirrus	−
G089.0+04.7 f01	20:49:47.2	+51:25:37	2017 Jun 08	few cirrus	99 %
G089.0+04.7 f02	20:44:39.9	+51:22:54	2017 Jun 09	clear	100 %
G089.0+04.7 f03	20:39:33.6	+51:19:21	2017 Jun 09	clear	100 %
G089.0+04.7 f04	20:50:02.0	+50:37:40	2017 Jun 10	clear	98 %
G089.0+04.7 f05	20:45:00.0	+50:35:00	2017 Jun 12	clear	88 %
G089.0+04.7 f06	20:39:58.8	+50:31:31	2017 Jul 05	clear	88 %
G089.0+04.7 f07	20:50:16.2	+49:49:45	2017 Jul 05	clear	88 %
G089.0+04.7 f08	20:45:19.3	+49:47:06	2017 Jul 05	clear	88 %
G089.0+04.7 f09 <sup>1</sup>	20:40:23.2	+49:43:41	2019 Apr 01	clear, little hazy	−
G111.7−02.1	23:23:26.0	+58:48:00	2018 Jul 18	clear	−
G114.3+00.3 f01	23:40:29.2	+62:18:36	2017 Jul 29	clear	−
G114.3+00.3 f02	23:33:36.1	+62:19:09	2017 Jul 29	clear	−
G114.3+00.3 f03	23:40:18.8	+61:30:35	2017 Jul 31	clear	56 %
G114.3+00.3 f04 <sup>2</sup>	23:33:36.9	+61:31:07	2017 Aug 03	clear	84 %
G116.5+01.1 f01 <sup>3</sup>	23:57:05.7	+63:39:55	2017 Aug 07	few cirrus	100 %
G116.5+01.1 f02 <sup>3</sup>	23:49:53.9	+63:37:41	2017 Aug 07	thick cirrus	100 %
G116.5+01.1 f03 <sup>3</sup>	23:57:19.7	+62:51:57	2017 Aug 07	few cirrus	100 %
G116.5+01.1 f04 <sup>3</sup>	23:50:19.9	+62:49:44	2017 Aug 07	few cirrus	100 %

<sup>1</sup>  $6 \times 600$  s; <sup>2</sup> 1st image on 2017 Jul 31; <sup>3</sup> high background

Continued.

Frame	RA [h:m:s]	DEC [d:m]	Date	Weather	Moon
G116.9+00.2	23:59:10.0	+62:26:00	2017 Jun 08	clear	99 %
G119.5+10.2 f01	00:12:10.1	+73:08:48	2017 Dec 12	clear	–
G119.5+10.2 f02	00:01:07.8	+73:08:39	2017 Dec 12	partly cloudy	–
G119.5+10.2 f03	00:11:57.6	+72:20:48	2017 Dec 12	partly cloudy	–
G119.5+10.2 f04	00:01:24.4	+72:20:40	2018 Sep 12	few cirrus	–
G120.1+01.4	00:25:18.0	+64:09:00	2017 Dec 07	clear	–
G130.7+03.1	02:05:41.0	+64:49:00	2018 Oct 14	clear	–
G132.7+01.3 f01	02:21:09.5	+63:09:10	2018 Sep 12	few cirrus	–
G132.7+01.3 f02	02:14:04.5	+63:08:30	2018 Sep 16	clear	–
G132.7+01.3 f03	02:21:09.7	+62:21:10	2018 Sep 16	clear	–
G132.7+01.3 f04	02:14:16.1	+62:20:31	2018 Sep 16	clear	–
G160.9+02.6 f01	05:07:50.5	+47:54:17	2018 Sep 16	clear	–
G160.9+02.6 f02	05:03:04.4	+47:52:53	2018 Sep 16	clear	–
G160.9+02.6 f03	04:58:18.6	+47:50:46	2018 Sep 17	party cloudy	–
G160.9+02.6 f04	04:53:33.2	+47:47:54	2018 Sep 17	clear, little hazy	–
G160.9+02.6 f05	05:07:56.6	+47:06:19	2018 Sep 17	clear, little hazy	–
G160.9+02.6 f06	05:03:14.7	+47:04:56	2018 Sep 17	clear, little hazy	–
G160.9+02.6 f07	04:58:33.1	+47:02:51	2018 Sep 17	clear, little hazy	–
G160.9+02.6 f08	04:53:52.0	+47:00:02	2018 Sep 17	clear, little hazy	–
G160.9+02.6 f09	05:08:02.5	+46:18:20	2018 Sep 17	clear, little hazy	–
G160.9+02.6 f10	05:03:24.8	+46:16:58	2018 Sep 20	clear	83 %
G160.9+02.6 f11	04:58:47.4	+46:14:54	2018 Sep 20	few cirrus	83 %
G160.9+02.6 f12	04:54:10.3	+46:12:08	2018 Sep 20	partly cloudy	83 %
G160.9+02.6 f13	05:08:08.2	+45:30:22	2018 Sep 20	few cirrus	83 %
G160.9+02.6 f14	05:03:34.5	+45:29:01	2018 Sep 20	few cirrus	83 %
G160.9+02.6 f15	04:59:01.0	+45:26:58	2019 Mar 29	few cirrus	–
G160.9+02.6 f16	04:54:28.0	+45:24:15	2019 Mar 29	few cirrus	–
G184.6–05.8	05:34:31.0	+22:01:00	2018 Oct 13	clear	–
G189.1+03.0	06:17:00.0	+22:34:00	2018 Oct 14	clear	–
G205.5+00.5 f01	06:45:32.4	+08:04:35	2018 Sep 27	clear	93 %
G205.5+00.5 f02	06:42:18.6	+08:05:19	2018 Sep 28	clear	87 %
G205.5+00.5 f03	06:39:04.8	+08:05:58	2018 Oct 14	clear	–
G205.5+00.5 f04	06:35:51.0	+08:06:31	2018 Oct 14	clear	–
G205.5+00.5 f05	06:32:37.2	+08:06:58	2018 Oct 14	clear	–
G205.5+00.5 f06	06:45:29.4	+07:16:37	2018 Nov 05	clear, little hazy	5 %
G205.5+00.5 f07	06:42:15.9	+07:17:21	2018 Nov 05	clear, little hazy	5 %
G205.5+00.5 f08	06:39:02.4	+07:17:59	2018 Nov 05	clear, little hazy	5 %
G205.5+00.5 f09	06:35:48.9	+07:18:33	2019 Jan 31	clear	–
G205.5+00.5 f10	06:32:35.4	+07:19:01	2019 Jan 31	clear	–
G205.5+00.5 f11	06:45:26.3	+06:28:39	2019 Jan 31	clear	–
G205.5+00.5 f12	06:42:13.2	+06:29:22	2019 Jan 31	clear	–
G205.5+00.5 f13	06:39:00.0	+06:30:00	2019 Jan 31	clear	–

---

Continued.

Frame	RA [h:m:s]	DEC [d:m]	Date	Weather	Moon
G205.5+00.5 f14	06:35:46.8	+06:30:34	2019 Jan 31	clear	–
G205.5+00.5 f15	06:32:33.6	+06:31:03	2019 Jan 31	clear	–
G205.5+00.5 f16	06:45:23.3	+05:40:41	2019 Jan 31	clear	–
G205.5+00.5 f17	06:42:10.5	+05:41:22	2019 Jan 31	clear	–
G205.5+00.5 f18 <sup>4</sup>	06:38:57.6	+05:42:00	2019 Mar 07	clear	–
G205.5+00.5 f19	06:35:44.7	+05:42:34	2019 Mar 29	few cirrus	–
G205.5+00.5 f20	06:32:31.9	+05:43:04	2019 Mar 29	few cirrus	–
G205.5+00.5 f21	06:45:20.3	+04:52:43	2019 Mar 29	few cirrus	–
G205.5+00.5 f22	06:42:07.8	+04:53:25	2019 Mar 21	few cirrus	99 %
G205.5+00.5 f23	06:38:55.2	+04:54:02	2019 Mar 21	few cirrus	99 %
G205.5+00.5 f24	06:35:42.6	+04:54:36	2019 Mar 30	clear	–
G205.5+00.5 f25	06:32:30.1	+04:55:07	2019 Mar 30	clear	–

<sup>4</sup> 1st image on 2019 Feb 07

# Appendix J

## *Python* code for calculating SNR light centres

Here, we show the *Python* code used for the determination of the light centres. It also contains the creation of a masked image according to a polygon created in *ds9* (see Appendix H for details). The value for the background subtraction corresponds to the example of IC 443. If an output image with the result is desired, the code requires the input *.fits* image to be exported as a *.png* image before.

```
import re
import sys
import numpy as np
from astropy import wcs
from astropy.io import fits
from PIL import Image, ImageDraw
import PIL
import matplotlib.pyplot as plt
from astropy.visualization import astropy_mpl_style
plt.style.use(astropy_mpl_style)
import os

#Give the desired SNR in the shell (must be consistent with file name), eg: G1891p030:
snr_name = str(input("SNR: "))

#clean up:
if os.path.isfile(snr_name+'_bg_s_mask.fits') == True:
    os.remove(snr_name+'_bg_s_mask.fits')
if os.path.isfile(snr_name+'_bg_s_poly.fits') == True:
```

```

os.remove(snr_name+'_bg_s_poly.fits')

#load input .fits file (stars should be removed):
with fits.open(snr_name+'_bg_s.fits') as hdul:

    scidat = hdul[0].data
    #Subtract the background from the image; use the lowest pixel value in the input .fits file:
    scidat = scidat - 413

    #define polygon of the SNR by loading the polygon file created with ds9 (has to be transformed to
    ↪ a list first):
    poly2 = np.loadtxt(snr_name+'_poly2.reg', skiprows = 5, delimiter=',')
    p = 0
    polygon2 = []
    for p in range(0,len(poly2)-1,2):
        xi = poly2[p]
        yi = poly2[p+1]
        polygon2.append((xi,yi))
    print ('polygon2 = '+str(polygon2))

    #create a mask for the defined polygon:
    maskIm = Image.new('L', (scidat.shape[1],scidat.shape[0]), 0)
    ImageDraw.Draw(maskIm).polygon(polygon2, outline=1, fill=1)
    mask = np.array(maskIm)

    #create numpy array with the masked pixel values:
    newImArray = np.empty(scidat.shape[0])
    newImArray = scidat*mask

    #create new fits files – mask and masked image:
    hdum = fits.PrimaryHDU(mask)
    hdum.writeto(snr_name+'_bg_s_mask.fits')

    hdun = fits.PrimaryHDU(newImArray)
    hdun.writeto(snr_name+'_bg_s_poly.fits')

#load masked fits image:
with fits.open(snr_name+'_bg_s_poly.fits') as hdulist:
    scidata = hdulist[0].data

```

*#The weighted mean position of the pixel values ("Lichtschwerpunkt") is calculated for the masked*

*↪ image:*

`A = 0`

`mx = 0`

`my = 0`

`with open('GC_'+snr_name+'_poly.txt', 'w') as g:`

*#define pixel coordinates to consider (here: complete image because it is already cropped):*

`x1 = 0`

`x2 = scidata.shape[1]`

`y1 = 0`

`y2 = scidata.shape[0]`

`print ("x= "+str(x1)+" to "+str(x2)+" ; y= "+str(y1)+" to "+str(y2))`

*#loop through the pixel coordinates in x-direction (j) and y-direction (i):*

`for j in range(x1,x2):`

`for i in range(y1,y2):`

*if scidata[i][j] > 12: #exclude the background, depending on its standard deviation*

*#calculation of the weighted mean (xs,ys) by adding the flux-weighted positions*

*↪ (mx,my) and dividing the result by the sum of the fluxes (A):*

`A += scidata[i][j]`

`mx += j*scidata[i][j]`

`my += i*scidata[i][j]`

`xs = mx/A`

`ys = my/A`

`print ("Light center: "+str(xs)+" "+str(ys)+"\n")`

*#the uncommented lines in the following should be included if more than one polygon will be used for*

*↪ determination of the light centre, e.g. from different scales in ds9*

*#load intermediate output file and calculate mean and standard deviation from the single results for*

*↪ each polygon:*

`#ctrs = np.loadtxt('GCs_'+snr_name+'_polytest.txt', skiprows=0)`

`#mean = np.mean(ctrs, axis = 0)`

`#std = np.std(ctrs, axis = 0)`

`#print (mean)`

`#print (std)`

`#x_cen = mean[0]`

`#y_cen = mean[1]`

```
#x_std = std[0]
```

```
#y_std = std[1]
```

```
#create final output file with result in pixel and RA/DEC:
```

```
with fits.open(snr_name+'_bg_s.fits') as hdul:
```

```
g.write("x_cen = "+str(xs)+", y_cen = "+str(ys)+"\n")
```

```
#g.write("x_std = "+str(x_std)+", y_std = "+str(y_std)+"\n")
```

```
w = wcs.WCS(hdul[0].header)
```

```
g.write(w.wcs.name)
```

```
pixcrd = np.array([[xs,ys]], np.float_)
```

```
#pixlcrd = np.array([[x_cen-x_std,y_cen-y_std]], np.float_)
```

```
world = w.wcs_pix2world(pixcrd, 1)
```

```
#worldl = w.wcs_pix2world(pixlcrd, 1)
```

```
#x_std_deg = abs(world[0][0] - worldl[0][0])
```

```
#y_std_deg = abs(world[0][1] - worldl[0][1])
```

```
g.write("RA/DEC: "+str(world)+" deg+"\n")
```

```
#g.write("RA/DEC std: "+str(x_std_deg)+" "+str(y_std_deg)+" deg")
```

```
#load SNR image as .png to draw a cross and error ellipse for the result (north is down! Default
```

```
↔ orientation in ds9!!)
```

```
im = Image.open(snr_name+'.png')
```

```
rgb_im = im.convert('RGB')
```

```
draw = ImageDraw.Draw(rgb_im, mode=None)
```

```
draw.line([(xs-20,len(scidata)-ys-20),(xs+20,len(scidata)-ys+20)], fill=(255,0,0,255), width
```

```
↔ =2)
```

```
draw.line([(xs+20,len(scidata)-ys-20),(xs-20,len(scidata)-ys+20)], fill=(255,0,0,255), width
```

```
↔ =2)
```

```
#draw.ellipse((x_cen-x_std, len(scidata)-y_cen-y_std, x_cen+x_std, len(scidata)-y_cen+y_std
```

```
↔ ), fill=None, outline=(255,0,0,255))
```

```
rgb_im.show()
```

```
rgb_im.save(snr_name+'_ls_poly.png')
```







# References

- Alarie, A., Bilodeau, A., and Drissen, L. (2014). A hyperspectral view of Cassiopeia A. *MNRAS*, 441(4):2996–3008.
- Allen, G. E., Chow, K., DeLaney, T., Filipović, M. D., Houck, J. C., Pannuti, T. G., and Stage, M. D. (2015). On the Expansion Rate, Age, and Distance of the Supernova Remnant G266.2-1.2 (Vela Jr.). *APJ*, 798(2):82.
- Anders, F., Khalatyan, A., Chiappini, C., Queiroz, A. B., Santiago, B. X., Jordi, C., Girardi, L., Brown, A. G. A., Matijevič, G., Monari, G., Cantat-Gaudin, T., Weiler, M., Khan, S., Miglio, A., Carrillo, I., Romero-Gómez, M., Minchev, I., de Jong, R. S., Antoja, T., Ramos, P., Steinmetz, M., and Enke, H. (2019). Photo-astrometric distances, extinctions, and astrophysical parameters for Gaia DR2 stars brighter than  $G = 18$ . *AAP*, 628:A94.
- Andrae, R., Fouesneau, M., Creevey, O., Ordenovic, C., Mary, N., Burlacu, A., Chaoul, L., Jean-Antoine-Piccolo, A., Kordopatis, G., Korn, A., Lebreton, Y., Panem, C., Pichon, B., Thévenin, F., Walmsley, G., and Bailer-Jones, C. A. L. (2018). Gaia Data Release 2. First stellar parameters from Apsis. *AAP*, 616:A8.
- Aoki, W. and Helminiak, K. (2014). *Data reduction of echelle spectra with IRAF, Version 1.2*. National Astronomical Observatory of Japan, Tokyo, Japan.
- Aoki, W., Helminiak, K., and Tajitsu, A. (2014). *Subaru Telescope High Dispersion Spectrograph (HDS) User Manual, Version 2.0.0*. National Astronomical Observatory of Japan, Tokyo, Japan.
- Arzoumanian, Z., Chernoff, D. F., and Cordes, J. M. (2002). The Velocity Distribution of Isolated Radio Pulsars. *APJ*, 568(1):289–301.
- Ashworth, W. B., J. (1980). A Probable Flamsteed Observation of the Cassiopeia A Supernova. *Journal for the History of Astronomy*, 11:1.
- Baade, W. and Zwicky, F. (1934). Cosmic Rays from Super-novae. *Proceedings of the National Academy of Science*, 20(5):259–263.
- Bagnulo, S., Jehin, E., Ledoux, C., Cabanac, R., Melo, C., Gilmozzi, R., and ESO Paranal Science Operations Team (2003). The UVES Paranal Observatory Project: A Library of High- Resolution Spectra of Stars across the Hertzsprung-Russell Diagram. *The Mes-*

## REFERENCES

---

- senger*, 114:10–14.
- Bai, Y., Liu, J., Bai, Z., Wang, S., and Fan, D. (2019). Machine-learning Regression of Stellar Effective Temperatures in the Second Gaia Data Release. *AJ*, 158(2):93.
- Bailer-Jones, C. A. L., Rybizki, J., Fouesneau, M., Mantelet, G., and Andrae, R. (2018). Estimating Distance from Parallaxes. IV. Distances to 1.33 Billion Stars in Gaia Data Release 2. *AJ*, 156(2):58.
- Baraffe, I., Chabrier, G., Allard, F., and Hauschildt, P. H. (1998). Evolutionary models for solar metallicity low-mass stars: mass-magnitude relationships and color-magnitude diagrams. *AAP*, 337:403–412.
- Baraffe, I., Homeier, D., Allard, F., and Chabrier, G. (2015). New evolutionary models for pre-main sequence and main sequence low-mass stars down to the hydrogen-burning limit. *AAP*, 577:A42.
- Betoya-Nonesa, J. G., Min, K. W., Park, J.-W., Kim, I.-J., Seon, K.-I., and Ryu, K.-S. (2009). FUV Interstellar Absorption Toward the Lupus Loop Region (abstract). In Karplus Hartline, B., Horton, R. K., and Kaicher, C. M., editors, *American Institute of Physics Conference Series*, volume 1119 of *American Institute of Physics Conference Series*, pages 204–204.
- Bietenholz, M. F. (2006). Radio Images of 3C 58: Expansion and Motion of Its Wisp. *APJ*, 645(2):1180–1187.
- Blaauw, A. (1961). On the origin of the O- and B-type stars with high velocities (the “runaway” stars), and some related problems. *BAIN*, 15:265.
- Blaauw, A. (1993). Massive Runaway Stars. In Cassinelli, J. P. and Churchwell, E. B., editors, *Massive Stars: Their Lives in the Interstellar Medium*, volume 35 of *Astronomical Society of the Pacific Conference Series*, page 207.
- Blaauw, A. and Morgan, W. W. (1954). The Space Motions of AE Aurigae and  $\mu$  Columbae with Respect to the Orion Nebula. *APJ*, 119:625.
- Blair, W. P., Sankrit, R., Torres, S. I., Chayer, P., and Danforth, C. W. (2009). Far Ultraviolet Spectroscopic Explorer Observations of KPD 2055+3111, a Star behind the Cygnus Loop. *APJ*, 692(1):335–345.
- Blanco-Cuaresma, S. (2019). Modern stellar spectroscopy caveats. *MNRAS*, 486(2):2075–2101.
- Blanco-Cuaresma, S., Soubiran, C., Heiter, U., and Jofré, P. (2014). Determining stellar atmospheric parameters and chemical abundances of FGK stars with iSpec. *AAP*, 569:A111.
- Bock, D. C. J., Turtle, A. J., and Green, A. J. (1998). A High-Resolution Radio Survey of the VELA Supernova Remnant. *AJ*, 116(4):1886–1896.
- Bodenheimer, P. (1965). Studies in Stellar Evolution. II. Lithium Depletion during the Pre-Main Contraction. *APJ*, 142:451.

- Boesgaard, A. M., Budge, K. G., and Ramsay, M. E. (1988). Lithium in the Pleiades and alpha Persei Clusters. *APJ*, 327:389.
- Boesgaard, A. M. and Tripicco, M. J. (1986). Lithium in the Hyades Cluster. *APJL*, 302:L49.
- Bombaci, I. (1996). The maximum mass of a neutron star. *AAP*, 305:871.
- Boubert, D., Fraser, M., Evans, N. W., Green, D. A., and Izzard, R. G. (2017). Binary companions of nearby supernova remnants found with Gaia. *AAP*, 606:A14.
- Bramich, D. and Moehler, S. (2017). *Reflex UVES Tutorial, Issue 6.10*. European Southern Observatory.
- Breitschwerdt, D., Feige, J., Schulreich, M. M., Avillez, M. A. D., Dettbarn, C., and Fuchs, B. (2016). The locations of recent supernovae near the Sun from modelling  $^{60}\text{Fe}$  transport. *NAT*, 532(7597):73–76.
- Bressan, A., Marigo, P., Girardi, L., Salasnich, B., Dal Cero, C., Rubele, S., and Nanni, A. (2012). PARSEC: stellar tracks and isochrones with the PAdova and TRieste Stellar Evolution Code. *MNRAS*, 427(1):127–145.
- Brown, W. R. (2015). Hypervelocity Stars. *ARAA*, 53:15–49.
- Brown, W. R., Geller, M. J., Kenyon, S. J., and Kurtz, M. J. (2005). Discovery of an Unbound Hypervelocity Star in the Milky Way Halo. *APJL*, 622(1):L33–L36.
- Burgay, M., D’Amico, N., Possenti, A., Manchester, R. N., Lyne, A. G., Joshi, B. C., McLaughlin, M. A., Kramer, M., Sarkissian, J. M., Camilo, F., Kalogera, V., Kim, C., and Lorimer, D. R. (2003). An increased estimate of the merger rate of double neutron stars from observations of a highly relativistic system. *NAT*, 426(6966):531–533.
- Burrows, A. and Hayes, J. (1996). Pulsar Recoil and Gravitational Radiation Due to Asymmetrical Stellar Collapse and Explosion. *PRL*, 76(3):352–355.
- Butler, R. P., Cohen, R. D., Duncan, D. K., and Marcy, G. W. (1987). The Pleiades Rapid Rotators: Evidence for an Evolutionary Sequence. *APJL*, 319:L19.
- Cannon, A. J. and Pickering, E. C. (1993). VizieR Online Data Catalog: Henry Draper Catalogue and Extension (Cannon+ 1918-1924; ADC 1989). *VizieR Online Data Catalog*, page III/135A.
- Carroll, B. W. and Ostlie, D. A. (2007). An Introduction to Modern Astrophysics. *Pearson International Edition*, Second Edition.
- Cassam-Chenaï, G., Decourchelle, A., Ballet, J., Sauvageot, J. L., Dubner, G., and Giacani, E. (2004). XMM-Newton observations of the supernova remnant RX J1713.7-3946 and its central source. *AAP*, 427:199–216.
- Chadwick, J. (1932). Possible Existence of a Neutron. *NAT*, 129(3252):312.
- Chatterjee, S., Cordes, J. M., Vlemmings, W. H. T., Arzoumanian, Z., Goss, W. M., and Lazio, T. J. W. (2004). Pulsar Parallaxes at 5 GHz with the Very Long Baseline Array. *APJ*, 604(1):339–345.

## REFERENCES

---

- Chevalier, R. A. (1982). Self-similar solutions for the interaction of stellar ejecta with an external medium. *APJ*, 258:790–797.
- Chini, R., Barr, A., Buda, L. S., Dembsky, T., Drass, H., Nasser, A., Hoffmeister, V. H., and Fuhrmann, K. (2013). The Multiplicity of High-mass Stars. *Central European Astrophysical Bulletin*, 37:295–310.
- Coluzzi, R. (1999). Revised version of the ILLSS Catalogue (Coluzzi 1993-1999). *VizieR Online Data Catalog*, page VI/71A.
- Coşkunoğlu, B., Ak, S., Bilir, S., Karaali, S., Yaz, E., Gilmore, G., Seabroke, G. M., Bienaymé, O., Bland-Hawthorn, J., Campbell, R., Freeman, K. C., Gibson, B., Grebel, E. K., Munari, U., Navarro, J. F., Parker, Q. A., Siebert, A., Siviero, A., Steinmetz, M., Watson, F. G., Wyse, R. F. G., and Zwitter, T. (2011). Local stellar kinematics from RAVE data - I. Local standard of rest. *MNRAS*, 412(2):1237–1245.
- Covino, E., Alcalá, J. M., Allain, S., Bouvier, J., Terranegra, L., and Krautter, J. (1997). A study of the Chamaeleon star-forming region from the ROSAT all-sky survey. III. High resolution spectroscopic study. *AAP*, 328:187–202.
- Cutri, R. M., Skrutskie, M. F., van Dyk, S., Beichman, C. A., Carpenter, J. M., Chester, T., Cambresy, L., Evans, T., Fowler, J., Gizis, J., Howard, E., Huchra, J., Jarrett, T., Kopan, E. L., Kirkpatrick, J. D., Light, R. M., Marsh, K. A., McCallon, H., Schneider, S., Stiening, R., Sykes, M., Weinberg, M., Wheaton, W. A., Wheelock, S., and Zacarias, N. (2003). VizieR Online Data Catalog: 2MASS All-Sky Catalog of Point Sources (Cutri+2003). *VizieR Online Data Catalog*, page II/246.
- D’Antona, F. and Mazzitelli, I. (1984). Lithium depletion in stars. *AAP*, 138:431–442.
- Davidson, K. and Fesen, R. A. (1985). Recent developments concerning the Crab Nebula. *ARAA*, 23:119–146.
- Dekker, H., D’Odorico, S., Kaufer, A., Delabre, B., and Kotzlowski, H. (2000). Design, construction, and performance of UVES, the echelle spectrograph for the UT2 Kueyen Telescope at the ESO Paranal Observatory. In Iye, M. and Moorwood, A. F., editors, *Optical and IR Telescope Instrumentation and Detectors*, volume 4008 of *Society of Photo-Optical Instrumentation Engineers (SPIE) Conference Series*, pages 534–545.
- Deliyannis, C. P., Anthony-Twarog, B. J., Lee-Brown, D. B., and Twarog, B. A. (2019). Li Evolution and the Open Cluster NGC 6819: A Correlation between Li Depletion and Spindown in Dwarfs More Massive Than the F-Dwarf Li-Dip. *AJ*, 158(4):163.
- Diñel, B., Neuhäuser, R., Yerli, S. K., Ankaý, A., Tetzlaff, N., Torres, G., and Mugrauer, M. (2015). Discovery of an OB runaway star inside SNR S147. *MNRAS*, 448(4):3196–3205.
- Dubner, G. M., Velázquez, P. F., Goss, W. M., and Holdaway, M. A. (2000). High-Resolution VLA Imaging of the Supernova Remnant W28 at 328 and 1415 MHz. *AJ*, 120(4):1933–1945.

- Duchêne, G. and Kraus, A. (2013). Stellar Multiplicity. *ARAA*, 51(1):269–310.
- Eastman, J., Siverd, R., and Gaudi, B. S. (2010). Achieving Better Than 1 Minute Accuracy in the Heliocentric and Barycentric Julian Dates. *PASP*, 122(894):935.
- Ekström, S., Georgy, C., Eggenberger, P., Meynet, G., Mowlavi, N., Wyttenbach, A., Granada, A., Decressin, T., Hirschi, R., Frischknecht, U., Charbonnel, C., and Maeder, A. (2012). Grids of stellar models with rotation. I. Models from 0.8 to 120 M at solar metallicity ( $Z = 0.014$ ). *AAP*, 537:A146.
- Evans, D. W., Riello, M., De Angeli, F., Carrasco, J. M., Montegriffo, P., Fabricius, C., Jordi, C., Palaversa, L., Diener, C., Busso, G., Cacciari, C., van Leeuwen, F., Burgess, P. W., Davidson, M., Harrison, D. L., Hodgkin, S. T., Pancino, E., Richards, P. J., Altavilla, G., Balaguer-Núñez, L., Barstow, M. A., Bellazzini, M., Brown, A. G. A., Castellani, M., Coccozza, G., De Luise, F., Delgado, A., Ducourant, C., Galletti, S., Gilmore, G., Giuffrida, G., Holl, B., Kewley, A., Koposov, S. E., Marinoni, S., Marrese, P. M., Osborne, P. J., Piersimoni, A., Portell, J., Pulone, L., Ragaini, S., Sanna, N., Terrett, D., Walton, N. A., Wevers, T., and Wyrzykowski, Ł. (2018). Gaia Data Release 2. Photometric content and validation. *AAP*, 616:A4.
- Ferrand, G. and Safi-Harb, S. (2012). A census of high-energy observations of Galactic supernova remnants. *Advances in Space Research*, 49(9):1313–1319.
- Fesen, R. A., Hammell, M. C., Morse, J., Chevalier, R. A., Borkowski, K. J., Dopita, M. A., Gerardy, C. L., Lawrence, S. S., Raymond, J. C., and van den Bergh, S. (2006). The Expansion Asymmetry and Age of the Cassiopeia A Supernova Remnant. *APJ*, 645(1):283–292.
- Fesen, R. A., Neustadt, J. M. M., Black, C. S., and Milisavljevic, D. (2018a). A distance estimate to the Cygnus Loop based on the distances to two stars located within the remnant. *MNRAS*, 475(3):3996–4010.
- Fesen, R. A., Weil, K. E., Cisneros, I. A., Blair, W. P., and Raymond, J. C. (2018b). The Cygnus Loop’s distance, properties, and environment driven morphology. *MNRAS*, 481(2):1786–1798.
- Fesen, R. A., Winkler, F., Rathore, Y., Downes, R. A., Wallace, D., and Tweedy, R. W. (1997). Optical Imaging and Spectroscopy of the Galactic Supernova Remnants CTB 1 (G116.9+0.2), G116.5+1.1, and G114.3+0.3. *AJ*, 113:767–779.
- Filippenko, A. V. (1997). Optical Spectra of Supernovae. *ARAA*, 35:309–355.
- Fraser, M. and Boubert, D. (2019). The Quick and the Dead: Finding the Surviving Binary Companions of Galactic Supernovae with Gaia. *APJ*, 871(1):92.
- Gaensler, B. M., Brazier, K. T. S., Manchester, R. N., Johnston, S., and Green, A. J. (1999). SNR G320.4-01.2 and PSR B1509-58: new radio observations of a complex interacting system. *MNRAS*, 305(3):724–736.

## REFERENCES

---

- Gaia Collaboration, Brown, A. G. A., Vallenari, A., Prusti, T., de Bruijne, J. H. J., Babusiaux, C., Bailer-Jones, C. A. L., Biermann, M., Evans, D. W., Eyer, L., and et al. (2018). Gaia Data Release 2. Summary of the contents and survey properties. *AAP*, 616:A1.
- Gaia Collaboration, Brown, A. G. A., Vallenari, A., Prusti, T., de Bruijne, J. H. J., Babusiaux, C., and Biermann, M. (2020). Gaia Early Data Release 3: Summary of the contents and survey properties. *arXiv e-prints*, page arXiv:2012.01533.
- Gaia Collaboration, Brown, A. G. A., Vallenari, A., Prusti, T., de Bruijne, J. H. J., Mignard, F., Drimmel, R., Babusiaux, C., Bailer-Jones, C. A. L., Bastian, U., and et al. (2016a). Gaia Data Release 1. Summary of the astrometric, photometric, and survey properties. *AAP*, 595:A2.
- Gaia Collaboration, Prusti, T., de Bruijne, J. H. J., Brown, A. G. A., Vallenari, A., Babusiaux, C., Bailer-Jones, C. A. L., Bastian, U., Biermann, M., Evans, D. W., and et al. (2016b). The Gaia mission. *AAP*, 595:A1.
- García-Berro, E. and Lorén-Aguilar, P. (2017). *Dynamical Mergers*, page 1237. Handbook of Supernovae. Editors: Alsabti, Athem W. and Murdin, Paul.
- Geier, S., Fürst, F., Ziegerer, E., Kupfer, T., Heber, U., Irrgang, A., Wang, B., Liu, Z., Han, Z., Sesar, B., Levitan, D., Kotak, R., Magnier, E., Smith, K., Burgett, W. S., Chambers, K., Flewelling, H., Kaiser, N., Wainscoat, R., and Waters, C. (2015). The fastest unbound star in our Galaxy ejected by a thermonuclear supernova. *Science*, 347(6226):1126–1128.
- Geier, S., Marsh, T. R., Wang, B., Dunlap, B., Barlow, B. N., Schaffenroth, V., Chen, X., Irrgang, A., Maxted, P. F. L., Ziegerer, E., Kupfer, T., Miszalski, B., Heber, U., Han, Z., Shporer, A., Telting, J. H., Gänsicke, B. T., Østensen, R. H., O’Toole, S. J., and Napiwotzki, R. (2013). A progenitor binary and an ejected mass donor remnant of faint type Ia supernovae. *AAP*, 554:A54.
- Gies, D. R. and Bolton, C. T. (1986). The Binary Frequency and Origin of the OB Runaway Stars. *APJS*, 61:419.
- Gotthelf, E. V., Helfand, D. J., and Newburgh, L. (2007). A Shell of Thermal X-Ray Emission Surrounding the Young Crab-like Remnant 3C 58. *APJ*, 654(1):267–272.
- Gravity Collaboration, Abuter, R., Amorim, A., Bauböck, M., Berger, J. P., Bonnet, H., Brandner, W., Clénet, Y., Coudé Du Foresto, V., de Zeeuw, P. T., Dexter, J., Duvert, G., Eckart, A., Eisenhauer, F., Förster Schreiber, N. M., Garcia, P., Gao, F., Gendron, E., Genzel, R., Gerhard, O., Gillessen, S., Habibi, M., Haubois, X., Henning, T., Hippler, S., Horrobin, M., Jiménez-Rosales, A., Jocou, L., Kervella, P., Lacour, S., Lapeyrière, V., Le Bouquin, J. B., Léna, P., Ott, T., Paumard, T., Perraut, K., Perrin, G., Pfuhl, O., Rabien, S., Rodríguez Coira, G., Rousset, G., Scheithauer, S., Sternberg, A., Straub, O., Straubmeier, C., Sturm, E., Tacconi, L. J., Vincent, F., von Fellenberg, S., Waisberg, I., Widmann, F.,



- Wieprecht, E., Wiezorrek, E., Woillez, J., and Yazici, S. (2019). A geometric distance measurement to the Galactic center black hole with 0.3% uncertainty. *AAP*, 625:L10.
- Gray, R. O. and Corbally, C. J. (1994). The Calibration of MK Spectral Classes Using Spectral Synthesis. I. The Effective Temperature Calibration of Dwarf Stars. *AJ*, 107:742.
- Green, D. A. (1984). Statistical studies of supernova remnants. *MNRAS*, 209:449–478.
- Green, D. A. (1988). A Revised Reference Catalogue of Galactic Supernova Remnants. *APSS*, 148(1):3–74.
- Green, D. A. (1991). Limitations Imposed on Statistical Studies of Galactic Supernova Remnants by Observational Selection Effects. *PASP*, 103:209.
- Green, D. A. (1996). A Catalogue of Galactic Supernova Remnants. In Kuhn, T. S., editor, *IAU Colloq. 145: Supernovae and Supernova Remnants*, pages 419–424.
- Green, D. A. (2004). Galactic supernova remnants: an updated catalogue and some statistics. *Bulletin of the Astronomical Society of India*, 32:335–370.
- Green, D. A. (2009). A revised Galactic supernova remnant catalogue. *Bulletin of the Astronomical Society of India*, 37(1):45–61.
- Green, D. A. (2014). A catalogue of 294 Galactic supernova remnants. *Bulletin of the Astronomical Society of India*, 42(2):47–58.
- Green, D. A. (2019). A revised catalogue of 294 Galactic supernova remnants. *Journal of Astrophysics and Astronomy*, 40(4):36.
- Green, D. A. and Gull, S. F. (1982). Distance to Crab-like supernova remnant 3C58. *Nat*, 299(5884):606–608.
- Green, D. A. and Stephenson, F. R. (2003). *Historical Supernovae*, volume 598, pages 7–19.
- Gualandris, A. and Portegies Zwart, S. (2007). A hypervelocity star from the Large Magellanic Cloud. *MNRAS*, 376(1):L29–L33.
- Guseinov, O. H., Ankay, A., and Tagieva, S. O. (2005). Searching for Runaway OB Stars in Supernova Remnants. *Astrophysics*, 48(3):330–343.
- Gvaramadze, V. V. (2009). HD271791: dynamical versus binary-supernova ejection scenario. *MNRAS*, 395(1):L85–L89.
- Hambaryan, V., Neuhäuser, R., Suleimanov, V., and Werner, K. (2014). Observational constraints of the compactness of isolated neutron stars. In *Journal of Physics Conference Series*, volume 496 of *Journal of Physics Conference Series*, page 012015.
- Hambaryan, V., Suleimanov, V., Haberl, F., Schwope, A. D., Neuhäuser, R., Hohle, M., and Werner, K. (2017). The compactness of the isolated neutron star RX J0720.4-3125. *AAP*, 601:A108.
- Heap, S. R. and Brown, T. M. (1997). Correction for the STIS Echelle Blaze Function. In Casertano, S., Jedrzejewski, R., Keyes, T., and Stevens, M., editors, *The 1997 HST Calibration Workshop with a New Generation of Instruments*, page 114.

## REFERENCES

---

- Heber, U., Edelmann, H., Napiwotzki, R., Altmann, M., and Scholz, R. D. (2008). The B-type giant HD 271791 in the Galactic halo. Linking run-away stars to hyper-velocity stars. *AAP*, 483(2):L21–L24.
- Heiter, U., Lind, K., Asplund, M., Barklem, P. S., Bergemann, M., Magrini, L., Masseron, T., Mikolaitis, Š., Pickering, J. C., and Ruffoni, M. P. (2015). Atomic and molecular data for optical stellar spectroscopy. *physscr*, 90(5):054010.
- Henden, A. A., Levine, S., Terrell, D., and Welch, D. L. (2015). APASS - The Latest Data Release. In *American Astronomical Society Meeting Abstracts #225*, volume 225 of *American Astronomical Society Meeting Abstracts*, page 336.16.
- Henry, T. J. and McCarthy, Donald W., J. (1993). The Mass-Luminosity Relation for Stars of Mass 1.0 to 0.08M(solar). *AJ*, 106:773.
- Hills, J. G. (1988). Hyper-velocity and tidal stars from binaries disrupted by a massive Galactic black hole. *NAT*, 331(6158):687–689.
- Hobbs, G., Lorimer, D. R., Lyne, A. G., and Kramer, M. (2005). A statistical study of 233 pulsar proper motions. *MNRAS*, 360(3):974–992.
- Høg, E., Fabricius, C., Makarov, V. V., Urban, S., Corbin, T., Wycoff, G., Bastian, U., Schwendendiek, P., and Wicenec, A. (2000). The Tycho-2 catalogue of the 2.5 million brightest stars. *AAP*, 355:L27–L30.
- Honda, S. and Aoki, W. (2002). Subaru Telescope High Dispersion Spectrograph - An Atlas of Th-Ar Spectra. ver. 1.1:136.
- Hoogerwerf, R., de Bruijne, J. H. J., and de Zeeuw, P. T. (2001). On the origin of the O and B-type stars with high velocities. II. Runaway stars and pulsars ejected from the nearby young stellar groups. *AAP*, 365:49–77.
- Houk, N. (1978). *Michigan catalogue of two-dimensional spectral types for the HD stars*. University Microfilms International, 1978-, Ann Arbor : Dept. of Astronomy, University of Michigan.
- Hulse, R. A. and Taylor, J. H. (1975). Discovery of a pulsar in a binary system. *APJL*, 195:L51–L53.
- Irrgang, A. (2014). *Origin of runaway OB stars*. Doctoral thesis, Friedrich-Alexander-Universität Erlangen-Nürnberg (FAU).
- Janka, H. T., Scheck, L., Kifonidis, K., Müller, E., and Plewa, T. (2005). Supernova Asymmetries and Pulsar Kicks — Views on Controversial Issues. In Humphreys, R. and Stanek, K., editors, *The Fate of the Most Massive Stars*, volume 332 of *Astronomical Society of the Pacific Conference Series*, page 372.
- Jeffries, R. D. and Oliveira, J. M. (2005). The lithium depletion boundary in NGC 2547 as a test of pre-main-sequence evolutionary models. *MNRAS*, 358(1):13–29.
- Johnson, D. R. H. and Soderblom, D. R. (1987). Calculating Galactic Space Velocities and

- Their Uncertainties, with an Application to the Ursa Major Group. *AJ*, 93:864.
- Justham, S., Wolf, C., Podsiadlowski, P., and Han, Z. (2009). Type Ia supernovae and the formation of single low-mass white dwarfs. *AAP*, 493(3):1081–1091.
- Katsuda, S. and Tsunemi, H. (2008). XMM-Newton observations across the Cygnus Loop from northeastern rim to southwestern rim. *Advances in Space Research*, 41(3):383–389.
- Katsuda, S., Tsunemi, H., Mori, K., Uchida, H., Petre, R., Yamada, S., and Tamagawa, T. (2012). Discovery of a Pulsar Wind Nebula Candidate in the Cygnus Loop. *APJL*, 754(1):L7.
- Kilpatrick, C. D., Biegging, J. H., and Rieke, G. H. (2016). A Systematic Survey for Broadened CO Emission toward Galactic Supernova Remnants. *APJ*, 816(1):1.
- Kippenhahn, R. and Weigert, A. (1967). Entwicklung in engen Doppelsternsystemen I. Massenaustausch vor und nach Beendigung des zentralen Wasserstoff-Brennens. *ZAP*, 65:251.
- Kippenhahn, R. and Weigert, A. (1990). *Stellar Structure and Evolution*, volume : Corrected 3rd Printing 1994. Springer-Verlag, Astronomy and Astrophysics Library, Berlin, Heidelberg.
- Knie, K., Korschinek, G., Faestermann, T., Wallner, C., Scholten, J., and Hillebrandt, W. (1999). Indication for Supernova Produced  $^{60}\text{Fe}$  Activity on Earth. *PRL*, 83(1):18–21.
- Kochanek, C. S. (2018). Cas A and the Crab were not stellar binaries at death. *MNRAS*, 473(2):1633–1643.
- Kothes, R. (2013). Distance and age of the pulsar wind nebula 3C 58. *AAP*, 560:A18.
- Kothes, R., Fedotov, K., Foster, T. J., and Uyaniker, B. (2006). A catalogue of Galactic supernova remnants from the Canadian Galactic plane survey. I. Flux densities, spectra, and polarization characteristics. *AAP*, 457(3):1081–1093.
- Kothes, R., Sun, X. H., Reich, W., and Foster, T. J. (2014). G141.2+5.0, a New Pulsar Wind Nebula Discovered in the Cygnus Arm of the Milky Way. *APJL*, 784(2):L26.
- Koyama, K., Yamaguchi, H., and Bamba, A. (2008). X-Ray Spectroscopy of SN1006 with Suzaku. *Chinese Journal of Astronomy and Astrophysics Supplement*, 8:165–168.
- Kramer, M., Lyne, A. G., Hobbs, G., Löhmer, O., Carr, P., Jordan, C., and Wolszczan, A. (2003). The Proper Motion, Age, and Initial Spin Period of PSR J0538+2817 in S147. *APJL*, 593(1):L31–L34.
- Kramer, M. and Wex, N. (2009). TOPICAL REVIEW: The double pulsar system: a unique laboratory for gravity. *Classical and Quantum Gravity*, 26(7):073001.
- Krause, O., Tanaka, M., Usuda, T., Hattori, T., Goto, M., Birkmann, S., and Nomoto, K. (2008). Tycho Brahe’s 1572 supernova as a standard type Ia as revealed by its light-echo spectrum. *NAT*, 456(7222):617–619.
- Kroupa, P. and Weidner, C. (2005). *Variations of the IMF*, volume 327 of *Astrophysics and Space Science Library*, page 175.

## REFERENCES

---

- Kurucz, R. L. (1993). *SYNTHÉ spectrum synthesis program and line data*. Kurucz CD-ROM, Cambridge, MA: Smithsonian Astrophysical Observatory.
- Kurucz, R. L. (2005). ATLAS12, SYNTHÉ, ATLAS9, WIDTH9, et cetera. *Memorie della Societa Astronomica Italiana Supplementi*, 8:14.
- Lambert, D. L. and Reddy, B. E. (2004). Lithium abundances of the local thin disc stars. *MNRAS*, 349(2):757–767.
- Leahy, D. A. and Tian, W. W. (2007). Radio spectrum and distance of the SNR HB9. *AAP*, 461(3):1013–1018.
- Lejeune, T. and Schaerer, D. (2001). Database of Geneva stellar evolution tracks and isochrones for  $(UBV)_J(RI)_C$  JHKLL'M, HST-WFPC2, Geneva and Washington photometric systems. *AAP*, 366:538–546.
- Leonard, P. J. T. (1991). The Maximum Possible Velocity of Dynamically Ejected Runaway Stars. *AJ*, 101:562.
- LIGO Scientific Collaboration, Virgo Collaboration, Abbott, B. P., Abbott, R., Abbott, T. D., Abernathy, M. R., Acernese, F., Ackley, K., and et al. (2016). Observation of Gravitational Waves from a Binary Black Hole Merger. *PRL*, 116(6):061102.
- Livne, E. (1990). Successive Detonations in Accreting White Dwarfs as an Alternative Mechanism for Type I Supernovae. *APJL*, 354:L53.
- Lorimer, D. and Kramer, M. (2005). *Handbook of Pulsar Astronomy*. Cambridge University Press.
- Lux, O. (2013). The movement of pulsars in the galaxy and determination of their kinematic ages. Master thesis, Rheinische Friedrich-Wilhelms Universität Bonn.
- Lux, O., Neuhäuser, R., Mugrauer, M., and Bischoff, R. (2021). A search for runaway stars in 12 Galactic supernova remnants. *Astronomische Nachrichten*, 342(3):553–577.
- Manchester, R. N., Hobbs, G. B., Teoh, A., and Hobbs, M. (2005). The Australia Telescope National Facility Pulsar Catalogue. *AJ*, 129(4):1993–2006.
- Mannucci, F., Della Valle, M., Panagia, N., Cappellaro, E., Cresci, G., Maiolino, R., Petrosian, A., and Turatto, M. (2005). The supernova rate per unit mass. *AAP*, 433(3):807–814.
- Marigo, P., Bressan, A., Nanni, A., Girardi, L., and Pumo, M. L. (2013). Evolution of thermally pulsing asymptotic giant branch stars - I. The COLIBRI code. *MNRAS*, 434(1):488–526.
- McCullough, P. R., Fields, B. D., and Pavlidou, V. (2002). Discovery of an Old, Nearby, and Overlooked Supernova Remnant Centered on the Southern Constellation Antlia Pneumatica. *APJL*, 576(1):L41–L44.
- Meyer, D. M. A., Langer, N., Mackey, J., Velázquez, P. F., and Gusdorf, A. (2015). Asymmetric supernova remnants generated by Galactic, massive runaway stars. *MNRAS*, 450(3):3080–3100.
- Meyer, D. M. A., Petrov, M., and Pohl, M. (2020). Wind nebulae and supernova remnants of

- very massive stars. *MNRAS*, 493(3):3548–3564.
- Moe, M. and Di Stefano, R. (2017). Mind Your Ps and Qs: The Interrelation between Period (P) and Mass-ratio (Q) Distributions of Binary Stars. *APJS*, 230(2):15.
- Mugrauer, M. (2019). Search for stellar companions of exoplanet host stars by exploring the second ESA-Gaia data release. *MNRAS*, 490(4):5088–5102.
- Mugrauer, M., Avila, G., and Guirao, C. (2014). FLECHAS - A new échelle spectrograph at the University Observatory Jena. *Astronomische Nachrichten*, 335(4):417.
- Mugrauer, M. and Berthold, T. (2010). STK: A new CCD camera at the University Observatory Jena. *Astronomische Nachrichten*, 331(4):449.
- Neuhäuser, R. (1997). Low-mass pre-main sequence stars and their X-ray emission. *Science*, 276:1363–1370.
- Neuhäuser, R., Gießler, F., and Hambaryan, V. V. (2019). A nearby recent supernova that ejected the runaway star  $\zeta$  Oph, the pulsar PSR B1706-16, and  $^{60}\text{Fe}$  found on Earth. *MNRAS*, page 2261.
- Neunteufel, P. (2020). Exploring velocity limits in the thermonuclear supernova ejection scenario for hypervelocity stars and the origin of US 708. *AAP*, 641:A52.
- Noutsos, A., Schnitzeler, D. H. F. M., Keane, E. F., Kramer, M., and Johnston, S. (2013). Pulsar spin-velocity alignment: kinematic ages, birth periods and braking indices. *MNRAS*, 430(3):2281–2301.
- Oppenheimer, J. R. and Volkoff, G. M. (1939). On Massive Neutron Cores. *Physical Review*, 55(4):374–381.
- Pastorelli, G., Marigo, P., Girardi, L., Chen, Y., Rubele, S., Trabucchi, M., Aringer, B., Bladh, S., Bressan, A., Montalbán, J., Boyer, M. L., Dalcanton, J. J., Eriksson, K., Groenewegen, M. A. T., Höfner, S., Lebzelter, T., Nanni, A., Rosenfield, P., Wood, P. R., and Cioni, M.-R. L. (2019). Constraining the thermally pulsing asymptotic giant branch phase with resolved stellar populations in the Small Magellanic Cloud. *MNRAS*, 485(4):5666–5692.
- Pecaut, M. J. and Mamajek, E. E. (2013). Intrinsic Colors, Temperatures, and Bolometric Corrections of Pre-main-sequence Stars. *APJS*, 208(1):9.
- Perets, H. B. and Šubr, L. (2012). The Properties of Dynamically Ejected Runaway and Hyper-runaway Stars. *APJ*, 751(2):133.
- Perlmutter, S., Aldering, G., della Valle, M., Deustua, S., Ellis, R. S., Fabbro, S., Fruchter, A., Goldhaber, G., Groom, D. E., Hook, I. M., Kim, A. G., Kim, M. Y., Knop, R. A., Lidman, C., McMahon, R. G., Nugent, P., Pain, R., Panagia, N., Pennypacker, C. R., Ruiz-Lapuente, P., Schaefer, B., and Walton, N. (1998). Discovery of a supernova explosion at half the age of the Universe. *NAT*, 391(6662):51–54.
- Perryman, M. A. C. (1989). Hipparcos: astrometry from space. *NAT*, 340(6229):111–116.
- Perryman, M. A. C., Lindegren, L., Kovalevsky, J., Hog, E., Bastian, U., Bernacca, P. L., Creze,

## REFERENCES

---

- M., Donati, F., Grenon, M., Grewing, M., van Leeuwen, F., van der Marel, H., Mignard, F., Murray, C. A., Le Poole, R. S., Schrijver, H., Turon, C., Arenou, F., Froeschle, M., and Petersen, C. S. (1997). The Hipparcos Catalogue. *AAP*, 500:501–504.
- Pfau, W. (1984). 20 Jahre Beobachtungsstation Großschwabhausen der Universitäts-Sternwarte Jena. *Jenaer Rundschau*, 29(3):121–122.
- Phillips, M. M. (1993). The Absolute Magnitudes of Type IA Supernovae. *APJL*, 413:L105.
- Pilachowski, C. A., Booth, J., and Hobbs, L. M. (1987). The abundance of lithium in Pleiades F stars. *PASP*, 99:1288–1291.
- Pinsonneault, M. H. and Stanek, K. Z. (2006). Binaries Like to Be Twins: Implications for Doubly Degenerate Binaries, the Type Ia Supernova Rate, and Other Interacting Binaries. *APJL*, 639(2):L67–L70.
- Plez, B. (2012). Turbospectrum: Code for spectral synthesis.
- Pols, O. R. (2009). Stellar structure and evolution. Lecture notes on 'Stars and Stellar evolution', Rheinische Friedrich-Wilhelms Universität Bonn, WS 2011-2012.
- Pols, O. R., Tout, C. A., Lattanzio, J. C., and Karakas, A. I. (2001). Thermal Pulses and Dredge-up in AGB Stars. In Podsiadlowski, P., Rappaport, S., King, A. R., D'Antona, F., and Burderi, L., editors, *Evolution of Binary and Multiple Star Systems*, volume 229 of *Astronomical Society of the Pacific Conference Series*, page 31.
- Pourbaix, D., Tokovinin, A. A., Batten, A. H., Fekel, F. C., Hartkopf, W. I., Levato, H., Morell, N. I., Torres, G., and Udry, S. (2009). SB9: 9th Catalogue of Spectroscopic Binary Orbits (Pourbaix+ 2004-2014). *VizieR Online Data Catalog*, page B/sb9.
- Poveda, A., Ruiz, J., and Allen, C. (1967). Run-away Stars as the Result of the Gravitational Collapse of Proto-stellar Clusters. *Boletín de los Observatorios Tonantzintla y Tacubaya*, 4:86–90.
- Przybilla, N., Fernanda Nieva, M., Heber, U., and Butler, K. (2008). HD 271791: An Extreme Supernova Runaway B Star Escaping from the Galaxy. *APJL*, 684(2):L103.
- Pskovskii, I. P. (1978). The light curves of five galactic supernovae. *AZH*, 55:737–754.
- Queiroz, A. B. A., Anders, F., Santiago, B. X., Chiappini, C., Steinmetz, M., Dal Ponte, M., Stassun, K. G., da Costa, L. N., Maia, M. A. G., Crestani, J., Beers, T. C., Fernández-Trincado, J. G., García-Hernández, D. A., Roman-Lopes, A., and Zamora, O. (2018). StarHorse: a Bayesian tool for determining stellar masses, ages, distances, and extinctions for field stars. *MNRAS*, 476(2):2556–2583.
- Reed, J. E., Hester, J. J., Fabian, A. C., and Winkler, P. F. (1995). The Three-dimensional Structure of the Cassiopeia A Supernova Remnant. I. The Spherical Shell. *APJ*, 440:706.
- Renzo, M., Zapartas, E., de Mink, S. E., Götzberg, Y., Justham, S., Farmer, R. J., Izzard, R. G., Toonen, S., and Sana, H. (2019). Massive runaway and walkaway stars. A study of the kinematical imprints of the physical processes governing the evolution and explosion of

- their binary progenitors. *AAP*, 624:A66.
- Reynolds, S. P., Borkowski, K. J., Hwang, U., Hughes, J. P., Badenes, C., Laming, J. M., and Blondin, J. M. (2007). A Deep Chandra Observation of Kepler’s Supernova Remnant: A Type Ia Event with Circumstellar Interaction. *APJL*, 668(2):L135–L138.
- Reynoso, E. M., Cichowolski, S., and Walsh, A. J. (2017). A high-resolution H I study towards the supernova remnant Puppis A and its environments. *MNRAS*, 464(3):3029–3039.
- Riess, A. G., Strolger, L.-G., Casertano, S., Ferguson, H. C., Mobasher, B., Gold, B., Challis, P. J., Filippenko, A. V., Jha, S., Li, W., Tonry, J., Foley, R., Kirshner, R. P., Dickinson, M., MacDonald, E., Eisenstein, D., Livio, M., Younger, J., Xu, C., Dahlén, T., and Stern, D. (2007). New Hubble Space Telescope Discoveries of Type Ia Supernovae at  $z \lesssim 1$ : Narrowing Constraints on the Early Behavior of Dark Energy. *APJ*, 659(1):98–121.
- Salpeter, E. E. (1955). The Luminosity Function and Stellar Evolution. *APJ*, 121:161.
- Sana, H., de Mink, S. E., de Koter, A., Langer, N., Evans, C. J., Gieles, M., Gosset, E., Izzard, R. G., Le Bouquin, J. B., and Schneider, F. R. N. (2012). Binary Interaction Dominates the Evolution of Massive Stars. *Science*, 337(6093):444.
- Sana, H. and Evans, C. J. (2011). The multiplicity of massive stars. In Neiner, C., Wade, G., Meynet, G., and Peters, G., editors, *Active OB Stars: Structure, Evolution, Mass Loss, and Critical Limits*, volume 272 of *IAU Symposium*, pages 474–485.
- Sbordone, L., Bonifacio, P., Castelli, F., and Kurucz, R. L. (2004). ATLAS and SYNTHE under Linux. *Memorie della Societa Astronomica Italiana Supplementi*, 5:93.
- Sbordone, L. and Ledoux, C. (2017). *UV-Visual Echelle Spectrograph User manual, Issue 100*. European Southern Observatory.
- Sbordone, L. and Ledoux, C. (2020). *UVES Calibration Plan, Issue 106*. European Southern Observatory.
- Schaefer, B. E. (1996a). Peak Brightnesses of Historical Supernovae and the Hubble Constant. *APJ*, 459:438.
- Schaefer, B. E. (1996b). Volume-limited Samples of Supernovae. *APJ*, 464:404.
- Schaller, G., Schaerer, D., Meynet, G., and Maeder, A. (1992). New grids of stellar models from 0.8 to 120  $M_{\text{sun}}$  at  $Z=0.020$  and  $Z=0.001$ . *AAPS*, 96:269.
- Schneider, F. R. N., Podsiadlowski, P., Langer, N., Castro, N., and Fossati, L. (2016). Rejuvenation of stellar mergers and the origin of magnetic fields in massive stars. *MNRAS*, 457(3):2355–2365.
- Schwarzschild, M. and Härm, R. (1965). Thermal Instability in Non-Degenerate Stars. *APJ*, 142:855.
- Sedov, L. I. (1959). *Similarity and Dimensional Methods in Mechanics*. Academic Press, New York, London.
- Sestito, P. and Randich, S. (2005). Time scales of Li evolution: a homogeneous analysis of

## REFERENCES

---

- open clusters from ZAMS to late-MS. *AAP*, 442(2):615–627.
- Siess, L., Dufour, E., and Forestini, M. (2000). An internet server for pre-main sequence tracks of low- and intermediate-mass stars. *AAP*, 358:593–599.
- Skiff, B. A. (2009). Catalogue of Stellar Spectral Classifications (Skiff, 2010). *VizieR Online Data Catalog*, page B/mk.
- Slane, P., Zimmerman, E. R., Hughes, J. P., Seward, F. D., Gaensler, B. M., and Clarke, M. J. (2004). X-Ray Observations of the Compact Source in CTA 1. *APJ*, 601(2):1045–1049.
- Snedden, C., Bean, J., Ivans, I., Lucatello, S., and Sobek, J. (2012). MOOG: LTE line analysis and spectrum synthesis.
- Soderblom, D. R. (2010). The Ages of Stars. *ARAA*, 48:581–629.
- Soderblom, D. R., Hillenbrand, L. A., Jeffries, R. D., Mamajek, E. E., and Naylor, T. (2014). Ages of Young Stars. In Beuther, H., Klessen, R. S., Dullemond, C. P., and Henning, T., editors, *Protostars and Planets VI*, page 219.
- Soderblom, D. R., Jones, B. F., Balachandran, S., Stauffer, J. R., Duncan, D. K., Fedele, S. B., and Hudon, J. D. (1993). The Evolution of the Lithium Abundances of Solar-Type Stars. III. The Pleiades. *AJ*, 106:1059.
- Sorokina, E. I., Blinnikov, S. I., Kosenko, D. I., and Lundqvist, P. (2004). Dynamics and Radiation of Young Type-Ia Supernova Remnants: Important Physical Processes. *Astronomy Letters*, 30(11):737–750.
- Steinhauer, A. (2003). *Formation and evolution of the open cluster lithium gap*. PhD thesis, Indiana University.
- Steinhauer, A. and Deliyannis, C. P. (2004). WIYN/Hydra Detection of Lithium Depletion in F Stars of the Young Open Cluster M35 and Implications for the Development of the Lithium Gap. *APJL*, 614(1):L65–L68.
- Steinhauer, A. and Deliyannis, C. P. (2021). submitted.
- Stephenson, F. R. and Green, D. A. (2002). Historical supernovae and their remnants. *International Series in Astronomy and Astrophysics*, 5.
- Stone, R. C. (1979). Kinematics, close binary evolution, and ages of the O stars. *APJ*, 232:520–530.
- Sushch, I., Hnatyk, B., and Neronov, A. (2011). Modeling of the Vela complex including the Vela supernova remnant, the binary system  $\gamma^2$  Velorum, and the Gum nebula. *AAP*, 525:A154.
- Swartz, D. A., Pavlov, G. G., Clarke, T., Castelletti, G., Zavlin, V. E., Bucciantini, N., Karovska, M., van der Horst, A. J., Yukita, M., and Weisskopf, M. C. (2015). High Spatial Resolution X-Ray Spectroscopy of the IC 443 Pulsar Wind Nebula and Environs. *APJ*, 808(1):84.
- Tauris, T. M. (2015). Maximum speed of hypervelocity stars ejected from binaries. *MNRAS*,



- 448:L6–L10.
- Tauris, T. M. and van den Heuvel, E. P. J. (2006). *Formation and evolution of compact stellar X-ray sources*, volume 39, pages 623–665.
- Taylor, G. (1950). The Formation of a Blast Wave by a Very Intense Explosion. I. Theoretical Discussion. *Proceedings of the Royal Society of London Series A*, 201(1065):159–174.
- Taylor, J. H. (1992). Pulsar Timing and Relativistic Gravity. *Philosophical Transactions of the Royal Society of London Series A*, 341(1660):117–134.
- Tetzlaff, N. (2013). *Identifying birth places of young neutron stars to determine their kinematic age*. Doctoral thesis, Friedrich-Schiller-Universität Jena (FSU).
- Tetzlaff, N., Dinçel, B., Neuhäuser, R., and Kovtyukh, V. V. (2014a). The origin of the young pulsar PSR J0826+2637 and its possible former companion HIP 13962. *MNRAS*, 438(4):3587–3593.
- Tetzlaff, N., Eisenbeiss, T., Neuhäuser, R., and Hohle, M. M. (2011a). The origin of RX J1856.5-3754 and RX J0720.4-3125 - updated using new parallax measurements. *MNRAS*, 417(1):617–626.
- Tetzlaff, N., Neuhäuser, R., and Hohle, M. M. (2009). The origin of the Guitar pulsar. *MNRAS*, 400(1):L99–L102.
- Tetzlaff, N., Neuhäuser, R., and Hohle, M. M. (2011b). A catalogue of young runaway Hipparcos stars within 3 kpc from the Sun. *MNRAS*, 410(1):190–200.
- Tetzlaff, N., Neuhäuser, R., Hohle, M. M., and Maciejewski, G. (2010). Identifying birth places of young isolated neutron stars. *MNRAS*, 402(4):2369–2387.
- Tetzlaff, N., Schmidt, J. G., Hohle, M. M., and Neuhäuser, R. (2012). Neutron Stars From Young Nearby Associations: The Origin of RX J1605.3+3249. *PASA*, 29(2):98–108.
- Tetzlaff, N., Torres, G., Bieryla, A., and Neuhäuser, R. (2014b). New radial velocities for 30 candidate runaway stars and a possible binary supernova origin for HIP 9470 and PSR J0152-1637. *Astronomische Nachrichten*, 335(9):981.
- Tetzlaff, N., Torres, G., Neuhäuser, R., and Hohle, M. M. (2013). The neutron star born in the Antlia supernova remnant. *MNRAS*, 435(1):879–884.
- Thorburn, J. A., Hobbs, L. M., Deliyannis, C. P., and Pinsonneault, M. H. (1993). Lithium in the Hyades. I. New Observations. *APJ*, 415:150.
- Thorstensen, J. R., Fesen, R. A., and van den Bergh, S. (2001). The Expansion Center and Dynamical Age of the Galactic Supernova Remnant Cassiopeia A. *AJ*, 122(1):297–307.
- Toor, A. (1980). X-ray characteristics of the Lupus loop and SN 1006 SNR. *AAP*, 85:184–190.
- Trimble, V. (1968). Motions and Structure of the Filamentary Envelope of the Crab Nebula. *AJ*, 73:535.
- Trimble, V. (1973). The Distance to the Crab Nebula and NP 0532. *PASP*, 85(507):579.
- Truelove, J. K. and McKee, C. F. (1999). Evolution of Nonradiative Supernova Remnants.

## REFERENCES

---

- APJS*, 120(2):299–326.
- Valenti, J. A. and Piskunov, N. (1996). Spectroscopy made easy: A new tool for fitting observations with synthetic spectra. *AAPS*, 118:595–603.
- Vennes, S., Nemeth, P., Kawka, A., Thorstensen, J. R., Khalack, V., Ferrario, L., and Alper, E. H. (2017). An unusual white dwarf star may be a surviving remnant of a subluminous Type Ia supernova. *Science*, 357(6352):680–683.
- Verbiest, J. P. W., Weisberg, J. M., Chael, A. A., Lee, K. J., and Lorimer, D. R. (2012). On Pulsar Distance Measurements and Their Uncertainties. *APJ*, 755(1):39.
- Vink, J. (2012). Supernova remnants: the X-ray perspective. *AAPR*, 20:49.
- Voroshilov, V. I., Guseva, N. G., Kalandadze, N. B., Kolesnik, L. N., Kuznetsov, V. I., Metreveli, M. D., and Shapovalov, A. N. (1985). *Catalogue of BV magnitudes and spectral classes for 6000 stars. Ukrainian Acad. Nauk, Kiev, 1-140.*
- Wallace, B. J., Landecker, T. L., and Taylor, A. R. (1994). H I voids around filled-center supernova remnants. *AAP*, 286:565–578.
- Wallner, A., Feige, J., Kinoshita, N., Paul, M., Fifield, L. K., Golser, R., Honda, M., Linnemann, U., Matsuzaki, H., Merchel, S., Rugel, G., Tims, S. G., Steier, P., Yamagata, T., and Winkler, S. R. (2016). Recent near-Earth supernovae probed by global deposition of interstellar radioactive  $^{60}\text{Fe}$ . *NAT*, 532(7597):69–72.
- Wang, Z. R., Qu, Q. Y., and Chen, Y. (1997). Is RX J1713.7-3946 the remnant of the AD393 guest star? *AAP*, 318:L59–L61.
- Welsh, B. Y., Sallmen, S., Sfeir, D., and Lallement, R. (2002). Interstellar NaI and CaII absorption observed towards the Cygnus Loop SNR. *AAP*, 391:705–711.
- Welsh, B. Y., Sfeir, D. M., Sallmen, S., and Lallement, R. (2001). Far Ultraviolet Spectroscopic Explorer observations of high-velocity gas associated with the Monoceros Loop SNR. *AAP*, 372:516–526.
- Winkler, P. F., J., Hearn, D. R., Richardson, J. A., and Behnken, J. M. (1979). Soft X-ray emission from the Lupus Loop and SN 1006 supernova remnants. *APJL*, 229:L123–L128.
- Winkler, P. F., Gupta, G., and Long, K. S. (2003). The SN 1006 Remnant: Optical Proper Motions, Deep Imaging, Distance, and Brightness at Maximum. *APJ*, 585(1):324–335.
- Woltjer, L. (1972). Supernova Remnants. *ARAA*, 10:129.
- Woosley, S. and Janka, T. (2005). The physics of core-collapse supernovae. *Nature Physics*, 1(3):147–154.
- Woosley, S. E., Heger, A., and Weaver, T. A. (2002). The evolution and explosion of massive stars. *Reviews of Modern Physics*, 74(4):1015–1071.
- Xue, Z. and Schaefer, B. E. (2015). Newly Determined Explosion Center of Tycho’s Supernova and the Implications for Proposed Ex-companion Stars of the Progenitor. *APJ*,

- 809(2):183.
- Yao, J. M., Manchester, R. N., and Wang, N. (2017). A New Electron-density Model for Estimation of Pulsar and FRB Distances. *APJ*, 835(1):29.
- Yar-Uyaniker, A., Uyaniker, B., and Kothes, R. (2004). Distance of Three Supernova Remnants from H I Line Observations in a Complex Region: G114.3+0.3, G116.5+1.1, and CTB 1 (G116.9+0.2). *APJ*, 616(1):247–256.
- Yu, B., Chen, B. Q., Jiang, B. W., and Zijlstra, A. (2019). Three-dimensional dust mapping of 12 supernovae remnants in the Galactic anticentre. *MNRAS*, 488(3):3129–3142.
- Zdziarski, A. A., Malyshev, D., de Oña Wilhelmi, E., Pedalletti, G., Yang, R., Chernyakova, M., López-Caniego, M., Mikołajewska, J., and Basak, R. (2016). The high-energy gamma-ray detection of G73.9+0.9, a supernova remnant interacting with a molecular cloud. *MNRAS*, 455(2):1451–1458.
- Zehe, T., Mugrauer, M., Neuhäuser, R., Pannicke, A., Lux, O., Bischoff, R., Wöckel, D., and Wagner, D. (2018). The radial and rotational velocity of  $\zeta$  Ophiuchi. *Astronomische Nachrichten*, 339(1):46–52.
- Zhao, H., Jiang, B., Gao, S., Li, J., and Sun, M. (2018). The Distance to and the Near-infrared Extinction of the Monoceros Supernova Remnant. *APJ*, 855(1):12.
- Zhou, X., Yang, J., Fang, M., Su, Y., Sun, Y., and Chen, Y. (2016). Interaction between the Supernova Remnant HB 3 and the Nearby Star-forming Region W3. *APJ*, 833(1):4.

REFERENCES

---

# Danksagung

An dieser Stelle möchte ich mich bei all den Menschen bedanken, die auf verschiedene Weise zum Gelingen dieser Arbeit beigetragen haben.

Zunächst danke ich Prof. Ralph Neuhäuser, der es mir ermöglicht hat, die Promotion am Astrophysikalischen Institut durchzuführen. Er hat das Thema konzipiert, die Finanzierung des Projekts eingeworben, stand mir immer mit Ratschlägen zur Seite und hat immer an mich geglaubt.

Meinem Zweitgutachter Prof. Ulrich Heber und dem Drittgutachter Prof. Ernst Paunzen danke ich einerseits für viele wertvolle Hinweise zur Verbesserung der Arbeit, die sie mir im Rahmen des Promotionsverfahrens und der Disputation gegeben haben, andererseits auch für viele interessante Gespräche bei Konferenzen und Kooperationsbesuchen.

Mein Dank gilt zudem meinen Kollegen, insbesondere Dr. Markus Mugrauer und Richard Bischoff für eine erfolgreiche Zusammenarbeit und zahlreiche Hinweise zum Gelingen des Projekts. Richard Bischoff hat zudem die Daten aus Abb. 5.5 digitalisiert, die dann zum Plotten der Kurven in Abb. 5.8 genutzt wurden. Ich danke meinen Ko-Investigatoren Ralph Neuhäuser, Markus Mugrauer, Anna Pannicke und Baha Dinçel, die mit ihrer Beobachtungserfahrung viele Tips zur Planung der Beobachtungen und zum Vorbereiten der Proposal geben konnten. Ein besonderer Dank geht an Wolfgang Stenglein für die erfolgreiche Zusammenarbeit bei den  $H\alpha$ -Beobachtungen von Supernova-Überresten und deren Auswertung; insbesondere für die Bildbearbeitung, die in großen Teilen von ihm gemacht wurde.

Weiterhin danke ich Jürgen Weiprecht und Dr. Frank Gießler für ihren IT-Support, bzw. für ihren unermüdlichen Einsatz, meine diversen Computer-Probleme zu beheben sowie Dr. Daniel Wagner, Dr. Valeri Hambaryan, Dr. Dr. Susanne Hoffmann und Dr. Christian Adam für viele erkenntnisreiche Gespräche.

Große Teile dieser Arbeit basieren auf Daten des ESO VLT aus Projekt 0100.D-0314 und des NAOJ Subaru-Teleskops aus Projekt S18B0195S. Daher danke ich den Mitarbeitern und Support-Astronomen der ESO und des NAOJ, insbesondere John Pritchard (ESO), Chie Yoshida und Akito Tajitsu (NAOJ) für die Durchführung der Service-Beobachtungen sowie wertvolle Hinweise zur Datenreduktion.

Ein großer Dank geht an Sergi Blanco-Cuaresma für viele wichtige Hinweise zum Umgang mit *iSpec* und der Analyse stellarer Spektren im Allgemeinen, an Eric Mamajek für das Bereitstellen von Daten und Fits zum Zusammenhang zwischen  $T_{\text{eff}}$  und  $EW_{\text{Li}}$  bei Sternhaufen verschiedener Alter, und an Aaron Steinhauer für das Bereitstellen der Daten zum Zusammenhang zwischen  $\log(N_{\text{Li}})$ ,  $v_{\text{rot}} \sin(i)$  und Sternalter.

Für das Korrekturlesen des Manuskripts dieser Arbeit und für viele wertvolle Hinweise bedanke ich mich herzlich bei Richard Bischoff, Michael Geymeier, Patrick Neunteufel und Daniel Wagner.

Diese Arbeit präsentiert Ergebnisse der ESA-Mission *Gaia*<sup>1</sup>. *Gaia*-Daten wurden vom *Gaia Data Processing and Analysis Consortium* (DPAC) verarbeitet und bereitgestellt. Die Arbeit konnte nur gelingen durch intensive Nutzung von *VizieR*, *Simbad* und *Aladin*, die vom *Centre de Donnée astronomiques de Strasbourg* (CDS) zur Verfügung gestellt werden. Außerdem wurde der Pulsar-Katalog der *Australia Telescope National Facility* (ATNF, Manchester et al. 2005) genutzt. Ich möchte den vielen Astronomen danken, die zum Zusammenstellen und Veröffentlichen dieser und weiterer im Text beschriebener Kataloge und Programme beigetragen haben.

Mein besonderer Dank gilt meiner Familie; meiner Mutter Sibille Lux für ihre große Unterstützung und dass sie immer für mich da ist, meinem Vater Hans-Dieter Lux, der mir so viel Gutes mit auf den Weg des Lebens gegeben hat, aber leider während dieser Promotion verstorben ist, und meiner Schwester Christina Lux, immer eine Quelle der Inspiration und Weiterentwicklung.

Nicht zuletzt danke ich einem ganz besonderen Menschen in meinem Leben: Melano Dadalauri für ihren tiefen Glauben an meine Stärken, für die schöne gemeinsame Zeit und dass sie es immer wieder schafft, mich zu begeistern.

Die Promotion wurde finanziert durch die Deutsche Forschungsgemeinschaft, Projekt NE 515/57-1.

---

<sup>1</sup><https://www.cosmos.esa.int/gaia>

# Ehrenwörtliche Erklärung

Ich erkläre hiermit ehrenwörtlich, dass ich die vorliegende Arbeit selbständig, ohne unzulässige Hilfe Dritter und ohne Benutzung anderer als der angegebenen Hilfsmittel und Literatur angefertigt habe. Die aus anderen Quellen direkt oder indirekt übernommenen Daten und Konzepte sind unter Angabe der Quelle gekennzeichnet.

Bei der Auswahl und Auswertung dieser Arbeit haben mir die nachstehend aufgeführten Personen in beratender Weise unentgeltlich geholfen:

- Prof. Dr. Ralph Neuhäuser
- Dr. Markus Mugrauer
- St.Ex. Richard Bischoff
- B.Sc. Wolfgang Stenglein

Weitere Personen waren an der inhaltlich-materiellen Erstellung der vorliegenden Arbeit nicht beteiligt. Insbesondere habe ich hierfür nicht die entgeltliche Hilfe von Vermittlungs- bzw. Beratungsdiensten (Promotionsberater oder andere Personen) in Anspruch genommen. Niemand hat von mir unmittelbar oder mittelbar geldwerte Leistungen für Arbeiten erhalten, die im Zusammenhang mit dem Inhalt der vorgelegten Dissertation stehen.

Die Arbeit wurde bisher weder im In- noch im Ausland in gleicher oder ähnlicher Form einer anderen Prüfungsbehörde vorgelegt.

Die geltende Promotionsordnung der Physikalisch-Astronomischen Fakultät ist mir bekannt.

Ich versichere ehrenwörtlich, dass ich nach bestem Wissen die reine Wahrheit gesagt und nichts verschwiegen habe.

Jena, 05.10.2021

---

Oliver Lux